



**A University of Sussex PhD thesis**

Available online via Sussex Research Online:

<http://sro.sussex.ac.uk/>

This thesis is protected by copyright which belongs to the author.

This thesis cannot be reproduced or quoted extensively from without first obtaining permission in writing from the Author

The content must not be changed in any way or sold commercially in any format or medium without the formal permission of the Author

When referring to this work, full bibliographic details including the author, title, awarding institution and date of the thesis must be given

Please visit Sussex Research Online for more information and further details



# Towards high resolution spectroscopy of molecular nitrogen ions

Laura Blackburn

Submitted for the degree of Doctor of Philosophy  
University of Sussex  
September 2021

# Declaration

I hereby declare that this thesis has not been, and will not be, submitted in whole or in part to another University for the award of any other degree. This thesis is my own work, except where explicitly stated.

Signature:

Laura Jane Blackburn  
September 29, 2021

## UNIVERSITY OF SUSSEX

Laura Jane Blackburn, Doctor of Philosophy

TOWARDS HIGH RESOLUTION SPECTROSCOPY OF MOLECULAR  
NITROGEN IONS

## Summary

High resolution spectroscopy of molecular nitrogen ions is a promising candidate for measurement of potential time variation in the proton-to-electron mass ratio. In our experiment, a vibrational Raman transition in a nitrogen ion will be compared with a quadrupole transition in an atomic calcium ion, which will act as a frequency reference and be used for the cooling and state detection of the nitrogen ion.

High resolution spectroscopy of molecular ions requires that the initial rovibronic state of the ion is well controlled. In low, homogenous electric fields, resonance-enhanced multiphoton ionisation (REMPI) can be used to load molecular ions into one state with high fidelity. However, in the presence of electric fields, ionisation spectra exhibit frequency shifts and the ionisation thresholds are broadened. The expected broadening of the ionisation threshold was simulated under various operating conditions of a typical linear Paul trap. In many cases, the width of the ionisation threshold exceeded the separation between rotational energy levels, preventing state-selective ionisation. Where other mitigation strategies are not sufficient, it may be necessary to switch the trapping fields off rapidly during loading. Rapid switching of the trap drive has been demonstrated without the loss of ions for switching of both the rf and dc fields and the consequent heating has been characterised. Nitrogen ions have been loaded into the ion trap via 2+2 REMPI while the electric trapping fields were minimised using this rapid switching technique.

In addition, the ten transition peaks and motional sidebands of the  $S_{1/2} \rightarrow D_{5/2}$  quadrupole transition in  $^{40}\text{Ca}^+$  were observed and characterised. Fits to the spectra yielded a fractional resolution of  $\frac{\Delta\nu}{\nu} \sim 1 \times 10^{-11}$ . Further stabilisation of the magnetic field will be necessary to improve these preliminary spectra.

# Acknowledgements

This thesis describes work done over the last four years under the supervision of Prof Matthias Keller in the ITCM group at the University of Sussex. Finishing a PhD in the midst of a global pandemic has brought its challenges and I have a lot of people to thank. First of all, I would like to thank my supervisor, Matthias, for giving me the opportunity to work on this experiment and for his patience and guidance throughout the process. I have really appreciated his encouragement and support through the more challenging times.

When I first joined the ITCM group, I was put in the hands of the brilliant and ever-patient Amy Gardner who taught me the ropes and welcomed me onto the experiment. I am hugely grateful for all the hours she spent explaining things to me and for her endless enthusiasm and good humour in the lab. Not to mention all of the work she put into the project! I would also like to thank Xavi Fernandez-Gonzalvo whose empathy and technical expertise in the lab over the last couple of years have been invaluable!

Over the past four years, I have enjoyed working with everyone in the ITCM group: Hiroki Takahashi, Ezra Kassa, Costas Christoforou, Corentin Pignot, Hamzah Shokeir, Tom Walker, Samir Vartabi Kashanian, Travers Ward, Callan Jobson, Nathan Gemmel, Sam Snowdon, David Kay and Graham Stutter. Thank you all for your help and support; it's been great working with you. In addition, I would like to thank Alan Butler and Chris Moore for their help in the mechanical workshop and Cassandra Churchwell for her help with the lab infrastructure, particularly with the air conditioning.

I am also very lucky to have such great support from my family and friends. To my parents and my siblings, Tom and Zo, thank you for all your support and encouragement through this process. And for taking on the mammoth task of proof-reading this thesis for me! To my wider family and friends, I can't thank everyone properly here, but I will thank you all individually!

# Contents

Summary . . . . .	iii
Acknowledgements . . . . .	iv
List of Tables . . . . .	vii
List of Figures . . . . .	viii
Abbreviations . . . . .	xvi
Diagram Key . . . . .	xvii
<b>1 Introduction</b>	<b>1</b>
1.1 Variation in Fundamental Constants . . . . .	1
1.2 Atoms and Molecules to Measure Fundamental Constants . . . . .	2
1.3 Candidates for New Measurements . . . . .	3
1.4 $N_2^+$ Ion for Probing Stability of $\mu$ . . . . .	4
1.5 Experiment Overview . . . . .	5
1.6 Thesis Overview . . . . .	6
<b>2 Theory: Ion Traps and Molecular Beams</b>	<b>8</b>
2.1 Linear Paul Traps . . . . .	8
2.2 Molecular Beams . . . . .	13
<b>3 Theory: Light and Matter</b>	<b>17</b>
3.1 Radiative Transitions . . . . .	17
3.2 Laser Cooling . . . . .	25
3.3 Atomic and Molecular Spectra . . . . .	27
<b>4 Ion Trap, Lasers and Imaging</b>	<b>32</b>
4.1 Ion Trap . . . . .	32
4.2 Imaging System . . . . .	35
4.3 Level System of $Ca^+$ . . . . .	39
4.4 Doppler Cooling and Ion Fluorescence . . . . .	40
4.5 Laser Stabilisation . . . . .	42
4.6 Trap Characterisation . . . . .	43
4.7 Crystal Weighing . . . . .	44
4.8 Micromotion Compensation . . . . .	48
<b>5 Photoionisation of Molecules in rf Ion Traps</b>	<b>55</b>
5.1 Introduction . . . . .	55
5.2 The Electric Trapping Field . . . . .	55
5.3 Rydberg Molecules in Electric Fields . . . . .	56
5.4 Ionisation Spectra in Electric Fields . . . . .	58
5.5 Simulation Methods . . . . .	59
5.6 Results . . . . .	68
5.7 Discussion . . . . .	74

<b>6</b>	<b>Switching of the Trap Drive</b>	<b>76</b>
6.1	Introduction . . . . .	76
6.2	Decay of the Electric Field in a Resonator . . . . .	77
6.3	Methods . . . . .	78
6.4	Results . . . . .	81
6.5	Discussion . . . . .	91
<b>7</b>	<b>Experimental Loading of Nitrogen Ions</b>	<b>93</b>
7.1	Introduction . . . . .	93
7.2	The 2+1' Ionisation Process . . . . .	94
7.3	Competing Ionisation Processes . . . . .	95
7.4	Simulated Ionisation Threshold . . . . .	97
7.5	Experimental Set-Up . . . . .	98
7.6	Electron Ionisation Measurements . . . . .	103
7.7	2+2 REMPI Measurements . . . . .	106
7.8	Discussion . . . . .	108
<b>8</b>	<b>Quadrupole Spectroscopy of Calcium Ions</b>	<b>110</b>
8.1	Introduction . . . . .	110
8.2	The $S_{1/2} \rightarrow D_{5/2}$ Transition . . . . .	110
8.3	Experimental Set-Up and Methods . . . . .	112
8.4	Results . . . . .	118
8.5	Discussion . . . . .	121
<b>9</b>	<b>Conclusions and Outlook</b>	<b>123</b>
9.1	Conclusions . . . . .	123
9.2	Outlook . . . . .	125
	<b>Bibliography</b>	<b>128</b>
	<b>Appendices</b>	<b>140</b>
<b>A</b>	<b>Data Availability</b>	<b>140</b>
<b>B</b>	<b>Automation of the Loading Process</b>	<b>141</b>
B.1	Overview . . . . .	141
B.2	Micromotion Compensation Sequence . . . . .	143
B.3	Crystal Weighing . . . . .	144
B.4	Crystal Cleaning . . . . .	144
<b>C</b>	<b>Nitrogen Ionisation Laser</b>	<b>146</b>
<b>D</b>	<b>Simulation Methods: Quadrupole Spectra</b>	<b>148</b>
D.1	The Quadrupole Spectrum . . . . .	148
D.2	The Motional Spectrum . . . . .	149

# List of Tables

1.1	Details of the $v = 0 \rightarrow v = 2$ transition in the $^{14}\text{N}_2^+$ ion. . . . .	4
3.1	Selection rules for electric dipole (one- and two-photon) and quadrupole transitions. <sup>1</sup> Selection rules marked with a star cannot occur between two states with $l = 0$ . . . . .	24
4.1	The lasers used in the experiments described in this thesis, their roles, locking wavelengths ( $\lambda$ ) and linewidths. <sup>2</sup> Acousto-optic modulators (AOMs) are used to shift the frequency of the cooling, repumping and spectroscopy lasers by approximately 400 MHz from the wavelengths listed here. . . . .	39
7.1	The parameters used for the molecular beamline. *The pulse valve is controlled by a homemade unit provided by the University of Oxford which quotes the set actuation voltage in %. . . . .	102
D.1	Table of Clebsch-Gordan (CG) coefficients and couplings for the relevant transitions in the calcium-40 ion . . . . .	149

# List of Figures

1.1	The experimental set-up for the experiment, showing the ion trap and molecular beam line. TMP = turbomolecular pump. Diagram made by A. Gardner. <sup>3</sup> . . . . .	6
2.1	Ince-Strutt stability diagrams for a linear Paul trap, plotted using the analytical expressions from E. Butikov. (a) The stability regions in $x$ and $y$ . The shaded regions represent regions where the ion motion is stable and trapping is possible. (b) The first stability region for calcium ions and nitrogen ions, in terms of the $q$ and $a$ parameters of calcium. . . . .	11
2.2	Motion of a trapped ion in one radial axis from a 3D molecular dynamics simulation. . . . .	12
2.3	Shock boundaries and expansion zones for the expansion of a supersonic molecular beam. . . . .	15
3.1	Energy level diagram for a two level system coupled by a laser. . . . .	18
3.2	Energy level system for a two photon process which proceeds from state $ 1\rangle$ to state $ 2\rangle$ via an intermediate virtual state $ v\rangle$ . . . . .	21
4.1	Schematic drawing of the ion trap and its housing. The inter-electrode distances are shown with a top view and a cut through the centre of the trap in the radial plane. . . . .	33
4.2	The ionisation scheme for loading $^{40}\text{Ca}^+$ into the ion trap. The first photon at 423 nm excites the atom from the ground $4s^2$ state into the first excited state $4s^1 4p^1$ . From this intermediate state, the atom is ionised with a photon of 375 nm. . . . .	34
4.3	Schematic diagram of the rf resonator circuit. A sinusoidal electronic signal is applied to the primary coil of a transformer. The amplified signal from the secondary coil is connected to two diagonal radial electrodes at a bias tee. The other two electrodes are held at rf ground. An additional dc voltage is connected to each electrode in order to compensate for stray fields that cause excess micromotion. . . . .	35

4.4	Images of rf circuit feedthrough box and circuit. (a) An external view of the box containing the rf circuit. (b) The endplate for the box showing the secondary/resonator coil and the nearby pick-up coil for monitoring of the rf drive. (c) An internal view of the box looking from the position of the rf feedthroughs. At the back of this image is the resonator coil which is mounted in a teflon holder. The signal from the resonator is split into two identical paths and each is combined with a dc micromotion compensation voltage. The paths for the grounded electrodes are very similar, but the fast input to the bias tee is held at ground. (d) A view of the circuit through one of the mesh covered holes used for ventilation of the circuit to prevent overheating. . . . .	36
4.5	The resonance of the rf circuit. Power measured on the monitor coil as the drive frequency was scanned over the resonance. A Lorentzian fit was used to extract a Q factor of approximately 260. . . . .	37
4.6	Circuit diagram for dc electronics. A dc trapping voltage is applied to each of the axial electrodes at a bias tee. The voltages $V_1$ and $V_2$ may be different to account for stray fields that cause excess micromotion along the axis of the trap. An additional fast signal can also be applied to the electrodes via the bias tee, usually to excite the motion of the trapped ions. . . . .	37
4.7	Details of the lens used for imaging the ions. The quoted magnification is 15x. . . . .	37
4.8	Schematic drawing of the new imaging system. Light emitted by the ions is focussed by the lens and reflected by the mirror. 2" lens tubing is used to exclude light from external sources without the loss of signal. There are two filters along the imaging path to select for fluorescence photons at 397 nm. The path is then split by a 90:10 beamsplitter between a CCD camera and a PMT. The PMT field of view is cropped by an iris and slit to maximise the signal-to-noise ratio. The molecular beam line is omitted from the schematic for clarity. . . . .	38
4.9	The energy levels of the $\text{Ca}^+$ ion. . . . .	39
4.10	The arrangement of lasers around the ion trap. The coloured mirrors are dichroic and reflect the lasers the same colour as them, transmitting all others. Details of the transitions the lasers address can be found in Table 7.1.	40
4.11	Example background-subtracted fluorescence data as the cooling laser frequency was scanned across the resonance and a fitted Lorentzian peak. On the blue side of the transition, the ion is heated and the fluorescence counts drop to zero. . . . .	41
4.12	Saturation parameters for the cooling transition for different intensities of the incident 397 nm laser. . . . .	41
4.13	The set-up used for the offset locking method. The laser is overlapped with a stable reference laser and the two lasers are coupled into a single fibre. The beat note signal from a photodiode placed after the fibre is used to generate a locking signal which is fed back to the laser. . . . .	43
4.14	The beat note recorded over approximately seven hours while the offset lock was in use. . . . .	44
4.15	Secular frequencies in the linear Paul trap as the amplitude of the rf voltage on the radial electrodes was scanned. Above, the radial secular frequencies. Below, the axial secular frequencies with the axial electrodes held at ground.	45
4.16	The axial secular frequencies for different voltages applied to the axial electrodes, fitted with a square-root function. . . . .	45

4.17	The changing gradient of the Lorentzian absorption line results in different amplitude of fluorescence modulation with the same frequency modulation. The fluorescence rate is most sensitive to changes in frequency where the gradient is maximised. . . . .	46
4.18	The set-up used for crystal weighing. . . . .	47
4.19	Example crystal weighing data. A Lorentzian fit to the FFT of the raw data is used to extract the secular frequency. . . . .	47
4.20	Labelling of electrodes for the purposes of micromotion compensation. . . .	49
4.21	Experimental set-up used for coarse compensation of excess micromotion. The ions are imaged using a CCD camera as the amplitude of the rf trap drive is varied. The micromotion compensation voltages are iteratively changed until the ions are stationary on the CCD image as the amplitude is changed. . . . .	50
4.22	The set-up used for the photon correlation micromotion compensation. A time-to-digital converter (TDC) correlates the arrival times of fluoresced photons to a rf signal synchronised to the rf trap drive. Due to the Doppler effect, the ion motion at the trap drive frequency is mapped to fluorescence modulation. The compensation values are varied systematically to minimise the amplitude of the observed oscillations. . . . .	51
4.23	Histograms of ion fluorescence photon counts, correlated to a signal at one fifth of the trap drive, triggered at the same phase each time, measured using a fast time-to-digital converter (TDC). Subplots (a), (b) and (c) show the photon correlation histograms (blue bars) for different applied “compensation” voltages respectively. Fitted to each is a sine wave (black line). The data in (a) and (b) were recorded with the ions displaced from the centre of the trap in the same direction. The data in (c) were recorded with the ions displaced from the trap centre in the opposite direction. The measurement time was 0.3 s, the histogram length was 250 ns and the resolution was 0.55 ns. $T$ was 8 V for the axial confinement. . . . .	52
4.24	The micromotion amplitude as the vertical micromotion compensation voltage is scanned and a fit to the linear portion of the graph. . . . .	53
4.25	$(H, V)$ coordinates corresponding to minima in the micromotion amplitude for each of the two radial lasers. Straight lines are fitted to each set of data. . . . .	53
5.1	Schematic diagram of the rf ion trap considered in the simulations. The ionisation lasers travel down the axis of the trap perpendicular to the molecular beam. The voltages applied to the electrodes are labelled, consistent with Equation 5.1. . . . .	56
5.2	Energy of Rydberg electron with distance from molecular core with (solid, black line) and without (dashed blue line) an external electric field. . . . .	57
5.3	The general case of ionisation by a REMPI process. Initially, the atom or molecule is excited to an intermediate state by one or more photons. Then, from this state, it is ionised by absorbing one or more additional photons. The photons for the excitation and ionisation steps may be of different colours. . . . .	58

5.4	Ionisation threshold distributions were simulated for 2+1' REMPI of $^{14}\text{N}_2$ . (a) Broadening of the ionisation threshold for different axial secular frequencies for loading from a molecular beam with waist $w_{\text{beam}} = 250 \mu\text{m}$ (solid line) and from a homogeneous background gas (dashed line). In both scenarios, $z_{\text{offset}} = 0$ . Inset, the normalised ionisation threshold distributions for an axial secular frequency of $2\pi \cdot 200 \text{ kHz}$ . (b) Broadening of the ionisation threshold for different axial secular frequencies and axial displacements from the trap centre for loading from a molecular beam with waist $w_{\text{beam}} = 250 \mu\text{m}$ . . . . .	69
5.5	Ionisation threshold distributions were simulated for 2+1' REMPI of $^{14}\text{N}_2$ with a trap drive frequency $\Omega = 2\pi \cdot 20 \text{ MHz}$ and ionisation laser beamwaists $w_{N/M} = 50 \mu\text{m}$ . The laser pulses were timed to the zero-crossing of the rf field, with temporal widths $\tau_{N/M} = 5 \text{ ns}$ . (a) Broadening of the ionisation threshold for different $q$ parameters, where the REMPI lasers pass through the centre of the trap. Inset, the normalised ionisation threshold distributions for $q = 0.05$ . (b) Broadening of the ionisation threshold for different $q$ values and radial displacements of the REMPI lasers from the trap centre. . . . .	70
5.6	Ionisation threshold distributions were simulated for 2+1' REMPI of $^{14}\text{N}_2$ for $q = 0.1$ and no radial displacement of the REMPI lasers. (a) Broadening of the ionisation threshold for different laser pulse durations where the lasers are timed to coincide with the zero-crossing of the rf field. Inset, the normalised ionisation threshold distribution for a laser pulse duration of 10% of the trap drive period. (b) Broadening of the ionisation threshold for different laser pulse durations and phases of the rf trap drive relative to the arrival times of the ionisation lasers. . . . .	71
5.7	Broadening of the ionisation threshold for different axial and radial confinements. Ionisation threshold distributions were simulated for loading from a molecular beam with beam waist $w_{\text{beam}} = 250 \mu\text{m}$ into a trap with drive frequency $\Omega = 2\pi \cdot 5 \text{ MHz}$ . The laser pulses were timed to the zero-crossing of the rf field, with temporal pulse widths $\tau_{N/M} = 5 \text{ ns}$ . . . . .	72
5.8	Broadening of the ionisation threshold for different axial and radial confinements. Ionisation threshold distributions were simulated for loading from a molecular beam with beam waist $w_{\text{beam}} = 250 \mu\text{m}$ into a trap with drive frequency $\Omega = 2\pi \cdot 5 \text{ MHz}$ . The timing of the ionisation lasers was uncorrelated to the phase of the rf drive. . . . .	73
5.9	Broadening of the ionisation threshold for different numbers of photons in the REMPI process, $N + M$ . The laser beamwaists were $50 \mu\text{m}$ and $q$ was 0.1. The lasers were timed to the zero-crossing of the rf field. Only the radial plane was considered because in scenario 1.) there is no dependence in the $z$ direction. . . . .	73
5.10	Broadening of the ionisation threshold for different excitation and ionisation laser wavelengths in scenario 2.). Only the axial dc voltages are considered. . . . .	74
6.1	(a) The decay of the resonator field, measured with the monitor coil, as the drive was switched off. (b) The recovery of the resonator field, measured with the monitor coil, as the drive was switched back on. . . . .	77

6.2	The set-up used to rapidly switch the trapping fields off and on again. The TTLs were supplied by a delay generator. a) The set-up used to switch the rf field. Initially, the resonator circuit is driven by a low amplitude signal from FG 1. The drive source is switched to FG 3 which supplies a high-amplitude signal, with a phase difference of $\pi$ , which interferes with the intra-resonator field. On reaching the minimum amplitude, the resonator input is switched to FG 2, a high-amplitude signal in-phase with the original drive, which restores the trapping field. Finally, the drive from FG 1 is reinstated. b) The set-up used to switch the dc field. c) The pulse sequence used for the switching. The duration of the high amplitude pulses for the rf switching can be varied. The dc switching is shown in the case where TTLs 1 and 2 are TTLs A and B also. However, longer dc switching times using different TTLs are possible. . . . .	79
6.3	(a) The set-up used to record the ion fluorescence during switching of the trap drives. A pulse generator outputs three TTL signals: the first triggers the delay generator (SRS, DG645) used to switch the rf trap drive; the second goes to the dc switch; and the third starts the TDC measurement window. The PMT output is connected to the stop input of the TDC. (b) The pulse sequence used to record the ion fluorescence while both the rf and dc trap voltages are switched off and on again. . . . .	81
6.4	The voltage on the rf electrodes as the rf field is rapidly switched off. Inset, the minimum of the rf field during switching. The trap drive frequency is 22 MHz. . . . .	82
6.5	The effect of phase on the extinction of the rf electric field in the ion trap. (a) The rf electrode voltage for different phases of the counter drive, $\phi_1$ , where a phase of $0^\circ$ corresponds to the optimised phase. (b) The rf electrode voltage for different phases of the normal trap drive when the trap is switched, $\phi_2$ . (The initial rf amplitude for the data in (a) was smaller than in (b).) . . . .	83
6.6	Fluorescence of a single ion as the rf trapping field is switched off for different rf confinements. . . . .	84
6.7	The fluorescence of a single ion as the rf trapping field was switched off for different durations of the switching sequence. (a) The fluorescence counts recorded with time as the rf field was switched after 5 ms. (b) The electrode voltage as the rf field was switched. . . . .	85
6.8	The fluorescence of a single ion after switching the rf trap drive for different dc confinements. . . . .	86
6.9	The ion fluorescence as the trap is switched off for different numbers of ions. . . . .	87
6.10	The normalised dc voltage measured at one axial electrode feedthrough while the dc field was switched off. . . . .	88
6.11	Switching of the dc voltage. (a) The recovery of the ion fluorescence rate as the dc voltage returns to its stationary value. (b) The dc voltage as it is switched back on during the switching process. (c) A false-colour CCD image shows how the ion moves between the micromotion-compensated initial position and its position when the trap is off. . . . .	89
6.12	Histogram of ion fluorescence as the dc electrode voltages are switched off and on again for different dc confinements. The switch-off time was 20 ms. The start of the falling and rising edges of the dc voltage during switching are denoted by vertical dashed lines. . . . .	90

6.13	Ion fluorescence histograms while the trapping voltages are switched off. (a) The dc electrode voltage was held at ground throughout the measurement and the micromotion was fully compensated. The rf field was switched off for 3 $\mu$ s. (b) The dc confinement was initially 7 V and was switched off for 15 ms. At the minimum of the dc voltage, the rf field was switched off for 3 $\mu$ s. . . . .	91
7.1	The ionisation scheme. The excitation and ionisation steps of the REMPI process from the ground state of the N <sub>2</sub> molecule to the ground state of the N <sub>2</sub> <sup>+</sup> molecular ion. . . . .	94
7.2	PGOPHER simulation of the S0 and S11 peaks for different rotational temperatures of <sup>14</sup> N <sub>2</sub> . Simulations were performed by A. Gardner. . . . .	95
7.3	The two competing REMPI processes. Ionisation from the intermediate level can proceed by the absorption of one 212 nm photon or two 255 nm photons. . . . .	97
7.4	The simulated ionisation threshold for parameters corresponding to normal operation of the Paul trap. Above, the expected distribution of thresholds based on the expected broadening of ionisation threshold and the splitting of rotational levels within the ion. Below, the expected ionisation probability (neglecting the natural width of the ionisation threshold) assuming that the ionisation probability is cumulative. In both cases, the blue line represents the zero-field ionisation threshold for the $J = 0$ state of the ion. . . . .	98
7.5	Simulated broadening of the ionisation threshold assuming a reduction in the radial electric field of a factor of 400 which has been previously achieved experimentally. Above, the expected distribution of thresholds based on the expected broadening of ionisation threshold and the splitting of rotational levels within the ion. The contributing rotational levels considered in this simulation are labelled. Below, the expected ionisation probability (neglecting the natural width of the ionisation threshold) assuming that the ionisation probability is cumulative. In both cases, the blue line represents the zero-field ionisation threshold for the $J = 0$ state of the ion. . . . .	99
7.6	The layout of the nitrogen ionisation lasers through the trap. The two ionisation lasers are overlapped before passing through the centre of the trap. They are reflected by a dichroic mirror onto a photodiode after the trap. . . . .	100
7.7	Set-up used to ensure that the pulse valve and skimmers were aligned such that the molecular beam passed through the centre of the trap. A guide laser was aligned to pass through the centre of the trap and was observed on the pulse valve. . . . .	101
7.8	The pressure recorded in the first beam line chamber (above) and trap chamber (below) for pulse valve repetition rates of 1, 2, 5 and 10 Hz. The stagnation pressure was $0.2 \pm 0.05$ bar above atmospheric pressure (atm). . .	102
7.9	The secular frequency of the Coulomb crystal in the ion trap with time after the nitrogen ionisation lasers were fired through the trap. The dashed horizontal lines show the expected frequency shift for the arrival of one <sup>14</sup> N <sub>2</sub> <sup>+</sup> ion into a crystal with four <sup>40</sup> Ca <sup>+</sup> ions. Superimposed images show the ion crystal for the two measured secular frequencies. . . . .	103
7.10	The probability of loading nitrogen ions for different pulse energies of the 255 nm excitation laser. . . . .	104

7.11	Nitrogen loading probability for different arrival times of the ionisation lasers with respect to the phase of the rf trap drive. Experimentally obtained ionisation probabilities (black diamonds) with error bars. The data are fitted with a convolution of a mod sine wave and a Gaussian of the width of the temporal profile (black line, error in pale blue). . . . .	105
7.12	The loading probability for different delays of the laser pulse from the opening of the pulse valve. . . . .	106
7.13	The laser pulse is timed to the minimum of the electric field. Above, the electrode voltage on the rf electrodes. Below, the laser pulse measured using the photodiode in Figure 7.13 . . . . .	107
7.14	Scan of the S0 and S11 peaks in the excitation spectrum, obtained by 2+2 REMPI. Lorentzians are fitted to the data. The wavenumbers refer to the energy of the two 255 nm photons for the excitation step of the 2+2 ionisation process. . . . .	108
7.15	Histogram of arrival times for nitrogen ions loaded by 2+2 REMPI. Loading delay is the time taken for the ion to crystallise, measured from the time the laser pulse is triggered. . . . .	109
8.1	The ten possible transitions from the $S_{1/2}$ state to the $D_{5/2}$ state. Arrows show transitions corresponding to $\Delta m_j = 0, \pm 1, \pm 2$ . . . . .	111
8.2	Harmonic potential with energy levels $E_n = \hbar\omega(n + 1/2)$ . The red arrow shows one of the motional transitions that contributes to the third red sideband, i.e. it corresponds to $\Delta n = -3$ . The blue arrow shows one of the motional transitions that contributes to the second blue sideband, i.e. it corresponds to $\Delta n = +2$ . . . . .	111
8.3	Layout of optics around the ion trap used for quadrupole spectroscopy of calcium ions. . . . .	112
8.4	The sequence used to perform quadrupole spectroscopy of a single trapped calcium ion. Initially the ion is laser cooled using the transition at 397 nm. This is followed by a period of state preparation using the repumping lasers to ensure the ion is in one of the $S_{1/2}$ states. Once the ion is in the desired state, a pulse at 729 nm excites the quadrupole transition. After this pulse is concluded, the cooling lasers are used to detect the state of the ion. (a) The sequence of laser pulses. (b) The four stages of the spectroscopy sequence.	113
8.5	The Zeeman sub-levels of the $D_{3/2}$ and $P_{1/2}$ states at zero magnetic field, and the possible transitions between them. These transitions are excited by $\sigma^+$ (red, solid), $\pi$ (green, dashed) and $\sigma^-$ (blue, solid) polarised light, corresponding to $\Delta m_J = +1, 0, -1$ transitions respectively. . . . .	114
8.6	Hanle dip measurements taken for no modulation of the 866 nm laser polarisation (a), and with polarisation modulation at 10 MHz applied using an EOM. (b) In each case the blue scattered points are data collected during multiple scans and the black lines are a simple mean of the scans. . . . .	115
8.7	A spectrum showing the ten peaks corresponding to the ten $D_{5/2} \leftarrow S_{1/2}$ transitions with $\Delta m_J = 0, \pm 1, \pm 2$ . Above, an example experimental spectrum. Below, a simulated spectrum with a magnetic field of 45 mG and linewidths of 12 kHz by fitting to these data using the simulation described in Appendix D. . . . .	116
8.8	Sideband spectra. (a) Example experimental sideband spectrum taken with an axial secular frequency of 480 kHz. The carrier is centred at a detuning of 0 MHz. Sidebands with negative detunings are red and with positive detunings are blue. (b) Simulated sideband spectrum (see Appendix D). . .	117

8.9	The magnetic field fluctuations measured close to the trap. (a) The magnetic field measured over 100 ms. (b) Spectrum of magnetic field noise from FFT of measurements from longer measurement times. . . . .	118
8.10	Peaks in the quadrupole spectrum for probe times of 20 $\mu$ s and 55 $\mu$ s. In the case of the Fourier limited peak with a 55 $\mu$ s probe time, the sinc wiggles arising from the square pulse of the probe laser are visible. . . . .	119
8.11	The effect of probe time on the quadrupole peak linewidths. (a) Example peaks for probe times between 50 $\mu$ s and 2 ms. (b) The full widths at half maximum (FWHM) of peaks with the probe time. . . . .	120
8.12	The effect of probe laser power on the quadrupole peak linewidths. (a) Peaks observed for probe powers 20 $\mu$ W and 1 mW with a probe time of 10 ms. (b) Full widths at half maximum (FWHM) for different powers of the 729 nm probe laser. . . . .	121
8.13	The peak excitation probability measured from spectra. The duration of the 729 nm laser pulse was scanned to observe Rabi oscillations. . . . .	122
9.1	The proposed quantum logic spectroscopy scheme. The crystal of one nitrogen ion and one calcium ion is cooled to the motional ground state. A) The clock transition in nitrogen is probed using a Raman transition. B) A walking wave at 780 nm excited the motional state of the nitrogen ion if step A was unsuccessful and not if the transition was successfully completed. The motion of the nitrogen ion is also transferred to the co-trapped calcium ion. C) The first red sideband of the calcium ion is driven and if the crystal is still in the motional ground state (if the nitrogen ion is in the $v = 2$ state) the calcium ion will remain in the light $S_{1/2}$ state. If the crystal has gained motional energy during the logic scheme (if the nitrogen is in the $v = 0$ state) then this transition can occur and the calcium ion will be excited to the dark $D_{5/2}$ state. The state of the calcium ion can be read out by detecting fluorescence. . . . .	126
B.1	Flowchart showing the automation sequence. . . . .	142
C.1	The temporal profiles of laser pulses for different Q-switch delays of the Nd:YAG laser used to pump the 255 nm dye laser. . . . .	146
C.2	The pulse energy of the excitation laser at different photon energies. The Q switch delays used in these measurements correspond to higher energies than were used in the experiment. . . . .	147

# Abbreviations

ac	alternating current
AOM	acousto-optical modulator
atm	atmospheric pressure
CCD	charge-coupled device
CG	Clebsch-Gordan
COM	centre-of-mass
CPT	charge-parity-time / coherent population trapping
DAQ	data acquisition device
dc	direct current
DOI	direct object identifier
EBIT	electron-beam ion trap
EI	electron ionisation
EOM	electro-optical modulator
FT	Fourier transform
FFT	fast Fourier transform
FG	function generator
FWHM	full width at half maximum
GPIO	general purpose interface bus
IR	infrared
LIF	laser-induced fluorescence
MD	molecular dynamics
OBE	optical Bloch equation
PBS	polarising beam splitter
PID	proportional integral differential
PMT	photomultiplier tube
REMPI	resonance-enhanced multiphoton ionisation
rf	radiofrequency
RC	resistor-capacitor
SM	Standard Model
TDC	time-to-digital converter
TDPT	time-dependent perturbation theory
TTL	transistor transistor logic
USB	universal serial bus
UV	ultraviolet

## Diagram Key

Optical drawings in this thesis are made using Inkscape, including using components from and based on the optical component library developed by Alexander Franzen. The keys below show the meaning of the symbols used throughout this thesis for reference:

laser		lenses	
laser beam path		knife-edge	
flip mirror		shutter	
mirror		iris	
beamsplitter		beam dumps	
dichroic mirror		switch	
fibre coupler		amplifier	
waveplate		low-pass filter	
photodetector		resonator	
CCD camera		function generator	
computer		dc signal source	
electrical signal path		OR gate	
communication path			

Key for optical and electronic symbols used in diagrams throughout this thesis.

# Chapter 1

## Introduction

Trapped molecular ions have developed into indispensable tools with applications spanning cold quantum chemistry,<sup>4,5</sup> quantum computing,<sup>6</sup> metrology<sup>7</sup> and the search for new physics beyond the Standard Model.<sup>8</sup> The realisation of novel cooling techniques<sup>9</sup> and quantum logic detection schemes<sup>10</sup> has made high-resolution measurements with molecular ions practicable, and led to a heightened interest in tabletop atomic and molecular physics experiments to probe fundamental physics.<sup>11–22</sup> This thesis describes work towards an experiment to use high resolution spectroscopy of molecular nitrogen ions to measure potential variation in the proton-to-electron mass ratio. In the following sections, the motivation and intentions for this experiment are explained.

### 1.1 Variation in Fundamental Constants

The Standard Model (SM) of particle physics has had unprecedented success in describing the building blocks of the universe. Recent discoveries of the remaining particles predicted by the SM, such as the Higgs boson, have completed the model.<sup>23–25</sup> However, there are inconsistencies between the SM predictions and the observed universe. These include the imbalance of matter and antimatter in the universe;<sup>26,27</sup> the incompatibility of the SM and general relativity;<sup>8</sup> the accelerating expansion of the universe, attributed to dark energy;<sup>28–30</sup> and galaxy formation, which suggests the existence of dark matter.<sup>31</sup> The SM also does not explain the reason for the fundamental constants' values, which are only known empirically. The Planck mission estimated that the universe is composed of 69 % dark energy, 26 % dark matter and 5 % particles from the SM.<sup>8</sup> These discrepancies motivate the search for new physics beyond the SM.

Extensions and alternatives to the Standard Model have been proposed to explain these phenomena. Measurements of permanent electric dipoles, Lorentz and CPT (charge-parity-time) symmetry violation and spatiotemporal variation in fundamental constants have been proposed to test these new theories.<sup>32</sup> Of these, the potential spatiotemporal variation of the dimensionless fundamental constants  $\alpha$  (the fine structure constant) and  $\mu$  (the proton-to-electron mass ratio) are of particular interest because they can be measured with atomic and molecular physics experiments. Spatiotemporal variation in fundamental

constants is predicted by string theory, discrete quantum gravity, loop quantum gravity, chameleon fields, quintessence fields, light dark matter and some dark energy models.<sup>32,33</sup> These theories fix the relations between the constants in the SM, so if one constant varies, all are predicted to vary.<sup>8</sup>

Variation in fundamental constants may present as slow drifts, which suggest new physics; oscillations, which suggest light dark matter;<sup>34</sup> or fast transients, which suggest topological defects.<sup>35</sup> The timescale of potential time variation in  $\alpha$  and  $\mu$  may range from very fast changes to slow drifts over cosmological timescales, depending on the mechanism responsible. However, experiments with atoms and molecules are typically limited to measurement repetition rates on the order of no less than seconds, to achieve the highest precision in their measurements, and are generally limited to taking measurements over a maximum of a few years.

Changes in fundamental constants may be measured by a number of methods: comparison of atomic and molecular clocks, astrophysical spectra, meteorite dating, stellar physics and cosmic microwave background radiation (CMB).<sup>32,36</sup> Some astrophysical measurements have hinted at variation in  $\alpha$ ,<sup>37-39</sup> but these have yielded inconsistent results.<sup>40</sup> Astronomical measurements offer the possibility to measure over distances and timescales far beyond the reach of atomic physics experiments, but they have low precision and poor control. In contrast, laboratory atomic and molecular physics experiments permit highly controlled environments and unique precision. As a result, these new precision measurements have unparalleled potential to search for variation in fundamental constants.

## 1.2 Atoms and Molecules to Measure Fundamental Constants

Atomic and molecular transitions are usually considered to have constant transition energies in the absence of external fields. This is the premise of atomic frequency standards, such as that used to define the second.<sup>41,42</sup> However, transition energies depend on the fine structure constant,  $\alpha$ , and proton-to-electron mass ratio,  $\mu$ , with different sensitivities specific to the transition. In general, fine and hyperfine transition frequencies depend on  $\alpha$  and hyperfine, vibrational and rotational transition frequencies depend on  $\mu$ .<sup>8</sup> Changes in  $\alpha$  or  $\mu$  would therefore translate to changes in transition frequency. This has implications for metrology, if there is not an equivalence between clocks of different types and in different locations, but it also offers the potential for probing potential changes in these constants.<sup>8</sup>

The sensitivity of a clock depends on the internal structure of the relevant atom or molecule. The sensitivities of a transition to the changes in  $\alpha$  ( $\kappa_\alpha$ ) and  $\mu$  ( $\kappa_\mu$ ) affect the transition frequency according to

$$\frac{\Delta\nu}{\nu} = \kappa_\alpha \frac{\Delta\alpha}{\alpha} + \kappa_\mu \frac{\Delta\mu}{\mu}, \quad (1.1)$$

where  $\Delta$  represents the variation in the succeeding quantity, and  $\nu$  is the frequency of the relevant transition.<sup>43,44</sup> As two clocks must be compared in order to detect a change in the ratio of their frequencies,  $r$ , this becomes

$$\frac{\Delta r}{r} = |\kappa_{\alpha 1} - \kappa_{\alpha 2}| \frac{\Delta \alpha}{\alpha} + |\kappa_{\mu 1} - \kappa_{\mu 2}| \frac{\Delta \mu}{\mu}, \quad (1.2)$$

where the subscript numbers correspond to clocks labelled 1 and 2 arbitrarily. The values  $\kappa_{\alpha}$  and  $\kappa_{\mu}$  are specific to the transition and species in question and depend on a number of factors.

Since the early 2000s, the achievable fractional uncertainties in the measurement of optical atomic transitions have decreased by more than five orders of magnitude to below  $10^{-18}$ .<sup>45</sup> At this level of precision, the fractional uncertainty is small enough that potential changes in  $\alpha$  and  $\mu$  can be constrained to a level that is meaningful within the predictions of some alternatives to the SM. By measuring the ratio between the frequencies of two transitions with different sensitivities, the variation of fundamental constants could be observed and/or constrained. This has already been done to impose constraints on the variation of fundamental constants. The existing constraints on  $\dot{\alpha}/\alpha$  and  $\dot{\mu}/\mu$ , imposed by tabletop experiments, are fractional changes of  $\sim 10^{-18} \text{ year}^{-1}$  and  $\sim 10^{-17} \text{ year}^{-1}$  respectively<sup>46–48</sup>.

### 1.3 Candidates for New Measurements

Improving existing limits on  $\alpha$  and  $\mu$  means reducing the uncertainties in the measured transitions, choosing transitions with different sensitivities or increasing the temporal or spatial scope of the measurements. To make meaningful measurements, we also need to be able to compare different clocks with different sensitivities. The search for phenomena such as topological dark matter requires these clocks to be distributed over large distances. Currently, atomic and molecular clocks have been proposed using neutral atoms and molecules; atomic and molecular ions; highly charged ions; and nuclear clocks. Molecular experiments currently lag behind atomic frequency precision, but molecular spectroscopy to fractional uncertainties below the current benchmark set by atomic spectra should be possible for some molecular transitions. Similarly, experiments with highly charged ions and nuclear transitions are still being developed, but may offer better sensitivity to fundamental constants and less sensitivity to external fields than existing atomic and molecular clocks.

Experiments with neutral species in lattice traps have the advantage that large numbers of atoms or molecules can be interrogated simultaneously, which gives them very good short term stability. Candidates for measuring potential changes in  $\alpha$  with optical atomic clocks include the Sr (which is insensitive to  $\alpha$ ),<sup>49</sup> Yb<sup>50</sup> and Hg<sup>51</sup> lattice clocks. Some neutral molecules have also been proposed for probing potential changes in  $\mu$ , including CaF<sup>52</sup> and Sr<sub>2</sub>.<sup>53</sup>

While it is usually only possible to interrogate one trapped ion at a time, it is possible to

Table 1.1: Details of the  $v = 0 \rightarrow v = 2$  transition in the  $^{14}\text{N}_2^+$  ion.

Quantity	Value
Transition frequency (THz)	129.4
Natural linewidth (Hz)	<0.1
Relative Zeeman shift ( $\text{G}^{-1}$ )	0
dc Stark shift ( $\text{cm}/\text{V}$ ) <sup>2</sup>	$8 \times 10^{-20}$
Quadrupole shift ( $\text{mm}^2/\text{V}$ )	$4 \times 10^{-18}$
Sensitivity	0.49

achieve very long lifetimes, compared to neutral species. Currently, neutral lattice clocks and atomic ion clocks have achieved similar uncertainties. There are several optical atomic ion clocks in operation, including  $\text{Yb}^+$ ,  $\text{Al}^+$ ,  $\text{Hg}^+$ ,  $\text{Sr}^+$ ,  $\text{In}^+$  and  $\text{Ca}^+$ .<sup>8,45,46,54</sup> However, most of these clocks are insensitive to  $\alpha$  with the exceptions of  $\text{Yb}^+$  and  $\text{Hg}^+$ , with  $\text{Sr}^+$  clocks providing a possible reference.<sup>8</sup> Molecular ions proposed as potential candidates for measurements of  $\mu$  include  $\text{H}_2^+$ ,<sup>55</sup>  $\text{HD}^+$ ,<sup>56</sup>  $\text{O}_2^+$ ,<sup>13</sup>  $\text{N}_2^+$ ,<sup>12</sup>  $\text{CaH}^+$ ,<sup>57-59</sup>  $\text{Cl}_2^+$ ,<sup>60</sup>  $\text{HfF}^+$ .<sup>60</sup>

Highly charged ions have strong internal electric fields which result in very large sensitivities to  $\alpha$ . They are also insensitive to external field fluctuations compared to singly-charged ions.<sup>61</sup> These highly charged ions can be formed in electron-beam ion traps (EBITs) and then co-trapped with an auxiliary ion in a Paul trap, for example. Highly charged ions generally require sympathetic cooling and a quantum logic method for state detection because the energy level spacings are too large. Quantum logic with highly charged ions has recently been demonstrated for  $\text{Ar}^{13+}$ .<sup>62</sup> A number of candidate highly charged ion clocks have been proposed for measuring potential changes in fundamental constants.<sup>61,63-65</sup>

Nuclear transitions are appealing for precise spectroscopy because the small size and electromagnetic moments of nuclei mean they are relatively insensitive to external perturbations.<sup>66,67</sup> In addition, nuclear clocks would be sensitive to changes in  $\alpha$  and quark masses.<sup>67,68</sup> However, typical nuclear energy scales are several orders of magnitude beyond the photon energies that can be achieved with lasers.  $^{229}\text{Th}$  is the only known nucleus with a transition that can potentially be accessed with lasers.<sup>69</sup> Experiments with  $\text{Th}$ ,  $\text{Th}^+$  and  $\text{Th}^{3+}$  have been proposed.<sup>67</sup>

## 1.4 $\text{N}_2^+$ Ion for Probing Stability of $\mu$

In  $^{14}\text{N}_2^+$ , the proposed transitions for probing changes in  $\mu$  are vibrational Raman transitions in the electronic ground state,  $X^2\Sigma_g^+$ , and  $I = 0$  nuclear spin state. Specifically, the  $(v, N, F, M) = (0, 0, 1/2, \pm 1/2) \rightarrow (1, 0, 1/2, \pm 1/2)$  or  $(2, 0, 1/2, \pm 1/2)$  transitions have natural linewidths narrower than 0.1 Hz and sensitivities of  $\kappa_\mu = 0.49$  (where 0.5 is the ideal case for a pure vibrational transition).<sup>12</sup> For this project, the  $v = 0 \rightarrow v = 2$  transition (see Table 1.1) will be measured indirectly using quantum logic spectroscopy.<sup>10</sup>

While blackbody radiation from room-temperature sources peaks in spectral density in the

vibrationally-active infrared region of the electromagnetic spectrum, dipole rovibrational transitions are forbidden in homonuclear diatomic molecules.<sup>12,70</sup> Therefore, the lifetime of the prepared rovibronic state is very long. Additionally, the blackbody radiation shift, due to the electric field of the blackbody radiation present in the trap, is largely mitigated by the lack of allowed rovibrational transitions, low transition dipole moment to the A  $^2\Pi$  state and the close spacing of the vibrational levels.<sup>12,71</sup> As there is no electric quadrupole in the rotational ground state, the electric quadrupole shift is zero for the proposed transitions. By choosing magic wavelengths for the Raman lasers, where the ac Stark shifts caused by the two lasers are equal, the ac Stark shift can also be brought to zero.<sup>12</sup> These characteristics give  $^{14}\text{N}_2^+$  some advantages over heteronuclear diatomic molecules and make it a promising candidate for high precision spectroscopy.

## 1.5 Experiment Overview

Our experiment aims to measure potential temporal variation in the proton-to-electron mass ratio by performing high resolution spectroscopy of molecular nitrogen ions. A single calcium ion will be co-trapped with a single nitrogen ion in a linear Paul trap. This enables high localisation, long trapping times and the exploitation of shared motional modes of the ion crystal for cooling and state detection of the nitrogen. A quantum logic scheme is necessary to detect the state of the nitrogen ion because excitation into a higher electronic state results in decay into many vibrational and rotational states, preventing cycling transitions that could be used for fluorescence detection.

The calcium ion was chosen as the auxilliary ion in this experiment because it has a clock transition, to facilitate ground state cooling and quantum logic, and a similar mass-to-charge ratio to nitrogen. This means they have strong shared motional modes which is important for quantum logic and for sympathetic cooling. The clock transition in calcium could in principle be used for comparison to the nitrogen transition as it is insensitive to  $\mu$ . However, while there are advantages to probing both ions in the same environment, the clock transition in calcium is not particularly well-suited to this application compared to other state-of-the-art atomic clocks.<sup>45,72</sup> Therefore, the frequency of the transition in the nitrogen ion will be compared to a frequency reference provided by the National Physics Laboratory as part of the QSnet collaboration.<sup>52</sup>

For high resolution spectroscopy of the  $v = 0 \rightarrow v = 2$  transition, the nitrogen must be prepared in the ground rovibronic state with high fidelity. Resonance-enhanced multiphoton ionisation (REMPI) just above the ionisation threshold has been shown to produce nitrogen ions in the rovibronic ground state with purities greater than 99%.<sup>73</sup> REMPI has also been used to load molecular ions into rf ion traps state-selectively for some species.<sup>74-76</sup> As pure rotational transitions are electric-dipole-forbidden, the state purity of the nitrogen ion (which is non-polar) will not be lost through interaction with the background blackbody radiation (BBR). For this reason, loading nitrogen into the ion trap via a state-selective REMPI scheme should enable state selectivity. This will be implemented using a 2+1'

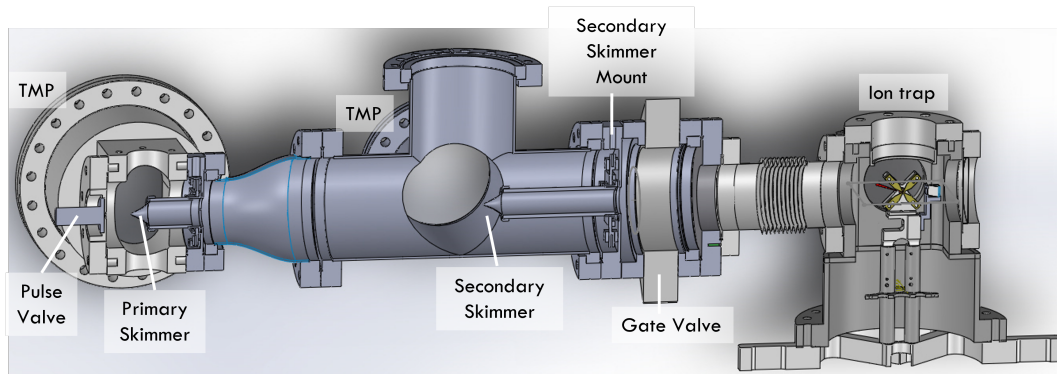


Figure 1.1: The experimental set-up for the experiment, showing the ion trap and molecular beam line. TMP = turbomolecular pump. Diagram made by A. Gardner.<sup>3</sup>

REMPI method, using lasers at 255 nm and 212 nm.<sup>73</sup>

Once the  $N_2^+$  ion has been loaded, the calcium-nitrogen crystal will then be cooled to its motional ground state using sideband cooling on the  $S_{1/2} \rightarrow D_{5/2}$  transition in the calcium ion. Then, the  $v = 0 \rightarrow v = 2$  vibrational transition in the ground  $X^2\Sigma_g^+$  state of the nitrogen ion will be driven as a Raman transition using lasers at 714 nm and 1030 nm. The state of the nitrogen ion will be read out using a quantum logic scheme (see Section 9.2).

The apparatus for this experiment consists of a chamber containing the linear Paul trap and a molecular beam line used to load nitrogen into the trap (see Figure 1.1). Calcium is evaporated from an oven below the trap and ionised using lasers aligned through the trap. The nitrogen is released from a pulsed valve and passes through two skimmers before reaching the centre of the ion trap. From here, it can be ionised by lasers aligned through the trap. The trap chamber has three windows which allow optical access along the axis of the trap and radially.

## 1.6 Thesis Overview

Previously, nitrogen had been loaded into an ion trap by a 2+1 REMPI scheme and the relevant molecular beamline and trap chamber were set up. This work is described in detail in A. Gardner's thesis.<sup>3</sup>

The work in this thesis addresses two steps towards high resolution spectroscopy of nitrogen ions: the state-selective loading of nitrogen for the nitrogen spectroscopy and the characterisation of the clock transition in calcium which will be used for cooling and non-destructively reading out the state of the nitrogen ion. This thesis is structured as follows. In Chapters 2 and 3, the theory needed to understand the general background to this thesis is explained. The experimental set-up consisting of a linear Paul trap, laser systems and imaging is described in Chapter 4. Chapter 5 presents the results of simulations performed to assess the impact of the electric trapping field on the state selectivity of photoionisation

processes. In response to this, the trap fields were rapidly switched off during loading of molecular ions. The heating observed during switching of the trap voltages is presented in Chapter 6. Chapter 7 contains the results of experimental loading of nitrogen ions into the ion trap by electron ionisation and 2+2 REMPI. The desired 2+1' mechanism was not attempted because the laser for the ionisation step of the process was not operational at the time the data was taken. Chapter 8 contains the preliminary results of quadrupole spectroscopy of calcium ions. Finally, Chapter 9 concludes the work and offers suggestions for future work.

The work in this thesis has led to the publication of:

- L. Blackburn and M. Keller, The effect of the electric trapping field on state-selective loading of molecules into rf ion traps. *Scientific Reports*, 2020, **10**, 18449. DOI 10.1038/s41598-020-74759-6.

## Chapter 2

# Theory: Ion Traps and Molecular Beams

This thesis describes simulations and experiments based on the trapping of ions in a linear Paul trap and the loading of molecular ions into the trap via a molecular beam. This chapter explains the theory of these techniques.

### 2.1 Linear Paul Traps

The simplest conceivable electric trap for charged particles would consist of static fields. However, while it is possible to confine a charged particle in two dimensions using static fields, this is not possible in three dimensions. This effect arises from Maxwell's equations and is referred to as Earnshaw's theorem. We consider a three-dimensional harmonic potential,  $\Phi(x, y, z)$ ,

$$\Phi(x, y, z) = \Phi_0 \cdot (\alpha x^2 + \beta y^2 + \gamma z^2), \quad (2.1)$$

experienced by a charged particle in an electric field where  $\alpha$ ,  $\beta$  and  $\gamma$  are constants and  $\Phi_0$  is a constant defining the gradient of the electric field. Laplace's equation dictates

$$\nabla^2 \Phi = 0, \quad (2.2)$$

for an electric field in free space. Then, assuming  $\Phi_0 \neq 0$ , which is a requirement for trapping, the Laplace equation may be rewritten

$$\nabla^2 \Phi(x, y, z) = \Phi_0 \cdot (2\alpha + 2\beta + 2\gamma) = 0. \quad (2.3)$$

In order to confine the particle in all three dimensions simultaneously, there must be a potential minimum in each at the same position. For this, the curvature of the potential must be positive in all three dimensions simultaneously. In other words,  $\alpha$ ,  $\beta$  and  $\gamma$  must all be positive. This is inconsistent with Equation 2.3 and so it is not possible to trap an ion in three dimensions with static electric fields.

There are two common solutions for this: the use of dynamic electric fields (Paul trap) and the use of a combination of static electric and static magnetic fields (Penning trap). The Paul trap is of interest to us and usually consists of an electric quadrupole which oscillates at radiofrequencies. Higher-order multipole traps, most commonly 22-pole traps, offer a larger low-field region in the centre and so are favoured in some applications.

The linear Paul trap confines the ions along one axis with a static electric field and in the perpendicular plane using a radiofrequency (rf) electric field. This trapping method relies on the interaction of the ion's electric charge with the trapping field and so does not depend on the internal state of the ion, nor does it change the internal state.

### 2.1.1 The Trapping Field

For a typical linear Paul trap a dc voltage is applied to each of the axial electrodes. This creates a potential which is trapping along the axis and anti-trapping in the directions perpendicular to the trap axis. The voltages applied to the four radial electrodes form an instantaneous quadrupole which oscillates at radiofrequencies. The electric field,  $\vec{\mathcal{E}}(x, y, z, t)$ , is given by

$$\begin{aligned} \vec{\mathcal{E}}(x, y, z, t) = \frac{1}{r_0^2} & \left[ \left( -V_{\text{rad}}^{\text{rf}} \cdot \cos(\Omega t) - \eta V_{\text{ax}}^{\text{dc}} \right) \vec{x} \right. \\ & \left. + \left( V_{\text{rad}}^{\text{rf}} \cdot \cos(\Omega t) - \eta V_{\text{ax}}^{\text{dc}} \right) \vec{y} + 4 \left( \eta V_{\text{ax}}^{\text{dc}} \right) \vec{z} \right], \end{aligned} \quad (2.4)$$

where  $t$  is time and  $\Omega$  is the trap drive frequency.  $\eta$  is the axial trap efficiency, which accounts for the axial electrode separation and geometry, and  $2r_0$  is the effective distance between the radial electrodes, which also takes into account the deviation from the ideal electrode geometry. The origin of the coordinate system is at the centre of the trap.<sup>77</sup>

It is desirable to use harmonic potentials to confine ions because the motional energy levels are equally spaced, regardless of the energy of the ions. They are also simple mathematically, making simulation of the ion motion more straightforward. The rf electric field of the Paul trap evolves very quickly relative to the ion motion in the trap and so is pseudo-harmonic. The harmonic approximation to the true rf potential is referred to as the pseudopotential.

### 2.1.2 The Equations of Motion

In the trap field, the ion of charge  $Q$  experiences a force,  $\vec{F} = -Q\vec{\mathcal{E}}$ , which can be used in conjunction with Newton's second law to describe the motion of the ion. In the two radial directions,

$$m \frac{d^2 x}{dt^2} + Q \left( -V_{\text{rad}}^{\text{rf}} \cdot \cos(\Omega t) - \eta V_{\text{ax}}^{\text{dc}} \right) x = 0, \quad (2.5)$$

and

$$m \frac{d^2 y}{dt^2} + Q \left( V_{\text{rad}}^{\text{rf}} \cdot \cos(\Omega t) - \eta V_{\text{ax}}^{\text{dc}} \right) y = 0. \quad (2.6)$$

These two differential equations are referred to as the Mathieu equations. They can be rewritten<sup>77</sup>

$$\frac{d^2 x}{d\Upsilon^2} - (a - 2q \cdot \cos(2\Upsilon))x = 0, \quad (2.7)$$

and

$$\frac{d^2 y}{d\Upsilon^2} - (a + 2q \cdot \cos(2\Upsilon))y = 0, \quad (2.8)$$

where  $\Upsilon = \frac{\Omega t}{2}$ , the  $q$  parameter is

$$q = \frac{2V_{\text{rad}}^{\text{rf}} Q}{mr_0^2 \Omega^2}, \quad (2.9)$$

and the  $a$  parameter is

$$a = -\frac{4Q\eta V_{\text{ax}}^{\text{dc}}}{m\Omega^2}. \quad (2.10)$$

The  $q$  and  $a$  parameters define the trap, and the stability and dynamics of the trapped ions are determined by these quantities alone.

The equation of motion in the axial direction is more straightforward,

$$m \frac{d^2 z}{dz^2} + 4Q\eta V_{\text{ax}}^{\text{dc}} z = 0. \quad (2.11)$$

### 2.1.3 Ion Stability

Not all solutions to the Mathieu equation correspond to stable trajectories in the trap. Where the trajectory is not stable, the ions are not trapped. In the  $q, a$  parameter space there are regions of stability for each of the radial directions. Where these regions overlap, ions can be stably trapped (Figure 2.1(a)). The stability with respect to the axial dc voltage is accounted for within the  $a$  parameter.

The parameters  $q$  and  $a$  depend on the charge-to-mass ratio of the ion, the electrode voltages and the frequency of the rf component of the electric field. This means that ions of different charge-to-mass ratios will be stable in different traps (Figure 2.1(b)). Where the charge-to-mass ratio is similar, different ions can be trapped in the same trap with the right choice of parameters. However, if they are sufficiently different, it may not be possible. The trap drive frequencies used in typical ion traps range from 100s MHz for light ions such as  $\text{H}^+$  to 10s Hz for macroparticles.<sup>77</sup>

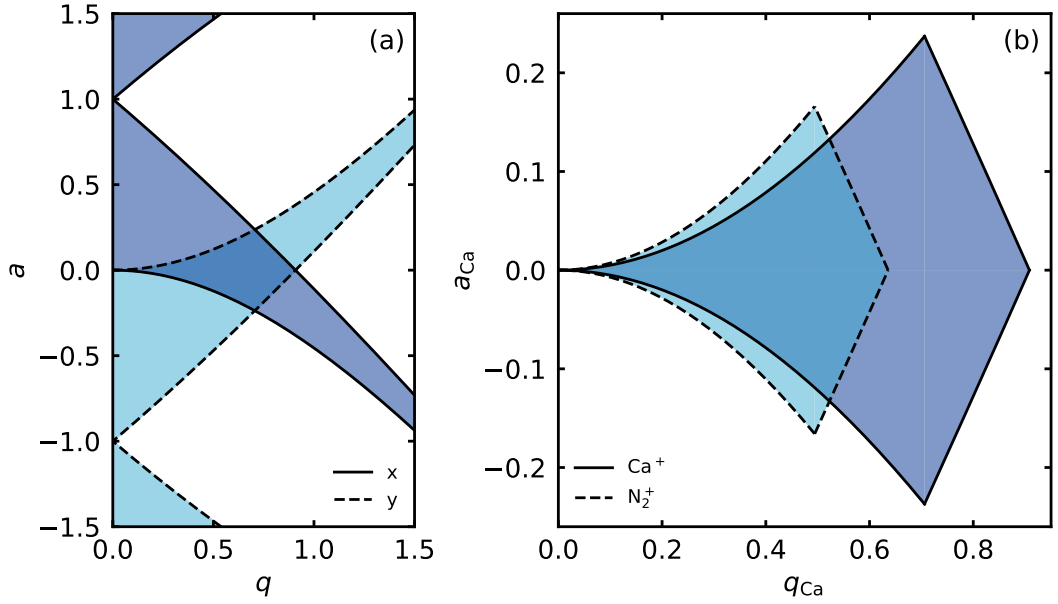


Figure 2.1: Ince-Strutt stability diagrams for a linear Paul trap, plotted using the analytical expressions from E. Butikov.<sup>78</sup> (a) The stability regions in  $x$  and  $y$ . The shaded regions represent regions where the ion motion is stable and trapping is possible. (b) The first stability regions for calcium ions and nitrogen ions in terms of the  $q$  and  $a$  parameters of calcium. Where the two stability regions overlap, the calcium and nitrogen ions can be stably trapped in the same ion trap.

#### 2.1.4 Secular Motion and Micromotion

In the approximation  $|q|, |a| \ll 1$ , ion motion in a Paul trap is governed in the radial directions by<sup>77</sup>

$$x(t) = x_0 [1 - q \cos(\Omega t)] \cos(\omega_x t + \phi_x), \quad (2.12)$$

and

$$y(t) = y_0 [1 - q \cos(\Omega t)] \cos(\omega_y t + \phi_y), \quad (2.13)$$

where

$$\omega_r = \frac{\sqrt{\frac{q^2}{2} \pm a}}{2} \Omega. \quad (2.14)$$

As the timescales of the two oscillating terms are very different, it is useful to consider them separately. The frequency  $\omega_r$  is the harmonic oscillator frequency of the ion trapped in the pseudopotential. This is referred to as the secular frequency. The faster motion at the trap drive frequency is called micromotion (Figure 2.2). Displacing the ions from the centre of the trap will result in an increase in micromotion amplitude. The micromotion is minimised at the trap centre, but it is intrinsic to the trapping method and cannot be eliminated. The depth of the trap,  $D$ , in the radial plane is<sup>77</sup>

$$D = \frac{m}{2} \omega_r^2 r_0^2. \quad (2.15)$$

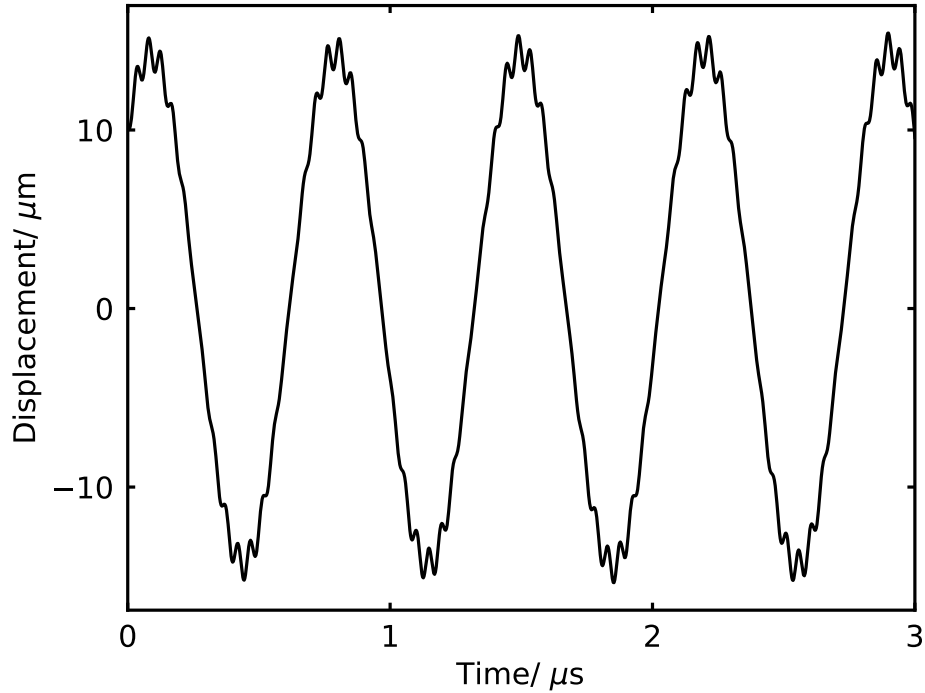


Figure 2.2: Motion of a trapped ion in one radial axis from a 3D molecular dynamics simulation.

Trap depths of several electronvolts are common, corresponding to temperatures of  $> 1 \times 10^4$  K. This allows very hot ions to be trapped.

In the axial direction, the motion is described by

$$z(t) = z_0 \cos(\omega_z t + \phi_z), \quad (2.16)$$

where

$$\omega_z = \sqrt{\frac{-a}{2}} \Omega. \quad (2.17)$$

In this case, there is only one motional frequency because there is no rf component to the trapping field along the axis of the trap.

### 2.1.5 Real Traps

A harmonic potential is achieved by hyperbolic electrodes. Real electrodes are often not truly hyperbolic, in order to facilitate better optical access. The resulting anharmonicities become significant for high energies. This is usually negligible at the very low motional energies used in most atomic physics experiments. It is usually assumed that the radial geometry of the trap is perfectly efficient. However, in a non-ideal trap this is not the case.<sup>79</sup>

In real traps, there are often stray electric fields caused by charge building up on dielectric surfaces in the vicinity of the trap. In addition, it is possible that the potential minimum of the dc electric field from the axial electrodes does not exactly coincide with the minimum of the rf field. When the ions are displaced from the centre of the rf trapping field, there is excess micromotion. Unlike the intrinsic micromotion discussed earlier, this excess micromotion can be compensated by dc voltages applied to the trapping electrodes.<sup>80</sup>

Additionally, if one diagonal pair of radial electrodes is driven with an rf voltage and the other pair is held at ground, the asymmetry of the trap drive results in a component of the rf field along the trap axis. In some cases, this may lead to rf confinement in all three dimensions of the trap. Whilst it may be advantageous under some circumstances, this also results in micromotion for ions displaced along the axis of the trap in addition to the radial directions.

### 2.1.6 Coulomb Crystals

Hot trapped ions exist as a plasma in which they interact with other trapped ions, through an effective potential created by the other ions. This is the case above a critical temperature given by the plasma parameter,  $\Gamma_{\text{plasma}}$ ,

$$\Gamma_{\text{plasma}} = \frac{E_p}{E_k} \gtrsim 160 \quad (2.18)$$

where  $E_p$  is the potential energy due to the interaction of an ion with its nearest neighbour and  $E_k$  is the average kinetic energy.<sup>81</sup> These temperatures are usually on the order of a few mK and are readily achieved with laser cooling.

Below this critical temperature the ions can crystallise to form a regular array or Coulomb crystal. In such crystals, the ions have shared motional modes and are well-localised. Individual ions are separated due to the Coulomb repulsion and can be resolved in camera images if the ions fluoresce. The crystal structure is dictated by the balance of the trapping force and the inter-ion Coulomb repulsion.

In the case of multi-species crystals, crystallisation still occurs, but the trapping force on the ion will depend on its charge-to-mass ratio. If the ions are sufficiently similar in charge-to-mass ratio, the crystal will be slightly distorted, but otherwise intact. The ions will have shared motional modes as in the case of a single-species crystal. In cases of extreme differences between the ions, they may localise in different regions of the trap, with lighter and more highly charged ions crystallised closer to the centre of the trap.<sup>82</sup>

## 2.2 Molecular Beams

Molecular ions can be loaded into rf traps by ionising molecules from a homogenous background gas. However, collisions between trapped ions and background molecules are un-

desirable. Thermalisation of the rotational state and charge-exchange reactions can cause loss of the internal state of the produced ion, which is detrimental in many applications.

One solution to this is to load ions into the trap via a molecular beam. A molecular beam is a stream of molecules travelling through a vacuum or low pressure environment. A high density of molecules can pass through the centre of the trap without conceding a high pressure in the wider trapping region. If the molecules in the tail of the molecular beam packet are ionised to load the ion trap, then damaging collisions are minimised.

The properties of supersonic beams are advantageous in many applications, because the adiabatic expansion results in effective cooling of the translational motion and some cooling of the rotational and vibrational degrees of freedom.<sup>83</sup> This is beneficial for experiments that require controlled, cold molecules for ionisation and reaction studies and for further deceleration by external fields (e.g. Zeeman deceleration). For example, many ionisation processes proceed via a resonant excitation step from the ground rovibronic state, and so the ionisation probability is maximised at low internal temperatures where the population is almost entirely in the ground state.

### 2.2.1 Dynamics of Supersonic Atomic Beams

We consider the dynamics of the atomic beam under the ideal gas approximation and assume a continuous free-jet rather than a pulsed source, although this is usually a good approximation.<sup>84</sup> The gas starts in a high pressure reservoir, and a small aperture is opened briefly to allow atoms to escape into an expansion region of lower pressure. Collisions between atoms at the aperture convert thermal energy in the reservoir to kinetic energy along the propagation axis of the beam. The resulting beam accelerates and cools as it expands. Supersonic expansion occurs when the pressure of the original container,  $P_0$ , is much higher than the pressure in the expansion region,  $P_b$ . The condition for supersonic expansion is

$$\frac{P_0}{P_b} > \left( \frac{\gamma + 1}{2} \right)^{\gamma/(\gamma-1)}, \quad (2.19)$$

where  $\gamma = c_p/c_v$  is the isentropic expansion factor of the gas. For an atomic beam,  $\gamma = 5/3$ .<sup>84</sup>

A supersonically expanding gas behaves differently in different zones after leaving the aperture (Figure 2.3). The zone of silence has the desired beam properties: high number density, low temperature and high velocity.<sup>85</sup> Beyond the Mach disk, which bounds the zone of silence along the beam axis, shock waves caused by the supersonic propagation disrupt the beam's properties. The Mach disk is positioned at a distance,  $Z_{\text{Mach}}$ ,

$$Z_{\text{Mach}} = 0.67 \text{ m} \cdot \left( \frac{P_0}{P_b} \right). \quad (2.20)$$

The first skimmer for collimation of the beam must be placed closer than this distance to conserve the desired properties of the beam.<sup>84</sup>

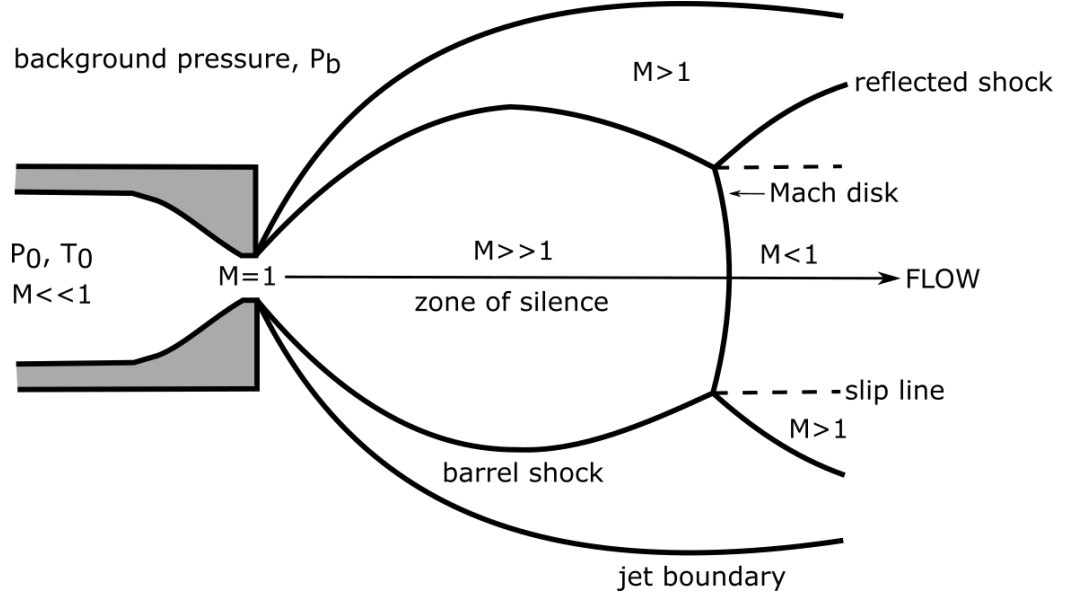


Figure 2.3: Shock boundaries and expansion zones for the expansion of a supersonic molecular beam. Adapted from G. Scoles.<sup>84</sup>

The propagation of the beam is characterised by the Mach number,  $M = v/v_s$ , where  $v$  is the velocity and

$$v_s = \sqrt{\frac{\gamma RT}{M_{\text{mol}}}}, \quad (2.21)$$

where  $R$  is the universal gas constant and  $M_{\text{mol}}$  is the molar mass of the constituent atoms.<sup>84</sup> The Mach number, found empirically, may also be written

$$M = A \left( \frac{z - z_0}{d} \right) - \left( \frac{\frac{1}{2} \left( \frac{\gamma+1}{\gamma-1} \right)}{A \left( \frac{z-z_0}{d} \right)^{(\gamma-1)}} \right), \quad (2.22)$$

where  $d$  is the diameter of the aperture,  $z$  is the propagation distance and  $A$  and  $z_0$  are empirical fit parameters. The Mach number increases from  $M \ll 1$  inside the initial chamber to  $M = 1$  at the aperture (Figure 2.3). As the beam flows, it accelerates ( $M > 1$ ) and cools as a result of the adiabatic expansion. As the beam expands, the velocity and temperature are

$$v = M \sqrt{\frac{\gamma RT_0}{M_{\text{mol}}}} \left( 1 + \frac{\gamma-1}{2} M^2 \right)^{-\frac{1}{2}}, \quad (2.23)$$

and

$$T = T_0 \left( 1 + \frac{\gamma-1}{2} M^2 \right)^{-1}, \quad (2.24)$$

respectively, where  $T_0$  is the initial temperature of the gas in the reservoir. If all of the thermal energy of the gas is converted to kinetic energy along the beam axis, then the terminal velocity  $v_t$  is reached<sup>85</sup>

$$v_t = \sqrt{\frac{2R}{M_{\text{mol}}} \left( \frac{\gamma}{\gamma-1} \right) T_0}. \quad (2.25)$$

The distribution of velocities in the atomic beam is narrower than in the thermalised gas before expansion, and the terminal peak velocity of the beam packet is greater than the initial peak velocity. Assuming that there is sufficient time for thermalisation, the velocity distribution is described by a Maxwell-Boltzmann distribution.

### 2.2.2 Dynamics of Supersonic Molecular Beams

The theory of the molecular beam differs from the ideal case for an atomic beam described above. The richer internal structure of molecules adds more complexity. For the expansion of the molecular beam, we must consider vibrational and rotational temperature of the beam in addition to the translational temperature. For a diatomic gas, such as  $\text{N}_2$ , the isentropic expansion factor is  $\gamma = 7/5$ , in the assumption that there is minimal vibrational excitation and some rotational excitation.<sup>86</sup>

In an atomic beam, the translational degrees of freedom are effectively cooled through collisions during the adiabatic expansion of the gas. In molecules, there is effective cooling of the translational motion, but the efficiency of the rotational and vibrational cooling depends on a number of factors. The probability of collisions driving molecules to lower vibrational and rotational states is higher if the energy levels are more closely spaced. Therefore, the rotational degrees of freedom are generally more effectively cooled than the vibrational degrees of freedom. The splitting of vibrational and rotational energy levels is also smaller for molecules with heavier nuclei. The efficiency of internal cooling also depends on the stagnation pressure in the reservoir and the diameter of the aperture.<sup>87</sup>

It is possible to improve the cooling of molecules by seeding the beam with an atomic species, usually a noble gas. Inelastic collisions transfer rotational and vibrational energy from the molecules to the translational energy of the atoms, which is then cooled during the expansion of the gas. This internal energy transfer is more effective for rotational degrees of freedom than for vibrational degrees of freedom. Seeding is typically only effective with less than about 5 % of the molecular species in the gas mixture.<sup>86,88</sup> Seeding also allows some control over the velocity of the molecular beam because the velocity depends on the molar mass of the atomic species and its heat capacity (in addition to the reservoir temperature).

## Chapter 3

# Theory: Light and Matter

This chapter introduces light-matter interactions. This includes the theory of radiative transitions, laser cooling and spectroscopy.

### 3.1 Radiative Transitions

There are many processes that atoms and molecules may undergo that result in transitions from one internal state to another. These can be radiative, involving the absorption or emission of photons, or non-radiative, such as through collisions with other particles, intersystem crossing or excitation by an electrical current (as in fluorescent light bulbs).<sup>89</sup> Of particular interest to the field of atomic and molecular physics are radiative transitions which form the basis of laser cooling, photoionisation and spectroscopy. In this section, we discuss these radiative processes assuming a classical electromagnetic wave interacting with the atom or molecule. Magnetic transitions are not considered.

#### 3.1.1 Atom Interacting with an Electromagnetic Wave

In the case of an atom interacting with a light field, the electron experiences a Lorentz force,  $\vec{F} = -e(\vec{\mathcal{E}} + \vec{v} \times \vec{\mathcal{B}})$ . The potential energy of the interaction,  $W = \vec{F} \cdot \vec{r}$ , is

$$W(\vec{r}, t) = -e\vec{\mathcal{E}}(\vec{r}, t) \cdot \vec{r} - e(\vec{v} \times \vec{\mathcal{B}}(\vec{r}, t)) \cdot \vec{r}, \quad (3.1)$$

where  $\vec{v}$  is the velocity,  $\vec{r}$  is the position,  $\vec{\mathcal{E}}$  is the electric field of the radiation,  $\vec{\mathcal{B}}$  is the magnetic field of the radiation,  $e$  is the charge of an electron and  $t$  is time. The Hamiltonian,  $\hat{H}'$ , for the atom-light system is

$$\hat{H}' = \hat{H}_a^{(0)} + \hat{W}(\vec{r}, t), \quad (3.2)$$

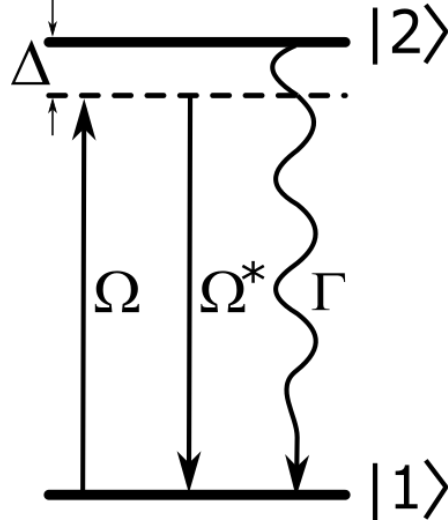


Figure 3.1: Energy level diagram for a two level system coupled by a laser.

where  $\hat{H}_a^{(0)}$  is the unperturbed Hamiltonian for the case of the one-electron atom.<sup>90</sup> In principle, we would then like to solve the Schrödinger equation for the wavefunction,  $\Psi$ ,

$$i\hbar \frac{\partial \Psi(\vec{r}, t)}{\partial t} = \hat{H} \Psi(\vec{r}, t). \quad (3.3)$$

The solutions to the unperturbed Schrödinger equation are of the form

$$\Psi_k^{(0)}(\vec{r}, t) = \psi_k(\vec{r}) \exp \left[ -\frac{iE_k t}{\hbar} \right], \quad (3.4)$$

where  $E_k$  is the energy of the state and  $\hbar$  is the reduced Planck constant. As the functions  $\psi_k(\vec{r})$  form a complete set of energy eigenfunctions, any wavefunction of the atom may be written as a linear combination of these functions, i.e.

$$\Psi^{(1)}(\vec{r}, t) = \sum_k c_k(t) \psi_k(\vec{r}) \exp \left[ -\frac{iE_k t}{\hbar} \right], \quad (3.5)$$

where the coefficients  $c_k(t)$  are a consequence of the time-dependent perturbation caused by the laser.  $|c_k(t)|^2$  is the instantaneous probability that the atom is in state  $k$  at time  $t$ , provided the wavefunction is normalised such that

$$\sum_k |c_k(t)|^2 = 1. \quad (3.6)$$

Considering a two-level system (Figure 3.1), the wavefunction can be written as a linear combination of the two basis states,

$$\Psi^{(1)}(\vec{r}, t) = c_1(t) \psi_1(\vec{r}) \exp \left[ -\frac{iE_1 t}{\hbar} \right] + c_2(t) \psi_2(\vec{r}) \exp \left[ -\frac{iE_2 t}{\hbar} \right], \quad (3.7)$$

where states 1 and 2 are the ground and excited states respectively (see Figure 3.1). The

Schrödinger equation for the interaction is given by

$$[\hat{H}_a^{(0)} + \hat{W}(\vec{r}, t)]\Psi^{(1)}(\vec{r}, t) = i\hbar \frac{\partial \Psi^{(1)}(\vec{r}, t)}{\partial t}. \quad (3.8)$$

After cancelling out the terms from the unperturbed Schrödinger equation, we find

$$\begin{aligned} c_1(t)\hat{W}(\vec{r}, t)\Psi_1^{(0)}(\vec{r}, t) + c_2(t)\hat{W}(\vec{r}, t)\Psi_2^{(0)}(\vec{r}, t) \\ = i\hbar \left[ \frac{dc_1(t)}{dt}\Psi_1^{(0)}(\vec{r}, t) + \frac{dc_2(t)}{dt}\Psi_2^{(0)}(\vec{r}, t) \right]. \end{aligned} \quad (3.9)$$

Substituting in the zero-order wavefunctions, multiplying from the front by  $\psi_1^*(\vec{r}) \cdot e^{\frac{iE_1 t}{\hbar}}$  and integrating with respect to  $\vec{r}$ , we get

$$\begin{aligned} i\hbar\dot{c}_1(t) &= c_1(t) \langle \psi_1(\vec{r}) | \hat{W}(\vec{r}, t) | \psi_1(\vec{r}) \rangle + c_2(t) \langle \psi_1(\vec{r}) | \hat{W}(\vec{r}, t) | \psi_2(\vec{r}) \rangle e^{-i\omega_0 t}; \\ i\hbar\dot{c}_2(t) &= c_1(t) \langle \psi_2(\vec{r}) | \hat{W}(\vec{r}, t) | \psi_1(\vec{r}) \rangle e^{-i\omega_0 t} + c_2(t) \langle \psi_2(\vec{r}) | \hat{W}(\vec{r}, t) | \psi_2(\vec{r}) \rangle, \end{aligned} \quad (3.10)$$

where  $\omega_0 = \frac{|E_1 - E_2|}{\hbar}$ . Using  $\langle \psi_i(\vec{r}) | \hat{W}(\vec{r}, t) | \psi_i(\vec{r}) \rangle = 0$ , the equations become

$$\begin{aligned} \dot{c}_1(t) &= \frac{-i}{\hbar} c_2(t) \langle \psi_1(\vec{r}) | \hat{W}(\vec{r}, t) | \psi_2(\vec{r}) \rangle e^{-i\omega_0 t}; \\ \dot{c}_2(t) &= \frac{-i}{\hbar} c_1(t) \langle \psi_2(\vec{r}) | \hat{W}(\vec{r}, t) | \psi_1(\vec{r}) \rangle e^{-i\omega_0 t} \end{aligned} \quad (3.11)$$

We assume that the incident laser has a frequency  $\omega = \omega_0 + \Delta$ , where  $\Delta$  is the detuning of the laser from the transition. The coupled equations 3.11 can be rewritten in terms of the Rabi frequency,  $\Omega_R$ ,

$$\Omega_R = \frac{\langle \psi_2(\vec{r}) | \hat{W}(\vec{r}) | \psi_1(\vec{r}) \rangle}{\hbar}. \quad (3.12)$$

Using the rotating wave approximation,<sup>90</sup> this results in

$$\begin{aligned} \dot{c}_1 &\approx -i\Omega_R c_2 e^{-i\Delta t}; \\ \dot{c}_2 &\approx -i\Omega_R^* c_1 e^{-i\Delta t} \end{aligned} \quad (3.13)$$

The Rabi frequency represents the frequency of oscillation between the two states under the laser field. Solving the coupled equations, assuming the population starts in the ground state at time  $t = 0$ , we obtain

$$\begin{aligned} c_2(t) &= \frac{\Omega_R^*}{2} \left( \frac{1 - e^{i\Delta t}}{\Delta} \right); \\ |c_1(t)|^2 &= 1 - |c_2(t)|^2. \end{aligned} \quad (3.14)$$

The oscillation between the two states, with the same probability of absorption and stimulated emission under the action of the laser, shows the symmetry of these processes.

### 3.1.2 Electric Transitions

In the case of electric interactions, the Hamiltonian simplifies to

$$\hat{H}'_{\mathcal{E}} = \hat{H}_a^{(0)} - e\vec{\mathcal{E}}(\vec{r}, t) \cdot \vec{r}. \quad (3.15)$$

The Schrödinger equation is rarely solved for the case of all electric transitions. In most cases, the so-called dipole approximation is used to reduce the problem to the simplest useful case. This is a very useful approximation which accounts for most probable transitions, referred to as (electric) dipole or E1 transitions. Higher order transitions, often referred to as dipole-forbidden transitions, are particularly relevant for metrology applications because they usually have very narrow linewidths. The most probable of these are electric quadrupole (or E2) transitions. Higher order transitions do also occur, but with each extra term in the expansion the probability decreases. In addition to single-photon transitions, multiphoton transitions can occur via the absorption of more than one photon. In the following sections, approximations are employed to consider the special cases of electric dipole, electric quadrupole and multiphoton transitions.

### 3.1.3 Electric Dipole Transitions

Assuming that the wavelength of the incident radiation is much longer than the spatial extent of the atom, it is reasonable to assume that the electric field experienced by the atom varies only in time. This electric dipole approximation yields

$$\vec{\mathcal{E}}_{\text{dipole}} = \mathcal{E}_0 \hat{e} \cdot e^{-i\omega t}, \quad (3.16)$$

where  $\hat{e}$  is the polarisation vector of the light and  $\mathcal{E}_0$  is the electric field amplitude.<sup>90</sup> The Rabi frequency in this case is

$$\Omega_{R,\mathcal{E}}^{\text{dipole}} = \frac{\langle \Psi_j(\vec{r}, t) | \vec{d} \cdot \vec{\mathcal{E}}(\vec{r}) | \Psi_i(\vec{r}, t) \rangle}{\hbar} \quad (3.17)$$

where  $\vec{d} = -e\vec{r}$  is the dipole moment of the atom. We define the transition dipole moment,  $\vec{\mathcal{D}}_{ij}$ , for a transition from state  $i$  to state  $j$  such that,

$$\vec{\mathcal{D}}_{ij} = -e \langle \Psi_j(\vec{r}, t) | \vec{r} | \Psi_i(\vec{r}, t) \rangle \quad (3.18)$$

There are four matrix components of the transition dipole moment associated with the possible combinations of states. A dipole transition is allowed if the transition dipole moment is non-zero.

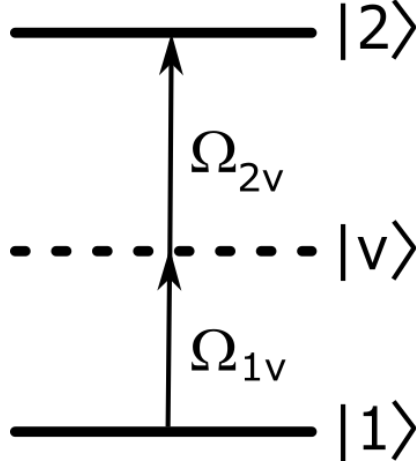


Figure 3.2: Energy level system for a two photon process which proceeds from state  $|1\rangle$  to state  $|2\rangle$  via an intermediate virtual state  $|v\rangle$ .

### 3.1.4 Electric Quadrupole Transitions

Electric quadrupole transitions arise from the spatial gradient of the electric field of the light across the atom.<sup>90</sup> The electric quadrupole moment,  $Q_{ij}$ , is

$$Q_{ij} = e(3x_i x_j - r^2 \delta_{ij}), \quad (3.19)$$

where  $x_i, x_j$  are the coordinates of the valence electron and  $\delta_{ij}$  is the delta function.<sup>91,92</sup> The quadrupole interaction energy,  $W_Q$ , is given by<sup>91,92</sup>

$$W_Q = -\frac{1}{6} \sum_{ij} Q_{ij} \left. \frac{\partial \mathcal{E}_j}{\partial x_i} \right|_{x=0}. \quad (3.20)$$

The electric field gradient is small compared to the temporal variation considered in the dipole approximation. This results in a low relative transition strength, characterised by the Rabi frequency

$$\Omega_{R,\mathcal{E}}^{\text{quad.}} = -\frac{1}{6\hbar} \sum_{ij} \langle \Psi_j(\vec{r}, t) | Q_{ij} | \Psi_i(\vec{r}, t) \rangle \left. \frac{\partial \mathcal{E}_j}{\partial x_i} \right|_{x=0}. \quad (3.21)$$

### 3.1.5 Multiphoton Transitions

Multiphoton excitations enable transitions in cases where the energy gap is too large for a single photon process, such as in multiphoton ionisation schemes.<sup>93</sup> Raman transitions are also commonly used to address forbidden transitions and to transfer population adiabatically between states.<sup>94</sup> These transitions occur between states via the absorption or emission of multiple photons. In practice, the photons interfere constructively and are absorbed simultaneously by the atom. However, for simplicity, we treat the photon absorption as a series of excitations from the ground state via virtual states until the excited

state is reached. Our focus will be the simplest case of this: the two-photon transition. Here, there are two real states and one virtual state, where the virtual state may lie between the two states in energy or above (Figure 3.2). The virtual state is purely a mathematical device (and is never occupied) so this is not the same as two consecutive transitions.

Within the dipole approximation, the electric field of the two photons, labelled a and b, is

$$\vec{\mathcal{E}}(t) = \vec{\mathcal{E}}_{0a}e^{-i\omega_a t} + \vec{\mathcal{E}}_{0b}e^{-i\omega_b t}, \quad (3.22)$$

where the two photons may have different frequencies. The two-photon process is treated as two consecutive single-photon transitions: from the ground state  $|1\rangle$  to the virtual state  $|v\rangle$  and from the virtual state  $|v\rangle$  to the excited state  $|2\rangle$ .<sup>3</sup> For each laser, we must consider the possible coupling between each pair of states. In this case, Equation 3.14 for the first transition to the virtual state becomes

$$c_v(t) = \frac{\Omega_{1va}}{2} \left( \frac{1 - e^{-i\delta_{1va}t}}{\delta_{1va}} \right) + \frac{\Omega_{1vb}}{2} \left( \frac{1 - e^{-i\delta_{1vb}t}}{\delta_{1vb}} \right), \quad (3.23)$$

where  $\delta_{1va} = \omega_v - \omega_1 - \omega_a$ ,  $\delta_{1vb} = \omega_v - \omega_1 - \omega_b$ . The population of the excited state is then given by

$$\begin{aligned} c_2(t) = & \left( \frac{\Omega_{1va}\Omega_{2va}}{4\delta_{1va}} + \frac{\Omega_{1vb}\Omega_{2va}}{4\delta_{1vb}} \right) \cdot \left( \frac{1 - e^{-i\delta_{2va}t}}{\delta_{2va}} \right) \\ & + \left( \frac{\Omega_{1va}\Omega_{2vb}}{4\delta_{1va}} + \frac{\Omega_{1vb}\Omega_{2vb}}{4\delta_{1vb}} \right) \cdot \left( \frac{1 - e^{-i\delta_{2vb}t}}{\delta_{2vb}} \right). \end{aligned} \quad (3.24)$$

If the two photons are the same colour, then this simplifies to

$$c_2(t) = \frac{\Omega_{1v}\Omega_{2v}}{\delta_{1v}} \cdot \left( \frac{1 - e^{-i\delta_{2v}t}}{\delta_{2v}} \right). \quad (3.25)$$

### 3.1.6 Spontaneous Emission

Spontaneous emission is the final radiative transition process. The semi-classical description, in which light was treated as a classical electromagnetic wave, is no longer sufficient. A rate equation treatment of spontaneous decay can be used to obtain the correct decay rate, now known as the Einstein A coefficient.<sup>90</sup> The rigorous derivation of spontaneous emission rates comes from Wigner-Weisskopf theory, but the details are not relevant to understand this thesis.

## Electric Dipole Transitions

For a dipole transition in a two level system, the rate of spontaneous emission is given by the product of the Einstein  $A_{ij}$  coefficient

$$A_{ij} = \frac{8\pi^2\nu_{ij}^3}{3\epsilon_0\hbar c^3} |\mathcal{D}_{ij}|^2, \quad (3.26)$$

and the population of the excited level, where  $\nu_{ij}$  is the transition frequency and  $\mathcal{D}_{ij}$  is the transition dipole moment.<sup>70,95</sup>

## Electric Quadrupole Transitions

For the quadrupole transition, the  $A_{ij}$  coefficient is different. In this case,

$$A_{ij} = \frac{4\pi^4\nu_{ij}^5}{5\epsilon_0\hbar c^3} |\mathcal{Q}_{ij}|^2, \quad (3.27)$$

where  $\mathcal{Q}_{ij}$  is the quadrupole transition moment.<sup>95,96</sup> There is a greater dependence on the transition frequency compared to the decay rate for dipole transitions.

### 3.1.7 Transition Moments, Symmetry and Selection Rules

We have, thus far, defined dipole and quadrupole transitions by the electric field interactions responsible for them without considering which transitions these correspond to within the atom. However, there are selection rules based on symmetry arguments which remove the need for laborious calculations in determining whether transitions occur between pairs of states.

Transition moments dictate the probability of excitation and decay between states. If a transition moment is zero, there is zero probability of that transition occurring. The transition moment expectation value is zero if the transition moment function (to be integrated as per  $\langle\psi|\hat{\mu}|\psi\rangle$ ) is antisymmetric, and non-zero if it is totally symmetric. In the case of a dipole transition, the operator  $\hat{\mu} = \mathcal{D}_{ij}$  is antisymmetric and so the product of the two states for the transition must be antisymmetric, to ensure the total product is symmetric. In the case of a quadrupole transition, the operator  $\hat{\mu} = \mathcal{Q}_{ij}$  is symmetric and so the product of the states for the transitions must also be symmetric. Transitions with zero dipole transition moments are referred to as dipole-forbidden or just forbidden transitions, because quadrupole transitions occur with probabilities  $\sim 10^8$  times lower than dipole transitions.<sup>70</sup> Some selection rules are given in Table 3.1.

Table 3.1: Selection rules for electric dipole (one- and two-photon) and quadrupole transitions.<sup>1</sup> Selection rules marked with a star cannot occur between two states with  $l = 0$ .

Quantum number	Dipole	Quadrupole	Two-photon (dipole)
$\Delta L$	$0^*, \pm 1$	$0^*, \pm 1, \pm 2$	$0, \pm 2$
$\Delta l$	$\pm 1$	$0, \pm 2$	$0, \pm 2$
$\Delta m_l$	$0, \pm 1$	$0, \pm 1, \pm 2$	$0, \pm 1, \pm 2$
$\Delta S$	0	0	0
$\Delta J$	$0^*, \pm 1$	$0^*, \pm 1, \pm 2$	$0, \pm 2$

### 3.1.8 The Optical Bloch Equations

The complete Hamiltonian for an atom-laser system includes the interaction Hamiltonian and the spontaneous emission operator. We can introduce a density matrix operator

$$\hat{\rho} = \sum_j P_j |\psi_j\rangle \langle \psi_j|, \quad (3.28)$$

which represents the state of the system, where  $P_j$  is the probability of the state. The density matrix is a 2x2 matrix for a two-level system

$$\hat{\rho} = \begin{pmatrix} \rho_{11} & \rho_{12} \\ \rho_{21} & \rho_{22} \end{pmatrix} = \begin{pmatrix} |c_1(t)|^2 & c_1(t)c_2^*(t) \\ c_2(t)c_1^*(t) & |c_2(t)|^2 \end{pmatrix}. \quad (3.29)$$

The diagonal elements represent the state populations and the other elements show the couplings between the states. We can write coupled equations to show the time evolution of each of the elements of the density matrix

$$\begin{aligned} \frac{d\rho_{11}}{dt} &= \Gamma\rho_{22} - i\frac{\Omega_R}{2} (\rho_{21}e^{i\Delta t} - \rho_{12}e^{-i\Delta t}); \\ \frac{d\rho_{22}}{dt} &= -\Gamma\rho_{22} + i\frac{\Omega_R}{2} (\rho_{21}e^{i\Delta t} - \rho_{12}e^{-i\Delta t}); \\ \frac{d\rho_{12}}{dt} &= -\frac{\Gamma\rho_{12}}{2} + i\frac{\Omega_R}{2} e^{i\Delta t} (\rho_{11} - \rho_{22}); \\ \frac{d\rho_{21}}{dt} &= -\frac{\Gamma\rho_{12}}{2} - i\frac{\Omega_R}{2} e^{i\Delta t} (\rho_{11} - \rho_{22}); \end{aligned} \quad (3.30)$$

where  $\Gamma$  is the spontaneous decay rate. These equations are known as the Optical Bloch Equations (OBEs) because of their resemblance to the Bloch equations for nuclear magnetisation. The steady state solutions are<sup>97</sup>

$$\begin{aligned} \rho_{22} &= \frac{s/2}{1 + s + (2\Delta/\Gamma)^2}; \\ \rho_{11} &= 1 - \rho_{22}, \end{aligned} \quad (3.31)$$

where  $s = I/I_s$  is the saturation parameter and the saturation intensity is given by

$$I_s = \frac{2\pi^2\hbar c\Gamma}{3\lambda^3}. \quad (3.32)$$

Similarly for the coherences

$$\tilde{\rho}_{21} = \rho_{21}e^{i\Delta t} = \frac{i\Omega_R}{2\left(\frac{\Gamma}{2} - i\Delta\right)\left(1 + \frac{2\Omega_R^2}{\Gamma^2 + 4\Delta^2}\right)}. \quad (3.33)$$

The decay rate  $\Gamma$  is the natural linewidth of the transition. This width arises from the Heisenberg Uncertainty principle due to the finite lifetime of the excited state. However, for saturation parameters greater than zero the linewidth is broadened to  $\Gamma'$ ,

$$\Gamma' = \Gamma\sqrt{1 + s}. \quad (3.34)$$

In order to extend this to multilevel systems, a density matrix can be constructed in the same way and the resulting OBEs can be solved for the evolution of the system.

## 3.2 Laser Cooling

Laser cooling methods allow cooling to sub-mK temperatures. The first of these techniques, Doppler cooling, was first achieved for trapped ions in 1978.<sup>98,99</sup> In the intervening years, the field of laser cooling has expanded. Additional techniques have been developed which are capable of cooling below the limit of Doppler cooling. These techniques include resolved-sideband cooling<sup>100</sup> and Sisyphus cooling.<sup>101</sup> Laser-cooled atomic ions may be used to sympathetically cool co-trapped molecular ions. In this section, we discuss the theory of Doppler cooling and sympathetic cooling.

### 3.2.1 Principle of Doppler Cooling

Photons have momentum equal to  $\hbar k$ , where  $k = \frac{2\pi}{\lambda}$  is the wavevector of the light. If a photon is absorbed by the atom, its momentum is imparted to the atom. If the atom then undergoes stimulated emission, the momentum kick is equal and opposite to the absorption kick and so the net force due to the absorption-emission process is zero. In contrast, if the ion decays back to the ground state by spontaneous emission, the photon is emitted in a random direction. The momentum kick experienced by the ion is in a direction that is uncorrelated to the absorption. This process is isotropic and, over many events, the effect of the momentum kicks caused by the spontaneous emission from the excited state is zero. However, because the laser field is highly directional, the kick caused by the absorption is always in the same direction. If the ion is moving towards the laser beam, it experiences a reduction in its momentum, corresponding to cooling. If it is moving away from the laser beam, it experiences an increase in its momentum, corresponding to heating. In the ion trap the ion oscillates and so, for a stable laser direction, moves both towards and away from the laser beam with varying velocity. In order to ensure that the net effect of the laser is to cool the ion, the laser must be detuned so that absorption is more probable when the ion moves towards the laser than when it moves away from it. In this way,

there are more cooling interactions than heating interactions. This relies on the Doppler effect shifting the frequency of the laser in the frame of the ion so that it sees the laser on-resonance when it is red-detuned.

The momenta of optical photons are very small and so cooling an ion typically requires thousands of absorption events. Central to this method is the need for a cyclical transition within the ion. Otherwise, population will leak out of the cooling cycle and only a small number of cycles will occur before the ion can no longer be cooled. This requirement is the reason that laser cooling of molecules is challenging: the rotational and vibrational structure means that decay into multiple channels is inevitable.

### 3.2.2 Doppler Cooling of a Two Level System

In the simplest case of Doppler cooling, there are only two levels: a ground state and an excited state. For this, we can use the results we calculated earlier for a dipole-allowed transition. The force on the atom through a cycle of absorption/emission will be

$$\vec{F} = \frac{d\vec{p}}{dt} = \hbar\vec{k}\Gamma\rho_{22} = \hbar\vec{k}\Gamma\frac{s_0/2}{1 + s_0 + (2\Delta/\Gamma)^2}, \quad (3.35)$$

provided the atom/ion is stationary with respect to the laser-propagation direction,  $\vec{k}$ . If the ion moves along the direction  $\hat{k}$  then the detuning seen by the atom becomes  $\Delta \rightarrow \Delta + \vec{v}_k\vec{k}$  and

$$\vec{F}(v_k) = \hbar\vec{k}\Gamma\frac{s_0/2}{1 + s_0 + \left(\frac{2(\Delta + \vec{v}_k\vec{k})}{\Gamma}\right)^2}. \quad (3.36)$$

If the velocity of the ion is sufficiently small, then a Taylor expansion about  $v_k$  can be used to write the force in two terms: one of which is dependent on the velocity. This gives

$$\vec{F}_v = \vec{F}_0 + \beta v_k \hat{k}, \quad (3.37)$$

where  $\beta$  is

$$\beta = -\frac{4\hbar k^2 \Delta}{\Gamma} \cdot \frac{s_0}{1 + s_0 + (2\Delta/\Gamma)^2}. \quad (3.38)$$

The velocity-dependent term acts in the opposite direction to the ion's velocity and so damps its motion. This result accounts for the damping of the ion motion caused by the Doppler cooling mechanism. However, there is a limit to the temperatures that can be achieved by this method. As the ion is cooled, it moves out of resonance with the cooling laser. This limits the minimum temperature,  $T_{\text{Doppler}}$ , that can be achieved by Doppler cooling to

$$T_{\text{Doppler}} = \frac{\hbar\Gamma}{2k_B}. \quad (3.39)$$

In addition, the random emission process contributes to heating of the ion. This recoil mechanism limits the achievable temperature to  $T_{\text{recoil}}$ ,

$$T_{\text{recoil}} = \frac{\hbar^2 k^2}{mk_{\text{B}}}. \quad (3.40)$$

The recoil limit is usually much lower than the Doppler limit and may be reached by sub-Doppler cooling methods such as Sisyphus cooling or velocity-selective coherent population trapping.<sup>97</sup>

### 3.2.3 Sympathetic Cooling

In buffer gas cooling, a colder species thermalises with one at a higher temperature, cooling the warmer species to a weighted mean temperature.<sup>102</sup> The requisites of this method are a large elastic collision cross-section to ensure thermalisation and low inelastic cross-section to prevent changes in the internal state.<sup>103</sup> For sympathetic cooling the cold species is laser cooled during thermalisation and the target species reaches the limit of the laser cooling. This is a powerful method for the cooling of molecules because there are very few constraints on the structure of the sympathetically cooled species. It has been used to cool molecular ions to the motional ground state<sup>104</sup> and has even been proposed for the cooling of graphene to temperatures below  $60 \mu\text{K}$ .<sup>105</sup>

## 3.3 Atomic and Molecular Spectra

### 3.3.1 Term Symbols

In spectroscopy and atomic physics, the configurations of atoms and molecules are often referred to using symbols which contain information about the quantum numbers and symmetries of the states. These are called term symbols and are different for atomic and molecular states. Transitions between energy levels are denoted  $T' \leftarrow T$  for absorption and  $T' \rightarrow T$  for emission (following the spectroscopic convention), where the term symbol for the higher energy level,  $T'$ , is always written first.<sup>70</sup> In the convention used in this thesis,  $T'$  is the initial state and  $T$  is the final state, regardless of state energy.

#### Atomic Term Symbols

Atomic term symbols contain the important information about the total state of the atom in a concise way. Atomic term symbols for energy levels are of the format

$$^{2S+1}L_J, \quad (3.41)$$

where  $S$  is the spin quantum number,  $L$  represents the orbital angular momentum quantum number (where quantum numbers of 0, 1, 2, 3, 4 are replaced by S, P, D, F, G) and  $J$  is the total angular momentum,  $J = L + S$ .  $(2S + 1)$  is the spin multiplicity. Specific states within an energy level may be referred to as  $(2S+1)L_J^{M_J}$  where  $M_J$  is the magnetic quantum number for the state.<sup>70</sup>

## Term Symbols for Diatomic Molecules

### Symmetry Labels

In addition to containing information about the angular momenta of atomic and molecular states, term symbols for diatomic molecules include symmetry labels for two types of symmetry: inversion and reflection. Specifically, if a state is symmetric with respect to inversion through the centre of the molecule (if such a centre exists), it is said to be of gerade (even) symmetry. If it is antisymmetric with respect to inversion, then it is said to have ungerade (odd) symmetry. A state is labelled '+' if it is symmetric with respect to reflection in a plane containing the internuclear axis, and '-' if it is antisymmetric with respect to this reflection. This only applies to  $\Sigma$  states and only states with an odd number of '-' orbitals have '-' reflection symmetry. Individual molecular orbitals are often defined in terms of their rotational symmetry about the internuclear axis. This leads to symmetry labels  $\sigma, \pi, \delta$ , etc.<sup>70</sup>

### Term Symbols

Molecular term symbols for diatomic molecules are analogous to atomic term symbols. They are of the form

$${}^{2S+1}\Lambda_{\Omega(g/u)}^{(+/-)}. \quad (3.42)$$

$L$  is replaced by the projection of the orbital angular momentum on the intermolecular axis,  $\Lambda$ . Angular momenta  $\Lambda = 0, 1, 2, 3$  are represented by symbols  $\Sigma, \Pi, \Delta, \Phi$  respectively. Similarly, the total angular momentum  $J$  is replaced by the projection of the total angular momentum onto the intermolecular axis,  $\Omega = \Lambda + \Sigma$  (where  $\Sigma$  is the projection of the spin onto the internuclear axis). The symmetry of the molecular state is also included. Symmetry labels are given for states of g/u (gerade/ungerade) and +/- symmetry.<sup>70</sup>

### 3.3.2 Transitions in Diatomic Molecules

The electronic orbitals in molecules are constructed from a basis of linear combinations of atomic orbitals according to molecular orbital theory.<sup>106</sup> While transitions between valence electronic states are typically on the order of visible or near-ultraviolet light, vibrational and rotational transitions are on the order of infrared (IR) and microwaves respectively. The electronic, vibrational and rotational states of molecules are not independent and

this adds to the complexity of molecular spectra. For transitions to be allowed, they must have a non-zero transition moment. Here, we consider only the transition electric dipole moment.<sup>70,107</sup>

### Rotational Transitions

Diatomic molecules rotate about an axis perpendicular to the bond axis of the molecule. The rotational energy levels are expressed in terms of quantum numbers  $J$  and  $M_J$  and rotational constants that depend on the moment of inertia. The degeneracy of energy levels is  $2J+1$ . For a rotating molecule, the energy,  $\tilde{E}(J)$ ,

$$\tilde{E}(J) = \tilde{B}J(J+1), \quad (3.43)$$

where  $\tilde{B}$  is the rotational constant,

$$\tilde{B} = \frac{\hbar}{4\pi c \mu_{\text{eff}} R_e^2}, \quad (3.44)$$

where  $\hbar$  is the reduced Plank constant,  $c$  is the speed of light in vacuum,  $\mu_{\text{eff}}$  is the effective mass and  $R_e$  is the equilibrium bond length.

Molecular bonds are not rigid and the bond length increases as the rotational energy increases. This changes the moment of inertia of the molecule and thus the energy levels of the rotor. This centrifugal distortion can be empirically described by a distortion constant,  $\tilde{D}_J$ , which adjusts the energies to

$$\tilde{E}(J) = \tilde{B}J(J+1) - \tilde{D}_J J^2(J+1)^2, \quad (3.45)$$

with

$$\tilde{D}_J(J) = \frac{\hbar^2}{4\pi k_f c \mu_{\text{eff}}^2 R_e^6}, \quad (3.46)$$

where  $k_f$  is the force constant of the bond. How easily the bond is stretched depends on the vibrational state of the molecule.

Transitions between rotational states are subject to a gross selection rule (under the Born-Oppenheimer approximation) that pure rotational transitions are only possible for polar molecules, so homonuclear molecules are not microwave active. The specific selection rules for the changes in quantum numbers are  $\Delta J = \pm 1$  and  $\Delta M_J = 0, \pm 1$ . The transition energy,  $\tilde{\nu}_J$ , between rotational states  $J+1 \leftarrow J$  is given by

$$\tilde{\nu}_J = 2\tilde{B}(J+1) - 4\tilde{D}_J(J+1)^3. \quad (3.47)$$

## Vibrational Transitions

The potential energy,  $E_v$ , of a vibrating diatomic molecule can be approximated as a quantum harmonic oscillator at low energies,

$$E_v = \left(v + \frac{1}{2}\right)\hbar\omega, \quad (3.48)$$

where  $v$  is the vibrational quantum number and  $\omega$  is the vibrational angular frequency. To account for the anharmonicity of the real potential, a common approximation is the Morse potential,  $V(x)$ ,

$$V(x) = hc\tilde{D}_e(1 - e^{-ax})^2, \quad (3.49)$$

where  $h$  is Plank's constant,  $\tilde{D}_e$  is the depth of the potential,  $x$  is the displacement from the equilibrium bond length and  $a$  is

$$a = \left(\frac{k_f}{2hc\tilde{D}_e}\right)^{\frac{1}{2}}. \quad (3.50)$$

Solving the Schrödinger equation for the Morse potential gives energy levels

$$E_v = \left(v + \frac{1}{2}\right)\hbar\omega - \left(v + \frac{1}{2}\right)^2\hbar\omega x_e, \quad (3.51)$$

where  $x_e$  is the anharmonicity constant such that

$$\omega x_e = \frac{a^2\hbar}{2\mu_{\text{eff}}}. \quad (3.52)$$

The potential is best approximated by a series of the form

$$E_v = \left(v + \frac{1}{2}\right)\hbar\omega - \left(v + \frac{1}{2}\right)^2\hbar\omega x_e + \left(v + \frac{1}{2}\right)^3\hbar\omega y_e \dots \quad (3.53)$$

where  $x_e$ ,  $y_e$  etc. are empirical constants. The dipole moment of the molecule must change during the extension of the bond for vibrational transitions to be allowed, which means that homonuclear diatomics are not IR active. The specific selection rule is  $\Delta v = \pm 1$ , although anharmonicities lead to weak overtones of transitions with  $\Delta v = \pm 2, \dots$ <sup>70,107</sup>

## Rotational Raman Transitions

During Raman transitions, the inelastic scattering of photons off molecules is accompanied by a change in molecular energy. There are three cases that give rise to Stokes (energy of molecule increases), Rayleigh (no exchange of energy) and anti-Stokes (energy of molecule decreases) lines. The mechanism for these transitions is excitation to a range of higher states followed by decay to one of the allowed final states, releasing a photon of the net energy change.<sup>70,107</sup>

The gross selection rule for rotational Raman transitions is that the molecule must be

anisotropically polarisable, which is the case for all diatomic molecules as the polarisability along the bond axis is maximum and perpendicular is minimum. The specific selection rule for rovibrational transitions is  $\Delta J = 0, \pm 2$ . This gives rise to three branches corresponding to  $\Delta J = -2$  (O branch),  $\Delta J = 0$  (Q branch) and  $\Delta J = 2$  (S branch). Vibrational Raman transitions require that the polarisability of the molecule changes during a vibration which is the case for all diatomic molecules.<sup>70,107</sup>

## Chapter 4

# Ion Trap, Lasers and Imaging

This chapter details the ion trap, lasers and imaging system used for the experiments described in Chapters 6 and 7.

### 4.1 Ion Trap

#### 4.1.1 Trap Design

The linear Paul trap confines the ions in the axial direction with a static dc voltage and in the perpendicular radial plane using an rf field. Two axial electrodes, with holes through their centres for laser access, provide the dc trapping voltages. The rf trapping field is provided by four radial blade electrodes. Two diagonally opposite electrodes are held at rf ground while a rf signal is applied to the other two blade electrodes. Due to the asymmetry of the trap drive, the rf field results in some trapping in the axial direction, sufficient to crystallise the ions without an additional dc voltage (see Section 4.5.2).

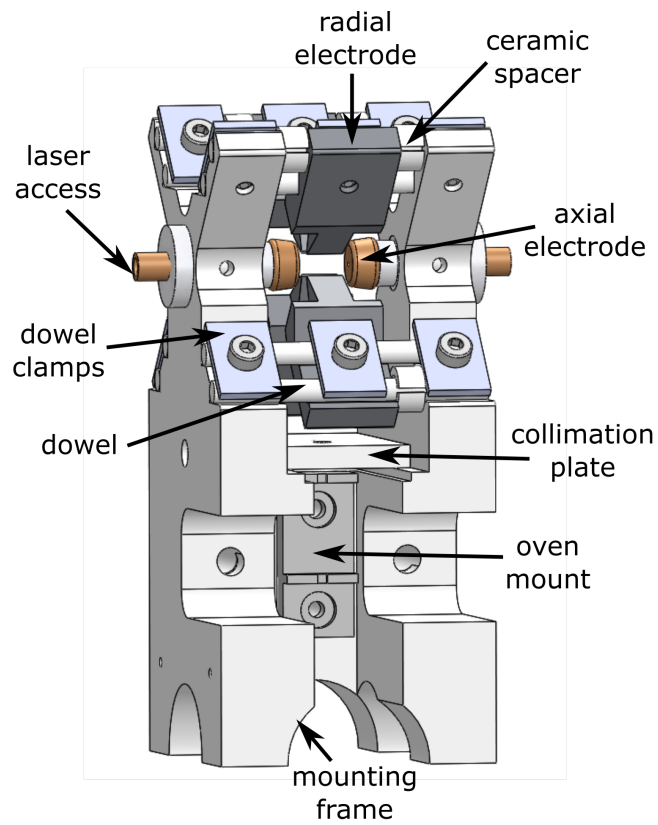
The trap is very similar to the trap shown in A. Gardner's thesis.<sup>3</sup> The key differences are that the radial electrode separation has been increased (from 460  $\mu\text{m}$  to 1.7 mm) and the electrodes are made from molybdenum rather than stainless steel (Figure 4.1). The separation was increased to reduce the scatter of the pulsed nitrogen ionisation lasers on the electrodes. The electrode material was changed to Mo as it does not have an oxide layer and so laser scatter is less likely to charge the electrode surfaces. It is also more resistant to laser ablation.

#### 4.1.2 Calcium Oven

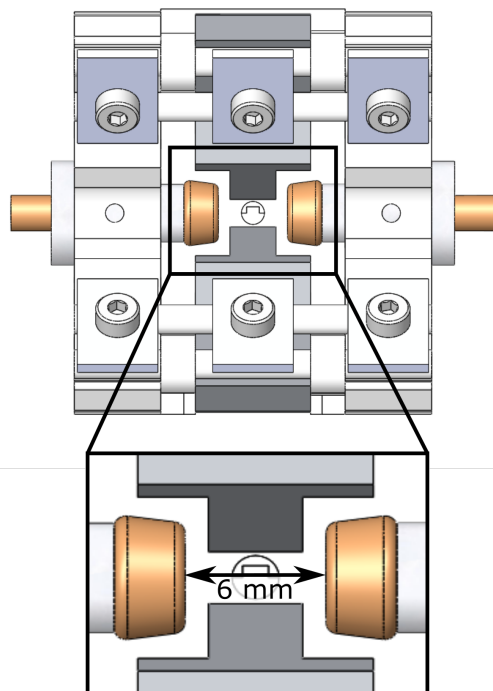
Calcium ions are loaded from an oven below the trap. The oven consists of a tantalum tube packed with powdered  $\text{Ca}^{\text{a}}$ . A current is passed through the wire wrapped around

---

<sup>a</sup>The oven design is described in detail in A. Gardner's thesis.<sup>3</sup>



TOP VIEW



CUT-THROUGH

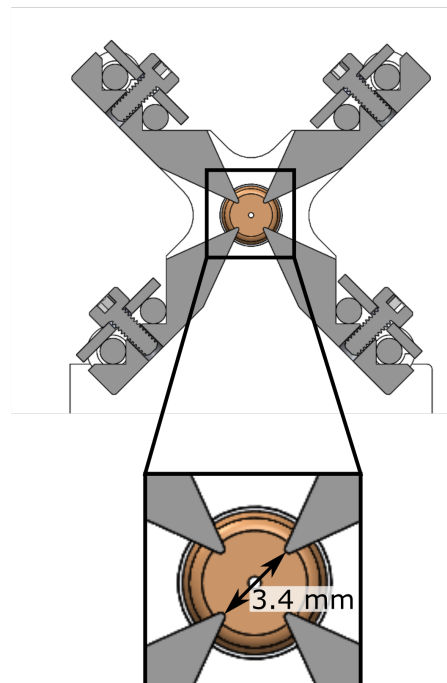


Figure 4.1: Schematic drawing of the ion trap and its housing. The inter-electrode distances are shown with a top view and a cut through the centre of the trap in the radial plane.

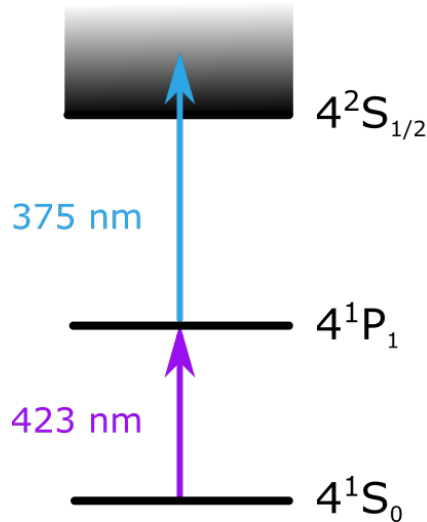


Figure 4.2: The ionisation scheme for loading  $^{40}\text{Ca}^+$  into the ion trap. The first photon at 423 nm excites the atom from the ground  $4s^2$  state into the first excited state  $4s^1 4p^1$ . From this intermediate state, the atom is ionised with a photon of 375 nm.

the tube to heat the Ca. Typical currents range from 1.3-2.5 A, corresponding to powers of 2-10 W. Calcium atoms evaporate from the oven to form a beam in the trapping region. Here, lasers at 423 nm and 375 nm resonantly excite and then ionise the atoms (Figure 4.2). As they are ionised within the trapping region, the Ca ions are then trapped. The first resonant step in the ionisation ensures that this is isotope-selective.

When trapping for the first time, the fluorescence of the neutral calcium atoms was observed by scanning the 423 nm laser over the  $4^1S_0 \rightarrow 4^1P_1$  transition. This was used as a means of aligning the ionisation lasers to the centre of the trap.

#### 4.1.3 Trap Electronics

The rf drive signal from a function generator passes through an amplifier before reaching the primary coil of a transformer (Figure 4.3). Impedance matching is achieved by moving the primary coil along the axis of the transformer to change the coupling constant (Figure 4.4(a)). The rf drive from the secondary coil of the transformer is connected to two diagonally opposite radial electrodes via a bias tee where it is combined with a dc signal. This dc signal is then used to compensate for stray electric fields and so minimise the excess micromotion (see Section 4.8). A small pick-up coil is placed close to the transformer to allow monitoring of the drive (Figure 4.4(b)). We refer to this as the monitor coil.

When the circuit was redesigned, the previous resistors were replaced by 2 M $\Omega$  resistors for the grounded electrodes and high power 3 M $\Omega$  resistors for the rf electrodes. This significantly increased the achievable drive powers and Q factor of the resonator. In addition, the wires connecting the resonator circuit to the feedthroughs were replaced with 3 mm-thick silver-plated copper wire to transmit higher powers (Figure 4.4(c),(d)).

To prevent overheating, the box containing the circuit was machined with a series of

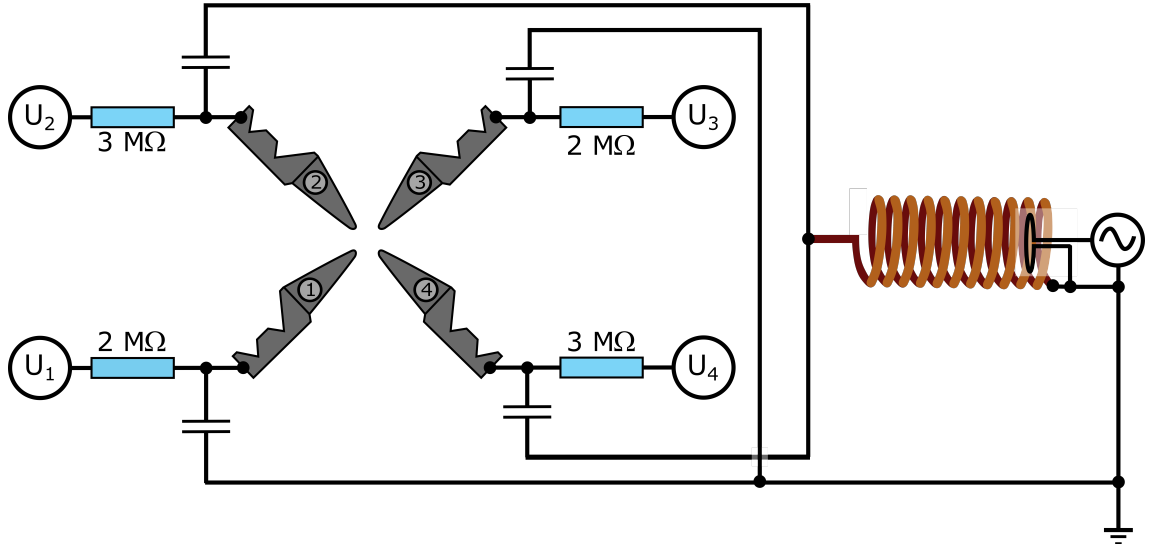


Figure 4.3: Schematic diagram of the rf resonator circuit. A sinusoidal electronic signal is applied to the primary coil of a transformer. The amplified signal from the secondary coil is connected to two diagonal radial electrodes at a bias tee. The other two electrodes are held at rf ground. An additional dc voltage is connected to each electrode in order to compensate for stray fields that cause excess micromotion.

circular holes covered with copper mesh and a fan was placed over a large rectangular opening to cool the circuit continuously. This allowed the circuit to operate without overheating for rf input powers up to 70 W (the limit to which it was tested).

The resonant frequency of the circuit was measured to be 22.088 MHz. The Q factor of the resonator was calculated according to

$$Q = \frac{f}{\Delta f}, \quad (4.1)$$

where  $f$  is the frequency of the resonance and  $\Delta f$  is the full-width half-maximum of the resonance. This was found to be 260 (Figure 4.5).

The circuit which supplies the axial electrode voltages is more straightforward. The dc voltage for the axial confinement is combined with an optional rf signal with a bias tee (Figure 4.6). This optional fast signal may be used to kick the ions (for example in crystal weighing) or to excite the ions using a rf signal close to the secular frequency of the crystal (as in cleaning the crystal and coarse measurements of the secular frequencies).

## 4.2 Imaging System

The imaging system sits outside vacuum above a recessed window at the top of the vacuum chamber. A lens, approximately 50 mm above the trap centre, collects light emitted by the ions. This light travels upwards and is reflected by 90° to travel horizontally. The mirror serves to increase the possible focussing length within the height constraints dictated by

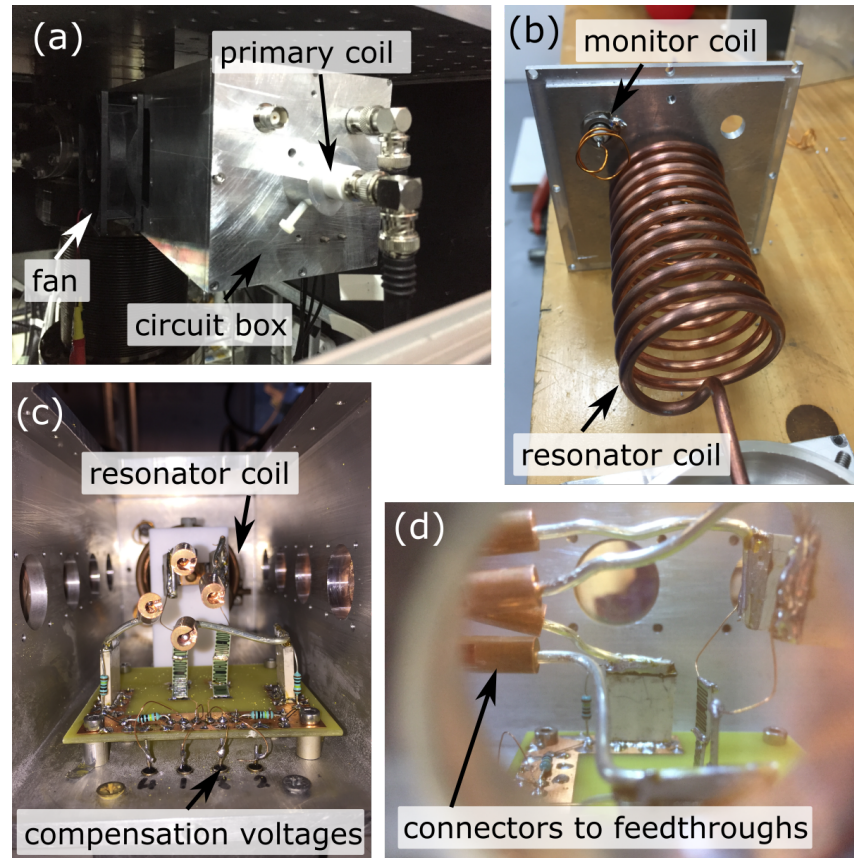


Figure 4.4: Images of rf circuit feedthrough box and circuit. (a) An external view of the box containing the rf circuit. (b) The endplate for the box showing the secondary/resonator coil and the nearby pick-up coil for monitoring of the rf drive. (c) An internal view of the box looking from the position of the rf feedthroughs. At the back of this image is the resonator coil which is mounted in a teflon holder. The signal from the resonator is split into two identical paths and each is combined with a dc micromotion compensation voltage. The paths for the grounded electrodes are very similar, but the fast input to the bias tee is held at ground. (d) A view of the circuit through one of the mesh covered holes used for ventilation of the circuit to prevent overheating.

the lab bench. The focal length of the lens is  $910 \pm 20$  mm (Figure 4.7). The solid angle of the light collection is approximately 0.259 sr. This corresponds, in the absence of further losses, to the capture of 2 % of the light.

The light passes through two filters: a bandpass filter centred at  $395 \text{ nm}^b$  and a short-pass filter with a cut off wavelength of  $450 \text{ nm}^c$ . The short-pass filter serves as an additional measure to prevent light from the oven or repumping lasers reaching the camera or photomultiplier tube (PMT)<sup>d</sup> (transmitted 90 %), and a charge-coupled device (CCD) camera<sup>e</sup> (reflected 10 %). An iris and a slit were placed before the PMT to cut out any light which had not been focused by the lens, such as scatter from the electrodes (Figure 4.8). The CCD camera is

<sup>b</sup>Semrock, BrightLine FF01-395/11

<sup>c</sup>Thorlabs, FESH0450

<sup>d</sup>Hamamatsu, H7360-02

<sup>e</sup>Andor, Luca

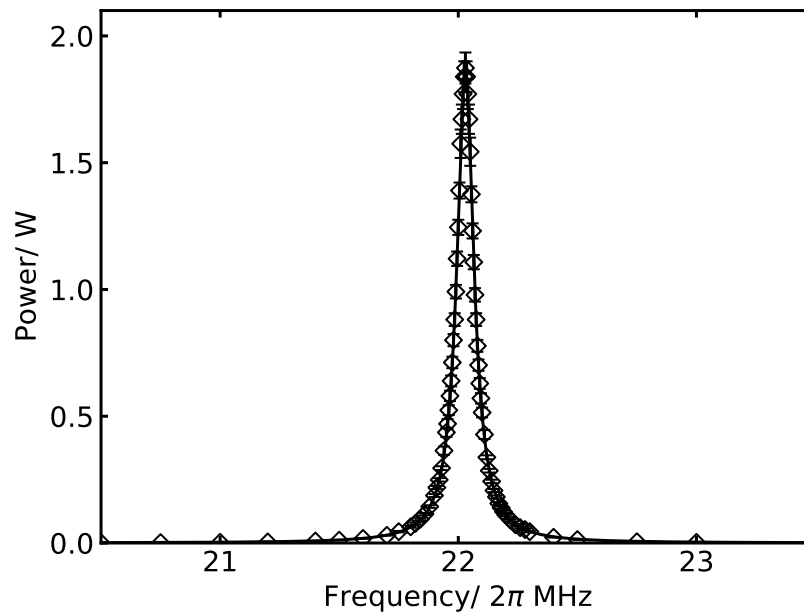


Figure 4.5: The resonance of the rf circuit. Power measured on the monitor coil as the drive frequency was scanned over the resonance. A Lorentzian fit was used to extract a  $Q$  factor of approximately 260.

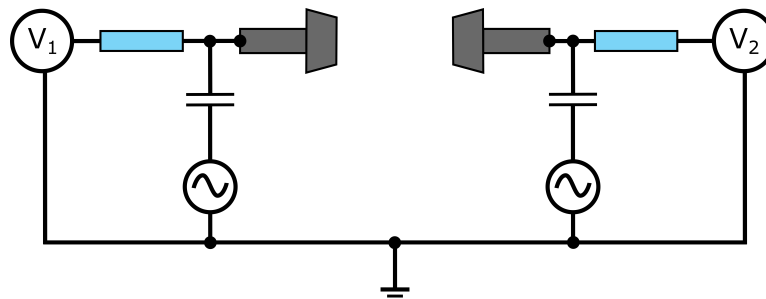


Figure 4.6: Circuit diagram for dc electronics. A dc trapping voltage is applied to each of the axial electrodes at a bias tee. The voltages  $V_1$  and  $V_2$  may be different to account for stray fields that cause excess micromotion along the axis of the trap. An additional fast signal can also be applied to the electrodes via the bias tee, usually to excite the motion of the trapped ions.

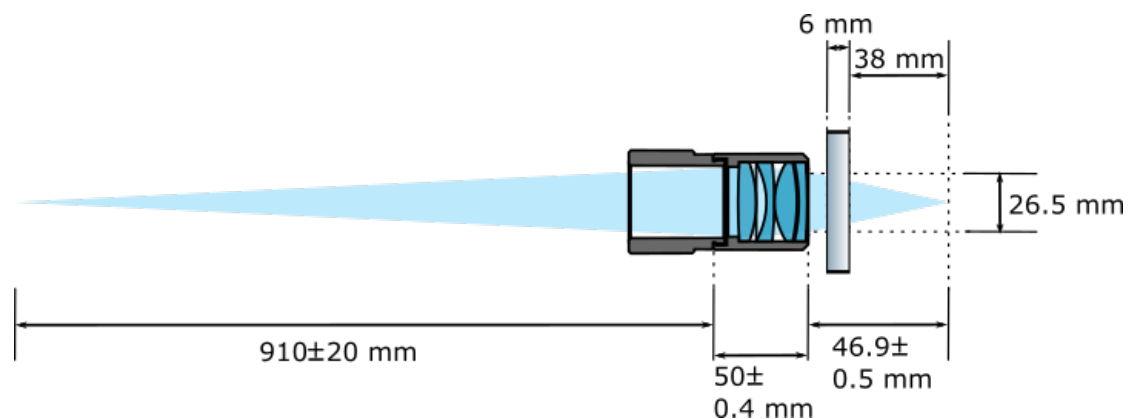


Figure 4.7: Details of the lens used for imaging the ions. The quoted magnification is 15x.

read-out using the Andor Solis software package and the PMT signal is directed to a data acquisition device (DAQ) counter channel, via a pulse-extender (which acts to ensure that the pulses are long enough to be counted by the DAQ).

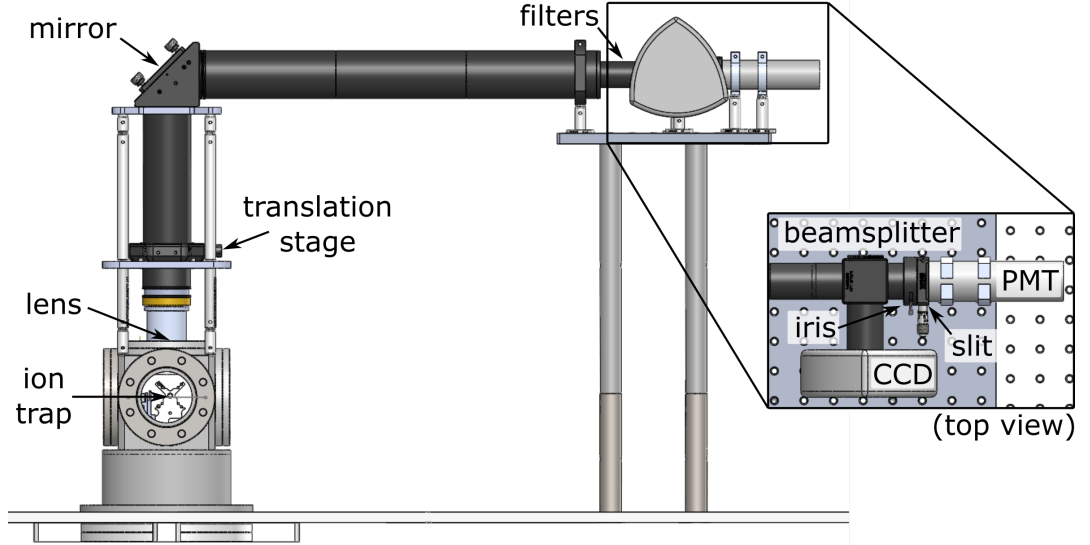


Figure 4.8: Schematic drawing of the new imaging system. Light emitted by the ions is focussed by the lens and reflected by the mirror. 2" lens tubing is used to exclude light from external sources without the loss of signal. There are two filters along the imaging path to select for fluorescence photons at 397 nm. The path is then split by a 90:10 beamsplitter between a CCD camera and a PMT. The PMT field of view is cropped by an iris and slit to maximise the signal-to-noise ratio. The molecular beam line is omitted from the schematic for clarity.

### Pixel Size Calibration

To calibrate the imaging system, the separation between two trapped ions in a linear crystal can be calculated from the secular frequency along the axis of the crystal, assuming a harmonic potential. The force due to the harmonic potential and the inter-ion repulsion can be balanced to find the equilibrium separation. This gives

$$m\omega_z^2 \frac{d_{\text{eq}}}{2} = \frac{Q^2}{4\pi\epsilon_0 d_{\text{eq}}^2}, \quad (4.2)$$

where  $m$  is the mass of the ion,  $\omega_z$  is the axial secular frequency,  $d_{\text{eq}}$  is the equilibrium displacement of the ion from the trap centre and  $Q$  is the charge of the ion. This can be rearranged to find

$$d_{\text{eq}} = \sqrt[3]{\frac{e^2}{2\pi\epsilon_0 m\omega_z^2}}. \quad (4.3)$$

For an axial secular frequency of  $2\pi \cdot 323$  kHz, this corresponds to an equilibrium inter-ion separation of  $12.5 \mu\text{m}$  for two  $^{40}\text{Ca}^+$  ions in a linear crystal. The equilibrium separation measured using the CCD camera for this confinement is  $18.5 \pm 0.5$  pixels, so the size of

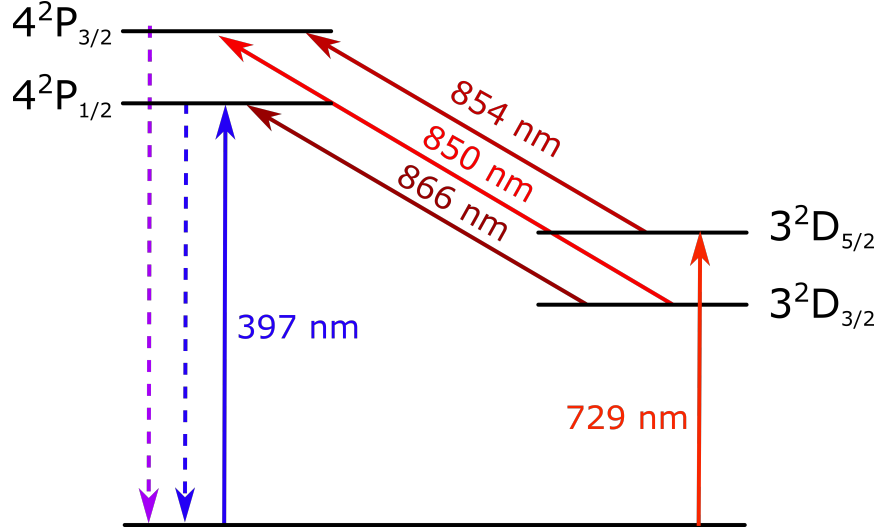


Figure 4.9: The energy levels of the  $\text{Ca}^+$  ion.

Table 4.1: The lasers used in the experiments described in this thesis, their roles, locking wavelengths ( $\lambda$ ) and linewidths.<sup>2</sup> Acousto-optic modulators (AOMs) are used to shift the frequency of the cooling, repumping and spectroscopy lasers by approximately 400 MHz from the wavelengths listed here.

Purpose	Transition	$\lambda$ / nm	Decay Rate/ $2\pi$
Ca ionisation	$4^1P_1 \leftarrow 4^1S_0$	422.79170	-
Ca ionisation	$4^2S_{1/2} \leftarrow 4^1P_1$	375 nm	-
Cooling	$4^2P_{1/2} \leftarrow 4^2S_{1/2}$	396.95919	20.67 MHz
Repumping	$4^2P_{3/2} \leftarrow 4^2D_{3/2}$	850.03542	180 kHz
Repumping	$4^2P_{3/2} \leftarrow 4^2D_{5/2}$	854.44400	1.58 MHz
Repumping	$4^2P_{1/2} \leftarrow 4^2D_{3/2}$	866.45195	1.69 MHz
Spectroscopy	$4^2D_{5/2} \leftarrow 4^2S_{1/2}$	729.147	0.1523 Hz

each pixel in the ion image is  $\sim 0.7 \times 0.7 \mu\text{m}$ . The size of the pixels on the CCD camera is  $10 \times 10 \mu\text{m}$  so this corresponds to a magnification of  $\sim 15\times$  which is the magnification quoted for the lens.

### 4.3 Level System of $\text{Ca}^+$

In order to Doppler cool the calcium ions, a laser at 397 nm excites the  $4^2S_{1/2} \rightarrow 4^2P_{1/2}$  transition. The probability of decay into the  $4^2D_{3/2}$  state necessitates the use of either one laser at 866 nm or two lasers at 850 nm and 854 nm to repump out of this state. The 854 nm laser is needed when repumping with the 850 nm because the  $4^2P_{3/2}$  state can decay to either of the two D states. A laser at 729 nm is used to probe the  $4^2S_{1/2} \rightarrow 4^2D_{5/2}$  quadrupole transition in calcium.

The calcium ionisation lasers, two radial 397 nm beams and the 866 nm laser enter the trap radially, whilst the remaining lasers travel along the trap axis (Figure 4.10). The ionisation lasers for nitrogen (at 255 nm and 212 nm) are discussed in more detail in

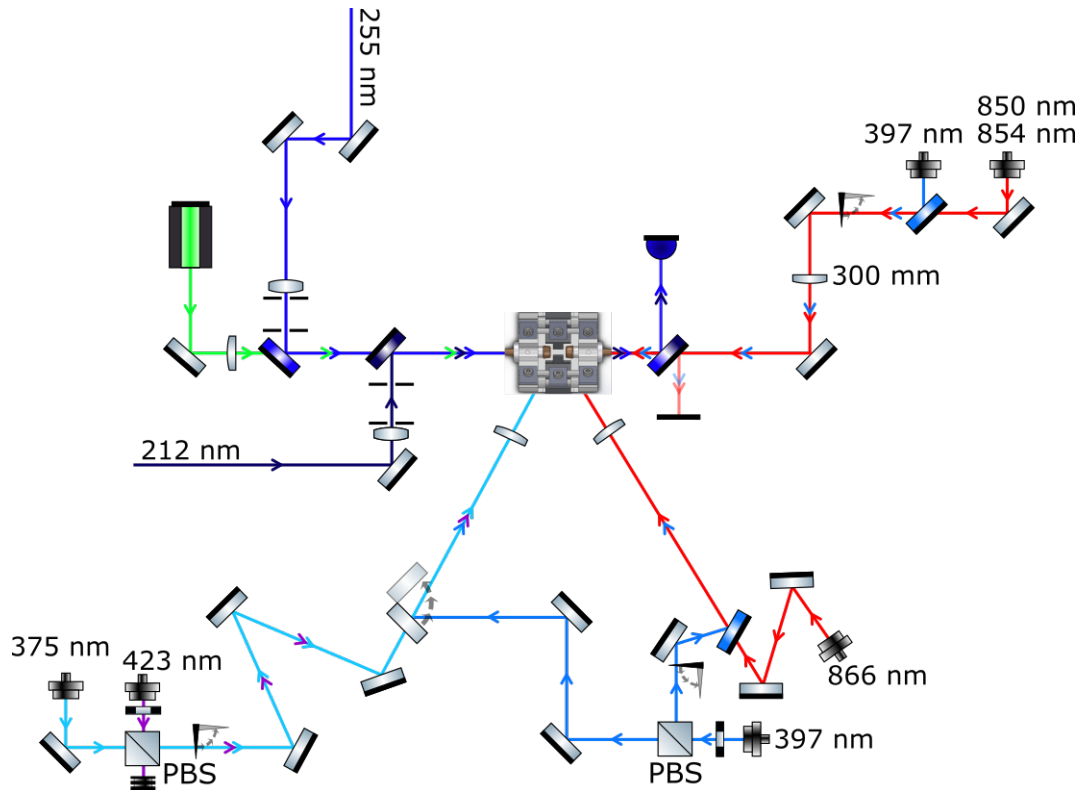


Figure 4.10: The arrangement of lasers around the ion trap. The coloured mirrors are dichroic and reflect the lasers the same colour as them, transmitting all others. Details of the transitions the lasers address can be found in Table 7.1.

Chapter 7.

#### 4.4 Doppler Cooling and Ion Fluorescence

The natural linewidth of the  $S_{1/2} \rightarrow P_{1/2}$  transition in  $^{40}\text{Ca}^+$  is 20.7 MHz.<sup>2</sup> However, in the real conditions of the trap, the transition may be broadened by a number of mechanisms including Doppler and saturation broadening. It is important to characterise the transition in order to understand the cooling process in our trap, the expected achievable cooling limit and to optimise photon-correlation data. The transition can be observed because the imaging system is set up to see photons fluoresced by the calcium ions as they relax back to the S state.

The linewidth of the broadened transition was measured by scanning the frequency of the 397 nm laser over the transition and recording the fluorescence counts on the PMT. Beyond the peak of the transition (where the laser was blue-detuned) the ions were heated and the fluorescence signal dropped to zero (Figure 4.11). As expected, it was observed that the saturation parameter increased linearly with the laser intensity (e.g. Figure 4.12). For the laser powers used in this experiment, the full-width half-maximum (FWHM) of the saturation-broadened peak was 33 MHz. This linewidth of 33 MHz corresponds to a saturation parameter of approximately 1.5.

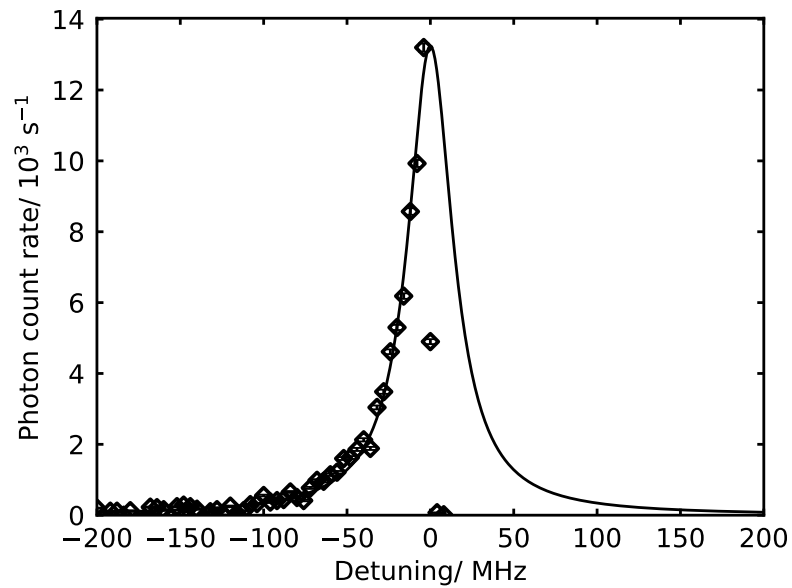


Figure 4.11: Example background-subtracted fluorescence data as the cooling laser frequency was scanned across the resonance and a fitted Lorentzian peak. On the blue side of the transition, the ion is heated and the fluorescence counts drop to zero.

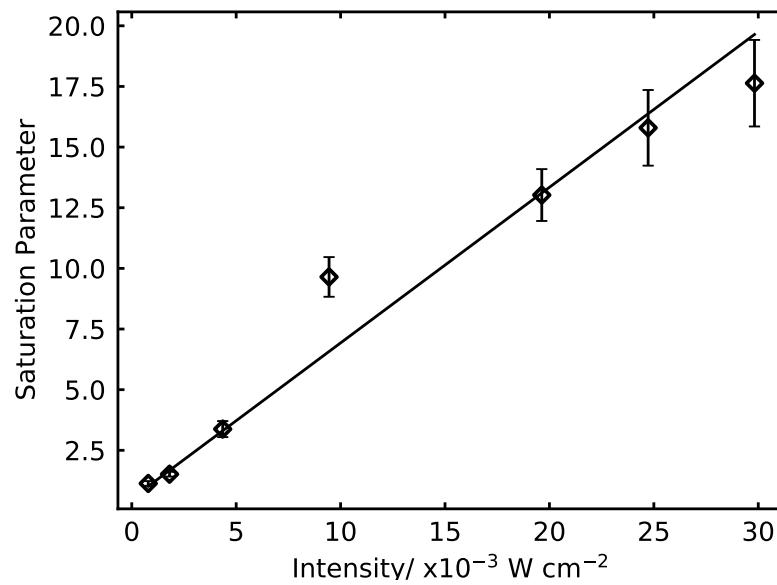


Figure 4.12: Saturation parameters for the cooling transition for different intensities of the incident 397 nm laser.

The natural linewidth of the transition is 20.67 MHz, which corresponds to a Doppler temperature of 0.48 mK. The minimum temperature that should be achievable with a linewidth of 33 MHz, which is the case in this experiment, is  $\sim 0.8$  mK.

## 4.5 Laser Stabilisation

With the exception of the 375 nm laser used in the last step of the photoionisation of Ca atoms, all of the diode lasers used for the Ca<sup>+</sup> formation and cooling need to be locked to the desired wavelength. This is because the lasers naturally drift in frequency if free-running. The laser frequency is stabilised by comparison to a reference frequency and feedback to the laser. The lasers can be locked by a number of methods. Here, we consider two: locking to the wavemeter and locking only the 397 nm to another stable laser via an offset lock (using the beat note).

### 4.5.1 Wavemeter Lock

The basic stabilisation of all of the lasers in use, apart from the 375 nm, was performed using a wavemeter<sup>f</sup> with a quoted stability of 60 MHz.

The lasers are each coupled into a multimode fibre connected to an optical switch<sup>g</sup>. The wavemeter reads the wavelength of each in turn. From the difference between the read wavelength and the set wavelength, a LabVIEW virtual instrument implements a feedback loop using proportional and integral gains. As the natural linewidth of the 397 nm transition is 20 MHz, variations on the order of 60 MHz are likely to result in significant fluctuations in fluorescence. This was observed when the lasers are locked to the wavemeter and is particularly problematic for the 397 nm laser. For this reason, an alternative locking method for the 397 nm laser has been implemented.

### 4.5.2 Offset Lock to Stabilised Laser

The frequency of the 794 nm laser, which is frequency-doubled to produce the 397 nm light used to cool the S<sub>1/2</sub> → P<sub>1/2</sub> transition, may be locked to that of a stable laser. This lock was used for the experiments described in Chapters 6 and 7.

The laser can be stabilised by taking a beat note between the two lasers and maintaining a constant offset between their frequencies, i.e. maintaining a constant beat note frequency (Figure 4.13). This stable laser was in turn locked to a transition in Cs via a scanning cavity lock.<sup>108</sup> The two lasers were overlapped at a 50/50 beam splitter and coupled into the same single-mode, polarisation-maintaining fibre. The output from this fibre was

---

<sup>f</sup>High Finesse, WS7

<sup>g</sup>High Finesse, MC8

focussed onto a fast photodiode<sup>h</sup>. The beat note signal from the photodiode was passed through a discriminator to convert the oscillations to 35 ns TTL pulses at the beat note frequency. These TTL pulses were read by a counter and used to determine the beat note frequency. A proportional-integral-differential (PID) feedback circuit was used to convert the count rate to a restoring output voltage. This feedback voltage was connected to the piezo control for the 794 nm diode laser grating. A constant offset of 10 MHz was maintained between the two lasers.

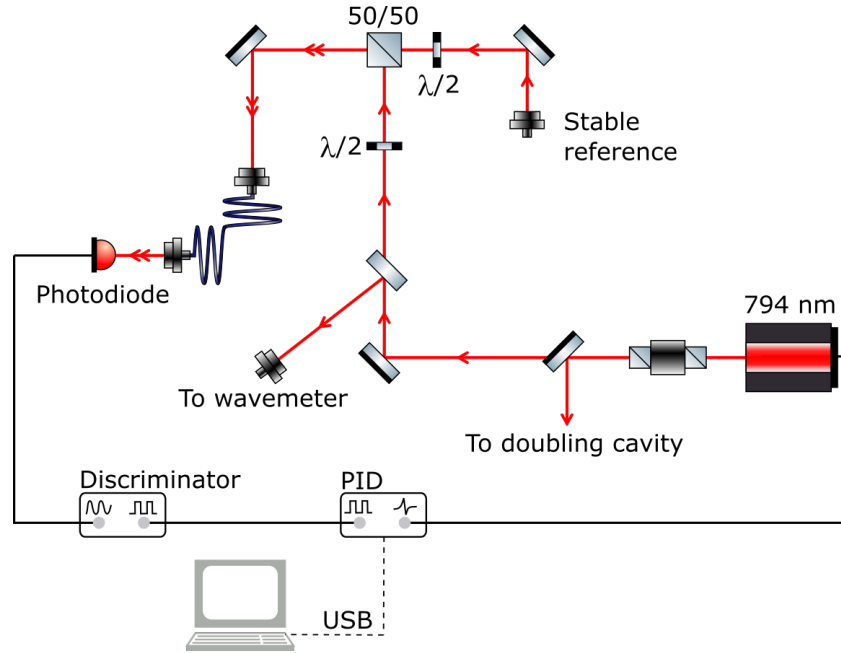


Figure 4.13: The set-up used for the offset locking method. The laser is overlapped with a stable reference laser and the two lasers are coupled into a single fibre. The beat note signal from a photodiode placed after the fibre is used to generate a locking signal which is fed back to the laser.

The standard deviation of the beat note during locking is on the order of 1 MHz, as can be seen from the example trace for which the standard deviation is  $0.665 \pm 0.003$  MHz (Figure 4.14). This should in theory result in very stable fluorescence. While a significant improvement was observed upon implementing this lock, there is still the potential for fluorescence fluctuations due to changes in the wavelengths of the repumping lasers.

## 4.6 Trap Characterisation

The linear Paul trap is characterised by its  $q$  and  $a$  parameters, which can be determined from measurements of the secular frequencies of ions crystallised in the trap (see Section 2.1). The axial and radial secular frequencies in the newly installed trap were measured for different confinements.

<sup>h</sup>Thorlabs, PDA10A

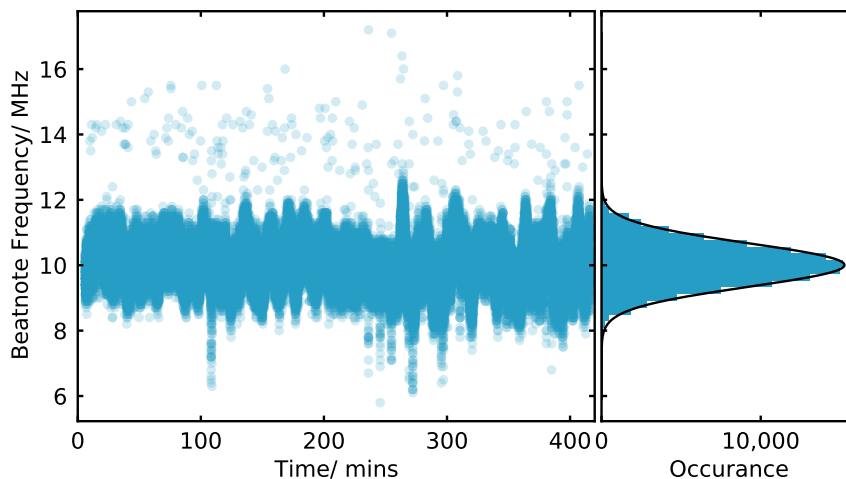


Figure 4.14: The beat note recorded over approximately seven hours while the offset lock was in use.

In order to measure the secular frequencies, a rf signal from a function generator<sup>i</sup> was applied to the high frequency input of the bias tee for the axial electrodes (Figure 4.6). When the frequency of this rf signal was resonant with one of the secular frequencies, the secular motion was excited. The consequent delocalisation of the ion crystal was observed on the CCD camera (Figure 4.8). A single secular frequency was measured for the radial motion because the resolution of the method was not sufficient to resolve the two frequencies.

The axial and radial secular frequencies increased linearly with the amplitude of the rf signal applied to the radial electrodes (Figure 4.15). The rate of increase in the axial secular frequency with the rf amplitude was approximately three times lower than for the radial motion.

The axial secular frequency is not zero when there is no voltage applied to the axial electrodes because the ions are also confined in the axial direction by the rf field of the radial electrodes. The axial secular frequency was proportional to the square root of the axial electrode voltage (Figure 4.16). Axial secular frequencies greater than 1 MHz have been achieved, which is promising for future spectroscopy.

## 4.7 Crystal Weighing

When a crystal contains more than one species of ion, it is usually the case that only one species can be imaged using fluorescence. In these cases, the composition of the ion crystal, and the identities of the dark ions, can be determined by measuring the COM (centre-of-mass) frequency of the crystal. This method was used to confirm the loading of

<sup>i</sup>SRS DS345

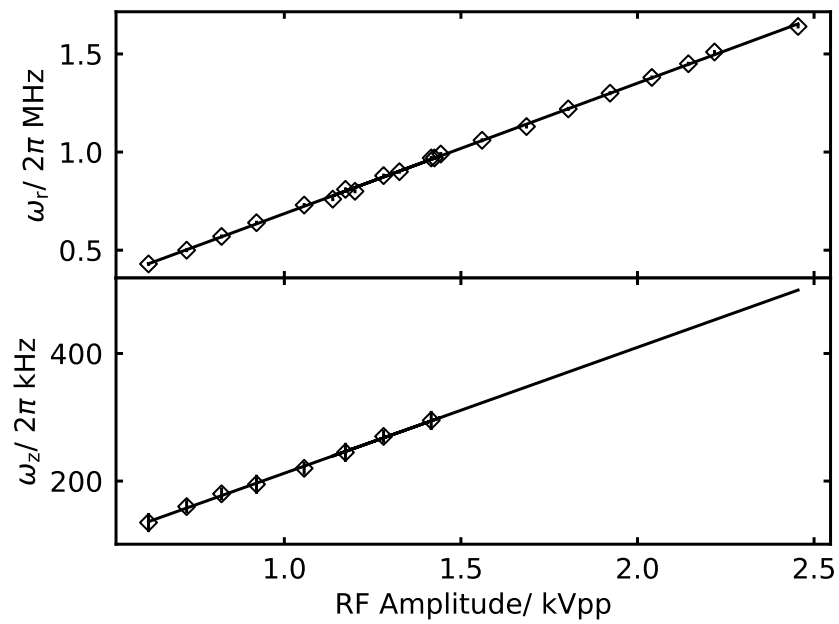


Figure 4.15: Secular frequencies in the linear Paul trap as the amplitude of the rf voltage on the radial electrodes was scanned. Above, the radial secular frequencies. Below, the axial secular frequencies with the axial electrodes held at ground.

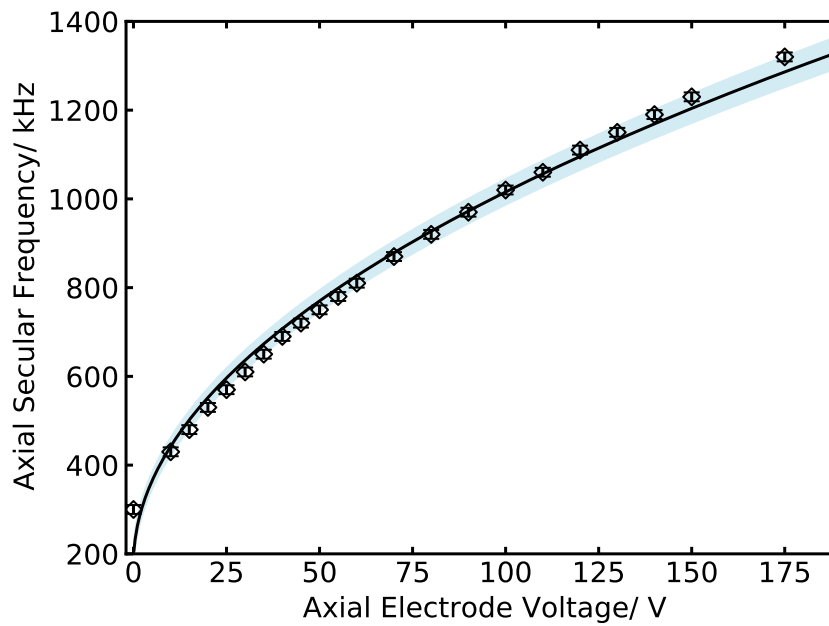


Figure 4.16: The axial secular frequencies for different voltages applied to the axial electrodes, fitted with a square-root function.

nitrogen ions into a calcium ion crystal, and is known as crystal weighing.

The COM frequency could be determined using the coarse method described in Section 4.5.2. However, it is possible to achieve much better resolution using a photon correlation method.<sup>109</sup> As the ion crystal oscillates in the trapping potential, the light absorbed by the fluorescing ions is Doppler-shifted. As a result, the laser frequency is modulated at the COM frequency in the frame of reference of the ions. As the laser is detuned to the half-maximum of the absorption line, this is mapped to a modulation in the fluorescence rate (Figure 4.17). This fluorescence modulation can be detected on the PMT (Figure 4.8).

In order to excite the secular motion, pulses of opposite polarity were applied to the high frequency input of the bias tees for the two axial electrodes. These pulses were repeated for the measurement time at a trigger rate that can be varied. This “kicking” of the ions resulted in excitation of their motion and amplified the modulation of the ion fluorescence. A time-to-digital converter (TDC) was used to correlate the arrival times of photons (measured with the PMT) to the TTL pulses applied to the trap electrodes (Figure 4.18). A fast Fourier transform (FFT) of this histogram was used to extract the COM frequency (Figure 4.19).

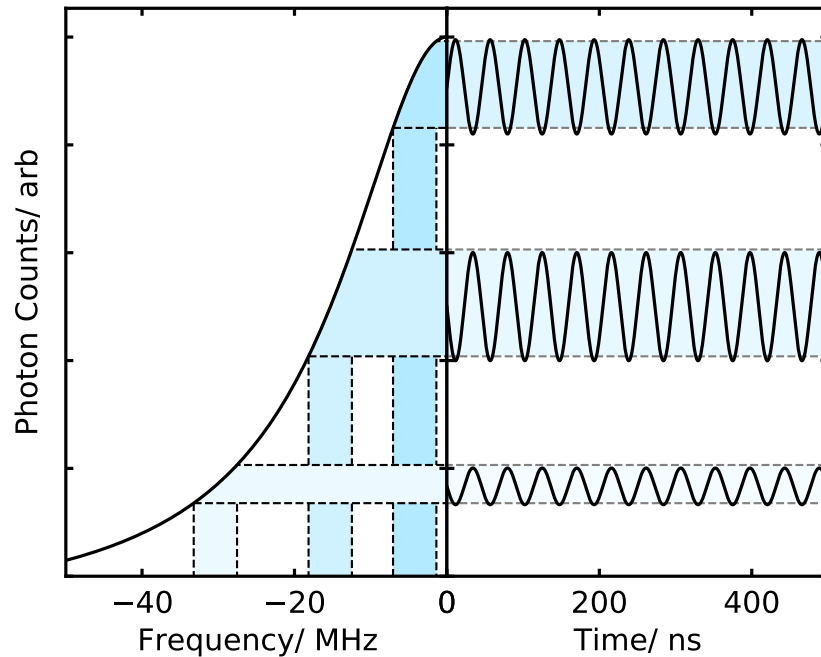


Figure 4.17: The changing gradient of the Lorentzian absorption line results in different amplitude of fluorescence modulation with the same frequency modulation. The fluorescence rate is most sensitive to changes in frequency where the gradient is maximised.

If there is a rf component to the trapping field in the axial direction, the axial secular motion in the ion trap is a result of a combination of the dc and rf trapping fields. The

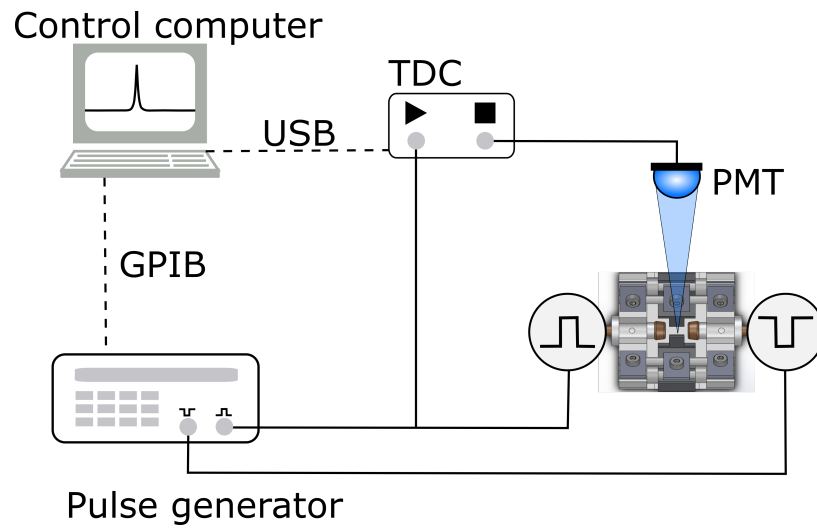


Figure 4.18: The set-up used for crystal weighing.

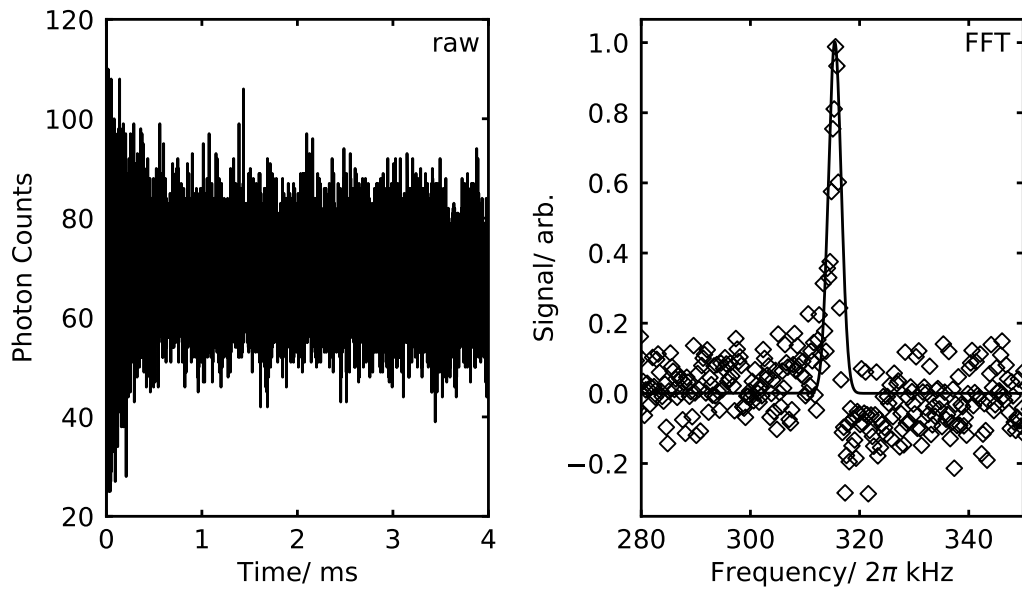


Figure 4.19: Example crystal weighing data. A Lorentzian fit to the FFT of the raw data is used to extract the secular frequency.

secular frequency is then

$$\omega_z = \sqrt{\left(\frac{\eta_{\text{rf,ax}}^2 V_{\text{rf}}^2}{8\Omega^2} \cdot \frac{\bar{Q}^2}{\bar{m}^2}\right) + \left(2\eta_{\text{dc,ax}} V_{\text{dc}} \cdot \frac{\bar{Q}}{\bar{m}}\right)}, \quad (4.4)$$

where  $\eta_{\text{rf,ax}}, \eta_{\text{dc,ax}}$  are the trap efficiencies in the axial direction for the rf and dc fields respectively, accounting for the trap geometry. It can be seen that the rf-driven component of the secular frequency will increase linearly with the average charge-to-mass ratio of the crystal while the dc component will increase proportional to the square root. The axial trap efficiency for the rf is low and so for high secular frequencies, the dc component is dominant and so  $\omega_z \propto \sqrt{\bar{Q}/\bar{m}}$ . In contrast, in the case of trapping with no dc voltage, all of the trapping in the axial direction is the result of the rf and so  $\omega_z \propto \bar{Q}/\bar{m}$ . These two regimes allow the average charge-to-mass ratio of the crystal to be determined.

In order to observe the crystal weighing signal, the ion crystal must have a strong COM mode and the excitation pulses must cause sufficient amplification of the ions' motion. In both respects, large mass-to-charge differences between ions in the crystal may make crystal weighing difficult. The measured excitation amplitude is proportional to  $\sin^2(\omega_{\text{COM}} \cdot \tau/2)$ , where  $\omega_{\text{COM}}$  is the COM frequency of the crystal and  $\tau$  is the length of the pulses applied to the electrodes.<sup>109</sup> As the COM frequency depends on the mass, the pulse duration may need to be chosen carefully to ensure a good signal if the component ions are sufficiently different in mass.

## 4.8 Micromotion Compensation

While there is a level of micromotion intrinsic to the use of radio frequency trapping fields, the presence of stray electric fields can cause additional micromotion. This is because they displace the ion crystal from the centre of the rf field inside the trap. The electric field amplitude in the centre should be zero, but increases rapidly as the ions move away from the centre. In these regions of higher field amplitude, the ion motion driven by the rf field directly is greater in amplitude too.

Micromotion can cause a number of problems experimentally. Firstly, in cases where more than one ion is trapped, interactions between the ions have a random phase relative to the motion driven at the trap electrode frequency. These interactions therefore result in heating, often referred to as rf heating. For frequency standards, the second order Doppler shift due to the excess motion and shifts due to stray fields can be significant and should be minimised for more precise measurements.<sup>80</sup> In the long term of this project, two ions will be colocated in the trap and used for precise measurement of the relative frequency of a transition. For this reason, it is very important to minimise excess micromotion. Because there is a reasonable degree of trapping rf in the axial direction as well as in the radial directions, it is necessary to minimise the excess micromotion along the trap axis

in addition to the two radial axes.

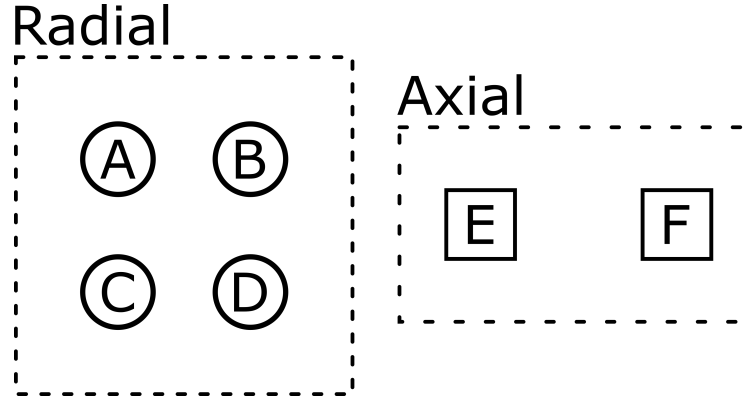


Figure 4.20: Labelling of electrodes for the purposes of micromotion compensation.

In order to compensate for the stray electric fields which displace the ions from the trap centre, dc voltages are applied to each of the six electrodes. For this, six values are used: the horizontal shift,  $H$ ; the vertical shift,  $V$ ; the electric quadrupole,  $Q$ ; the dc offset,  $S$ ; the axial trapping voltage,  $T$ ; and the axial shift,  $X$ . These values are converted to the voltages on electrodes A to F (Figure 4.20) according to

$$\begin{aligned}
 H &= (B + D) - (A + C); \\
 V &= (A + B) - (C + D); \\
 Q &= (A + D) - (B + C); \\
 S &= A + B + C + D; \\
 T &= \frac{1}{2}(E + F); \\
 X &= (E - F);
 \end{aligned} \tag{4.5}$$

where  $A$ - $F$  are the voltages applied to electrodes A-F respectively. The values listed above are those that are varied during the process of compensation to enable the compensation of stray electric fields. The voltages on the electrodes are then set to

$$\begin{aligned}
 A &= \frac{1}{4}(2S - H + V + Q); \\
 B &= \frac{1}{4}(2S + H + V - Q); \\
 C &= \frac{1}{4}(2S - H - V - Q); \\
 D &= \frac{1}{4}(2S + H - V + Q); \\
 E &= T + \frac{1}{2}X; \\
 F &= T - \frac{1}{2}X.
 \end{aligned} \tag{4.6}$$

These voltages (which include the axial trapping voltage) are supplied by a DAQ. There are two methods used for micromotion compensation: a coarse method and a more sensitive photon-correlation method. These methods are described in the following subsections.

#### 4.8.1 Coarse Micromotion Compensation

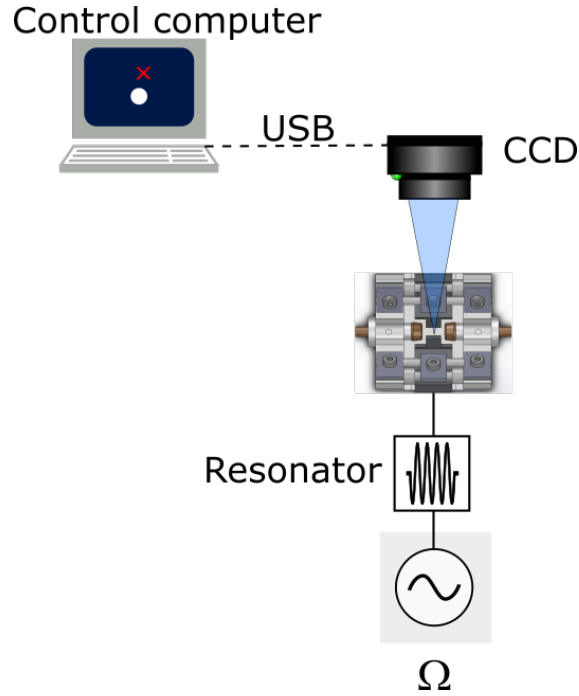


Figure 4.21: Experimental set-up used for coarse compensation of excess micromotion. The ions are imaged using a CCD camera as the amplitude of the rf trap drive is varied. The micromotion compensation voltages are iteratively changed until the ions are stationary on the CCD image as the amplitude is changed.

If there are stray dc electric fields in the trap, these will displace the ion crystal from the minimum of the rf field. This enables a simple meter of the degree of micromotion present in the trap. If the amplitude of the rf trapping voltage is raised and lowered, the ions will move in the trap unless the stray fields are compensated. Using the CCD camera image, this movement can be observed in its plane of view (Figure 4.21): the axial direction and one radial direction. Motion along the third axis for compensation, along the axis of the imaging lens, cannot be easily resolved from the CCD camera. For this reason, the signal on the PMT may be used as a rough guide.

In this method, the ion position at high rf confinement is marked on the CCD image and then the rf confinement is lowered. At low confinement, the compensation voltages  $H$  and  $X$  are adjusted to move the ions to the high-confinement position. The confinement is then raised again and the process is repeated iteratively until the ions no longer move when the rf amplitude is varied. For the vertical direction, the  $V$  compensation voltage is adjusted to reduce the heating of the ion and to reduce the variation in fluorescence counts as the rf amplitude is raised and lowered. The small depth of focus of the lens

ensures that there is a reasonable level of sensitivity.

#### 4.8.2 Photon Correlation Method

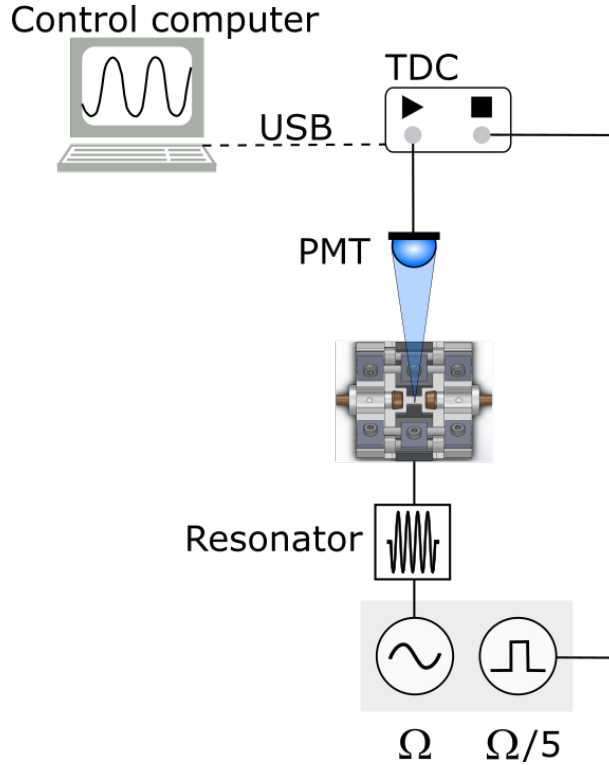


Figure 4.22: The set-up used for the photon correlation micromotion compensation. A time-to-digital converter (TDC) correlates the arrival times of fluoresced photons to a rf signal synchronised to the rf trap drive. Due to the Doppler effect, the ion motion at the trap drive frequency is mapped to fluorescence modulation. The compensation values are varied systematically to minimise the amplitude of the observed oscillations.

The coarse method is not sensitive enough to eliminate all excess micromotion. A more sensitive method for detecting micromotion is to observe the fluorescence from the ion. The periodic motion of the ion results in a varying Doppler shift of the absorbed photons. This is observed as a sinusoidal modulation of the ion's fluorescence (Figure 4.17). The amplitude of the oscillations in the fluorescence are proportional to the amplitude of the ion motion. Greater micromotion will result in a greater amplitude in the fluorescence modulation.

In the photon-correlation method, three lasers are used with different angles between them. Three lasers are needed because fluorescence modulation is only driven by motion in the axis of the incident laser; motion in the plane perpendicular to the laser beam is invisible. The ions are illuminated by one laser at a time. The function generator which drives the trap outputs a second square wave signal with a frequency one fifth of the trap drive frequency. For each laser, the fluorescence counts from the ion are binned by the delay between the photon arrival time and the subsequent square pulse signal from the function generator (Figure 4.22).

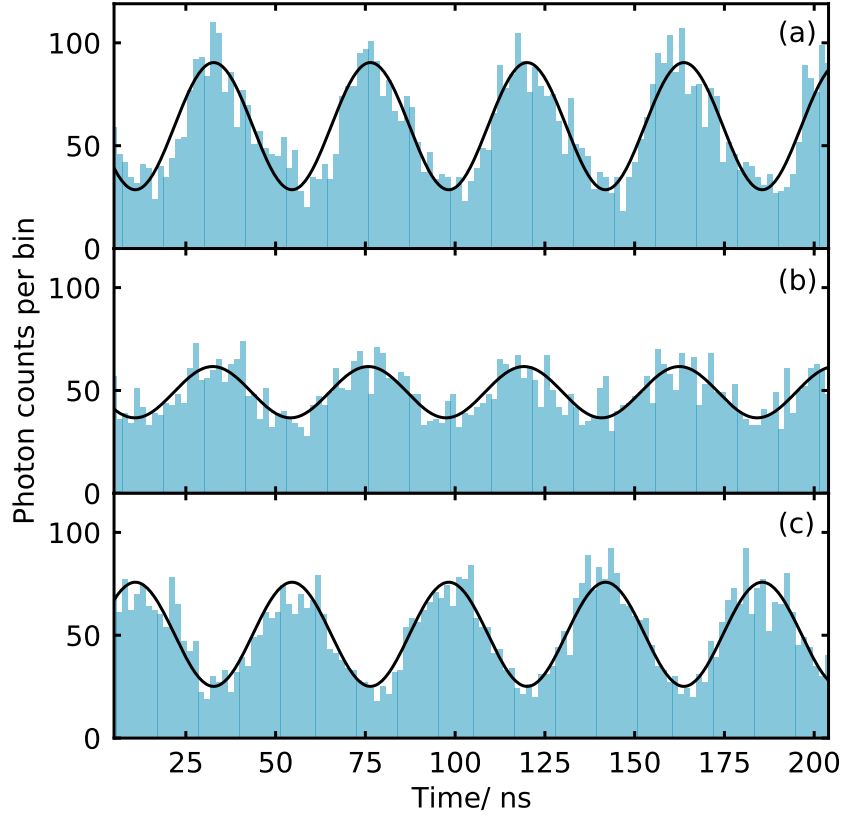


Figure 4.23: Histograms of ion fluorescence photon counts, correlated to a signal at one fifth of the trap drive, triggered at the same phase each time, measured using a fast time-to-digital converter (TDC). Subplots (a), (b) and (c) show the photon correlation histograms (blue bars) for different applied “compensation” voltages respectively. Fitted to each is a sine wave (black line). The data in (a) and (b) were recorded with the ions displaced from the centre of the trap in the same direction. The data in (c) were recorded with the ions displaced from the trap centre in the opposite direction. The measurement time was 0.3 s, the histogram length was 250 ns and the resolution was 0.55 ns.  $T$  was 8 V for the axial confinement.

Micromotion occurs at the trap drive frequency and so excess micromotion manifests as a modulation of the ion fluorescence at this same frequency (see Section 4.4). The fluorescence is modulated by a sine wave (Figure 4.23). The phase of the rf trapping field is different either side of the trap centre. If static electric fields displace the ions to one side of the trap, there will be excess micromotion. If the ions are displaced less, the amplitude of the micromotion will be reduced (compare Figure 4.23(a) and (b)). If the ions are displaced in the opposite direction from the trap centre, the phase of the micromotion will change by  $\pi$  (compare Figure 4.23(a) to (c)).

The amplitude,  $A_{\text{MM}}$ , of the micromotion is defined as

$$A_{\text{MM}} = \frac{A_{\text{fluor}}}{\bar{n}}, \quad (4.7)$$

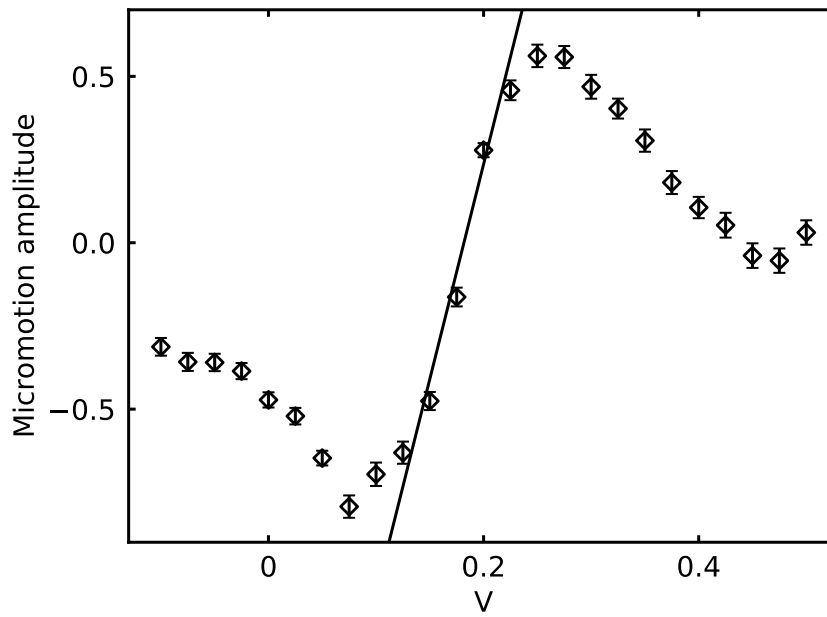


Figure 4.24: The micromotion amplitude as the vertical micromotion compensation voltage is scanned and a fit to the linear portion of the graph.

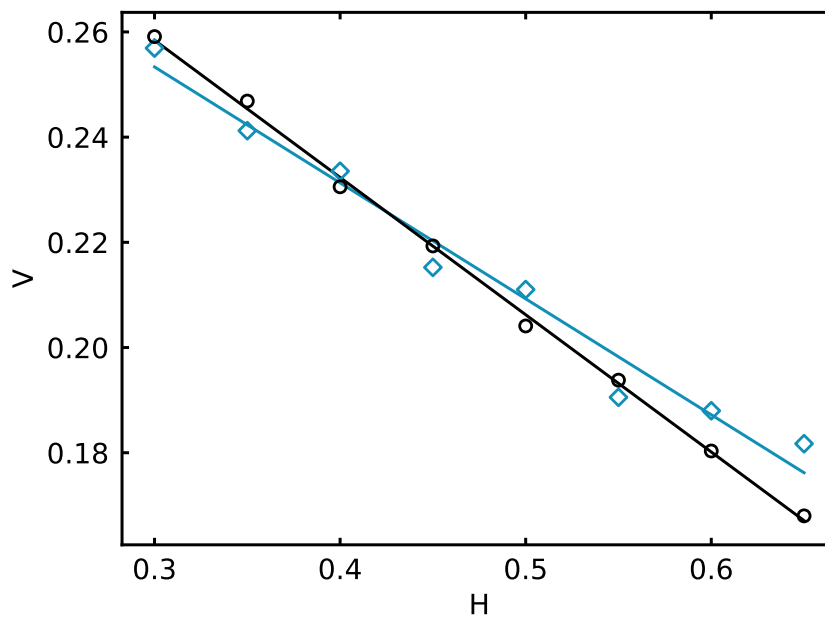


Figure 4.25:  $(H, V)$  coordinates corresponding to minima in the micromotion amplitude for each of the two radial lasers. Straight lines are fitted to each set of data.

where  $A_{\text{fluor}}$  is the amplitude of the fluorescence modulation and  $\bar{n}$  is the mean number of photon counts. The amplitude and offset for determining the micromotion amplitude are extracted from a fit of a sine wave of the form  $A_{\text{fluor}} \sin(f \cdot t + \phi) + \bar{n}$ , where  $f$  is the modulation frequency and  $\phi$  is the phase (Figure 4.23). If the phase  $\phi$  is constrained, the phase change can be transferred to a change in the sign of the amplitude. In this case, the relevant compensation voltage can be scanned and the micromotion amplitude can be recorded. The zero-crossing of the micromotion amplitude extracted from this contrived fitting yields the best compensation voltage. A linear fit to the points close to the zero crossing was used to improve the reliability of the extracted voltage (Figure 4.24).

For compensation in the axial direction, the axial laser is used. A single voltage,  $X$ , is scanned during micromotion compensation. For the radial directions, the micromotion is coupled between the two directions. For this reason, the process is slightly more complicated. The two lasers in the radial directions are used in turn. For each  $H$  compensation value, a range of  $V$  values are scanned and the  $V$  value corresponding to the minimum micromotion amplitude is chosen. These  $(H, V)$  coordinates are then plotted and should lie on a straight line. The lines obtained for the two different lasers should intersect somewhere (Figure 4.25). This intersection point dictates the  $H$  and  $V$  values to be used for compensation.

## Chapter 5

# Photoionisation of Molecules in rf Ion Traps

### 5.1 Introduction

One method for loading positively charged molecular ions into ion traps is to use a photoionisation process to remove an electron from a neutral molecule within the trapping region. In many cases it is possible, in the absence of external electromagnetic fields, to ionise deterministically into one specific internal state of the molecular ion. This is usually achieved using a resonance-enhanced multi-photon ionisation (REMPI) process.<sup>76</sup>

However, while the internal state of the molecular ion can be well controlled in low and uniform electric fields, the strong radiofrequency electric fields within typical Paul traps pose a threat to the achievable state-selectivity when loading into ion traps in this way. The extent to which the loading fidelity is compromised depends on many factors relating to the chosen REMPI process and trap parameters. This chapter focuses on one mechanism by which the ionisation thresholds are broadened under different conditions and assesses their impact on state-selectivity. Strategies for mitigating the broadening are also discussed. The data and simulation code are available (Appendix A).

### 5.2 The Electric Trapping Field

In a typical linear Paul trap, a rf electric field is used to confine the ions radially and a dc electric field confines the ions along the trap axis. The electric field generated by the trapping electrodes can be expressed in terms of the radial rf voltage,  $V_{\text{rad}}^{\text{rf}}$ , and the axial dc voltage,  $V_{\text{ax}}^{\text{dc}}$ . In Cartesian coordinates, where  $x$  and  $y$  form the radial plane and  $z$  is collinear with the trap axis (see Figure 5.1), the magnitude of the total electric field,  $\mathcal{E}$ ,

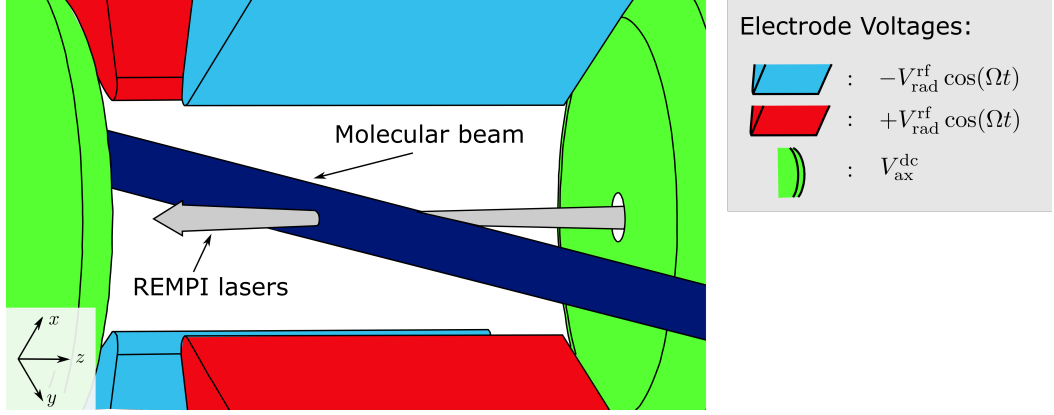


Figure 5.1: Schematic diagram of the rf ion trap considered in the simulations. The ionisation lasers travel down the axis of the trap perpendicular to the molecular beam. The voltages applied to the electrodes are labelled, consistent with Equation 5.1.

is<sup>77</sup>

$$\begin{aligned} \mathcal{E}(x, y, z, t) = \frac{1}{r_0^2} & \left[ \left( -V_{\text{rad}}^{\text{rf}} \cdot \cos(\Omega t) - \eta V_{\text{ax}}^{\text{dc}} \right)^2 x^2 \right. \\ & \left. + \left( V_{\text{rad}}^{\text{rf}} \cdot \cos(\Omega t) - \eta V_{\text{ax}}^{\text{dc}} \right)^2 y^2 + 4 \left( \eta V_{\text{ax}}^{\text{dc}} \right)^2 z^2 \right]^{\frac{1}{2}}, \end{aligned} \quad (5.1)$$

where  $t$  is the time and  $\Omega$  is the trap drive frequency.  $\eta$  is the axial trap efficiency, which accounts for the axial electrode separation and geometry, and  $2r_0$  is the effective distance between the radial electrodes, which also takes the deviation from the ideal electrode geometry into account. The origin of the coordinate system is at the centre of the trap.

### 5.3 Rydberg Molecules in Electric Fields

We are interested in the case where a molecule is excited to a Rydberg state close to the ionisation threshold. In the presence of an external electric field, the potential well for a Rydberg electron is distorted. We can treat the molecular ion core-Rydberg electron system like two interacting charges due to the large radius of a Rydberg electron orbital. The Coulomb potential,  $U_{\text{Coulomb}}$ , is

$$U_{\text{Coulomb}} = -\frac{Ze}{4\pi\epsilon_0|r|}, \quad (5.2)$$

where  $\epsilon_0$  is the vacuum permittivity,  $Z$  is the charge of the molecular core,  $r$  is the core-electron distance and  $e$  is the charge of the Rydberg electron. In the presence of a static electric field, this is distorted and the resulting potential,  $U_{\text{total}}$ , is

$$U_{\text{total}} = -\frac{Ze}{4\pi\epsilon_0|r|} - \mathcal{E} \cdot z, \quad (5.3)$$

where  $\mathcal{E}$  is the electric field strength along the field direction,  $z$ .<sup>110</sup>

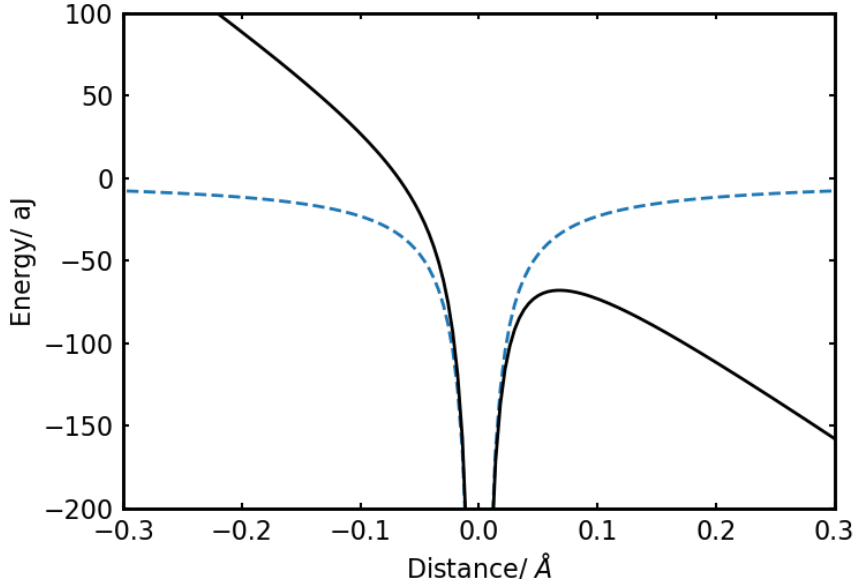


Figure 5.2: Energy of Rydberg electron with distance from molecular core with (solid, black line) and without (dashed blue line) an external electric field.

The potential increases compared to the zero-field case in one direction and decreases in the other, exhibiting a saddle point (Figure 5.2). Molecules in states above this saddle point are ionised. This radiationless ionisation process is referred to as field ionisation (or forced autoionisation).<sup>111</sup> In the case of photoionisation in an external electric field, ionisation can occur below the zero-field ionisation threshold.

The ionisation threshold in the electric field is found by solving the Schrodinger equation for this distorted Hamiltonian. To a first order approximation, the ionisation threshold is red-shifted by

$$\Delta = \alpha \cdot \sqrt{\mathcal{E}}, \quad (5.4)$$

where  $\Delta$  is the wavenumber shift of the ionisation threshold from the zero-field ionisation energy and  $\alpha$  is a constant of proportionality that depends on the diabaticity of the ionisation process.<sup>111</sup> The diabaticity of ionisation from a specific state is quantified by the Landau-Zener formula, which gives the probability of diabatic ionisation from that state in a given field. This probability,  $P_{\text{diabatic}}$ , is

$$P_{\text{diabatic}} = \exp \left[ \frac{-2\pi V_{12}}{(dE/dt)} \right], \quad (5.5)$$

where  $V_{12}$  is the interaction term for the splitting and  $dE/dt = (dE/d\mathcal{E}) \cdot (d\mathcal{E}/dt)$ , where  $E$  is the energy of the ionisation threshold. The former derivative is the difference in the gradients of the two energy curves at the crossing and the latter is the slew rate of the electric field applied.<sup>111,112</sup>

The first implication of this is that, in the case of a dc ionising field, field ionisation will be adiabatic. In this case, and always for adiabatic ionisation, the proportionality factor is

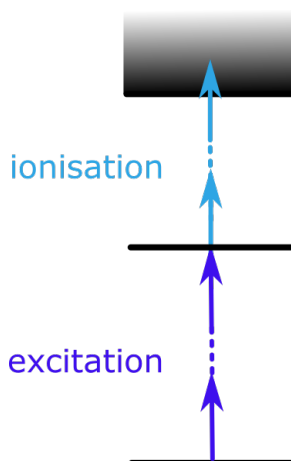


Figure 5.3: The general case of ionisation by a REMPI process. Initially, the atom or molecule is excited to an intermediate state by one or more photons. Then, from this state, it is ionised by absorbing one or more additional photons. The photons for the excitation and ionisation steps may be of different colours.

6.12  $\frac{1}{\text{cm}} \cdot \sqrt{\frac{\text{V}}{\text{cm}}}$ . The probability of diabatic ionisation then increases with increasing slew rate of the electric field and depends on the available states. In the limit where all field ionisation is diabatic, the value of  $\alpha$  is  $4 \frac{1}{\text{cm}} \cdot \sqrt{\frac{\text{V}}{\text{cm}}}$ . This occurs during pulsed spectroscopy with large slew rates.<sup>111</sup> In rf ion traps, the slew rate of the field is fast, but the oscillatory nature of the electric fields in this case is likely to result in mixing of the states over many cycles, resulting in adiabatic ionisation.<sup>76</sup>

If the electric field becomes sufficiently large, higher order effects on the ionisation threshold must be considered.

## 5.4 Ionisation Spectra in Electric Fields

A REMPI process ionises a molecule via the absorption of multiple photons (Figure 5.3). In order to enhance the probability of ionisation, the process occurs via a resonant excitation. In the first (excitation) step, the neutral molecule absorbs one or more photons which are tuned to be resonant with a transition to an intermediate state. From the intermediate state, the excited molecule can absorb additional photons which ionise it. The photon energies for the excitation and ionisation steps of the process do not need to be the same.

This study focuses on a two-colour REMPI process, where the photon energy for the first step differs from the photon energy for the second step. Here, we focus on the effect of electric field inhomogeneities on the ionisation step and therefore disregard the details of the REMPI scheme.

In the absence of an external electric field, the ionisation process can be resonantly enhanced by exciting the molecule into an autoionising Rydberg state near the ionisation threshold. This leads to clear resonances at which the molecule is predominantly ionised

into a specific internal state. These resonances can be spectroscopically well-separated.<sup>113</sup> In this case, molecular ions can be generated in almost any internal state as long as the spectral overlap between the ionisation resonances is small.

In the presence of a homogeneous external electric field, the differential Stark shift of the underlying Rydberg states broadens the ionisation resonances in addition to lowering the ionisation threshold as described in the previous section. This leads to a change from distinct resonances to a continuous ionisation spectrum with threshold behaviour (e.g. Figure 2 from Gardner *et al.*<sup>73</sup>). If the laser for the ionisation step is tuned to or slightly above the ionisation threshold for the desired state, ionic states above this energy are energetically forbidden. Molecular ions will only be generated in states below this threshold. As this is a threshold ionisation process, state-selectivity can only be achieved for the lowest-lying ionic states.

Exciting a specific intermediate state can facilitate preferential ionisation into specific states within the molecular ion. However, in the absence of strict rotational selection rules for the ionisation step of the process, this measure alone is usually not sufficient to achieve high state-selectivity. Certain levels in the ionised molecule can be precluded by careful choice of the initial and intermediate states. For example, the number of accessible states in the ion can be restricted by the symmetry of the wavefunction of the initial state of the neutral molecule. Ionisation of homonuclear molecules between  $\Sigma_g^+$  electronic states in the neutral molecule and ion results in an even-odd staggering of the rotational states due to constraints imposed by the symmetry of the nuclear wavefunction.<sup>73</sup>

The threshold must be well defined to enable state-selective ionisation, requiring a low electric field inhomogeneity and that other broadening mechanisms and the laser line widths are small compared to the rotational constant. Otherwise, molecules at different positions will have different thresholds, producing molecular ions in various internal states. While the conditions on the broadening mechanisms and laser line widths are usually fulfilled for experiments with nanosecond laser pulses, the electric field inhomogeneity is challenging in rf ion traps. Although highly homogeneous electric fields are possible in spectroscopic set-ups, the principle of rf ion traps is fundamentally based on the inhomogeneity of the trapping field. This can severely compromise the state-selectivity of the ionisation process.

## 5.5 Simulation Methods

In order to simulate the effect of the electric field on the ionisation threshold, we must consider the spatial and temporal overlap of the molecules, ionisation lasers and trap field. These overlaps mean that the ionisation threshold will be different for molecules ionised at different times and in different positions. This results in a distribution of ionisation thresholds, each corresponding to ionisation at a different electric field strength.

In these simulations, we find the laser intensity distributions, molecular distributions and trap geometry to find the distributed probability of ionisation at different positions in the

trap. We then integrate this distribution with respect to the electric field to extract the distribution of ionisation thresholds across the ion trap. These methods are described in detail in the following subsections.

### 5.5.1 Simulation Scenarios

The following simulations explore the effects of the electric trapping potential and ionisation laser timings on the broadening of the ionisation threshold for a  $N + M'$  REMPI process. In the low intensity approximation,<sup>114</sup>

$$P_{\text{ion}}^{\text{thr}} = \chi \rho_{\text{mol}} I_{\text{N}}^N I_{\text{M}}^M, \quad (5.6)$$

where the ionisation probability,  $P_{\text{ion}}^{\text{thr}}$ , is proportional to the molecular density  $\rho_{\text{mol}}$  and the intensities  $I_{\text{N/M}}$  of the two lasers to the power of the numbers of photons,  $N$  and  $M$ , absorbed in the excitation and ionisation steps respectively.  $\chi$  contains all other details of the ionisation process such as the laser detunings, transition moments and laser polarisations. Because we focus on the structure of the ionisation probability rather than its magnitude, we disregard proportionality constants. We do not consider any other broadening mechanisms. We have considered two scenarios:

- 1.) The neutral molecules are supplied via a molecular beam, perpendicular to the ionisation lasers.
- 2.) The neutral molecules are ionised from a homogeneous background gas.

In both cases, the REMPI lasers are collinear with each other and the trap axis (Figure 5.1). We have assumed that the lasers are Gaussian beams with width  $w_{\text{N/M}}$  and a Gaussian temporal shape with a pulse width of  $\tau_{\text{N/M}}$ , such that

$$I_{\text{N/M}} \propto \frac{1}{1 + \left(\frac{2z}{z_{\text{RN/M}}}\right)^2} \cdot \exp\left(-\frac{x^2 + y^2}{w_{\text{N/M}}^2}\right) \cdot \exp\left(-\frac{t^2}{\tau_{\text{N/M}}^2}\right). \quad (5.7)$$

In scenario 1.) we use a molecular beam with Gaussian cross section  $\rho_{\text{mol}} \propto \exp(-z^2/w_{\text{beam}}^2)$  of width  $w_{\text{beam}}$ . Assuming that  $w_{\text{N/M}} \ll w_{\text{beam}}$  and  $z_{\text{RN/M}} \gg w_{\text{beam}}$ , Equation 5.6 can be approximated by

$$P_{\text{ion}}^{\text{thr}}(x, y, z, t) \propto \exp\left[ -\left((x - x_{\text{offset}})^2 + (y - y_{\text{offset}})^2\right) \left(\frac{N}{w_{\text{N}}^2} + \frac{M}{w_{\text{M}}^2}\right) - \frac{(z - z_{\text{offset}})^2}{w_{\text{beam}}^2} - (t - t_{\text{offset}})^2 \left(\frac{N}{\tau_{\text{N}}^2} + \frac{M}{\tau_{\text{M}}^2}\right) \right]. \quad (5.8)$$

The REMPI lasers can be displaced from the centre of the trap in the  $x$  and  $y$  directions by distances  $x_{\text{offset}}$  and  $y_{\text{offset}}$  respectively and the molecular beam can be displaced in the  $z$  direction by  $z_{\text{offset}}$ . It is assumed that these displacements are significantly smaller than the dimensions of the trap. The relative timing of the laser pulses to the phase of the rf field can also be varied by changing the delay time,  $t_{\text{offset}}$ , between the peak of a rf

oscillation and the arrival time of the REMPI lasers. In scenario 2.), the molecular density is constant and Equation 5.6 becomes

$$P_{\text{ion}}^{\text{thr}}(x, y, z, t) \propto \left( \frac{1}{1 + \left( \frac{2(z - z_{\text{offset}})}{z_{\text{RN}}} \right)^2} \right)^N \cdot \left( \frac{1}{1 + \left( \frac{2(z - z_{\text{offset}})}{z_{\text{RM}}} \right)^2} \right)^M \cdot \exp \left[ - \left( (x - x_{\text{offset}})^2 + (y - y_{\text{offset}})^2 \right) \left( \frac{N}{w_{\text{N}}^2} + \frac{M}{w_{\text{M}}^2} \right) - (t - t_{\text{offset}})^2 \left( \frac{N}{\tau_{\text{N}}^2} + \frac{M}{\tau_{\text{M}}^2} \right) \right], \quad (5.9)$$

where  $z_{\text{offset}}$  is the  $z$ -displacement of the laser focuses from the centre of the trap.

The probability of ionising at a given field magnitude  $\mathcal{E}$  is given by the integral of the ionisation probability over the surface,  $S_{\mathcal{E}}$ , defined by the ellipsoid of constant electric field described in Equation 5.1, where

$$P_{\text{ion}}(\mathcal{E}) \propto \int \oint P_{\text{ion}}^{\text{thr}}(x, y, z, t) dS_{\mathcal{E}} dt. \quad (5.10)$$

In general, this integral needs to be solved numerically, using the ellipsoidal parameterisation of the electric field

$$\vec{\mathbf{r}}(u, v) = a \cos(u) \sin(v) \cdot \hat{\mathbf{i}} + b \sin(u) \sin(v) \cdot \hat{\mathbf{j}} + c \cos(v) \cdot \hat{\mathbf{k}}, \quad (5.11)$$

where  $u$  is the azimuth angle from the positive  $x$ -axis and  $v$  is the polar angle with respect to the  $z$ -axis to positions on the surface of the ellipsoid;  $\hat{\mathbf{i}}$ ,  $\hat{\mathbf{j}}$  and  $\hat{\mathbf{k}}$  are unit vectors along the  $+x$ ,  $+y$  and  $+z$  directions respectively; and  $a$ ,  $b$  and  $c$  are parameters that depend on the electric field. In the general case, where all electrode voltages are considered,

$$\begin{aligned} a &= \frac{\mathcal{E} \cdot r_0^2}{\left( \eta V_{\text{ax}}^{\text{dc}} + V_{\text{rad}}^{\text{rf}} \cdot \cos(\Omega t) \right)}, \\ b &= \frac{\mathcal{E} \cdot r_0^2}{\left( \eta V_{\text{ax}}^{\text{dc}} - V_{\text{rad}}^{\text{rf}} \cdot \cos(\Omega t) \right)}, \\ c &= \frac{\mathcal{E} \cdot r_0^2}{(2\eta V_{\text{ax}}^{\text{dc}})}. \end{aligned} \quad (5.12)$$

With these substitutions, the integral becomes

$$P_{\text{ion}}(\mathcal{E}) = \int_{-\infty}^{\infty} \int_0^{\pi} \int_0^{2\pi} P_{\text{ion}}^{\text{thr}}(x(u, v), y(u, v), z(u, v), t) \left\| \frac{\partial \vec{\mathbf{r}}}{\partial u} \times \frac{\partial \vec{\mathbf{r}}}{\partial v} \right\| du dv dt, \quad (5.13)$$

where the term  $\| \dots \|$  represents the Jacobi determinant. From Equation 5.4, the electric field can be replaced by

$$\mathcal{E} = \frac{\Delta^2}{\alpha^2}, \quad (5.14)$$

to convert from electric field strength to the shift of the ionisation threshold from the

zero-field value. In this work, we assume that ionisation takes place in the adiabatic regime for the reasons described by Stollenwerk *et al.*<sup>76</sup> Under this assumption, we take  $\alpha = 6.1 \frac{1}{\text{cm}} \cdot \sqrt{\frac{\text{V}}{\text{cm}}}$ . In order to make the results of our investigations independent of the exact electrode geometry, and hence applicable to the most common linear rf ion traps, we replace the applied voltages with the trap  $q$ -parameter,  $q$ , and the axial secular frequency,  $\omega_z$ :

$$\begin{aligned} V_{\text{rad}}^{\text{rf}} &= \frac{mqr_0^2\Omega^2}{2Q}, \\ V_{\text{ax}}^{\text{dc}}\eta &= \frac{m\omega_z^2r_0^2}{2Q}, \end{aligned} \quad (5.15)$$

where  $Q$  is the charge of the ion produced in the ionisation process and  $m$  is its mass.<sup>77</sup> In this way, Equation 5.13 only depends on  $q$ ,  $\Omega$  and  $\omega_z$ , and the results of the numerical analysis can be easily scaled to other ion traps.

It is informative to consider the effects of certain special cases. In addition to the general case, we have considered the effects of varying the radial confinement, the timing of the REMPI laser pulses and the dc voltages applied to the electrodes. As these cases consider the rf and dc voltages separately, it is possible to simplify the parameterisations used in the integration of Equation 5.13.

### 5.5.2 The Axial Electric Field

The first special case of interest is to consider only the dc voltages applied to the axial electrodes. The dc electric field varies along the trap axis as well as radially, but is time independent. The axially applied electric field,  $\mathcal{E}_{\text{ax}}$ , can be written in terms of the axial secular frequency,  $\omega_z$ , to give

$$\mathcal{E}_{\text{ax}} = \frac{m\omega_z^2}{2Q} \sqrt{r^2 + 4z^2}, \quad (5.16)$$

where  $r^2 = x^2 + y^2$ . The circular symmetry in the radial plane allows the parameterisation

$$\vec{\mathbf{r}}(u, v) = a \cos(u) \sin(v) \cdot \hat{\mathbf{i}} + a \sin(u) \sin(v) \cdot \hat{\mathbf{j}} + b \cos(v) \hat{\mathbf{k}}, \quad (5.17)$$

where

$$\begin{aligned} a &= \frac{2\mathcal{E}_{\text{ax}}e}{m\omega_z^2} = \frac{\Delta^2}{\alpha^2} \cdot \frac{2e}{m\omega_z^2}, \\ b &= \frac{\mathcal{E}_{\text{ax}}e}{m\omega_z^2} = \frac{\Delta^2}{\alpha^2} \cdot \frac{e}{m\omega_z^2}. \end{aligned} \quad (5.18)$$

The Jacobian,  $J$ , for integration is

$$J = \left\| \frac{\partial \vec{\mathbf{r}}}{\partial u} \times \frac{\partial \vec{\mathbf{r}}}{\partial v} \right\|. \quad (5.19)$$

The derivatives are

$$\begin{aligned}\frac{\partial \vec{r}}{\partial u} &= (-a \sin(u) \sin(v)) \hat{\mathbf{i}} + (a \cos(u) \sin(v)) \hat{\mathbf{j}}, \\ \frac{\partial \vec{r}}{\partial v} &= (a \cos(u) \cos(v)) \hat{\mathbf{i}} + (a \sin(u) \cos(v)) \hat{\mathbf{j}} + (-b \sin(v)) \hat{\mathbf{k}}.\end{aligned}\tag{5.20}$$

The Jacobian is then

$$\begin{aligned}J &= \left[ a^2 b^2 \sin^2(u) \sin^4(v) + a^2 b^2 \sin^4(v) \cos^2(u) \right. \\ &\quad \left. + \left( -a^2 \sin^2(u) \sin(v) \cos(v) - a^2 \sin(v) \cos^2(u) \cos(v) \right)^2 \right].\end{aligned}\tag{5.21}$$

### Scenario 1: Molecular Beam

The axially applied field is dc and so the time dependence in Equation 5.8 can be omitted, simplifying it to

$$P_{\text{ion}}(x, y, z) \propto \exp \left[ -((x - x_{\text{offset}})^2 + (y - y_{\text{offset}})^2) \left( \frac{N}{w_{\text{N}}^2} + \frac{M}{w_{\text{M}}^2} \right) - \frac{(z - z_{\text{offset}})^2}{w_{\text{beam}}^2} \right].\tag{5.22}$$

Equation 5.22 can be rewritten by making the substitutions

$$\begin{aligned}x &= a \cos(u) \sin(v), \\ y &= a \sin(u) \sin(v), \\ z &= b \cos(v).\end{aligned}\tag{5.23}$$

The result is a change of coordinates and a probability function of

$$\begin{aligned}P_{\text{ion}}(u, v) &\propto \exp \left[ \left( \frac{M}{w_{\text{M}}^2} + \frac{N}{w_{\text{N}}^2} \right) \cdot \left( - (a \sin(u) \sin(v) - y_{\text{offset}})^2 \right. \right. \\ &\quad \left. \left. - (a \sin(v) \cos(u) - x_{\text{offset}})^2 \right) - \frac{1}{w_{\text{MB}}^2} (b \cos(v) - z_{\text{offset}})^2 \right].\end{aligned}\tag{5.24}$$

This function can be integrated to generate the distribution of ionisation threshold probabilities,  $\mathcal{P}_{\text{ion}}$ ,

$$\mathcal{P}_{\text{ion}}(\Delta) \propto \int_0^\pi \int_0^{2\pi} P_{\text{ion}}(u, v) J du dv.\tag{5.25}$$

Performing the integral for multiple values of  $\Delta$  results in a spectrum of ionisation threshold probability.

## Scenario 2: Background Gas

Again, as we consider only the axially applied dc voltages, the time dependance can be omitted from Equation 5.42 to give

$$P_{\text{ion}}(x, y, z) \propto \left( \frac{1}{1 + \left( \frac{2(z - z_{\text{offset}})}{z_{\text{RN}}} \right)^2} \right)^N \cdot \left( \frac{1}{1 + \left( \frac{2(z - z_{\text{offset}})}{z_{\text{RM}}} \right)^2} \right)^M \cdot \exp \left[ -((x - x_{\text{offset}})^2 + (y - y_{\text{offset}})^2) \left( \frac{N}{w_{\text{N}}^2} + \frac{M}{w_{\text{M}}^2} \right) \right]. \quad (5.26)$$

Making the substitutions from Equation 5.23, this can be rewritten

$$P_{\text{ion}}(u, v) \propto \left( \frac{1}{1 + \frac{4}{z_{\text{RM}}^2} (b \cos(v) - z_{\text{offset}})^2} \right)^M \left( \frac{1}{1 + \frac{4}{z_{\text{RN}}^2} (b \cos(v) - z_{\text{offset}})^2} \right)^N \cdot \exp \left[ \left( \frac{M}{w_{\text{M}}^2} + \frac{N}{w_{\text{N}}^2} \right) \left( - (a \sin(u) \sin(v) - y_{\text{offset}})^2 - (a \sin(v) \cos(u) - x_{\text{offset}})^2 \right) \right]. \quad (5.27)$$

The integral becomes

$$\mathcal{P}_{\text{ion}}(\Delta) \propto \int_0^\pi \int_0^{2\pi} P_{\text{ion}}(u, v) J du dv. \quad (5.28)$$

This integration can be performed numerically to obtain the ionisation threshold probability spectrum.

### 5.5.3 The Radial Electric Field

The radially applied electric field increases linearly from the centre of the trap and oscillates in time. In an ideal linear Paul trap the electric field, close to the trap centre, does not change along the trap axis. The temporal oscillation of the field leads to several possible scenarios. The arrival times of the lasers may be uncorrelated to the phase of the rf trap drive or they may be timed to coincide exactly with a specific phase of the rf field. Furthermore, the solution can be simplified if the lasers pass precisely through the centre of the trap.

## Specific Arrival Phase

### No Displacement of the Lasers

In this case, the laser pulses are timed to coincide with a specific phase of the rf drive field and the ionisation lasers pass through the centre of the trap ( $x_{\text{offset}} = y_{\text{offset}} = 0$ ). The integration over the spatial degrees of freedom has an analytic solution, but the integration with respect to time must be done numerically. Equation 5.13 becomes

$$P_{\text{ion}}(\Delta) \propto \Delta^2 \int_{-\infty}^{+\infty} \frac{1}{|\cos(\Omega t)|} \exp \left[ - \left( \frac{\Delta^2}{\alpha^2} \cdot \frac{r_0^2}{V_{\text{rad}}^{\text{rf}} \cos(\Omega t)} \right)^2 \cdot \left( \frac{N}{w_{\text{N}}^2} + \frac{M}{w_{\text{M}}^2} \right) - (t - t_{\text{offset}})^2 \left( \frac{N}{\tau_{\text{N}}^2} + \frac{M}{\tau_{\text{M}}^2} \right) \right] dt. \quad (5.29)$$

### Displacement of the Lasers

If the lasers are offset from the centre of the trap, Equation 5.13 must be solved numerically. The electric field strength has radial symmetry

$$\mathcal{E}_{\text{rad}}^2 = \frac{V_{\text{rad}}^{\text{rf}^2} \cos^2(\Omega t)}{r_0^4} \cdot (x^2 + y^2). \quad (5.30)$$

Due to the radial symmetry of the electric field produced by the rf electrodes, it is possible to simplify the integration by using the circular parameterisation

$$\vec{\mathbf{r}}(u) = a \cos(u) \hat{\mathbf{i}} + a \sin(u) \hat{\mathbf{j}}, \quad (5.31)$$

where

$$a = \frac{E_{\text{rad}} r_0^2}{V_{\text{rad}}^{\text{rf}} |\cos(\Omega t)|} = \frac{\Delta^2}{\alpha^2} \cdot \frac{r_0^2}{V_{\text{rad}}^{\text{rf}} |\cos(\Omega t)|}, \quad (5.32)$$

and  $\mathcal{E}_{\text{rad}}$  is the time-dependent electric field applied by the radial electrodes (see Equation 5.1). With this change of variables,

$$P_{\text{ion}}(u, t) \propto \exp \left[ - ((a \cos(u) - x_{\text{offset}})^2 + (a \sin(u) - y_{\text{offset}})^2) \left( \frac{N}{w_{\text{N}}^2} + \frac{M}{w_{\text{M}}^2} \right) - (t - t_{\text{offset}})^2 \left( \frac{N}{\tau_{\text{N}}^2} + \frac{M}{\tau_{\text{M}}^2} \right) \right]. \quad (5.33)$$

The integral becomes

$$\mathcal{P}_{\text{ion}}(\Delta) = \int_{-\infty}^{\infty} \int_0^{2\pi} a(t) \cdot P_{\text{ion}}(u, t) du dt. \quad (5.34)$$

### Random Arrival Phase

If the arrival of the laser pulses is uncorrelated to the rf phase, it is necessary to integrate over all phases.

### No Displacement of the Lasers

If the lasers are not displaced from the centre of the trap, the integration over the spatial degrees of freedom still has an analytic solution. Equation 5.29 can be adapted to integrate over all phases of the rf,

$$\begin{aligned} \mathcal{P}_{\text{ion}}(\Delta) \propto \Delta^2 \int_0^{2\pi/\Omega} \int_{-\infty}^{+\infty} \frac{1}{|\cos(\Omega t)|} \exp \left[ - \left( \frac{\Delta^2}{\alpha^2} \cdot \frac{r_0^2}{V_{\text{rad}}^{\text{rf}} \cos(\Omega t)} \right)^2 \cdot \left( \frac{N}{w_{\text{N}}^2} + \frac{M}{w_{\text{M}}^2} \right) \right. \\ \left. - (t - t_{\text{offset}})^2 \left( \frac{N}{\tau_{\text{N}}^2} + \frac{M}{\tau_{\text{M}}^2} \right) \right] dt dt_{\text{offset}}. \end{aligned} \quad (5.35)$$

This integrates over the time offsets of the laser pulses from the zero-crossing of the rf between zero and the period of the rf drive.

### Displacement of the Lasers

If the lasers are displaced from the centre of the trap, the integration of Equation 5.33 must be performed with respect to the arrival phase. The resulting integral is

$$\mathcal{P}_{\text{ion}}(\Delta) = \int_0^{2\pi/\Omega} \int_{-\infty}^{\infty} \int_0^{2\pi} a(t) \cdot P_{\text{ion}}(u, t, t_{\text{offset}}) du dt dt_{\text{offset}}. \quad (5.36)$$

#### 5.5.4 The General Case: Axial and Radial Electric Fields

The superposition of the rf and dc electric fields breaks the radial symmetry used to simplify the integrals in the previously considered cases. However, the general case has special cases associated with the special cases considered for the axial and radial cases. There is no longer an analytic solution to the spatial integral in the case where there is no offset of the lasers. The full three-dimensional integration is necessary in this case.

Substituting for  $\mathcal{E}$ , the parameters  $a, b, c$  are

$$\begin{aligned} a &= \frac{\Delta^2}{\alpha^2} \cdot \frac{r_0^2}{\left(\eta V_{\text{ax}}^{\text{dc}} + V_{\text{rad}}^{\text{rf}} \cdot \cos(\Omega t)\right)}, \\ b &= \frac{\Delta^2}{\alpha^2} \cdot \frac{r_0^2}{\left(\eta V_{\text{ax}}^{\text{dc}} - V_{\text{rad}}^{\text{rf}} \cdot \cos(\Omega t)\right)}, \\ c &= \frac{\Delta^2}{\alpha^2} \cdot \frac{r_0^2}{(2\eta V_{\text{ax}}^{\text{dc}})}. \end{aligned} \quad (5.37)$$

The Jacobian,  $J$ , in this case is given by Equation 5.19. The result is

$$\begin{aligned} J &= \left[ a^2 c^2 \sin^2(u) \sin^4(v) + b^2 c^2 \sin^4(v) \cos^2(u) \right. \\ &\quad \left. + \left( -ab \sin^2(u) \sin(v) \cos(v) - ab \sin(v) \cos^2(u) \cos(v) \right)^2 \right]^{\frac{1}{2}}. \end{aligned} \quad (5.38)$$

### Scenario 1: Molecular Beam

The change of variables for Equation 5.8 gives

$$\begin{aligned} P_{\text{ion}}(u, v, t) &\propto \exp \left[ - \left( (a \cos(u) \sin(v) - x_{\text{offset}})^2 \right. \right. \\ &\quad \left. \left. + (b \sin(u) \sin(v) - y_{\text{offset}})^2 \right) \left( \frac{N}{w_{\text{N}}^2} + \frac{M}{w_{\text{M}}^2} \right) \right. \\ &\quad \left. - \frac{(c \cos(v) - z_{\text{offset}})^2}{w_{\text{beam}}^2} - (t - t_{\text{d}})^2 \left( \frac{N}{\tau_{\text{N}}^2} + \frac{M}{\tau_{\text{M}}^2} \right) \right]. \end{aligned} \quad (5.39)$$

### Specific Arrival Phase

For the case of the lasers arriving at a specific phase of the rf drive, the integral becomes

$$\mathcal{P}_{\text{ion}}(\Delta) = \int_{-\infty}^{\infty} \int_0^{\pi} \int_0^{2\pi} P_{\text{ion}}(u, v, t) \cdot J \cdot dudvdt. \quad (5.40)$$

### Random Arrival Phase

For the case of the lasers arriving at a random phase of the rf drive, the integral becomes

$$\mathcal{P}_{\text{ion}}(\Delta) = \int_0^{2\pi/\Omega} \int_{-\infty}^{\infty} \int_0^{\pi} \int_0^{2\pi} P_{\text{ion}}(u, v, t, t_{\text{offset}}) \cdot J \cdot dudvdt dt_{\text{offset}}. \quad (5.41)$$

## Scenario 2: Background Gas

In the case of loading from a background gas,

$$\begin{aligned}
P_{\text{ion}}(u, v, t) \propto & \left( \frac{1}{1 + \left( \frac{2(c \cos(v) - z_{\text{offset}})}{z_{\text{RN}}} \right)^2} \right)^N \cdot \left( \frac{1}{1 + \left( \frac{2(c \cos(v) - z_{\text{offset}})}{z_{\text{RM}}} \right)^2} \right)^M \\
& \cdot \exp \left[ - \left( (a \cos(u) \sin(v) - x_{\text{offset}})^2 + (b \sin(u) \sin(v) - y_{\text{offset}})^2 \right) \left( \frac{N}{w_{\text{N}}^2} + \frac{M}{w_{\text{M}}^2} \right) \right. \\
& \left. - (t - t_{\text{offset}})^2 \left( \frac{N}{\tau_{\text{N}}^2} + \frac{M}{\tau_{\text{M}}^2} \right) \right]. \quad (5.42)
\end{aligned}$$

### Specific Arrival Phase

For the case of the lasers arriving at a specific phase of the rf drive, the integral becomes

$$\mathcal{P}_{\text{ion}}(\Delta) = \int_{-\infty}^{\infty} \int_0^{\pi} \int_0^{2\pi} P_{\text{ion}}(u, v, t) \cdot J \cdot dudvdt. \quad (5.43)$$

### Random Arrival Phase

For the case of the lasers arriving at a random phase of the rf drive, the integral becomes

$$\mathcal{P}_{\text{ion}}(\Delta) = \int_0^{2\pi/\Omega} \int_{-\infty}^{\infty} \int_0^{\pi} \int_0^{2\pi} P_{\text{ion}}(u, v, t, t_{\text{offset}}) \cdot J \cdot dudvdt dt_{\text{offset}}. \quad (5.44)$$

## 5.6 Results

The following subsections present the effect of the trap parameters and laser pulse timings on the broadening of the ionisation threshold. This broadening is quantified by the full-width at half-maximum (FWHM) of the ionisation threshold. These simulations explore the effects of the radial confinement, laser pulse timings and axial confinement separately before considering the general case, where voltages are applied to both the radial and axial electrodes. The state-selectivity of a chosen REMPI process can be assessed by comparing the width of the ionisation threshold to the splitting of energy levels within the molecular ion. As an example ionisation process, we take the case of 2+1' REMPI of  $^{14}\text{N}_2$  molecules in a linear Paul trap.

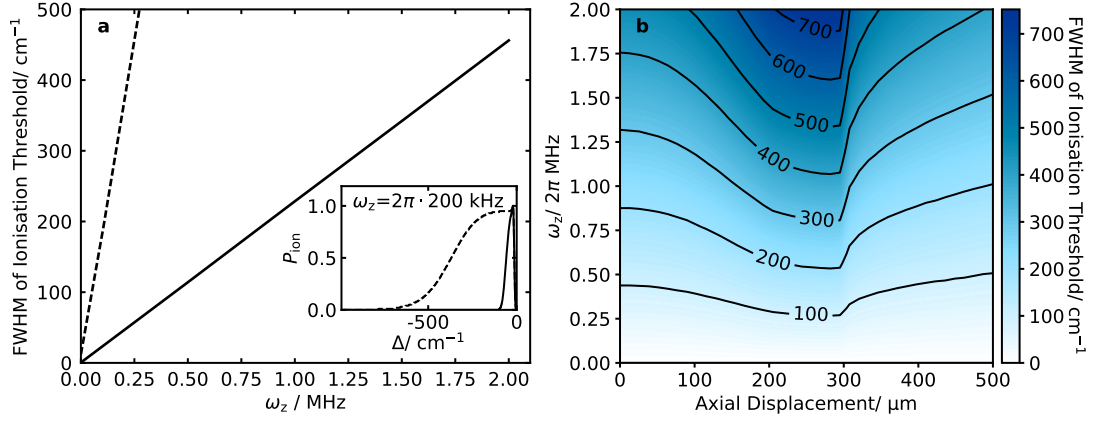


Figure 5.4: Ionisation threshold distributions were simulated for 2+1' REMPI of  $^{14}\text{N}_2$ . (a) Broadening of the ionisation threshold for different axial secular frequencies for loading from a molecular beam with waist  $w_{\text{beam}} = 250 \mu\text{m}$  (solid line) and from a homogeneous background gas (dashed line). In both scenarios,  $z_{\text{offset}} = 0$ . Inset, the normalised ionisation threshold distributions for an axial secular frequency of  $2\pi \cdot 200 \text{ kHz}$ . (b) Broadening of the ionisation threshold for different axial secular frequencies and axial displacements from the trap centre for loading from a molecular beam with waist  $w_{\text{beam}} = 250 \mu\text{m}$ .

### 5.6.1 Axial Electric Field

#### Scenario 1: Molecular Beam

The broadening of the ionisation threshold increases linearly with the axial secular frequency (Figure 5.4(a)). Here, by way of example, we considered ionisation from a molecular beam of waist  $w_{\text{beam}} = 250 \mu\text{m}$  passing through the centre of the trap. For these parameters, the increase in the broadening with axial confinement is approximately  $225 \text{ cm}^{-1} \text{ MHz}^{-1}$ , which is significant compared to the splitting of rotational levels in a typical molecular ion. The shape of the ionisation threshold differs from that seen in the radial, due to the different electric field gradients along the trap axis and out radially from the trap centre. The result is an initial spike followed by a slow decrease (Figure 5.4(a), inset). Increasing the displacement of the molecular beam from the centre of the trap leads to an initial increase in the broadening followed by a decrease as the displacement exceeds the width of the beam (Figure 5.4(b)). This is a consequence of the square-root relationship between the electric field and the corresponding spectral shift (Equation 5.4). At higher electric fields, the gradient of the shift is smaller, so the range of shifts seen by the target molecules is smaller. While smaller peak widths can be obtained for large offsets from the trap centre, it is not desirable to ionise there due to the large energy acquired by ions produced in strong electric fields. It is therefore preferable to ionise as close as possible to the centre of the trap.

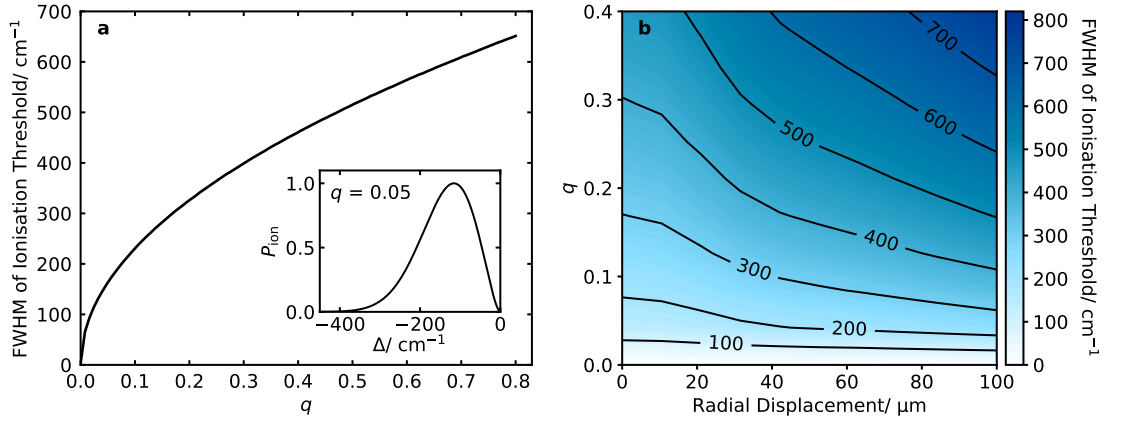


Figure 5.5: Ionisation threshold distributions were simulated for 2+1' REMPI of  $^{14}\text{N}_2$  with a trap drive frequency  $\Omega = 2\pi \cdot 20$  MHz and ionisation laser beamwaists  $w_{\text{N/M}} = 50$   $\mu\text{m}$ . The laser pulses were timed to the zero-crossing of the rf field, with temporal widths  $\tau_{\text{N/M}} = 5$  ns. (a) Broadening of the ionisation threshold for different  $q$  parameters, where the REMPI lasers pass through the centre of the trap. Inset, the normalised ionisation threshold distributions for  $q = 0.05$ . (b) Broadening of the ionisation threshold for different  $q$  values and radial displacements of the REMPI lasers from the trap centre.

## Scenario 2: Background Gas

In scenario 2.), we consider ionisation laser beam waists  $w_{\text{N/M}} = 50$   $\mu\text{m}$  and wavelengths  $\lambda_{\text{N}} = 255$  nm,  $\lambda_{\text{M}} = 212$  nm.

The FWHM of the ionisation threshold increases linearly with the axial secular frequency (Figure 5.4(a)), but more rapidly than in scenario 1.). The gradient in this case is  $\sim 1,800$   $\text{cm}^{-1} \text{MHz}^{-1}$ . This is because the intense part of the laser beam extends much further than the width of the molecular beam previously considered. We do not consider the impact of displacing the focus from the trap centre, but the effect is likely to be smaller due to the larger extent of the ionisation volume in the axial direction.

### 5.6.2 Radial Electric Field

The width of the threshold distribution shows a square-root behaviour for increasing  $q$ -parameter (Figure 5.5(a)). With a trap drive frequency of  $2\pi \cdot 20$  MHz, the broadening exceeds  $100$   $\text{cm}^{-1}$  for  $q$  values as low as 0.05. This is significantly larger than the typical rotational constants of molecules.

The Gaussian laser profiles and size of the surface element result in a shell-like ionisation threshold distribution (Figure 5.5(a), inset), with no photoionisation at the centre of the trap ( $\Delta = 0$   $\text{cm}^{-1}$ ) due to the small volume element. From the centre of the trap, the photoionisation probability increases due to the increased ionisation volume and then decreases again due to the lasers' intensity profiles. While the FWHM reflects the broadening of the threshold distribution, it neglects the shift of the threshold which can be large compared to the broadening.

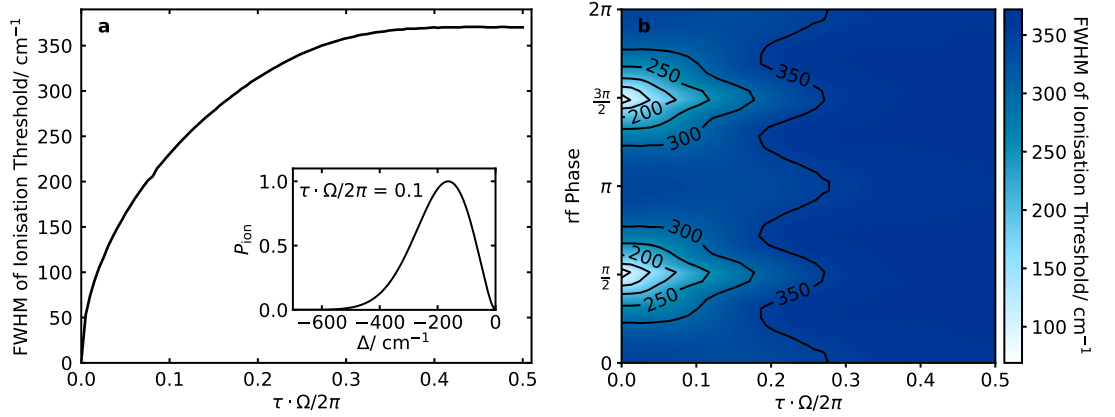


Figure 5.6: Ionisation threshold distributions were simulated for 2+1' REMPI of  $^{14}\text{N}_2$  for  $q = 0.1$  and no radial displacement of the REMPI lasers. (a) Broadening of the ionisation threshold for different laser pulse durations where the lasers are timed to coincide with the zero-crossing of the rf field. Inset, the normalised ionisation threshold distribution for a laser pulse duration of 10% of the trap drive period. (b) Broadening of the ionisation threshold for different laser pulse durations and phases of the rf trap drive relative to the arrival times of the ionisation lasers.

For a radial displacement of the photoionisation lasers, the broadening of the ionisation threshold increases with the displacement from the trap centre (Figure 5.5(b)). For a displacement of  $100 \mu\text{m}$  from the trap centre, the increase in the broadening is already significant for higher confinements. The ionisation threshold broadening is therefore sensitive to small misalignments of the ionisation lasers in the trap. Depending on the design of the trap, sufficient alignment precision may be difficult within the tolerance of the ionisation scheme.

### 5.6.3 Laser Pulse Timing

With the laser pulses timed to coincide with the zero-crossing of the rf drive, the FWHM of the ionisation threshold increases with the temporal pulse width (Figure 5.6(a)). For a pulse width of  $\sim 1\%$  of the period of the rf field, the broadening of the ionisation threshold is approximately  $50 \text{ cm}^{-1}$  for a trap  $q$  value of 0.1. As the temporal pulse width increases, the rate of broadening decreases until it begins to plateau at around 50% of the trap drive period, as the laser pulses begin to extend significantly beyond one period of the rf drive. When the rf phase at which the laser pulses arrive is varied, the periodicity of the broadening is notable for pulse durations less than 20% of the trap drive period (Figure 5.6(b)). The plateauing of the ionisation threshold widths can be seen for all phases. For larger pulse durations the effect of the trap drive phase is minimal.

### 5.6.4 General Case

In the general case, we only present results for the case of loading from a molecular beam to assess state-selectivity, as this case results in less broadening. For the ionisation process considered, ionisation is only possible into rotational states that are either only odd or only even, due to the symmetry of the nuclear wavefunction. The rotational constant for  $^{14}\text{N}_2^+$  is  $1.9 \text{ cm}^{-1}$ .<sup>115</sup> For trap parameters of  $\Omega = 2\pi \cdot 5 \text{ MHz}$ ,  $q = 0.01$  and  $\omega_z = 2\pi \cdot 50 \text{ kHz}$ , the ionisation threshold distributions are sufficiently well-separated to allow rotationally selective ionisation into either the  $J=0$  or  $J=1$  state (Figure 5.8), depending on the initial state of the molecule. Higher rotational levels have not been included for the sake of simplicity, but would reduce the maximum state purity that could be achieved in cases where there is spectral overlap. Although a high degree of state-selectivity can be achieved, there is a balance between the state-selectivity and efficiency (Figure 5.8(b)).

While the broadening increases linearly for the axial confinement and with a square-root behaviour for the radial case, the combined broadening in the presence of both the axial and radial voltages is more complicated (Figure 5.7) because the radial component of the dc confinement partially compensates the rf electric field.

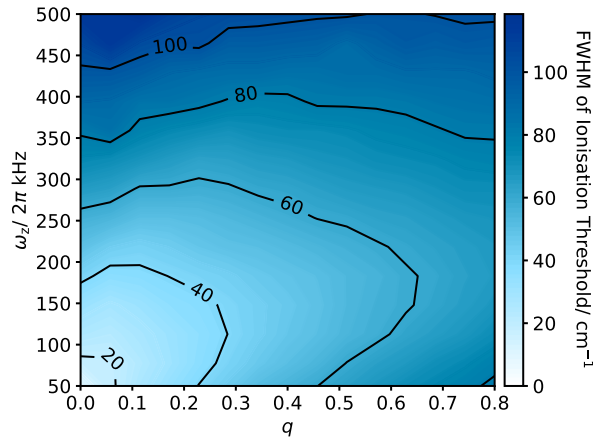


Figure 5.7: Broadening of the ionisation threshold for different axial and radial confinements. Ionisation threshold distributions were simulated for loading from a molecular beam with beam waist  $w_{\text{beam}} = 250 \mu\text{m}$  into a trap with drive frequency  $\Omega = 2\pi \cdot 5 \text{ MHz}$ . The laser pulses were timed to the zero-crossing of the rf field, with temporal pulse widths  $\tau_{N/M} = 5 \text{ ns}$ .

### 5.6.5 Ionisation Process

In addition to the trap parameters, different ionisation schemes will result in different field broadening. This depends on the number of photons involved in the ionisation process and the wavelengths of those photons if loading from a molecular source much wider than the Rayleigh length of the lasers. The broadening decreases for larger numbers of photons involved in the process (Figure 5.9), although it is worth noting that this is accompanied by a reduced efficiency for the process as more photons have to be absorbed by the molecule.

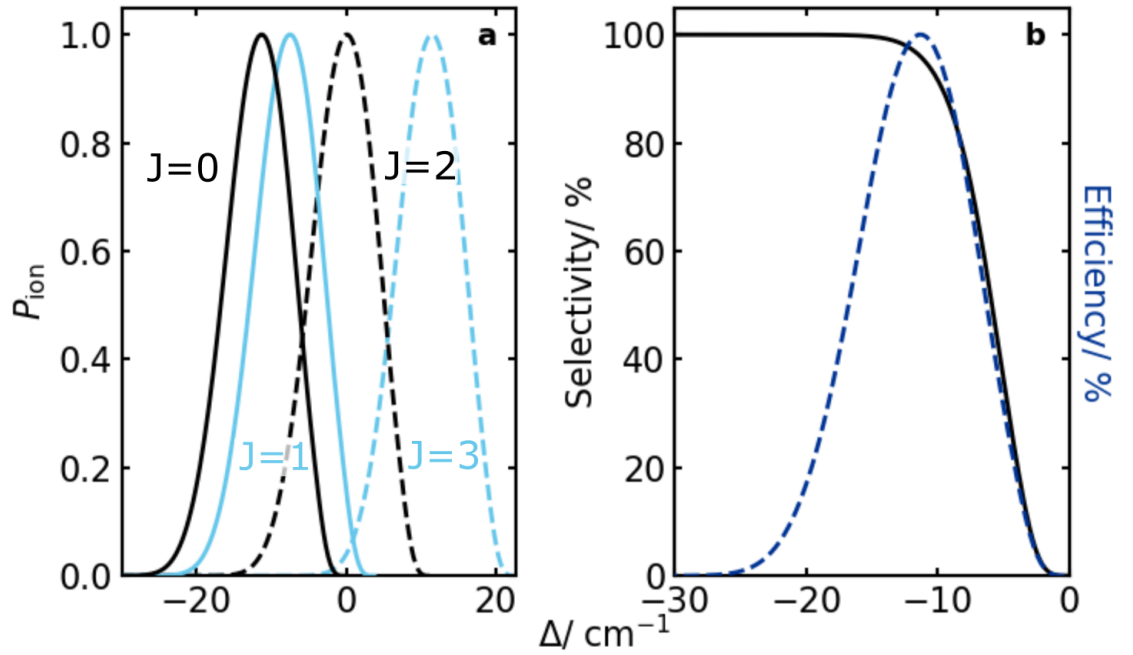


Figure 5.8: Broadening of the ionisation threshold for different axial and radial confinements. Ionisation threshold distributions were simulated for loading from a molecular beam with beam waist  $w_{\text{beam}} = 250 \mu\text{m}$  into a trap with drive frequency  $\Omega = 2\pi \cdot 5 \text{ MHz}$ . The timing of the ionisation lasers was uncorrelated to the phase of the rf drive.

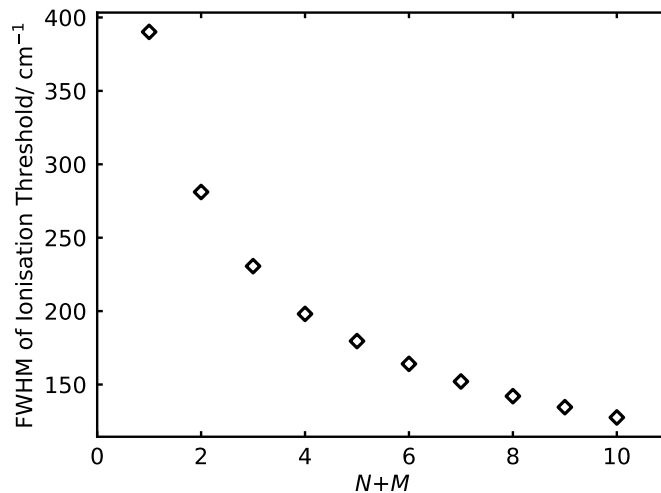


Figure 5.9: Broadening of the ionisation threshold for different numbers of photons in the REMPI process,  $N+M$ . The laser beamwaists were  $50 \mu\text{m}$  and  $q$  was 0.1. The lasers were timed to the zero-crossing of the rf field. Only the radial plane was considered because in scenario 1.) there is no dependence in the  $z$  direction.

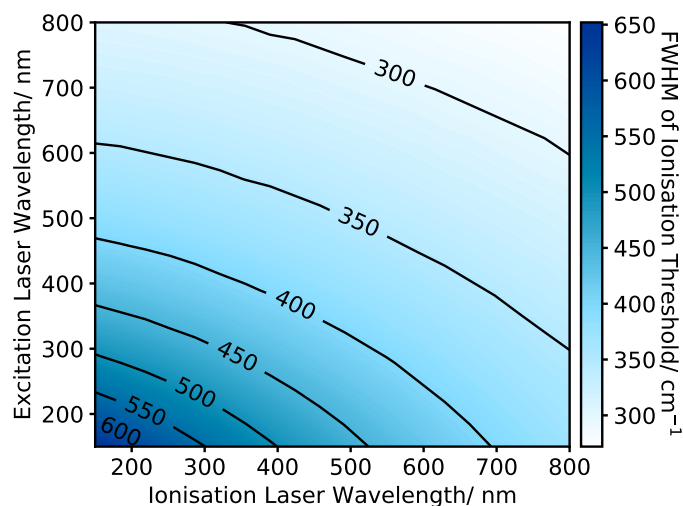


Figure 5.10: Broadening of the ionisation threshold for different excitation and ionisation laser wavelengths in scenario 2.). Only the axial dc voltages are considered.

In the case of loading from a source with a broader spatial extent than the Rayleigh length of the lasers along the laser axis, the broadening depends on the wavelengths of the photons. Here, the shorter the wavelength, the larger the Rayleigh length and the greater the broadening (Figure 5.10).

## 5.7 Discussion

In order to achieve rovibronic state-selectivity, the broadening of the ionisation threshold due to the electric trapping field must be smaller than the rotational state splitting of the molecular ion during the loading process. For ion traps with high secular frequencies and a high drive frequency, the electric field inhomogeneity significantly broadens the ionisation threshold, hampering rotational state-selectivity.

In some circumstances, it may be beneficial to use a multipole trap in order to have a smaller electric field gradient near the centre of the trap. This could sufficiently reduce the broadening to allow state-selective ionisation. However, in many cases where a quadrupole trap is used, a higher order multipole trap would not be suitable. For example, the quantum logic scheme for high resolution spectroscopy of nitrogen is only possible using a quadrupole ion trap. Synchronising the laser pulses with the minimum of the rf drive can significantly reduce the broadening. However, this strategy is most effective when the pulse duration is significantly shorter than the period of the rf drive (Figure 5.6), favouring short laser pulses in conjunction with low trapping frequencies.

Another way to reduce the broadening is to shrink the spatial region in which ionisation can take place. In the radial plane, this can be done by tightening the focuses of the ionisation lasers. However, in set-ups where dye lasers are used, very tight focusing is challenging due to their poor beam profile. In the axial direction, loading from a molecular beam rather

than from a homogeneous background gas has been shown to reduce the broadening for typical laser parameters by a factor of eight for a molecular beam width of  $250\ \mu\text{m}$  (Figure 5.4). An additional consideration is that, if loading from a background gas, collisions with the produced ions cannot be prevented. Thermalisation of the rotational state and charge-exchange reactions can cause loss of the produced state. To further reduce the broadening for two-colour and multi-colour REMPI processes, it may be possible to cross the ionisation lasers so that ions are only produced in the volume where they intersect. For the trap we have considered, this would reduce the ionisation region along the axis of the trap, reducing the broadening due to the dc axial electrode voltage. If these steps are inadequate, a final strategy would be to minimise the voltages applied to the electrodes during loading. This can be done by choosing to work at lower confinements during loading. However, where it is not possible to trap with low enough electric fields to resolve the ionisation thresholds for different rovibrational levels, rapid switching of the trap drive may be necessary. This is explored in Chapter 6.

## Chapter 6

# Switching of the Trap Drive

### 6.1 Introduction

The ionisation threshold for molecules in a rf ion trap can become prohibitively broad, preventing state-selective ionisation at relatively low confinements (see Chapter 5). Loading nitrogen ions into our trap, the broadening would significantly exceed the separation between rotational levels for all feasible combinations of trapping and laser parameters.

This may be mitigated by lowering the trapping voltages before loading and then raising them again after ionisation. For this to work, the trap voltages need to be switched off and back on again sufficiently fast to retain the trapped ions. Switching the trap off whilst loading may have additional benefits, such as preventing the acceleration of photoelectrons (released from the electrodes by the ionisation lasers) into the ion crystal. However, it may also cause heating of ions already in the trap.

One way to facilitate fast trap switching is to use a digital trap in which the rf voltage switches between three discrete levels to resemble an oscillation (see e.g. Deb *et al.*<sup>116</sup>). Within the rf cycle, there can be a period when the voltage on the rf electrodes is zero and applying the REMPI lasers during this period could facilitate state-selective loading. Alternatively, in the case of an ion trap driven by a resonant circuit, the resonant circuit can be dumped by a built-in high voltage switch. After the resonator field is extinguished, no voltage is present at the rf electrodes. Both methods are well suited for low frequency ion traps but are difficult to implement for high frequencies.

We have explored the switching of the resonant circuit for a linear Paul trap. In this chapter, we examine the speed and quality of switching which can be achieved and the consequent heating of the existing trapped ions. For this, we have used Coulomb crystals of calcium ions and measured the fluorescence after switching as the ions recoil to their initial temperature. The effects of switching off both the rf and dc voltages have been explored.

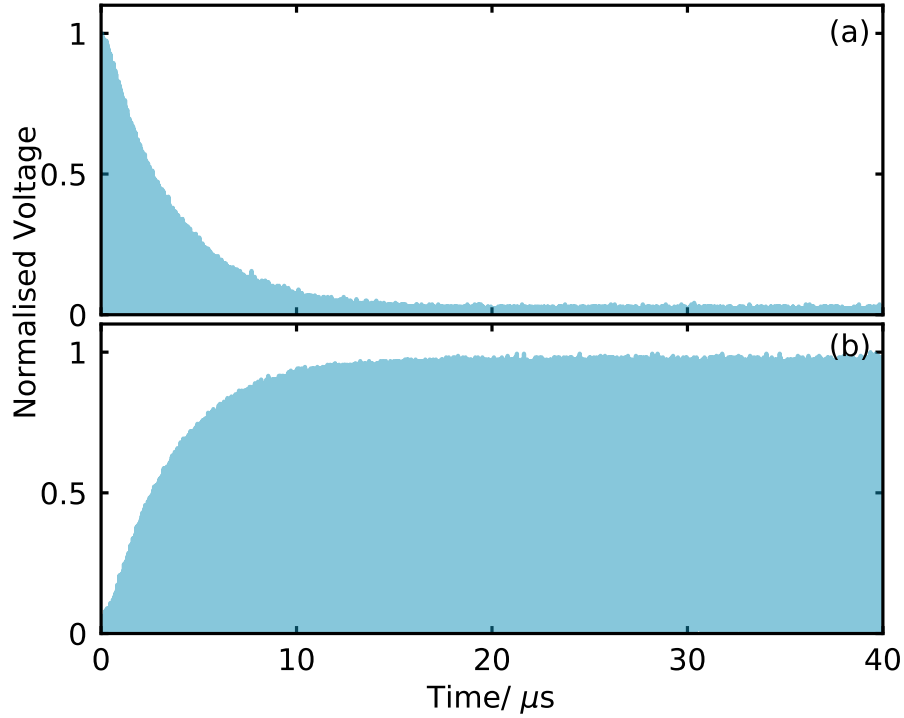


Figure 6.1: (a) The decay of the resonator field, measured with the monitor coil, as the drive was switched off. (b) The recovery of the resonator field, measured with the monitor coil, as the drive was switched back on.

## 6.2 Decay of the Electric Field in a Resonator

The rf trap drive is mediated by a high-Q-factor resonator circuit. The Q factor of the resonator is the ratio of the resonator frequency to the width of the resonance (Equation 4.1). The decay of energy in the resonator depends on the Q factor according to

$$Q = \frac{\tau\omega_0}{2}, \quad (6.1)$$

where  $\tau$  is the time constant of the decay and  $\omega_0$  is the resonant frequency of the circuit. As our ion trap resonator has a Q factor of 260, it will take tens of  $\mu\text{s}$  to switch the trap off and on again with good extinction of the field (Figure 6.1). The slow switching time can make the trap unstable during the recovery of the trapping potential. If the trap voltages are lowered and raised slowly, there is a risk of losing ions that were already trapped, due to small disturbances such as collisions with residual background gas. Switching the trap off for a very short time reduces this risk, but is technically more complex.

## 6.3 Methods

The methods used to switch off the rf and dc trap voltages are explained in the following subsections. To assess the impact of the switching process on trapped ions, the fluorescence rate during and after switching was recorded.

### 6.3.1 rf Switching

In the following experiments, the intra-circuit field was interfered with a counter-driving field to increase the extinction rate of the resonator field. Three function generator outputs at 22 MHz were connected via two rf switches<sup>a</sup> to an amplifier<sup>b</sup> which was then connected to the trap's resonator circuit (Figure 6.2(a)). Initially, the resonator was driven by a signal characteristic of normal trap operation. By switching the phase of the trap drive by  $\pi$  and increasing its amplitude, the resonator field was subsequently eliminated. This occurred faster than the natural decay rate of the resonator due to the additional destructive interference between the intra-circuit and out-of-phase drives. Similarly, by applying a high-amplitude, in-phase drive, the rf field was recovered. Once the original drive amplitude was restored, the drive was switched back to the in-phase low-amplitude drive (Figure 6.2(c)).

The switch-off and recovery times depend on the relative amplitudes of the high-amplitude and low-amplitude driving fields. In practice, these are limited by the amplitude required for normal trap operation and the maximum power that can reasonably be supplied to the resonator circuit. In our trap, a total switching time of 2  $\mu$ s is feasible.

During the switching process, the signal picked up by the monitor coil (Figure 4.4) was recorded on an oscilloscope<sup>c</sup>. To convert from the rf voltage detected by the monitor coil to the voltage on the radial electrodes, the monitor coil voltage was first converted to a radial secular frequency by interpolating a linear calibration plot of monitor coil voltage and secular frequency. Once the secular frequency was determined, the electrode voltage was given by

$$V = \frac{\sqrt{2}m\omega_r\Omega r_0^2}{Q}. \quad (6.2)$$

### 6.3.2 dc Switching

The switching of the dc field is more straightforward in principle. The two axial electrodes are held at different voltages to compensate stray fields that cause excess micromotion along the trap axis. In order to switch off the dc field for the duration of the rf switching, an OR gate was used to combine either the two TTL pulses used for the rf switches or a

<sup>a</sup>Mini Circuits, ZASWA-2-50DR and ZASWA-2-50DR-FT+

<sup>b</sup>Mini Circuits, LZY-22+

<sup>c</sup>Agilent, MSO6054A

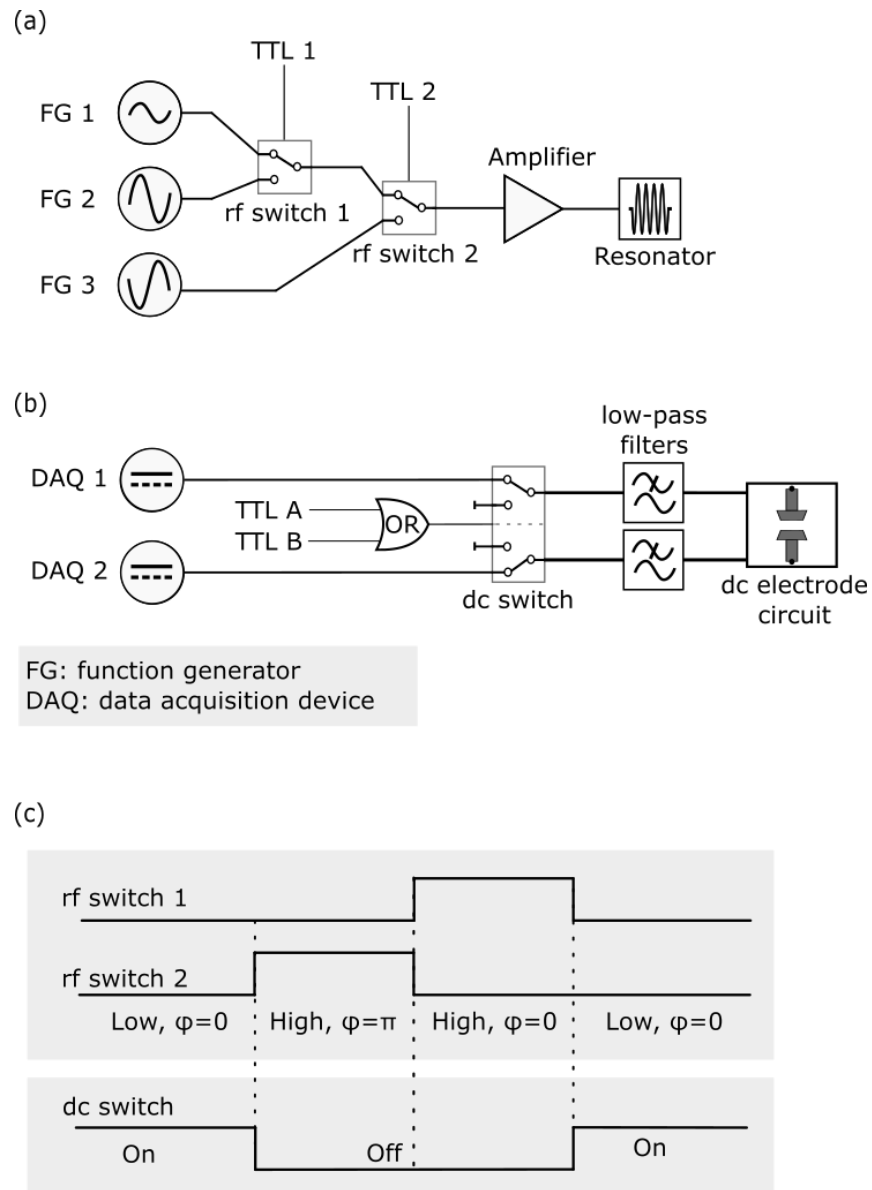


Figure 6.2: The set-up used to rapidly switch the trapping fields off and on again. The TTLs were supplied by a delay generator. a) The set-up used to switch the rf field. Initially, the resonator circuit is driven by a low amplitude signal from FG 1. The drive source is switched to FG 3 which supplies a high-amplitude signal, with a phase difference of  $\pi$ , which interferes with the intra-resonator field. On reaching the minimum amplitude, the resonator input is switched to FG 2, a high-amplitude signal in-phase with the original drive, which restores the trapping field. Finally, the drive from FG 1 is reinstated. b) The set-up used to switch the dc field. c) The pulse sequence used for the switching. The duration of the high amplitude pulses for the rf switching can be varied. The dc switching is shown in the case where TTLs 1 and 2 are TTLs A and B also. However, longer dc switching times using different TTLs are possible.

longer TTL pulse and ground. A quad SPDT switch<sup>d</sup> switches between the axial electrode voltages and ground (Figure 6.2(b),(c)). After the switch, a low pass RC filter was used to smooth the switching pulse.

While it may at first glance appear that the ideal option is to switch the dc confinement off for the shortest possible duration, this is not the case due to the strong kick given to the ions during the switch. The rf switching time is on the order of a few  $\mu\text{s}$  (in total to switch off and on again). It was found that when the dc voltage was switched off for similar durations, the ions were lost from the trap. To reduce the heating rate, the dc voltage should be switched off as gradually as possible to move the ion adiabatically to the zero-voltage position. This can be changed by varying the low pass filter RC values. In order to be able to switch without loss of ions, the RC values were varied to lower the cut-off frequency and the lengths of the pulses used to switch the trap were increased to ensure the complete extinction of the field. The switch-off time and RC filter cut-off frequency were optimised to minimise the drop in ion fluorescence. A cut-off frequency of 100 Hz was chosen for these experiments. The bias tee (Figure 4.6) acts as an additional low-pass filter.

### 6.3.3 Doppler Recooling Measurements

The cycle-averaged fluorescence rate of a trapped ion depends on its motional energy because of the Doppler effect (Figure 4.17). If a hot ion is cooled, the fluorescence rate will change and approach the steady-state fluorescence rate.<sup>117,118</sup> The time taken for the ion fluorescence rate to recover increases with the ion's temperature. This relationship can be used to both qualitatively and quantitatively assess the temperature of trapped ions. In the following experiments, the switching process heats the trapped ions, resulting in a drop in fluorescence. The rate at which the original fluorescence level is recovered provides an indication of the heating caused by the switching.

The TTLs supplied to the rf switches were generated by a delay generator<sup>e</sup>. A homemade pulse generator was used to trigger the delay generator and deliver the TTL for the dc switch. A third signal from the pulse generator triggered the TDC, which recorded the arrival times of photons from the PMT relative to this trigger (Figure 6.3(a)). During the measurement time of the TDC, the rf and/or dc trapping fields could be switched off as part of the measurement sequence (Figure 6.3(b)). Measurements were taken with different confinements and timings.

---

<sup>d</sup>Analogue Devices, ADG413B

<sup>e</sup>SRS DG645

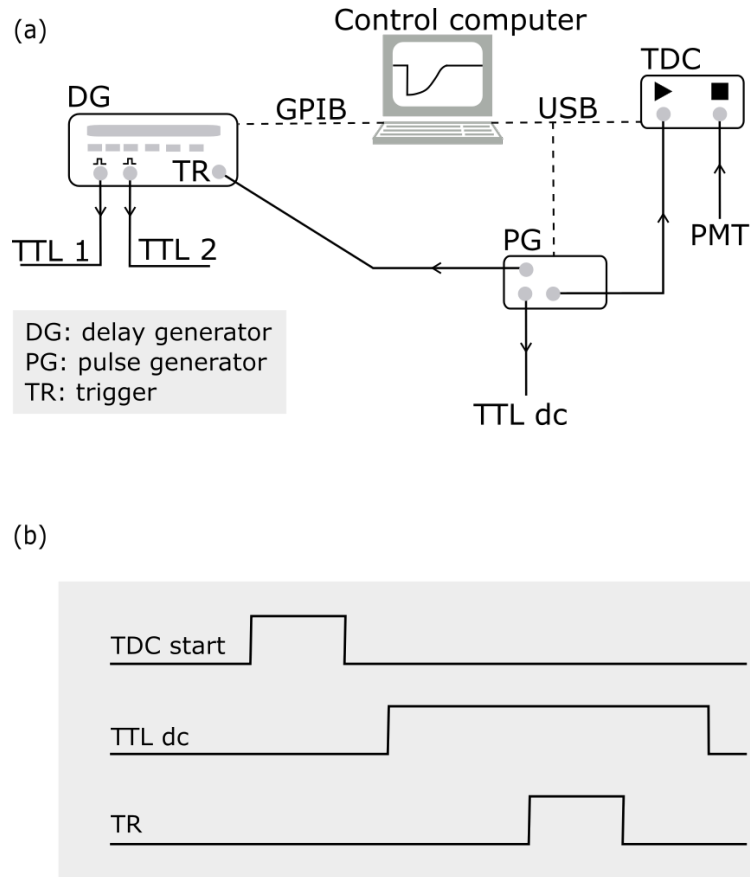


Figure 6.3: (a) The set-up used to record the ion fluorescence during switching of the trap drives. A pulse generator outputs three TTL signals: the first triggers the delay generator (SRS, DG645) used to switch the rf trap drive; the second goes to the dc switch; and the third starts the TDC measurement window. The PMT output is connected to the stop input of the TDC. (b) The pulse sequence used to record the ion fluorescence while both the rf and dc trap voltages are switched off and on again.

## 6.4 Results

The following subsections present the achievable field extinction and the effect of the rf and dc switching processes on the fluorescence of trapped ions. The rf field extinction was explored for different drive phases. The heating of the ions caused by switching the rf and dc voltages is qualified by the rate at which the original fluorescence rate is recovered after switching. The effects of the switching time, rf and dc confinements, and number of ions are explored.

### 6.4.1 rf Switching

#### Achievable Field Reduction

The reduction in the rf amplitude that can be achieved depends on several factors: the phase and amplitude of the counter drive, the switching time and the phase of the trap

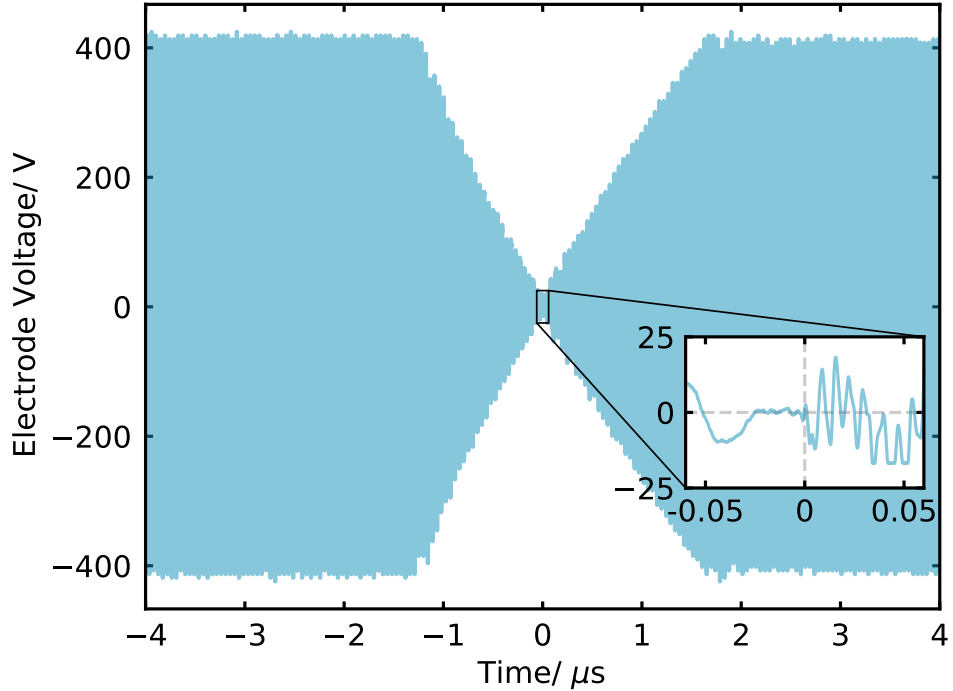


Figure 6.4: The voltage on the rf electrodes as the rf field is rapidly switched off. Inset, the minimum of the rf field during switching. The trap drive frequency is 22 MHz.

drive field when the switching starts. In the best case, a reduction in the rf amplitude by a factor of  $>1000$  was achieved (Figure 6.4). There is a high sensitivity to the phase of the counter drive; a change of just a couple of degrees from the optimal phase results in a significant decrease in the extinction of the field (Figure 6.5(a)). Additionally, a small dependence on the start phase was observed (Figure 6.5(b)). The field is most effectively extinguished when the duration of the switching is increased, although this must be balanced with the heating caused by increasing the timing (see Fig 6.7). Even for times as short as  $3 \mu\text{s}$  the field was almost completely extinguished.

Whilst switching, a higher frequency ( $\sim 120$  MHz) signal is visible after switching from the counterdrive to the high amplitude in-phase drive. This was not observed after the first switch (from the normal drive to the counter drive). It is suspected that this is caused by a resonance in the amplifier. This additional signal is greater in amplitude when switching with higher amplitude drives (compare Figure 6.5(a),(b)) and subsides after a few periods. This may cause heating by disturbing the ions when the trap field is minimised.

### Effect of Switching on the Ion Temperature

Here we present the effect of the rf switching on existing trapped ions. These data were taken with the dc electrode voltage set to 0 V, unless otherwise stated. A single ion was used for the measurements, except where the number of ions was explicitly varied. For each confinement, a full micromotion compensation was performed using the photon-correlation

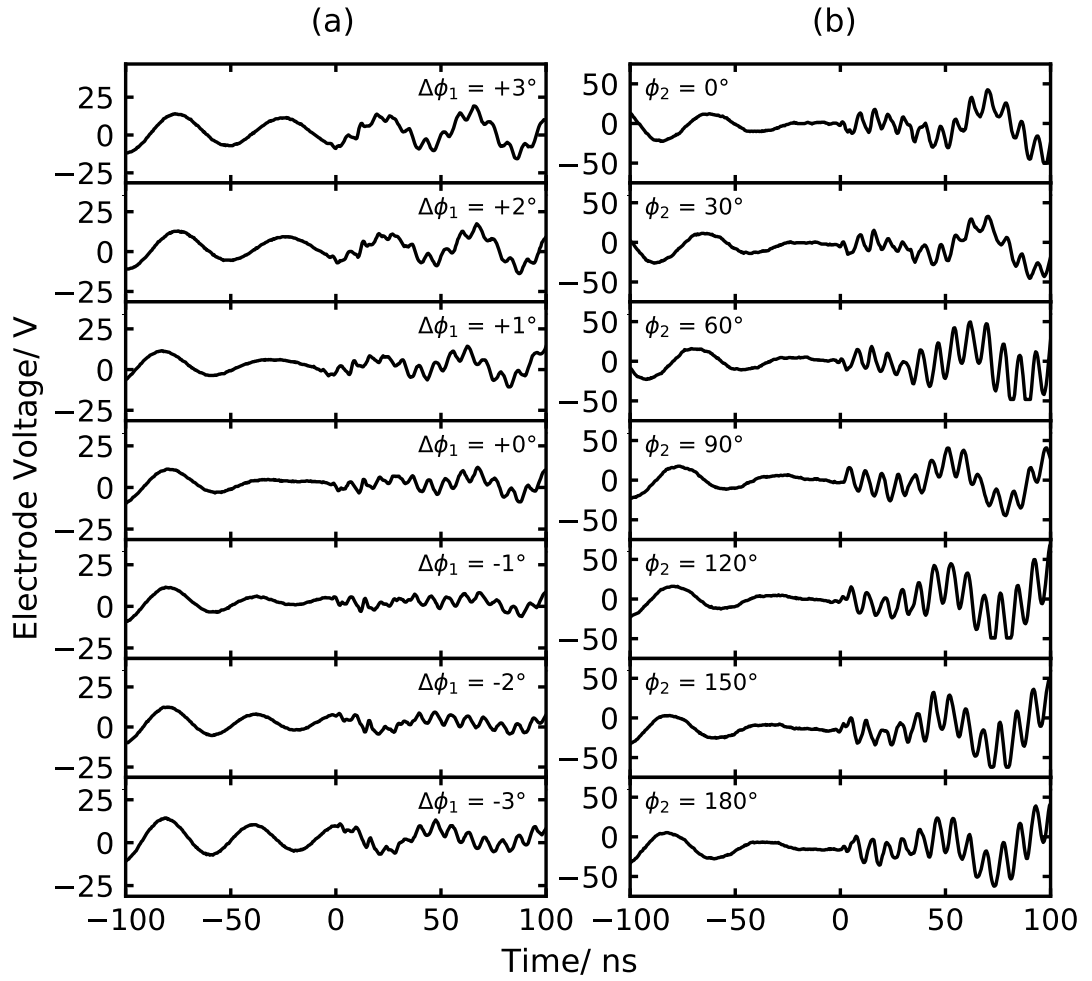


Figure 6.5: The effect of phase on the extinction of the rf electric field in the ion trap. (a) The rf electrode voltage for different phases of the counter drive,  $\phi_1$ , where a phase of  $0^\circ$  corresponds to the optimised phase. (b) The rf electrode voltage for different phases of the normal trap drive when the trap is switched,  $\phi_2$ . (The initial rf amplitude for the data in (a) was smaller than in (b).)

method (see Section 4.8).

### rf Confinement

As the rf confinement was increased from  $2\pi \cdot 500$  kHz to  $2\pi \cdot 900$  kHz, the ion fluorescence recovery time increased from 10 ms to 12 ms (Figure 6.6). Increasing the rf confinement leads to a slight increase in the heating during the switching process (for the same switching time), but this effect is small.

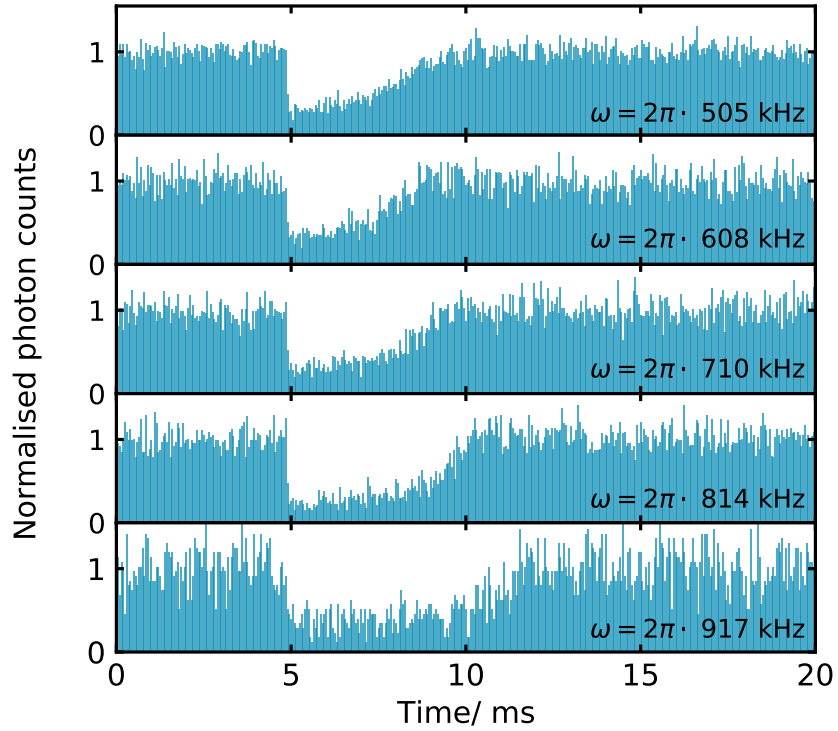


Figure 6.6: Fluorescence of a single ion as the rf trapping field is switched off for different rf confinements.

### Switching Time

Ideally, the trap would be switched off for a time that is very short compared to the period of the secular motion of the trapped ion. However, in practice, this may not be possible due to the constraints imposed by the available amplifier power. Increasing the time between the initiation of the counter drive and the recovery of the original drive amplitude results in an increase in the ion temperature (Figure 6.7). Beyond a switch-off time of  $8 \mu\text{s}$  it was not possible to retain the ions whilst switching the trap off at a rate of 1 Hz for more than a couple of switching cycles. This illustrates the flaw of the natural decay switching shown in Figure 6.1; after such times the ions would be lost. Using the shortest possible switching time within the constraints of the amplifier minimises heating and loss of ions.

It is notable that the shape of the rf decay for short switching times, dominated by the effects of the counterdrive, shows a roughly linear decrease in rf amplitude, both when switching off and back on. In contrast, the shape of the envelope of the rf signal for longer switching times resembles the natural exponential decay.

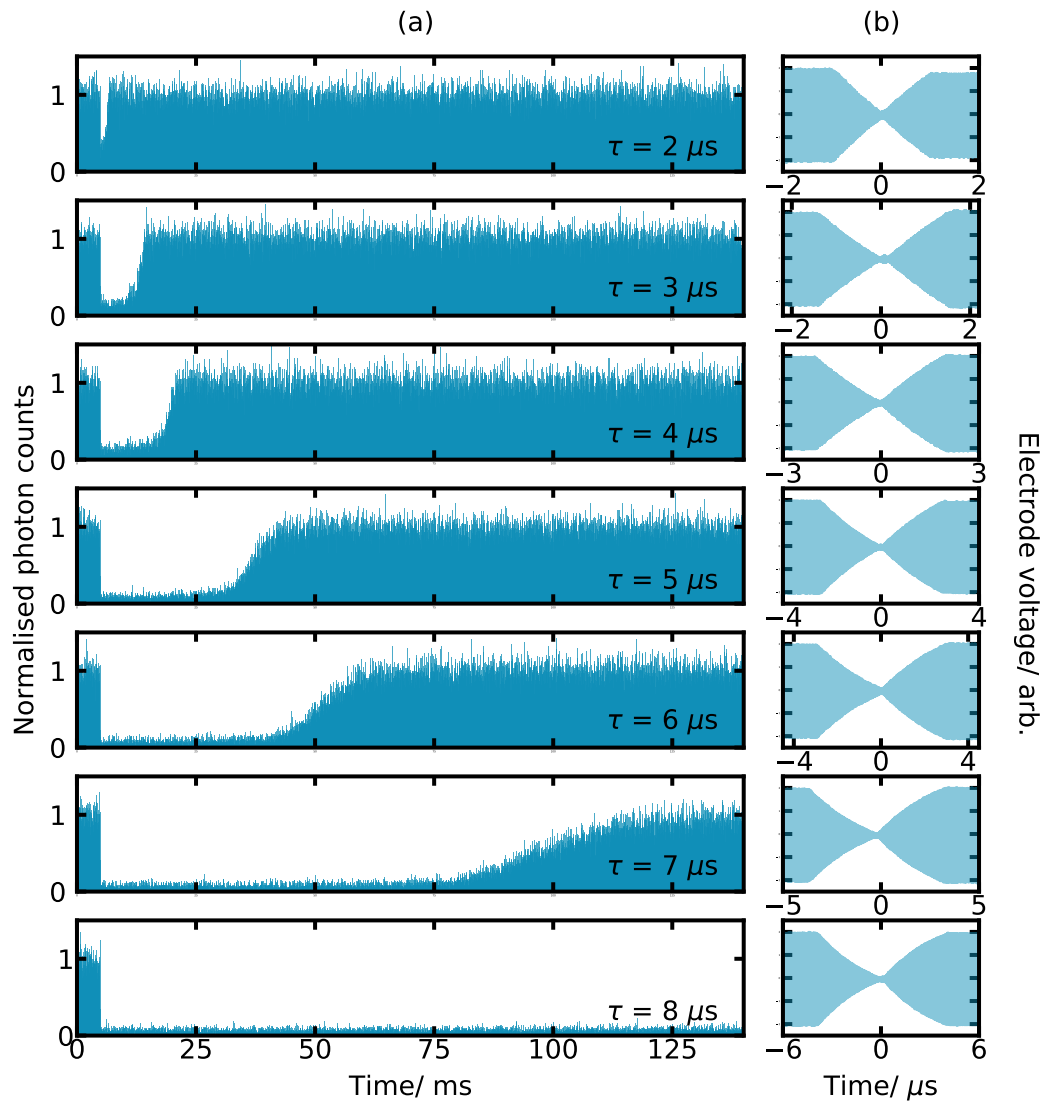


Figure 6.7: The fluorescence of a single ion as the rf trapping field was switched off for different durations of the switching sequence. (a) The fluorescence counts recorded with time as the rf field was switched after 5 ms. (b) The electrode voltage as the rf field was switched.

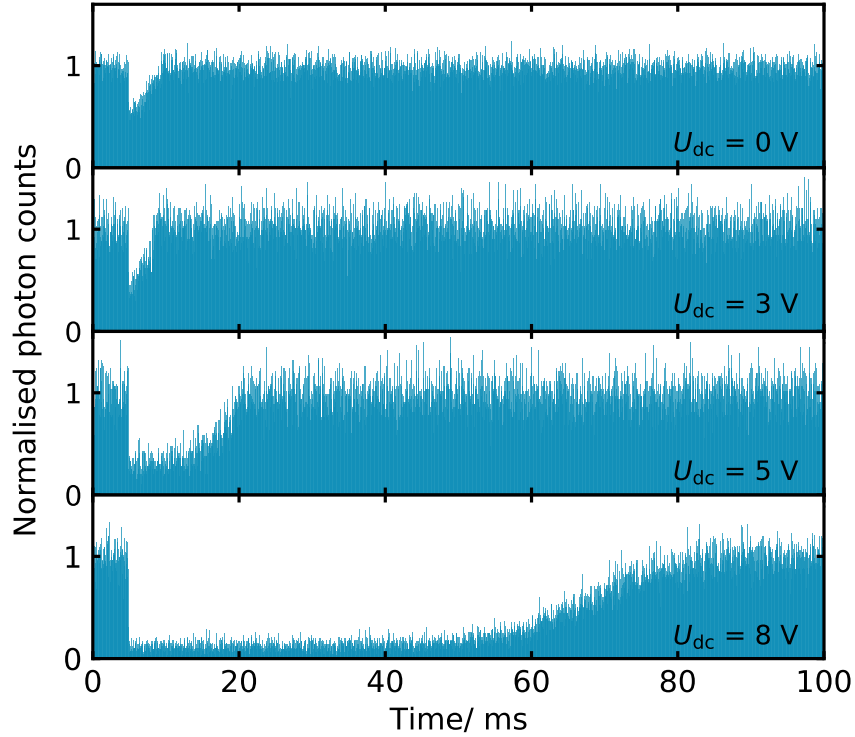


Figure 6.8: The fluorescence of a single ion after switching the rf trap drive for different dc confinements.

#### dc Confinement

Increasing the dc voltage from 0 V to 8 V increased the recovery time from a few ms to more than 80 ms (Figure 6.8). The dc field is trapping in the axial direction, but anti-trapping in the radial plane. The strong dependence of the ion heating on the original dc electrode voltage is likely to be caused by this anti-trapping field. There is an additional consideration that the micromotion compensation is performed only for the initial trapping voltage. If the rf field is switched while the dc field is maintained, the dc voltage should be minimised to reduce the heating effect experienced by the ion(s).

#### Number of Ions

The heating was found to increase slightly with the number of ions, although the difference was small (Figure 6.9). The inter-ion repulsion may increase the rate of delocalisation of the ions and consequently increase the heating. For large crystals, space-charge effects might be expected to have a significant destabilising effect. However, these data suggest that for small ion crystals of one to five ions, the consequences of increasing the ion number are not large.

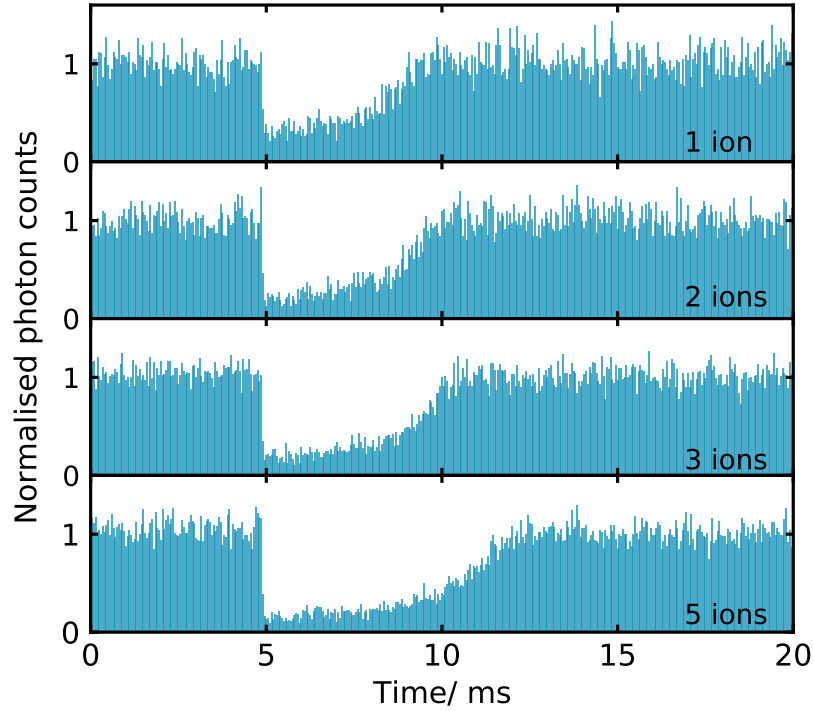


Figure 6.9: The ion fluorescence as the trap is switched off for different numbers of ions.

#### 6.4.2 dc Switching

##### Achievable Field Reduction

The dc field was switched off by a factor of more than 1000 over 20 ms (Figure 6.10). In this trap, the bias tee and low pass filter limit the rate at which the trap is switched off. This necessitates a switch-off time of at least 15 ms to achieve a reduction in the field to less than 1% of the original electrode voltage. The long switch-off time is dictated by the requirement to retain the existing trapped ions during the switch. It could potentially be reduced at the expense of ion retention and heating.

##### Effect of Switching on the Ion Temperature

Here, we examine how switching the dc electrode voltage affects existing trapped ions. These data were taken with a constant rf amplitude and a single ion was used for the measurements. For each confinement, a full micromotion compensation was performed using the photon-correlation method (see Section 4.8).

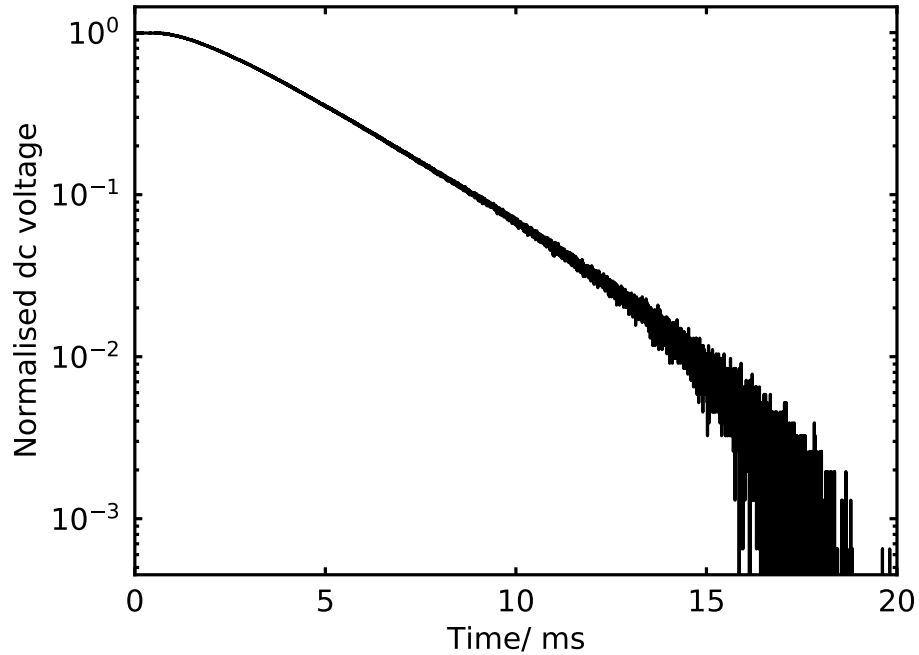


Figure 6.10: The normalised dc voltage measured at one axial electrode feedthrough while the dc field was switched off.

### Switching Time

No correlation was observed between the ion fluorescence recovery and the switching duration, provided that the same low-pass filter was used. This is because the kick experienced by the ions during switching depends only on the gradient of the voltage during switching, which is not affected by the duration for which the voltage is off. When the trapping field was switched back on, the fluorescence recovery rate was instead comparable to the recovery of the dc voltage (Figure 6.11(a),(b)). This suggests that the fluorescence recovery was limited by the rising edge of the voltage signal. This is consistent with the ion moving back to its original position as the voltage recovers. However, the initial switching edge causes a sustained loss of signal which suggests significantly greater heating is caused by the first edge. The ion position whilst the trap is off is visible to the photon detector so displacement with respect to the imaging system is not the dominant cause of the loss of signal. This is supported by the increasingly delayed onset of the recovery for different dc confinements (Figure 6.12). The movement of the ion from the centre of the rf trapping field by  $30 \mu\text{m}$  (Figure 6.11(c)) results in excess micromotion which may also contribute to heating.

### dc Confinement

The initial dc trapping voltage was varied for a fixed switch-off time of 20 ms. In the case of low trapping voltages, the ion fluorescence recovered from the kick (caused by

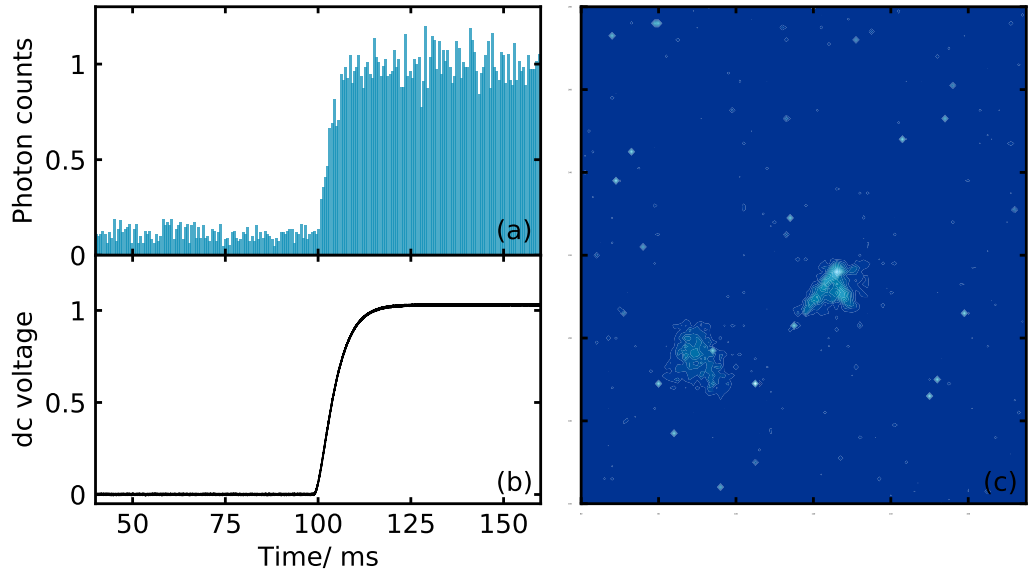


Figure 6.11: Switching of the dc voltage. (a) The recovery of the ion fluorescence rate as the dc voltage returns to its stationary value. (b) The dc voltage as it is switched back on during the switching process. (c) A false-colour CCD image shows how the ion moves between the micromotion-compensated initial position and its position when the trap is off.

the first, falling edge of the voltage) before the second, rising edge (Figure 6.12). These data were taken with the same RC filter in place; in other words, the electric field was extinguished in the same time for each initial dc voltage. In the case of higher initial axial voltages, the ion fluorescence does not appreciably recover in the switching time and there is significant heating. There appears to be a considerable change in the fluorescence recovery for trapping voltages between 6 V and 7 V. The ion fluorescence is non-linear with temperature and this change may correspond to greater delocalisation of the ion or even decrystallisation.

#### 6.4.3 Reducing dc and rf Confinement

There are two different ways that the dc electric field in our trap can be reduced to zero: the dc trap voltages can be set to zero from the start (only possible if the rf provides sufficient axial trapping); or they can start at a non-zero value and the dc voltage can be switched at the same time as the rf field. It is preferable to only switch the rf field due to the heating inherent to the fast switching of the dc voltage. This is borne out by a comparison of the heating that results from switching the rf field at 0 V dc with that from the switching of both the dc and rf fields (Figure 6.13).

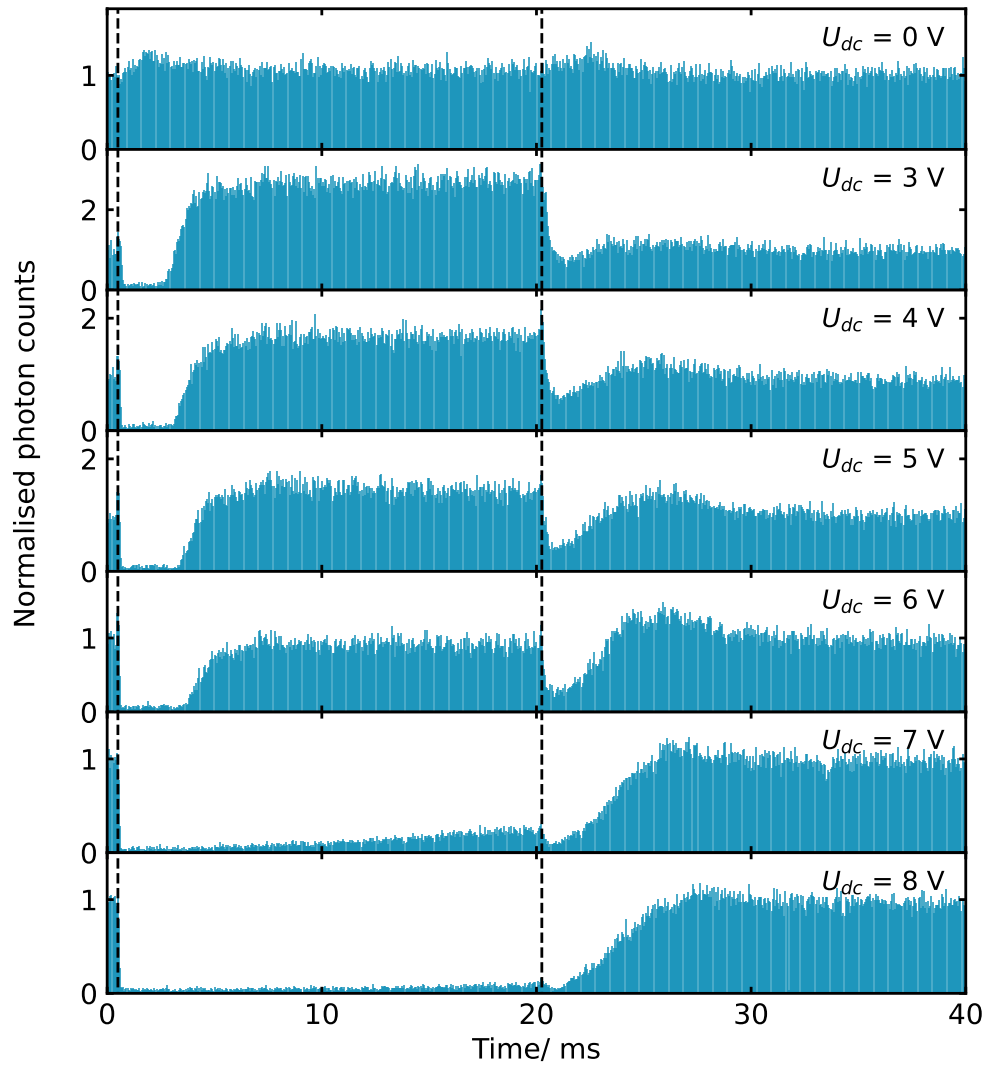


Figure 6.12: Histogram of ion fluorescence as the dc electrode voltages are switched off and on again for different dc confinements. The switch-off time was 20 ms. The start of the falling and rising edges of the dc voltage during switching are denoted by vertical dashed lines.

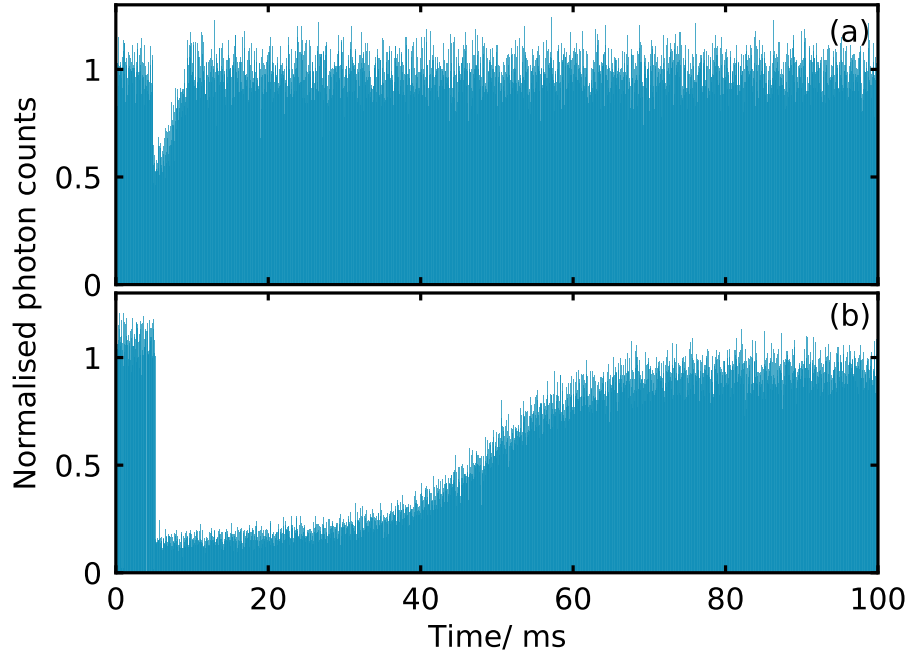


Figure 6.13: Ion fluorescence histograms while the trapping voltages are switched off. (a) The dc electrode voltage was held at ground throughout the measurement and the micromotion was fully compensated. The rf field was switched off for  $3 \mu\text{s}$ . (b) The dc confinement was initially 7 V and was switched off for 15 ms. At the minimum of the dc voltage, the rf field was switched off for  $3 \mu\text{s}$ .

## 6.5 Discussion

The rf field has been extinguished by a factor of  $>1000$ . The field can be most effectively minimised by optimising the phase of the counter-drive and the phase of the switching pulses relative to the normal rf drive (Figure 6.5). The second switching edge results in some high frequency noise, but this always occurs after the minimum amplitude of the rf field and so will not coincide with the lasers.

The dc field was reduced by a factor of  $>1000$ . The speed of the dc switching was limited by the ion heating. This heating was particularly noticeable after the first (falling) edge of the switching pulse. Retention of the ions was only possible when using long switching times ( $\sim \text{ms}$ ) in conjunction with low pass filters. Under these conditions the ion was displaced by approximately  $30 \mu\text{m}$  from the trap centre, resulting in excess micromotion. In theory, it should be possible to eliminate the dc field completely and arbitrarily fast. However, this requires the stray fields in the trap to be compensated throughout the duration of the switching pulse. If the micromotion compensation and trapping voltages do not follow the same path during the switching, the ion(s) will experience a kick. Additionally, a low pass filter is needed to prevent the voltage overshooting which would repel the ions from the trap centre. Preventing the heating of the ions is therefore technically complex and may be challenging to achieve in practice.

In the specific ion trap used, the rf field alone is enough to trap the ions in all three dimensions. Therefore, it was not possible to test the effect of switching the axial trapping field off completely for longer than the rf switching time. In another ion trap, switching the dc voltage off while retaining the ions may be unfeasible. If the dc voltages were the only trapping field along the axis, it may be impractical to find a suitable balance between the requirements for smooth switch-off and short off-time to reduce the heating effects.

It was found that the heating caused by switching the rf field was predominantly influenced by the switching time, which should be as short as possible (Figure 6.7), and the dc trapping voltage (Figure 6.8). The dc switching was shown to cause significant heating for higher confinements (Figure 6.12), but there was no apparent dependence on the switch-off time for the same low pass filter (Figure 6.11) which suggests that the heating is dependent on the rate of change of the electric field during the switch. The minimal dependence of the switching on the time that the trap is switched off is likely to be due to the trapping force from the rf field which is sufficient to prevent the ions delocalising and the consequent heating.

As the micromotion compensation voltages were not optimised as the dc field was switched off, stray fields in the trap were no longer compensated and so the true dc electric field in the trap centre was not 0 V when the electrode voltages were minimised. This persisting electric field broadens the ionisation threshold. This would have consequences for ionisation spectroscopy and state-selective loading of molecular ions. If conducting a REMPI experiment using this method, the off voltage should not be grounded, but rather set to appropriate micromotion compensation voltages for 0 V of trapping voltage.

In the context of our own experiment, the key information to extract from this data is what trapping and switching parameters are most suitable for using REMPI in a rf ion trap. There are two points of interest: the broadening of the ionisation threshold and the time taken for the nitrogen ions loaded to cool into the Coulomb crystal. This is a balance of the electric field extinction achievable and the resulting ion heating. Given the possibility to operate the ion trap with no dc trapping voltage and the significant heating caused by switching the dc field, it makes sense to operate the trap in this way. Regarding the rf field, it makes sense to operate the trap with as fast a switching time as possible without compromising on the stability of the trap.

## Chapter 7

# Experimental Loading of Nitrogen Ions

### 7.1 Introduction

In order to perform high resolution spectroscopy of molecular ions, they need to be prepared with high fidelity into a specific internal state. As a non-polar molecular ion, nitrogen cannot be pumped into the rovibronic ground state.<sup>119–123</sup> Once prepared, the state purity is not lost through interaction with the background blackbody radiation (BBR), because pure rotational transitions are electric-dipole-forbidden. This makes resonance-enhanced multiphoton ionisation (REMPI) an appropriate state preparation method. REMPI has been used to load molecular ions into rf ion traps state-selectively for some species.<sup>74–76</sup> Although photoionisation may be used to load ions into rf traps, the trapping fields can broaden and lower the ionisation threshold which may compromise the state-selectivity of the process (Chapter 5).<sup>76,111,124</sup> Field-induced shifts of the ionisation threshold must be mitigated to ensure state-selectivity in many typical trapping fields. One way to reduce the electric field while loading is to switch the trap off rapidly for the duration of the ionisation process.

The lifetime of the prepared state of the nitrogen ion is likely to be limited by inelastic collisions with background gas. The lifetime of the nitrogen ions with respect to reactions with background water molecules is expected to be on the order of a few minutes. The loading time should be much shorter than this to enable the experiment to be repeated many times without reloading. The cooling time will depend on the number of laser-cooled calcium ions trapped, the initial energy of the nitrogen molecules and whether the trap-switching method is used.

This chapter describes experiments to characterise the loading of nitrogen ions into the ion trap using electron ionisation and 2+2 REMPI in preparation for loading by state-selective 2+1' REMPI in the future. The molecular beam and synchronisation have been characterised and the desired S0 excitation transition has been observed. In addition, the switching technique (described in Chapter 6) was demonstrated to load nitrogen ions into

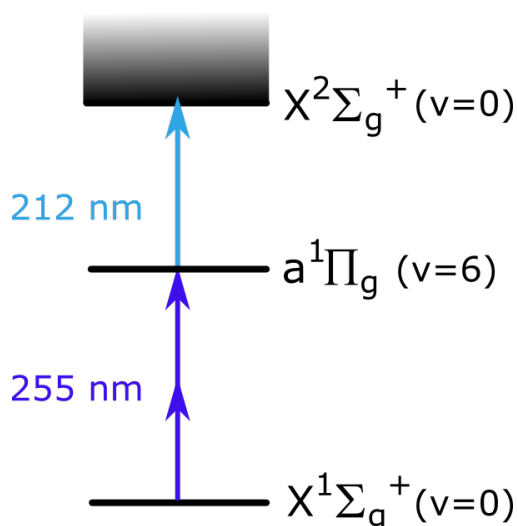


Figure 7.1: The ionisation scheme. The excitation and ionisation steps of the REMPI process from the ground state of the  $N_2$  molecule to the ground state of the  $N_2^+$  molecular ion.

the trap.

## 7.2 The 2+1' Ionisation Process

A number of REMPI schemes have been developed for  $N_2$ .<sup>73,125–127</sup> These schemes proceed via different intermediate states and with different state-selectivities. High purity of the desired state is best achieved when the photon energy for the ionisation step is different from the excitation step. This allows the second photon energy to be tuned to a chosen resonance or threshold. For a two-colour process, it is preferable for the energy change of the ionisation step to be larger than for the excitation step. This is because there is always the possibility of ionisation by the absorption of additional “excitation” photons after the excitation step. Therefore, if the energy of the second step is smaller than the energy of an excitation photon, an e.g. 2+1' process competes with a 2+1 process. This competition limits the maximum selectivity. However, if the second step is larger in energy, the 2+1' process competes with a 2+2 process instead. The probability of ionisation decreases as the number of photons required for the process increases (Equation 5.6), so the 2+2 process is less likely. The 2+1' dominates at lower laser pulse energies. For these reasons, we intend to use the 2+1' process developed by Gardner *et al.*<sup>73</sup>

This ionisation process uses photons at 255 nm for the excitation step and at 212 nm for the ionisation step (Figure 7.1). The first step is the resonant excitation of the  $X^1\Sigma_g^+(v=0) \rightarrow a^1\Pi_g(v=6)$  transition. The following step is ionisation from the  $a^1\Pi_g(v=6)$  state of the molecule to the  $X^2\Sigma_g^+(v=0)$  state of the molecular ion (Figure 7.1). This state is selected by tuning the ionisation laser to an energy above the ionisation threshold for the ground rovibronic state of the ion but below the threshold for the next accessible state. As the nitrogen molecule has a nuclear spin of  $I = 1$ , there is even-odd staggering of the

transition strengths depending on the nuclear spin state. The high precision spectroscopy requires the rotational ground state in the ion,<sup>12</sup> which can be achieved by tuning the excitation step to the S0 transition which proceeds from the rotational ground state of the neutral molecule.

As the 2+1' process competes with a 2+2 process, it should be possible to achieve a high degree of selectivity for low pulse energies. In order to prevent broadening effects due to the electric trapping fields, the REMPI lasers were aligned down the axis of the trap and the trap can be switched off during the loading.

### The S0 Transition

The state-selective 2+1' REMPI process will proceed via the S0 transition and so this is the transition of interest to us in the 2+2 spectrum. As an S-branch transition, this corresponds to a change in the rotational state of  $\Delta J = +2$ . The S0 peak in the spectrum sits next to the S11 peak. The excitation probabilities for the S0 and S11 transitions depend on the initial distribution of molecules in the  $J = 0$  and  $J = 11$  states respectively. The relative strengths of the two transition peaks will vary with the rotational temperature of the molecular beam (Figure 7.2).

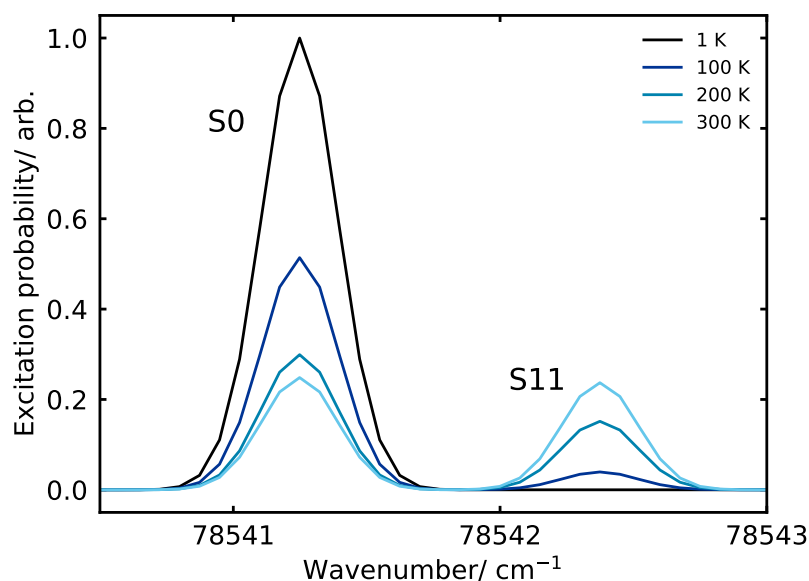


Figure 7.2: PGOPHER simulation of the S0 and S11 peaks for different rotational temperatures of  $^{14}\text{N}_2^+$ . Simulations were performed by A. Gardner.<sup>73</sup>

### 7.3 Competing Ionisation Processes

There are two likely ionisation mechanisms that may compete with the 2+1' REMPI process: impact ionisation caused by electrons liberated from the trap electrodes by the pulsed

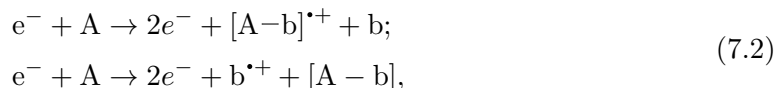
lasers; and the 2+2 ionisation process. The state-selectivity of ionisation is compromised by a combination of three factors: 1. non-REMPI ionisation processes such as electron ionisation; 2. ionisation via the competing 2+2 REMPI process; and 3. non-selective ionisation via the desired 2+1' process.

### 7.3.1 Electron Ionisation

If the laser pulse energy and the trap voltages are high, nitrogen can be loaded even when the excitation laser is detuned from any resonance. This occurs via electron ionisation (EI).<sup>128</sup> In this mechanism, electrons are accelerated from a metal surface and interact with the molecule, producing a radical cation,



where A is the molecule and  $e^{-}$  are electrons. There is also the possibility of the ionisation process being accompanied by fragmentation of the molecule,



where b is a fragment of the original molecule. This propensity for fragmentation is the reason that this method is considered a hard ionisation technique. The probability of ionisation by EI increases with the energy of the incident electrons.<sup>128</sup> In some applications, such as mass spectrometry, fragmentation patterns can be useful in distinguishing the molecule from others that have the same mass (within the resolution of the spectrometer). However, in the generation of molecular ions for precision spectroscopy, this is highly undesirable as it does not deterministically produce the target ion and there is no state-selectivity.

Despite this lack of state-selectivity, the insensitivity of this method makes it appropriate for characterisation of the set-up. Photoelectron ionisation has been demonstrated for the ionisation of molecules within a rf quadrupole mass spectrometer.<sup>129</sup> In this case, the emitted electrons are accelerated into the molecules by the rf electric field of the spectrometer. This ionisation mechanism can occur in the ion trap where the electric fields are analogous. Assuming the photon energy of the ionisation lasers exceeds the work function of the electrode surfaces, the number of electrons emitted will be proportional to the pulse energy of the laser. The probability of ionisation will also depend on the electric field strength, which dictates the kinetic energy of the accelerated electrons.

### 7.3.2 The 2+2 Process

The 2+2 process shares its excitation step with the 2+1' process. From the resulting excited state the molecule can either absorb one photon of the second colour or two

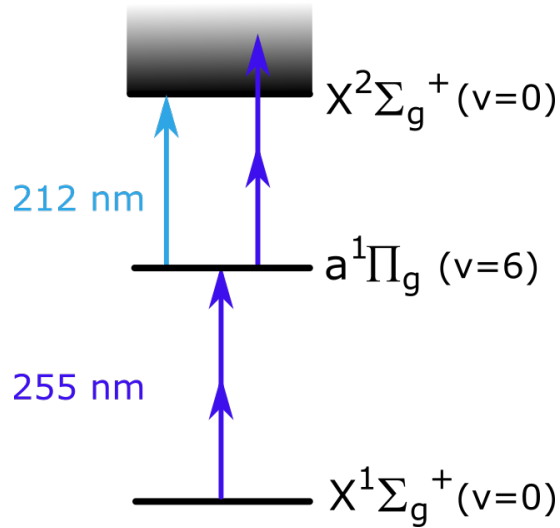


Figure 7.3: The two competing REMPI processes. Ionisation from the intermediate level can proceed by the absorption of one 212 nm photon or two 255 nm photons.

photons of the same colour as in the first step (Figure 7.3). The total energy of the four 2+2 photons exceeds the ionisation threshold considerably and so the latter of these options results in a non-state-selective ionisation of the nitrogen molecule. At low pulse energies the 2+1' process is expected to be dominant, with the state-selectivity decreasing as the pulse energy increases. This trend was observed by Gardner *et al.*<sup>73</sup>

### 7.3.3 Undesired 2+1' ionisation

The 1' photon in the final stage of the 2+1' ionisation scheme can be tuned to different energies above the ionisation threshold. In principle, this allows the ionisation process to proceed into the desired state. However, if the ionisation threshold is broadened by external fields so that transitions into neighbouring states overlap, it may not be possible to load into only one state. In this case, the desired ionisation process will compete with other pathways within the 2+1' process. The extent of the problem can be estimated by simulating the broadening of the ionisation threshold.

## 7.4 Simulated Ionisation Threshold

We consider two cases. The first is loading of the ion trap under typical operating conditions and the second is loading of the ion trap during a short period in which the electric field within the trap is minimised (as described in Chapter 6).

In this first case, where the electric field amplitude in the trap is large, the broadening is expected to be correspondingly large. For this reason, it is important to synchronise the arrival times of the ionisation lasers to the zero-crossing of the electric field. However, in these conditions the simulated broadening is still significant and would be expected to

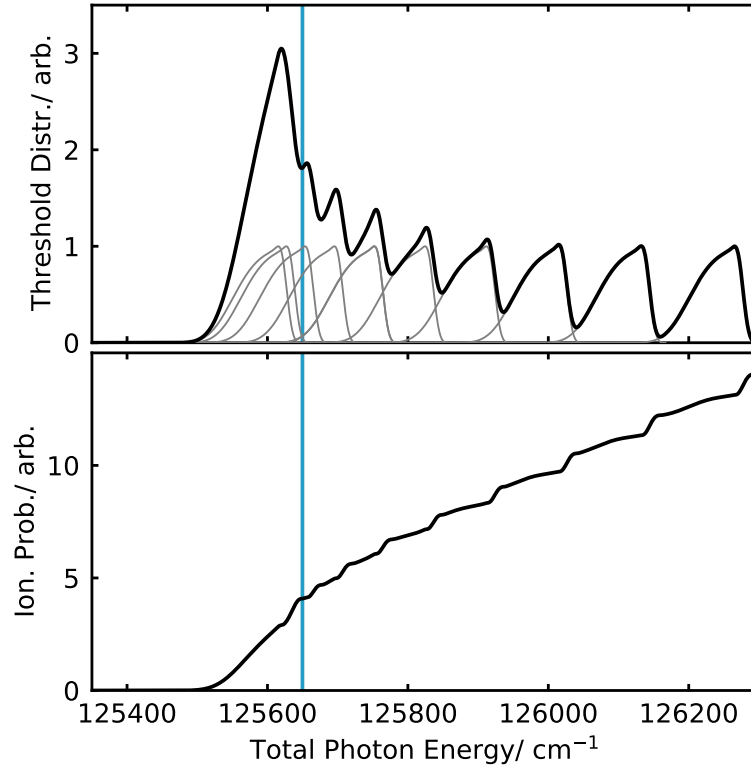


Figure 7.4: The simulated ionisation threshold for parameters corresponding to normal operation of the Paul trap. Above, the expected distribution of thresholds based on the expected broadening of ionisation threshold and the splitting of rotational levels within the ion. Below, the expected ionisation probability (neglecting the natural width of the ionisation threshold) assuming that the ionisation probability is cumulative. In both cases, the blue line represents the zero-field ionisation threshold for the  $J = 0$  state of the ion.

inhibit selective loading of the ion trap (Figure 7.4).

Next we consider the case of the dc field in the trap being switched off and the rf field being minimised. Here, we assume an attenuation of the trap field by a factor of 400. This results in clear steps in the probability of ionisation with the exception of the first two states where there is some overlap (Figure 7.5). The state we are interested in reaching is the  $J = 0$  state which is the lowest of the states and the only state where selective ionisation is possible (in the case of even staggering). Despite some overlap between the thresholds for the  $J = 0$  and  $J = 2$  states, there is minimal overlap at lower energies and high state-selectivity should be achievable.

## 7.5 Experimental Set-Up

The loading process was automated as described in Appendix B. The initial experiments were carried out using electron ionisation and 2+2 REMPI mechanisms.

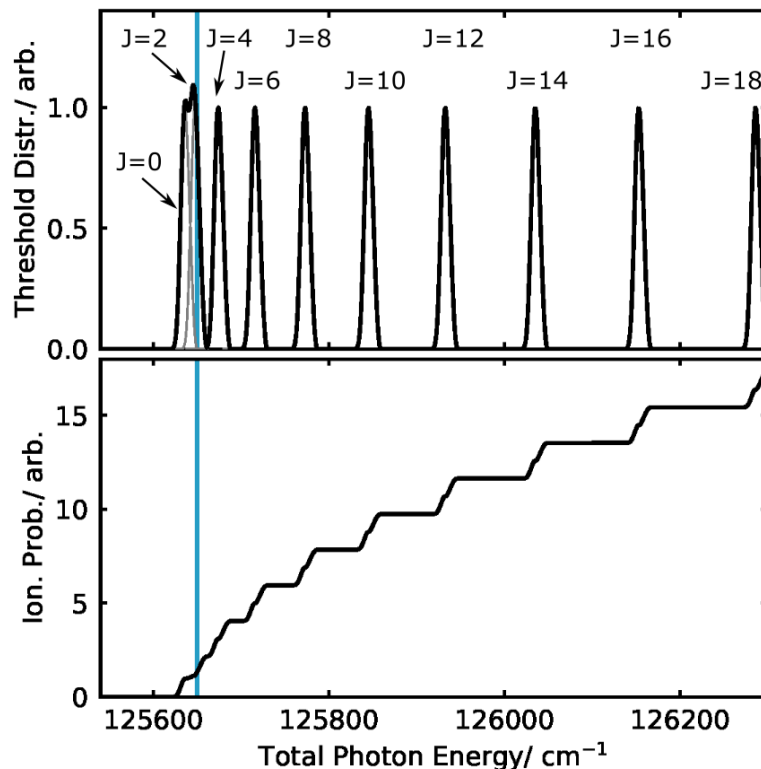


Figure 7.5: Simulated broadening of the ionisation threshold assuming a reduction in the radial electric field of a factor of 400 which has been previously achieved experimentally. Above, the expected distribution of thresholds based on the expected broadening of ionisation threshold and the splitting of rotational levels within the ion. The contributing rotational levels considered in this simulation are labelled. Below, the expected ionisation probability (neglecting the natural width of the ionisation threshold) assuming that the ionisation probability is cumulative. In both cases, the blue line represents the zero-field ionisation threshold for the  $J = 0$  state of the ion.

### 7.5.1 Ionisation Lasers

The nitrogen REMPI lasers are directed axially (Figure 7.6) and focussed into the centre of the trap in order to reduce the ionisation volume. If the ionisation lasers arrived radially, the ionisation volume would only be confined along the axis of the molecular beam by the Rayleigh lengths of the lasers. They have beam diameters of approximately  $150 \mu\text{m}$  (beam waist of  $\sim 75 \mu\text{m}$ ) at the focuses, so this would correspond to Rayleigh lengths of 6.93 mm and 8.34 mm for the 255 nm and 212 nm lasers respectively. Further details of the 255 nm laser used in these experiments can be found in Appendix C.

The lasers were aligned initially with the use of a guide beam from an alignment laser which had been pre-aligned through the trap. They were overlapped with the alignment laser using a temporary mirror to increase the path length without sending the lasers through the trap. Once the REMPI lasers were overlapped with the alignment laser, their overlap with each other was carefully checked at a position equivalent to the trap centre. They were then directed through the trap to a photodiode on the other side. (Figure 7.6).

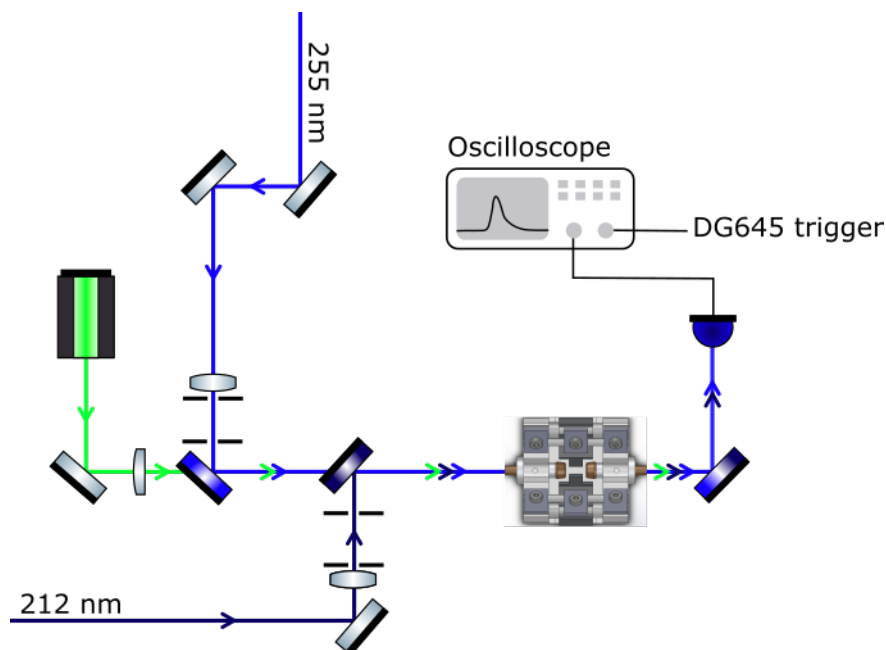


Figure 7.6: The layout of the nitrogen ionisation lasers through the trap. The two ionisation lasers are overlapped before passing through the centre of the trap. They are reflected by a dichroic mirror onto a photodiode after the trap.

To synchronise the timings of the lasers, a mirror was used to direct the lasers onto a fast photodiode<sup>a</sup> which was read out on an oscilloscope<sup>b</sup>. The dynamics of the dye laser were considered and accounted for (Appendix C). It was shown by Gardner *et al.*<sup>73</sup> that the ionisation probability does not decrease rapidly if the excitation laser arrives before the ionisation laser, due to the finite lifetime of the intermediate state and the time the molecules stay in the beam. With this in mind, the excitation laser can be set to arrive before the ionisation laser. Increasing the delay could potentially be used to tune the loading rate.

It is important to be able to control the phase of the trap drive during photoionisation to minimise inhomogeneous broadening of the ionisation threshold (Chapter 5). Additionally, as the kinetic energy of photoelectrons generated by the lasers depends on the electric field strength, the electron ionisation probability increases when the field is larger. To synchronise the lasers to the minimum of the rf field, the Q switch triggers for each of the dye lasers are synchronised to a signal from the function generator which drives the ion trap. The phase of the trap drive when the laser pulses cross the centre of the trap can be varied arbitrarily by adding an additional delay to all pulse outputs from the delay generator. The standard deviation of the delay generator trigger timing with respect to the rf drive is 0.3% of the trap drive period over the short term. There is an additional jitter of 2 ns in the laser pulse arrival times from the dye lasers.

There is a measurement delay due to the time taken for the lasers to travel from the centre of the trap to the photodiode and delays in the cables. This means that the zero-crossing

<sup>a</sup>EOT, ET-2030A

<sup>b</sup>Agilent Technologies, MSO6045A

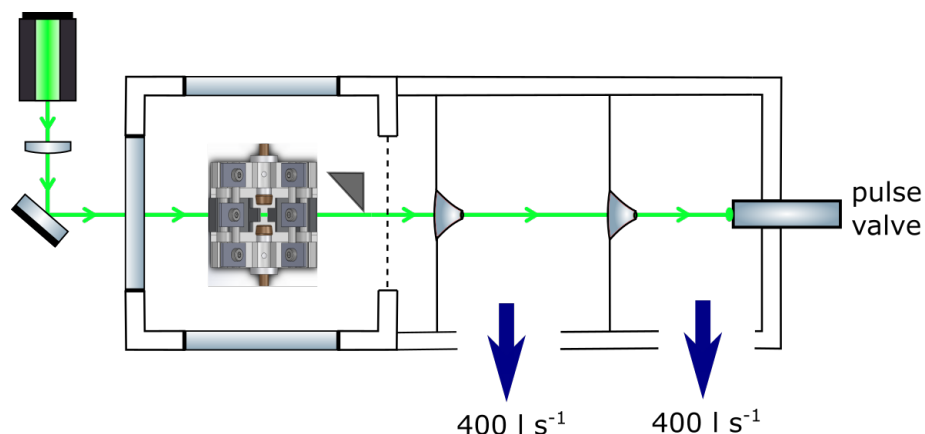


Figure 7.7: Set-up used to ensure that the pulse valve and skimmers were aligned such that the molecular beam passed through the centre of the trap. A guide laser was aligned to pass through the centre of the trap and was observed on the pulse valve.

seen on the oscilloscope does not necessarily coincide with the coincidence at the trap centre. This has been calibrated using electron ionisation.

### 7.5.2 Molecular Beam

Loading nitrogen ions from a molecular beam has advantages over loading from a homogeneous background gas (see Chapter 2). It reduces inelastic collisions that could destroy the prepared rovibronic state and result in charge-exchange reactions. The finite beam width limits the spatial extent of the ionisation region in the trap and minimises broadening of the ionisation threshold. The cooling from the supersonic expansion also maximises the number of molecules in the ground state of the REMPI process.

The molecular beamline is described in A. Gardner's thesis.<sup>3</sup> A pulse valve is opened and the resulting free jet expands into the first chamber. This jet reaches a skimmer which partially collimates the beam and the remaining gas is pumped out of the chamber. The beam then enters the second chamber and passes through a second collimation skimmer. These skimmers are aligned to ensure that the collimated beam passes through the centre of the trap (Figure 7.7).

The molecular beam had been aligned previously (see A. Gardner's thesis<sup>3</sup>). In order to check the alignment of the beamline, a low power alignment laser was shone through the centre of the trap and the skimmers. The laser dot was observed on the pulse valve to confirm there was a line of sight between the pulse valve and the path of the ionisation lasers through the centre of the trap (Figure 7.7).

Before attempting to load nitrogen ions into the trap, the molecular beam parameters were varied to achieve a clear release of gas without raising the pressure in the trap chamber beyond acceptable levels. Increases in the pressure should be avoided because the lifetime of the prepared molecular state can be lost through collisions with background gas. The collision rate between trapped ions and background gas increases with the pressure.

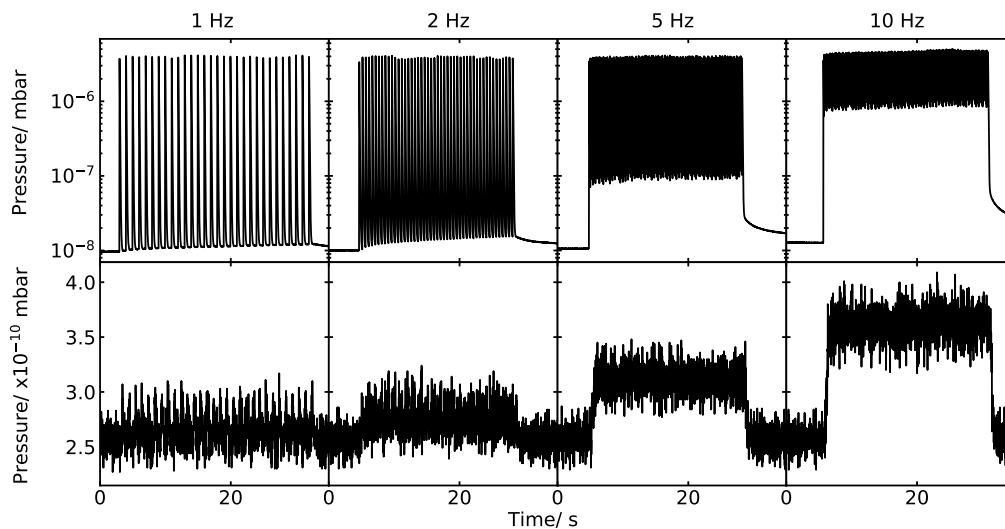


Figure 7.8: The pressure recorded in the first beam line chamber (above) and trap chamber (below) for pulse valve repetition rates of 1, 2, 5 and 10 Hz. The stagnation pressure was  $0.2 \pm 0.05$  bar above atmospheric pressure (atm).

Table 7.1: The parameters used for the molecular beamline. \*The pulse valve is controlled by a homemade unit provided by the University of Oxford which quotes the set actuation voltage in %.

Parameter	Value
Pulse valve opening time	100 $\mu$ s
Pulse valve opening voltage	18 %*
Stagnation pressure	$0.35 \pm 0.05$ bar (above atm)

The repetition rate (at which the pulse valve was triggered) was varied and the pressure was recorded in the trap chamber<sup>c</sup> and in the first chamber<sup>d</sup> of the beam line. For higher repetition rates of 5-10 Hz, the initial pressure was not recovered between shots (Figure 7.8). The final beamline parameters are shown in Table 7.1.

### 7.5.3 Pulse Energy Stabilisation

It is important to confirm that any trends we observe in the REMPI spectroscopy data are not artefacts of the scanning process but rather true physical effects. For this reason, the pulse energy of the excitation laser was stabilised to ensure the photon energy was constant across the full scanning range (Appendix C). The scan region for the excitation laser was chosen based on the experimental findings from Gardner *et al.* for the S0 transition.<sup>73</sup> The pulse energy was stabilised to ensure that the loading rate for different photon energies was not influenced by the relative pulse energies across the scan.

<sup>c</sup>Leybold, IM520

<sup>d</sup>Leybold, PTR90

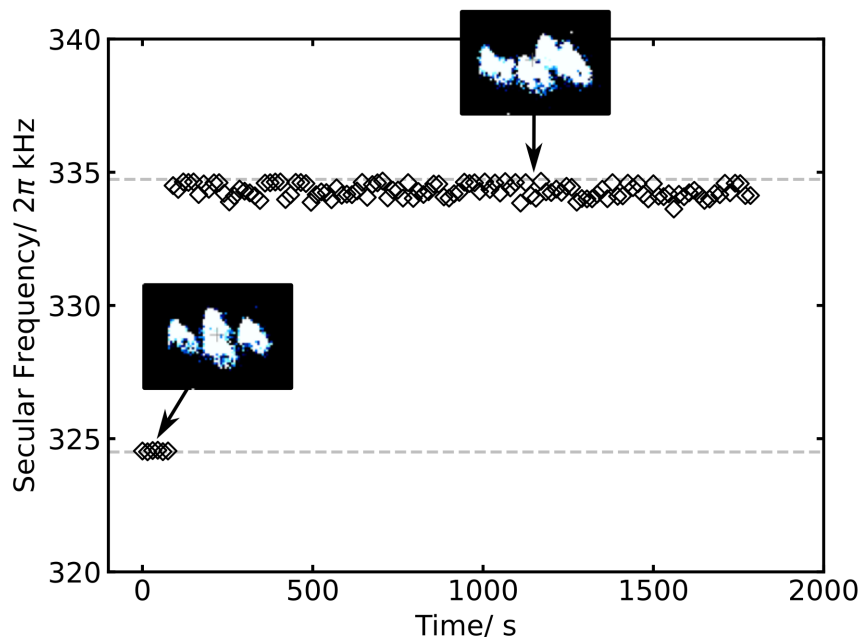


Figure 7.9: The secular frequency of the Coulomb crystal in the ion trap with time after the nitrogen ionisation lasers were fired through the trap. The dashed horizontal lines show the expected frequency shift for the arrival of one  $^{14}\text{N}_2^+$  ion into a crystal with four  $^{40}\text{Ca}^+$  ions. Superimposed images show the ion crystal for the two measured secular frequencies.

#### 7.5.4 Detection of Nitrogen Ions

Nitrogen ions do not have a cyclic transition that can be used for fluorescence collection. As a result, the nitrogen ions are dark and cannot be observed directly. Instead, their influence is observed as a distortion of the crystal structure of the bright trapped calcium ions. The nitrogen ions appear as dark ions in the crystal because only calcium ions will fluoresce under the cooling lasers in the trap.

In addition to appearing dark, nitrogen ions have a different charge-to-mass ratio to calcium ions. The two-species crystal has common motional modes and the average charge-to-mass ratio will change if nitrogen ions are loaded into a pure calcium crystal. This change in charge-to-mass ratio can be detected by crystal weighing. Ionisation of nitrogen was observed as the arrival of a dark ion and a shift in the COM frequency of the crystal (Figure 7.9).

## 7.6 Electron Ionisation Measurements

Before loading the ion trap via REMPI, the laser timings and molecular beam need to be characterised to ensure synchronisation. In the following we present the results of these characterisation measurements, conducted via electron ionisation.

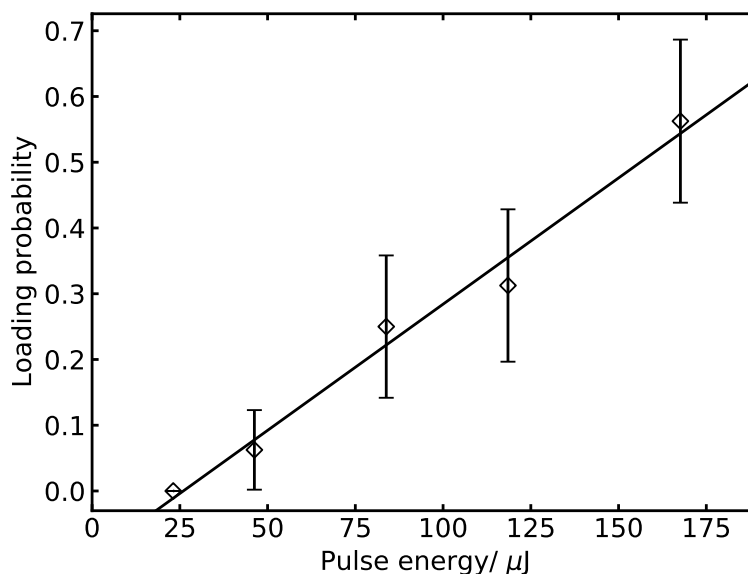


Figure 7.10: The probability of loading nitrogen ions for different pulse energies of the 255 nm excitation laser.

### 7.6.1 Effect of Pulse Energy

Using the excitation laser, the non-REMPI loading rate was measured for different pulse energies. A single shot of the 255 nm laser was fired through the trap to coincide with the molecular beam and the crystal was observed for five minutes to observe whether any dark ions arrived. The probabilities of loading were determined from the average of 16 repeats at each pulse energy.

In these measurements, there was a linear correlation between the pulse energy and the loading probability (Figure 7.10). This is consistent with ionisation caused by collisions between nitrogen molecules and electrons released from the electrode surfaces by stray light from the laser. The number of photons in each laser pulse increases linearly with the pulse energy. The photoelectron emission rate is proportional to the number of photons incident on the electrode surface. This was performed away from any of the excitation transitions to confirm that there is no REMPI contribution. It is notable that the probability of ionisation becomes negligible below a certain pulse energy. In this case, no loading was observed for a pulse energy of 25  $\mu\text{J}$ . The loading rate was observed to be highly dependent on the laser alignment.

### 7.6.2 Phase of the Trap Field

The phase of the rf trap drive when the lasers are triggered is important for two reasons: 1. to reduce the rate of the undesired electron ionisation and 2. to minimise broadening of the ionisation threshold for the desired REMPI process. The rf trap drive and laser

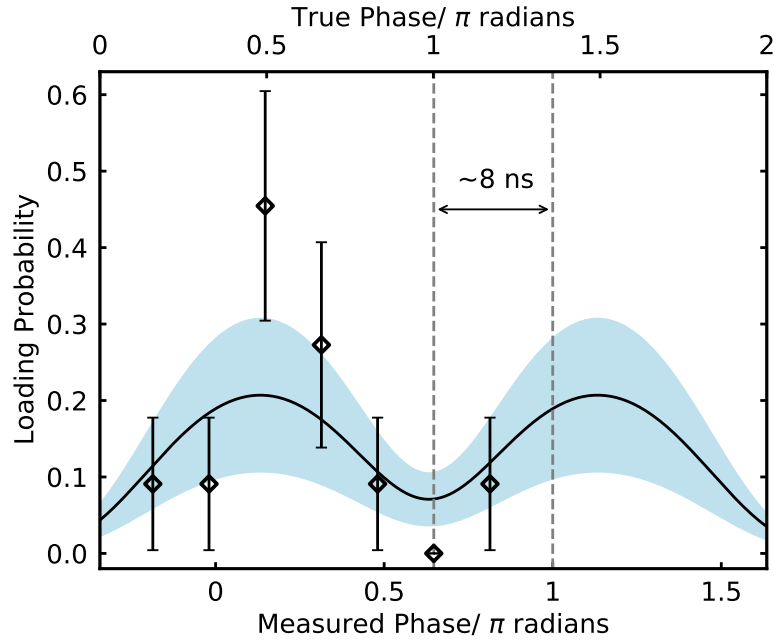


Figure 7.11: Nitrogen loading probability for different arrival times of the ionisation lasers with respect to the phase of the rf trap drive. Experimentally obtained ionisation probabilities (black diamonds) with error bars. The data are fitted with a convolution of a mod sine wave and a Gaussian of the width of the temporal profile (black line, error in pale blue).

pulses are simultaneously recorded on a fast oscilloscope<sup>e</sup> and in principle the phase of the trapping field during the pulses can be determined. However, intrinsic delays in the cables and the time taken for the light to travel from the centre of the trap to the photodiode are not accounted for in these measurements.

Determining the true phase of the trapping field when the lasers pass through the centre of the trap requires a method that is sensitive to this. One such method is to measure the rate of ions loaded for different delays of the laser pulse. The loading rate would be expected to vary with the phase as a higher electric field would correspond to greater acceleration of photoelectrons. The expected relationship would be a convolution of a  $|\sin(\phi)|$  (for phase  $\phi$ ) function with the Gaussian laser pulse. As this function repeats every  $\pi$  radians it is only possible to determine the phase relative to the zero-crossing of the electric field.

In order to characterise the delay, the 255 nm laser was triggered with different delays relative to the trap drive zero-crossing. The measured ionisation probabilities were consistent with the expected trend (Figure 7.11). There was an intrinsic delay of approximately 8 ns between the oscilloscope reading of the field zero-crossing and the delay corresponding to the minimum loading rate. This delay corresponds to a  $\sim 2.5$  m path length difference in the set-up.

<sup>e</sup>Agilent Technologies, MSO6054A

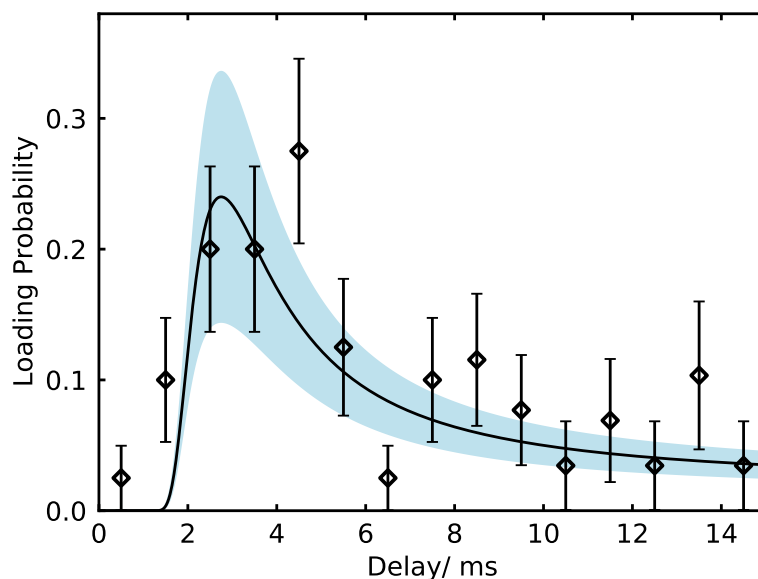


Figure 7.12: The loading probability for different delays of the laser pulse from the opening of the pulse valve.

### 7.6.3 Molecular Beam Temporal Profile

Knowing the temporal profile of the molecular beam is important to ensure the ionisation laser pulses arrive in coincidence with the molecular beam pulse. Additionally, it is desirable to ionise in the tail of the molecular beam rather than at its onset to reduce the probability of inelastic collisions that could destroy the prepared state. The molecular beam was therefore characterised before the subsequent REMPI measurements were taken.

The delay between the pulse valve firing and the laser pulse arrivals was scanned. The temporal profile of the molecular beam was determined from the loading probability (Figure 7.12). The result was fitted assuming a Maxwell-Boltzmann velocity distribution to extract a peak arrival time of 3.2 ms. The fitted distribution corresponds to a translational temperature of  $100 \pm 10$  K along the beam axis. The velocity of the beam for a delay of 3.2 ms is  $\sim 310 \text{ m s}^{-1}$ .

## 7.7 2+2 REMPI Measurements

The photon energy of the excitation laser at 255 nm was scanned over the S0 and S11 resonances and the probability of loading nitrogen ions into the trap was recorded. The axial dc electrode voltage was set to 0 V and the radial rf field was switched off rapidly using the method described in Chapter 6 (Figure 7.13).

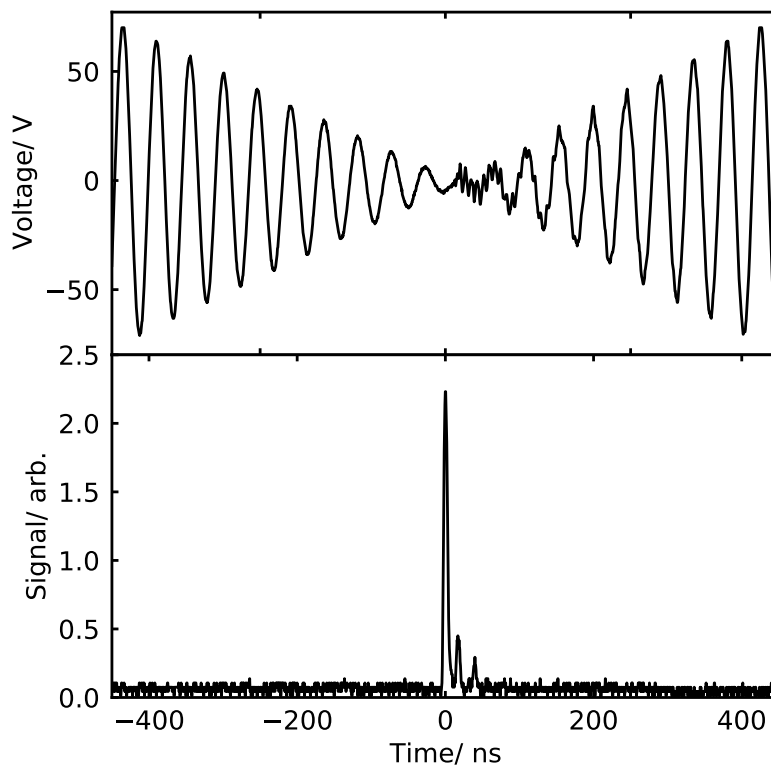


Figure 7.13: The laser pulse is timed to the minimum of the electric field. Above, the electrode voltage on the rf electrodes. Below, the laser pulse measured using the photodiode in Figure 7.13

### 7.7.1 The S0 Transition

The photon energy of the excitation laser at 255 nm was scanned over the S0 and S11 resonances and the probability of loading nitrogen ions into the trap was recorded (Figure 7.14). The splitting between the two transitions was fixed to  $1.1 \text{ cm}^{-1}$  which was measured by Gardner *et al.*<sup>73</sup> The rotational temperature of the molecular beam was determined from this to be  $139^{+54}_{-41} \text{ K}$ . The initial temperature of the gas in the reservoir is approximately 297 K and so this corresponds to some cooling of the rotational states. The linewidth of the S0 peak was measured to be  $0.33 \pm 0.05 \text{ cm}^{-1}$ . The measured shot-to-shot variation of the dye laser fundamental was approximately  $\pm 0.03 \text{ cm}^{-1}$ . Accounting for the inhomogeneous broadening mechanism, considering that the fundamental is frequency-doubled and the excitation step is a two-photon process, the expected linewidth of the laser is approximately  $\pm 0.12 \text{ cm}^{-1}$ . The measured transition linewidth is likely to be limited by the laser linewidth, rather than the mixing between the intermediate and continuum states caused by the photons for the ionisation step.

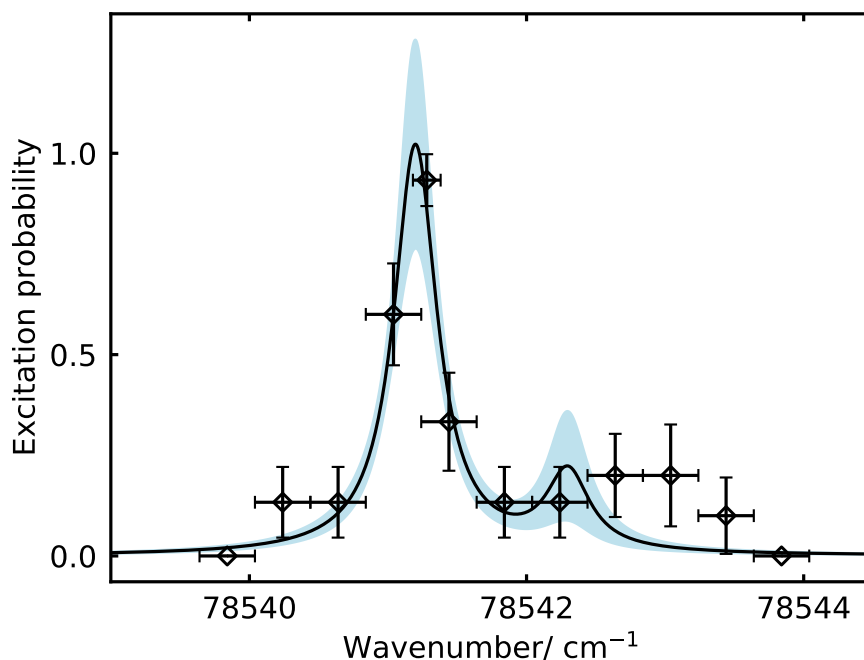


Figure 7.14: Scan of the S0 and S11 peaks in the excitation spectrum, obtained by 2+2 REMPI. Lorentzians are fitted to the data. The wavenumbers refer to the energy of the two 255 nm photons for the excitation step of the 2+2 ionisation process.

### 7.7.2 Ion Cooling Rates

The reactive lifetime of nitrogen ions in the trap is expected to be on the order of minutes and the experiment will need to be repeated many times. For these reasons, the loading time for nitrogen should be as short as possible. The 2+2 data was analysed to extract a mean arrival time of  $80 \pm 10$  s (Figure 7.15). The data suggest that the nitrogen ion arrives in less than 60 s approximately 50 % of the time. Crystal weighing data taken at the end of each loading attempt (after 5 minutes) showed that reactions of nitrogen ions with water were common within the measurement window. The background pressure in the trap is  $1 \times 10^{-10}$  mbar.

## 7.8 Discussion

The ionisation set-up has been characterised using electron ionisation to map out the temporal profile of the molecular beam. This yielded an arrival delay of approximately 3.2 ms with an estimated translational temperature of 100 K. From the relative excitation probabilities of the S0 and S11 peaks, the rotational temperature of the beam was measured to be  $139^{+54}_{-41}$  K. This is consistent with the measured translational temperature. The temperature of the laboratory is 297 K and so this demonstrates some cooling in the molecular beam. Nitrogen ions have been loaded into the trap via 2+2 REMPI whilst the

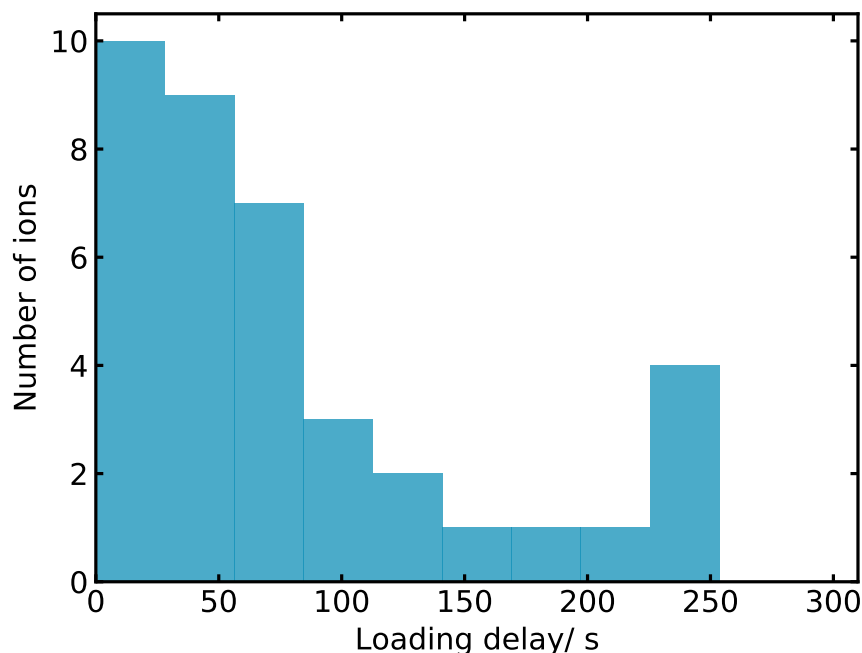


Figure 7.15: Histogram of arrival times for nitrogen ions loaded by 2+2 REMPI. Loading delay is the time taken for the ion to crystallise, measured from the time the laser pulse is triggered.

trap was switched using the technique described in Chapter 6. The 2+2 REMPI mechanism was confirmed by a scan over the  $S_0$  and neighbouring  $S_{11}$  peaks in the excitation spectrum. This showed a clear  $S_0$  resonance as the photon energy was scanned over the peak. Additionally, the ionisation mechanism was confirmed as REMPI by the absence of a trapping electric field while the laser passed through the trap, which eliminated the electron ionisation mechanism.

The cooling dynamics have not been fully investigated, but preliminary results suggest mean cooling times of more than a minute when using the trap switching technique with small ion crystals. Equivalent measurements have not been made in the absence of the switching technique so it is not possible to draw conclusions about the effect this is having on the cooling time. However, the newly trapped nitrogen ion's energy (as a high-velocity ion in a strong electric field) is likely to be the dominant source of thermal energy requiring cooling. In the future, it will be necessary to explore the effect of the trapping parameters on the sympathetic cooling dynamics to reduce the loading time. It may also be necessary to take steps to reduce the reaction rate by further reducing the pressure in the chamber.

## Chapter 8

# Quadrupole Spectroscopy of Calcium Ions

### 8.1 Introduction

Spectroscopy of nitrogen ions requires the use of an auxiliary ion for state read-out and cooling. The nitrogen transition frequency must also be compared to another reference transition that is not sensitive to the proton-to-electron mass ratio. In the intended experiment, the calcium will act as a frequency reference and be used for ground state cooling and state read-out of the nitrogen ion. These three roles all involve the use of a quadrupole transition from the  $S_{1/2}$  to  $D_{5/2}$  state of  $^{40}\text{Ca}^+$ . It is therefore necessary to characterise the transition.

The quadrupole spectroscopy discussed in this chapter has been performed before (e.g. <sup>130,131</sup>), and much narrower linewidths have been achieved. It is included here because it had not previously been attempted in this group and because it is a critical step towards realising our experiment. The data in this chapter were taken using a different ion trap set-up compared to the rest of the experiments described in the thesis.

### 8.2 The $S_{1/2} \rightarrow D_{5/2}$ Transition

The  $S_{1/2} \rightarrow D_{5/2}$  transition is electric-dipole forbidden. That is, it involves a change in orbital angular momentum of two quanta in contrast to the dipole selection rule  $\Delta l = \pm 1$ . The decay process is very weak and the lifetime of the D state is  $\sim 1.2$  s.<sup>132</sup> It is referred to as metastable, as decay over typical timescales for atomic processes is negligible. The natural linewidth of the transition of interest is 0.2 Hz.<sup>133</sup> This narrowness makes it suitable for use as a frequency standard; as such, it is often referred to as a “clock” transition.

For the quadrupole transition we consider, the change in orbital angular momentum is  $\Delta l = 2$ . The selection rule for the magnetic quantum number  $m_j$  is then  $\Delta m_j = 0, \pm 1, \pm 2$ .

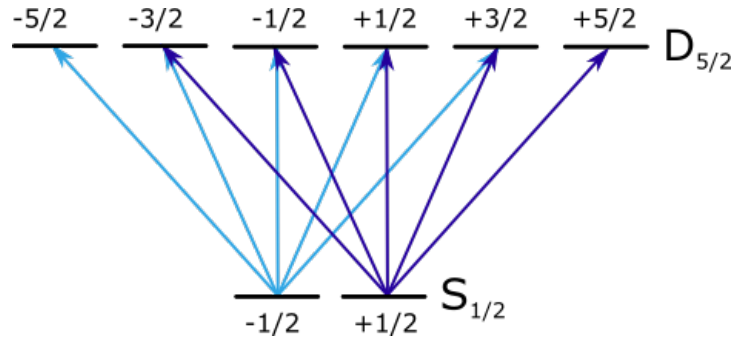


Figure 8.1: The ten possible transitions from the  $S_{1/2}$  state to the  $D_{5/2}$  state. Arrows show transitions corresponding to  $\Delta m_j = 0, \pm 1, \pm 2$ .

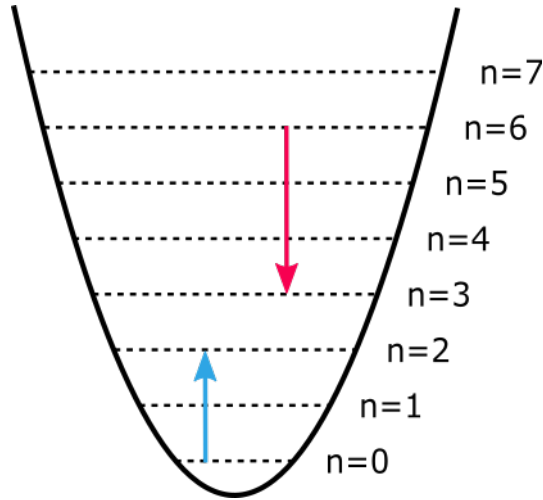


Figure 8.2: Harmonic potential with energy levels  $E_n = \hbar\omega(n + 1/2)$ . The red arrow shows one of the motional transitions that contributes to the third red sideband, i.e. it corresponds to  $\Delta n = -3$ . The blue arrow shows one of the motional transitions that contributes to the second blue sideband, i.e. it corresponds to  $\Delta n = +2$ .

Consequently, there are 10 transitions between the  $S_{1/2}$  (multiplicity 2) and  $D_{5/2}$  (multiplicity 6) states (Figure 8.1). In the absence of an external field, these transitions occur at the same frequency. However, as the magnetic field increases, the energy levels separate due to the Zeeman effect and individual peaks can be resolved for each of the ten transitions.

In addition to electronic energy levels, the trapped calcium ion has motional energy levels. In the case of the Doppler cooling transition, the natural linewidth is much larger than the motional energy level separation and the Doppler effect causes broadening. In contrast, the narrowness of the quadrupole transitions means that the individual motional transitions appear as sidebands alongside the carrier band. Each sideband corresponds to a transition in which integer numbers of motional quanta (or phonons) are absorbed or emitted by the atom (Figure 8.2).

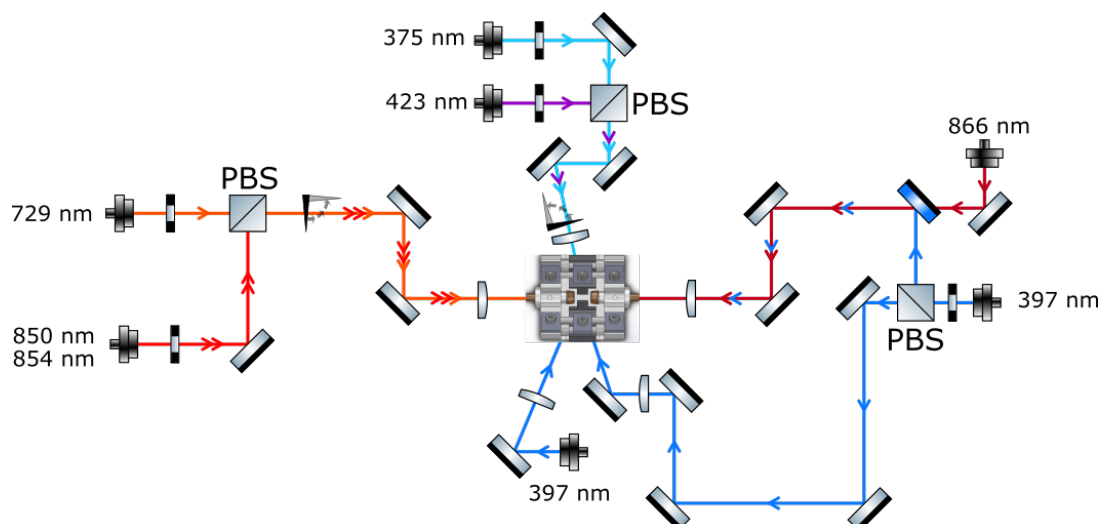


Figure 8.3: Layout of optics around the ion trap used for quadrupole spectroscopy of calcium ions.

## 8.3 Experimental Set-Up and Methods

### 8.3.1 The Trap and Lasers

The calcium quadrupole spectroscopy was done in a different ion trap from the rest of the results presented in this thesis. The ion trap used for these experiments is described in K. Sheridan's thesis.<sup>134</sup> The 729 nm spectroscopy laser and magnetic field were directed along the axis of the trap (Figure 8.3). The imaging system consisted of a 10x lens<sup>a</sup> with a 90:10 beamsplitter to share light between a CCD camera<sup>b</sup> and PMT<sup>c</sup>.

### 8.3.2 Spectroscopy Sequence

The spectroscopy sequence was repeated many times. This sequence consisted of four main sections: Doppler cooling of the ion for 100  $\mu$ s; state preparation to ensure the ion was in the  $S_{1/2}$  state; probing with the spectroscopy laser; and detection of the ion's state. Short 2  $\mu$ s waits were integrated to ensure the lasers from the previous stage were completely off (Figure 8.4). The lasers were switched off by sending TTL pulses to the oscillators which controlled the acousto-optical modulators (AOMs) in the paths of each laser. In order to scan the frequency of the 729 nm laser, a double-pass AOM was used to shift the frequency of the laser by approximately 400 MHz. The sequence was repeated 255 times and, based on a fluorescence count threshold, success (1) or failure (0) was assigned to each attempt. A mean of these repeats was taken for each scan frequency and used as the probability of excitation.

<sup>a</sup>Nikon 10x, 24812

<sup>b</sup>Andor, Luca

<sup>c</sup>Hamamatsu, H7360-02

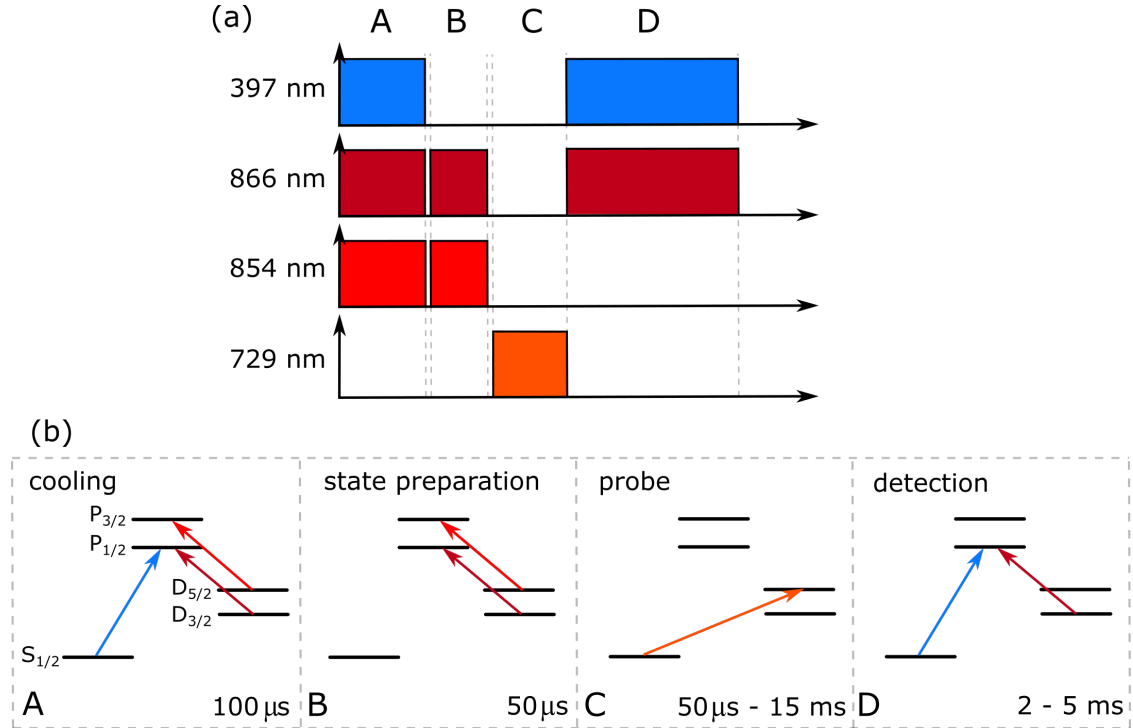


Figure 8.4: The sequence used to perform quadrupole spectroscopy of a single trapped calcium ion. Initially the ion is laser cooled using the transition at 397 nm. This is followed by a period of state preparation using the repumping lasers to ensure the ion is in one of the  $S_{1/2}$  states. Once the ion is in the desired state, a pulse at 729 nm excites the quadrupole transition. After this pulse is concluded, the cooling lasers are used to detect the state of the ion. (a) The sequence of laser pulses. (b) The four stages of the spectroscopy sequence.

### 8.3.3 Coherent Population Trapping in the Calcium $\Lambda$ System

The energy levels of the  $\text{Ca}^+$  ion form a double- $\Lambda$  system. During the Doppler cooling cycle, the population is excited from the  $S_{1/2}$  state to the  $P_{1/2}$  state, where the most probable decay pathway is back to the  $S_{1/2}$  state. The  $P_{1/2}$  state can also decay into the  $D_{3/2}$  state. If the 850 nm and 854 nm lasers are used as repumpers, the population in the D states returns to the  $S_{1/2}$  state via the  $P_{3/2}$  state, which can also decay into both the  $D_{3/2}$  and  $D_{5/2}$  states.

In the experiments described in the previous chapters, lasers at 850 nm and 854 nm were used to repump the ion out of the D states during laser cooling. However, in this experiment, the detection mechanism relies on being able to distinguish between the case where the ion is in the light  $S_{1/2}$  state and the dark  $D_{5/2}$  state. For this reason, the system was repumped with the 866 nm laser so that the Doppler cooling cycle was independent of the  $D_{5/2}$  state.

When repumping with the 866 nm laser, the population can become trapped in the  $D_{3/2}$  state. Figure 8.5 shows the possible  $\sigma^+$ ,  $\pi$  and  $\sigma^-$  transitions from the  $D_{3/2}$  state to the  $P_{1/2}$  state of the  $\Lambda$  system. In the absence of a magnetic field, the laser fields can drive

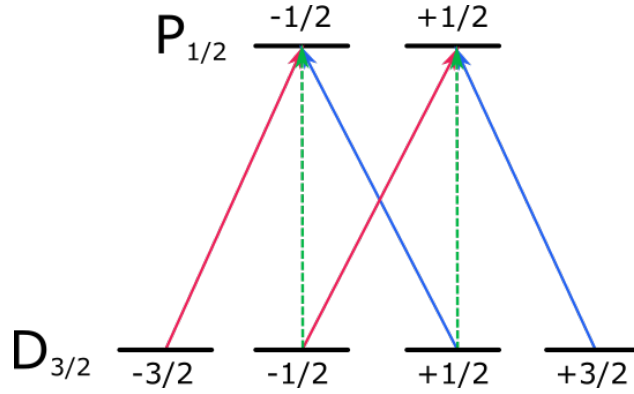


Figure 8.5: The Zeeman sub-levels of the  $D_{3/2}$  and  $P_{1/2}$  states at zero magnetic field, and the possible transitions between them. These transitions are excited by  $\sigma^+$  (red, solid),  $\pi$  (green, dashed) and  $\sigma^-$  (blue, solid) polarised light, corresponding to  $\Delta m_J = +1, 0, -1$  transitions respectively.

the atom into a superposition of the  $D_{3/2}$  Zeeman sublevels. The probability of excitation into the one of the  $P_{1/2}$  states is given by the sum of the excitation probabilities from the states in the superposition. For any constant polarisation of the 866 nm light, there is destructive quantum interference between these different excitation pathways which prevents excitation to the  $P_{1/2}$  state. The consequence of this coherent population trapping (CPT) is that the population becomes trapped in the dark  $D_{3/2}$  state, preventing Doppler cooling and fluorescence imaging and detection. The dark state does not evolve so it remains dark.<sup>135–137</sup>

There are two effective and commonly implemented ways to destabilise these dark states: splitting the energy levels, usually by applying a magnetic field; and modulating the polarisation of the repumping laser.<sup>137,138</sup> At magnetic fields on the order of the Earth’s magnetic field, the dark states are effectively destabilised. Approaching zero magnetic field at the position of the ion, the fluorescence rate drops as the population becomes trapped. Scanning the magnetic field shows a dip in fluorescence close to zero field, referred to as a Hanle dip.<sup>139</sup> To prevent CPT when working at low magnetic fields, an electro-optic modulator (EOM) was used as a variable waveplate to modulate the polarisation of the 866 nm laser at  $>10$  MHz. The result of this polarisation modulation can be seen from Hanle dip measurements (Figure 8.6).

### 8.3.4 Magnetic Field Compensation

Due to the sensitivity of the sub-levels to magnetic fields, a very stable and well-controlled magnetic field is needed. This requires a method of control over the magnetic field in the trap. For this purpose, six coils are placed around the trap in pairs (Helmholtz configuration) along each of three perpendicular axes, one of which is collinear with the trap axis. The current passed through each coil is controlled, allowing the magnetic field to be compensated and set to a chosen value. At present, only slow drifts in the magnetic field have been compensated using Hanle dip measurements. Fast variations in

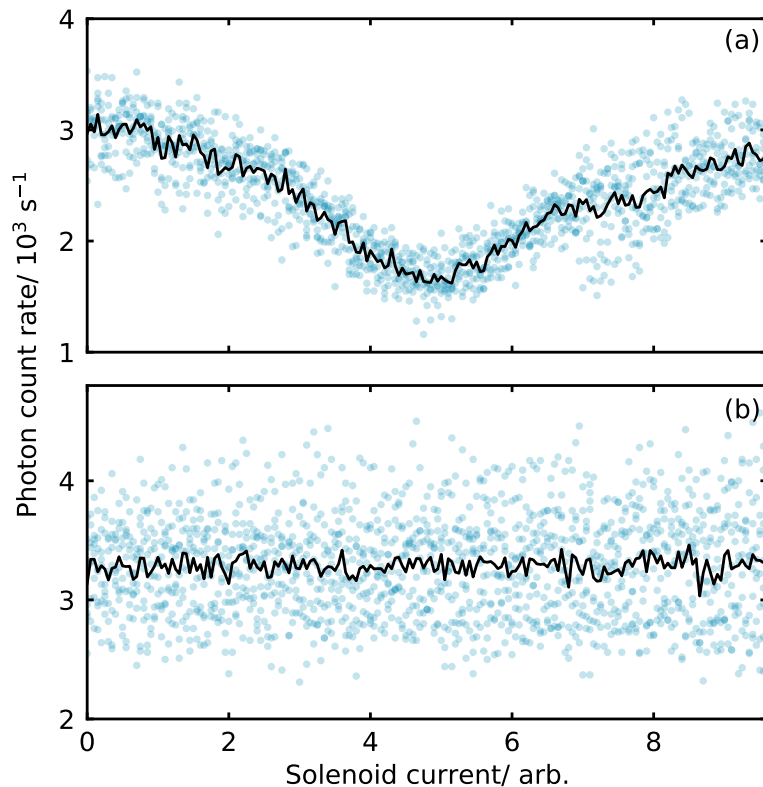


Figure 8.6: Hanle dip measurements taken for no modulation of the 866 nm laser polarisation (a), and with polarisation modulation at 10 MHz applied using an EOM. (b) In each case the blue scattered points are data collected during multiple scans and the black lines are a simple mean of the scans.

the magnetic field, such as due to mains electrical fields have not been compensated at this stage. The current corresponding to zero magnetic field in each of the three dimensions was determined using Hanle dip measurements.<sup>139</sup>

The Hanle dip measurement exploits CPT and the destabilising effect of magnetic fields. The current supplied to the pair of coils is scanned (scanning the magnetic field experienced by the ion) and the fluoresced photons are counted. As the minimum magnetic field is approached, the dark states are no longer effectively destabilised and the fluorescence rate drops. The current at which there is a minimum in photon counts corresponds to zero magnetic field.

During the spectroscopic measurements presented here, the magnetic field in the  $x$  and  $y$  directions (the radial directions) was held at zero while the magnetic field in the  $z$  direction was varied to observe the ten separate transitions associated with the  $S_{1/2} \rightarrow D_{5/2}$  transition. Once the field was minimised based on the Hanle dip measurements, the field was reduced until a single peak was observed in the spectrum (instead of the ten component peaks) and the linewidth of this peak was minimised. The values obtained from this minimisation were used to calibrate zero-field.

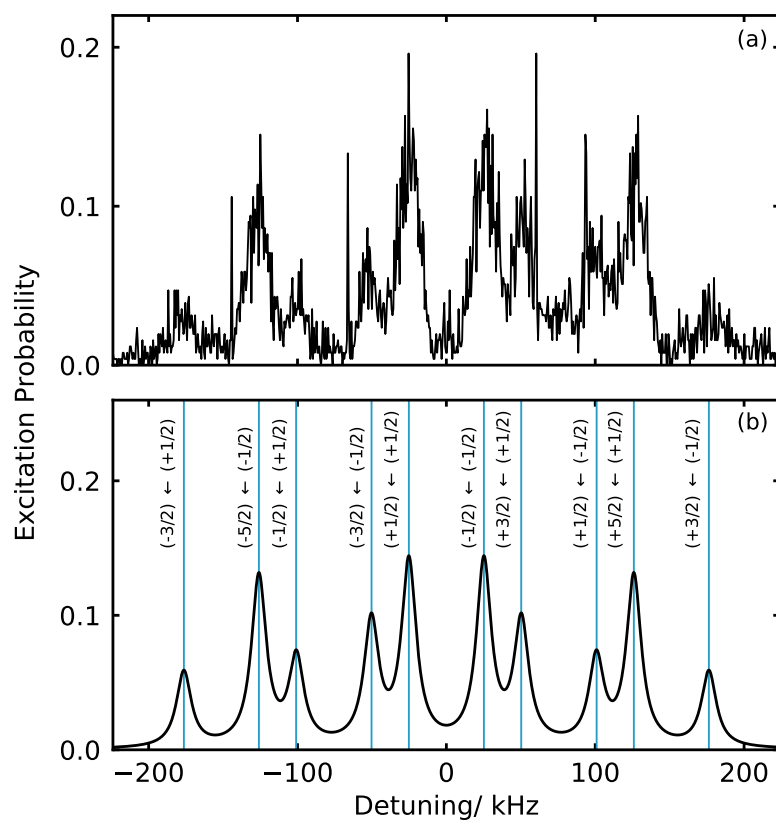


Figure 8.7: A spectrum showing the ten peaks corresponding to the ten  $D_{5/2} \leftarrow S_{1/2}$  transitions with  $\Delta m_J = 0, \pm 1, \pm 2$ . Above, an example experimental spectrum. Below, a simulated spectrum with a magnetic field of 45 mG and linewidths of 12 kHz by fitting to these data using the simulation described in Appendix D.

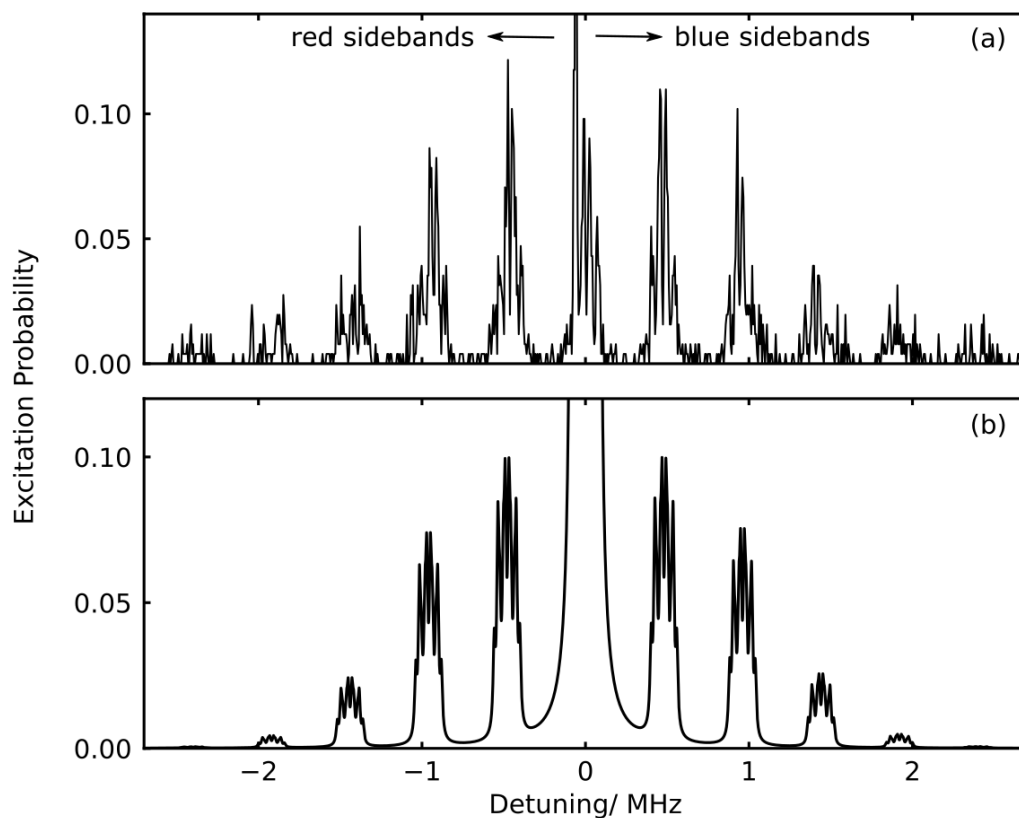


Figure 8.8: Sideband spectra. (a) Example experimental sideband spectrum taken with an axial secular frequency of 480 kHz. The carrier is centred at a detuning of 0 MHz. Sidebands with negative detunings are red and with positive detunings are blue. (b) Simulated sideband spectrum (see Appendix D).

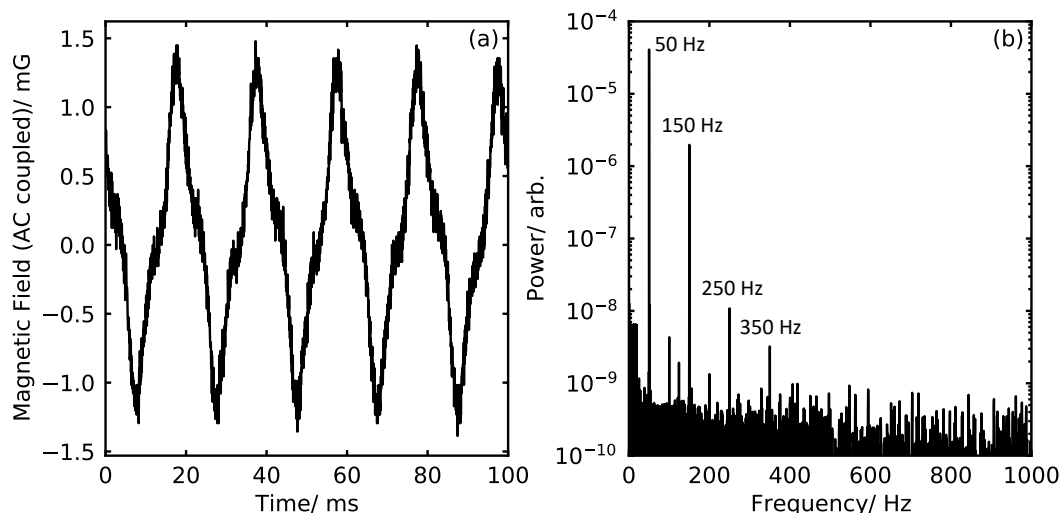


Figure 8.9: The magnetic field fluctuations measured close to the trap. (a) The magnetic field measured over 100 ms. (b) Spectrum of magnetic field noise from FFT of measurements from longer measurement times.

## 8.4 Results

### 8.4.1 Quadrupole Spectra

The magnetic field was set so that the Zeeman splitting was smaller than the secular frequency (e.g. Figure 8.7(a)). Peak splittings and relative strengths were consistent with simulations. Fitting the experimental data using the simulation (with free parameters of magnetic field, linewidth and an overall multiplying factor), yielded a reasonable fit (Figure 8.7(b)).

In addition to high resolution spectroscopy, this quadrupole transition will be used to cool the ions into the ground state by exciting red sideband transitions. With a low magnetic field to prevent overlap between sidebands, a broad spectrum was taken. For a secular frequency of  $2\pi \cdot 480$  kHz, five sidebands on either side of the carrier band were clearly visible (Figure 8.8).

### 8.4.2 Magnetic Field Broadening

The magnetic field in the laboratory changes on multiple timescales. There is a dc component caused by the Earth's magnetic field and other permanent magnets in the vicinity. In addition, there is a large component at 50 Hz and multiples thereof which comes from the mains electricity supply and devices that use it. There is also some noise at other frequencies, fast and slow, from unknown sources.

The magnetic field in the laboratory was measured using a homemade magnetic field

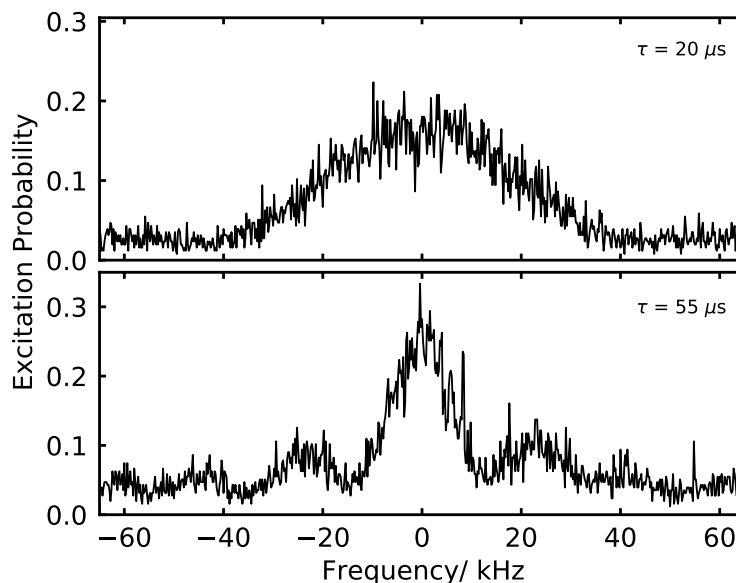


Figure 8.10: Peaks in the quadrupole spectrum for probe times of  $20 \mu\text{s}$  and  $55 \mu\text{s}$ . In the case of the Fourier limited peak with a  $55 \mu\text{s}$  probe time, the sinc wiggles arising from the square pulse of the probe laser are visible.

sensor<sup>d</sup>. The field was measured near to the trap after the magnetic field had been reduced by changing the current source for the compensation solenoids. The observed field was a triangular wave composed of harmonics of 50 Hz (Figure 8.9). The amplitude of this wave was approximately 2 mG.

As the energies of the Zeeman sublevels depend on the magnitude of the magnetic field, any changes of the magnetic field on a fast timescale relative to the scan rate will be observed as broadening. Each transition has a different dependence on the magnetic field and so the different peaks in the spectrum will be broadened by different amounts. The realistic magnetic field, approximately triangular in shape, is expected to result in a “squaring” of the lineshape.

### 8.4.3 Linewidths

The linewidth is important for future spectroscopy. In metrology applications, the important parameter is the ratio of the frequency resolution to the frequency. In order to perform high resolution spectroscopy, a linewidth of  $<10$  Hz is desirable. To reduce the linewidth, a single peak was isolated and narrowed by eliminating unnecessary magnetic field fluctuations and increasing the duration of the excitation pulse.

Initially, spectra were obtained using a probe time of  $20 \mu\text{s}$  for which the Fourier limit is approximately 22 kHz. However, the width and shape of the lines observed showed that the Fourier limit was not reached at this stage (Figure 8.10).

<sup>d</sup>Honeywell HMC1001

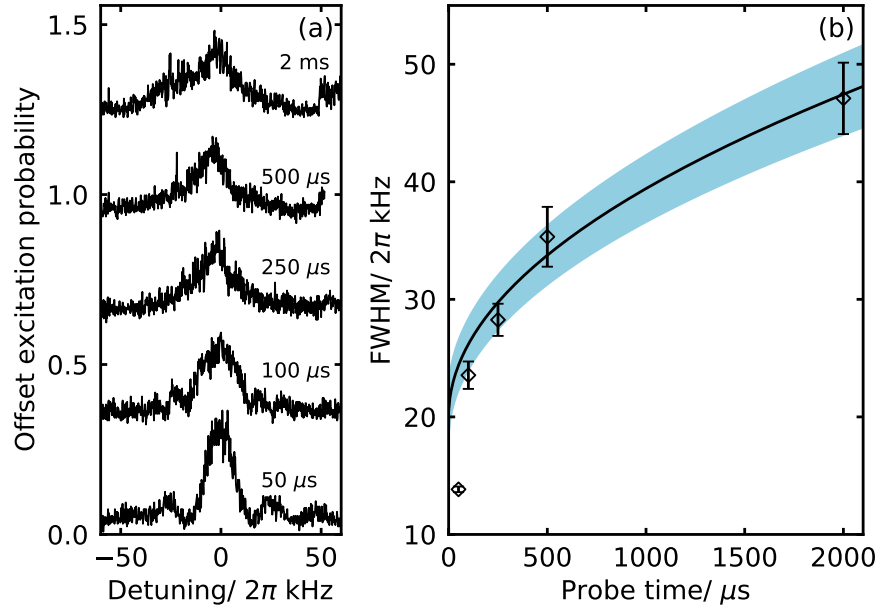


Figure 8.11: The effect of probe time on the quadrupole peak linewidths. (a) Example peaks for probe times between  $50\mu\text{s}$  and  $2\text{ ms}$ . (b) The full widths at half maximum (FWHM) of peaks with the probe time.

Reaching the Fourier limit required mitigation of the dominant broadening mechanism. The magnetic field noise at harmonics of  $50\text{ Hz}$  was identified as the source of this broadening. The current supply for the field compensation solenoids was found to produce magnetic field noise at harmonics of  $50\text{ Hz}$  so it was replaced by three separate laser current controllers, one for each pair of solenoids. This significantly reduced the linewidth to the Fourier limit for a pulse duration of  $55\mu\text{s}$  (Figure 8.10).

To reduce the linewidth further, longer measurement times were needed to push the Fourier limit to lower linewidths. Initially, when the probe time was increased, the linewidth decreased. However, as the probe time was increased further, the linewidth began to increase (Figure 8.11). This broadening could be countered by reducing the power of the probe laser until a limit was reached (Figure 8.12).

Increasing the pulse duration from  $20\mu\text{s}$  to  $15\text{ ms}$  decreased the linewidth to approximately  $3\text{ kHz}$ , which corresponds to a fractional resolution of  $\frac{\Delta\nu}{\nu} \sim 1 \times 10^{-11}$ . This is still limited by the magnetic field noise.

#### 8.4.4 Rabi Flopping and Decoherence

One measure of the stability of important parameters such as the magnetic field is the decoherence of Rabi oscillations. The probability of excitation of one transition in the spectrum was recorded for different probe times (see Figure 8.4). This yielded Rabi oscillations with a decay constant of  $100\mu\text{s}$ . It was notable that increasing the power of the  $729\text{ nm}$  laser did not increase the Rabi frequency, which may be due to a large contribution

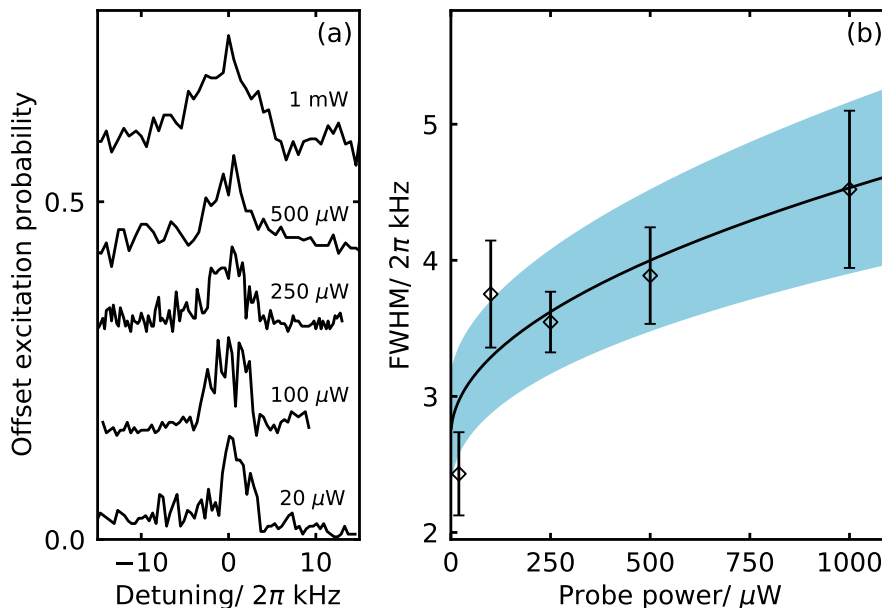


Figure 8.12: The effect of probe laser power on the quadrupole peak linewidths. (a) Peaks observed for probe powers 20  $\mu$ W and 1 mW with a probe time of 10 ms. (b) Full widths at half maximum (FWHM) for different powers of the 729 nm probe laser.

of amplified spontaneous emission at higher powers caused by the tapered amplifier in the 729 nm set-up.

## 8.5 Discussion

The existing results have demonstrated spectroscopy on the quadrupole transitions which are consistent with the simulations of the expected spectra. The linewidths are still about three orders of magnitude larger than should be possible e.g.<sup>130</sup>, most likely due to the magnetic field fluctuations measured in the laboratory. Sideband spectra have also been obtained which can be used in the future for sideband cooling to the ground state.

The spectrum of the magnetic field noise in the laboratory near the ion trap is dominated by noise from mains equipment at 50 Hz and harmonics thereof. This is very difficult to eliminate due to the need to run many devices from the mains in order to run this experiment and others. One option would be to install magnetic shielding. However, this is expensive and limited by the need for holes to allow laser, vacuum pump, molecular beam and imaging access. The alternative is dynamic stabilisation which is the route we intend to go down in the short term. This method uses magnetic field sensors placed around the trap to interpolate the magnetic field within the trap. From these measurements, a compensating signal would be generated as feedback for the magnetic field compensation coils. It should be possible to implement this feedback fast enough to compensate for 50+ Hz fluctuations.

One of the next steps for this part of the experiment is to implement this dynamic magnetic

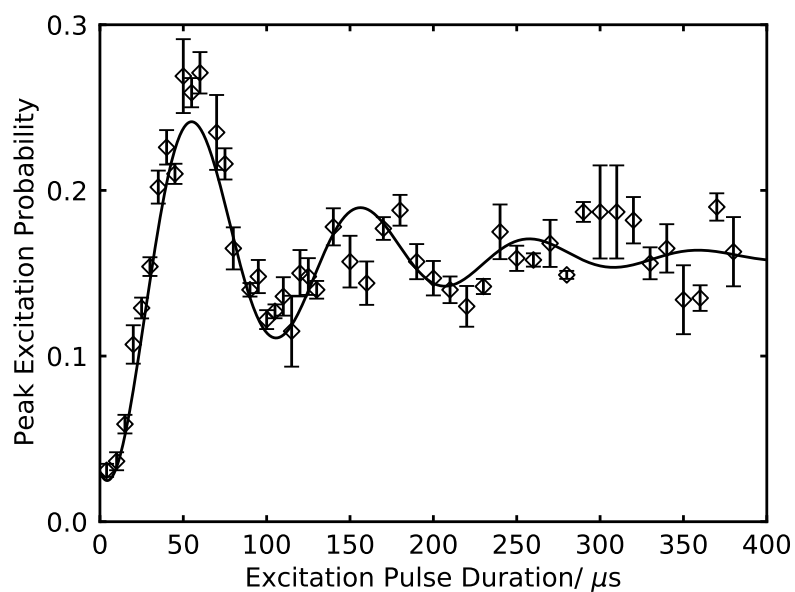


Figure 8.13: The peak excitation probability measured from spectra. The duration of the 729 nm laser pulse was scanned to observe Rabi oscillations.

field stabilisation to reduce the linewidths of the peaks in the spectrum. This is important because the fractional uncertainty in the high resolution spectroscopy measurements will depend on the precision of the calcium spectra. In addition, the quantum logic scheme relies on ground state cooling of the calcium ion's motional state along the trap axis. This will be achieved by exciting red sidebands. Finally, these techniques need to be implemented in the nitrogen trap and integrated into the main experiment.

## Chapter 9

# Conclusions and Outlook

Observations contradictory to the predictions of the Standard Model have led to many theories which predict changes in fundamental constants. High resolution spectroscopy of rotational and vibrational transitions in molecular ions can probe this potential variation in fundamental constants. Of these, there is a vibrational transition in the nitrogen molecular ion of particular interest.

In order to perform the desired high resolution spectroscopy, the ion must first be loaded in the rovibronic ground state with high fidelity. Spectroscopy of the quadrupole transition in calcium, which will be used for cooling and state readout of the nitrogen state, must also be characterised. The next step is to implement a quantum logic spectroscopy scheme to perform high resolution spectroscopy of nitrogen.

When this doctoral project started, the ion trap and molecular beam system were already in place (see A. Gardner's thesis<sup>3</sup>). The aim of the work in this project was to do ground work for high resolution spectroscopy of calcium and nitrogen ions. In the following sections, the main conclusions are discussed and the future of this work is explored.

### 9.1 Conclusions

The distribution of ionisation thresholds across the trapping region in a typical rf trap can be broad enough to prevent state-selective ionisation of molecules. The extent of the broadening and its impact depend on the specific target molecular ion, the trapping parameters and the level of selectivity required. While some ion traps already operate with sufficiently low drive frequencies and electrode voltages, many experiments require high confinements which must be adjusted whilst loading to obtain a high purity of ions in the desired internal state. In these cases, the width of the ionisation threshold can be reduced by adjusting the trap parameters or by rapidly switching the trap off and on again to coincide with the timing of the ionisation lasers. For state-selective REMPI in an ion trap, the choice of trap parameters is crucial and, by employing other mitigation

techniques such as trap switching, loading of high frequency traps is feasible.

Switching the trap off rapidly can reduce the electric fields in the ion trap without the loss of ions. This switching does, however, cause heating of the trapped ions. This effect worsens for long rf switch-off times and for high field gradients during dc switching. It is unclear how dc field switching might be possible in a trap where the ions were not trapped by the rf field alone. This is because switching without the loss of ions requires switch-off times on the order of 10 ms, which is very long compared to the period of the secular motion. When the rf field is switched off for similar times, the ions are unrecoverable.

Switching the trap off should enable state-selective ionisation by reducing broadening by a factor of  $>1000$  for both the rf and dc fields. In a trap where there is sufficient axial trapping with low to no dc voltage, this is a promising option for the state-selective loading of molecular ions by threshold photoionisation methods. Nitrogen molecular ions have been trapped in this way. The effect of any heating caused on the rate at which new ions cool into the crystal is not yet known, but the high energy of the incoming nitrogen ion is likely to dominate.

Nitrogen ions have been loaded into the trap via electron ionisation in order to characterise the system before REMPI was attempted. This was facilitated by the scatter of a pulsed laser on the electrodes, resulting in the acceleration of electrons by the strong electric fields inside the trap. The ionisation probability increased linearly with the pulse energy of the laser and was maximised at the maximum of the rf electric field oscillation. This was used to obtain the temporal profile of the molecular beam, showing a peak in ionisation probability approximately  $3.2 \mu\text{s}$  after the pulse valve was triggered.

The trap switching method was used to load nitrogen ions into the ion trap. This offers a proof-of-concept that loading molecular ions while the trap is switched off is practicable. The S0 transition was scanned and a clear resonance was observed, confirming that the ions were loaded via 2+2 REMPI. The mean arrival time of ions was  $80 \pm 10 \text{ s}$ , which is long relative to the chemical lifetime of trapped nitrogen ions. Further investigation of the factors affecting the sympathetic cooling dynamics is needed.

Spectroscopy has been carried out on the  $S_{1/2} \rightarrow D_{5/2}$  transition in a single  $^{40}\text{Ca}^+$  ion in a linear Paul trap. This facilitated peak widths of  $\sim 3 \text{ kHz}$  in the best case, corresponding to a Q factor of  $\sim 1 \times 10^{11}$ . Fluctuations in the magnetic field in the laboratory were the dominant cause of the persisting broadening. To achieve narrow peaks, the power of the probe laser was reduced significantly as otherwise saturation broadening was observed for longer pulse times. In addition to broadening, the magnetic field instability resulted in a fast decay of Rabi oscillations. This fast decoherence is likely to be the result of poor magnetic field stability in the laboratory.

## 9.2 Outlook

In order to load nitrogen ions state-selectively, it remains to load via the desired  $2+1'$  process and explore the effect of switching the trap drive on the ionisation threshold experimentally. The techniques required to do this have been thoroughly characterised. However, the cooling dynamics have not been fully explored. The chemical lifetime of nitrogen in the ion trap is reasonably short, and so in order to maximise the time available for spectroscopy, the loading time should be as short as possible. The sympathetic cooling of nitrogen ions into the trap under different loading conditions can be explored to optimise the loading parameters for future experiments. The difference between the cooling rate with and without trap switching has yet to be explored.

Once the loading of nitrogen has been investigated and reliably implemented, the next steps will be towards carrying out spectroscopy of the  $(v, N, F, M) = (0, 0, 1/2, \pm 1/2) \rightarrow (2, 0, 1/2, \pm 1/2)$  transition of the  $X^2\Sigma_g$  state. This requires further optimisation of the calcium quadrupole spectroscopy and implementation of sideband cooling. The lasers for the Raman spectroscopy need to be set up and the quantum logic detection scheme needs to be implemented.

In order to perform precision spectroscopy, the linewidths of the calcium quadrupole spectra will need to be made narrower. The limiting factor is currently the magnetic field fluctuations in the laboratory. The predominant source of this noise is mains electricity with typical frequencies at harmonics of 50 Hz. The magnetic field will be stabilised in the future using active stabilisation, with magnetic field sensors placed around the trap.

Once these steps are completed, the nitrogen spectroscopy will be carried out using a quantum logic scheme. The calcium-nitrogen crystal will be cooled to its motional ground state using sideband cooling on the  $S_{1/2} \rightarrow D_{5/2}$  transition in the calcium ion. The  $v = 0 \rightarrow v = 2$  vibrational transition in the ground  $X^2\Sigma_g^+$  state of the nitrogen ion will be driven as a Raman transition using lasers at 714 nm and 1030 nm (Figure 9.1, A). This will leave the nitrogen ion in either the  $v = 2$  state (if the transition is successful) or in the original  $v = 0$  state (if the transition is unsuccessful).

In the following step, two counter-propagating lasers at 780 nm, separated in frequency by the sum of the Zeeman detuning and the secular frequency, form a walking wave. This will drive population in the  $v = 0$  to the other magnetic sublevel and transfer the crystal into the  $n = 1$  motional state (Figure 9.1, B I). If the nitrogen ion is in the  $v = 2$  state, then it does not gain any motional energy and remains in the  $n = 0$  state (Figure 9.1, B II). This maps the state of the nitrogen ion onto the shared motion of the crystal.

The motional state of the crystal can be interrogated by driving the first red sideband of the  $S_{1/2} \rightarrow D_{5/2}$  transition in calcium. If the spectroscopy transition was successful, then the calcium ion will remain in the light  $S_{1/2}$  state and fluorescence photons will be detected (Figure 9.1, C I). Whereas, if the transition was unsuccessful, the calcium ion will be excited to the dark  $D_{5/2}$  state and it will not fluoresce (Figure 9.1, C II). By photon

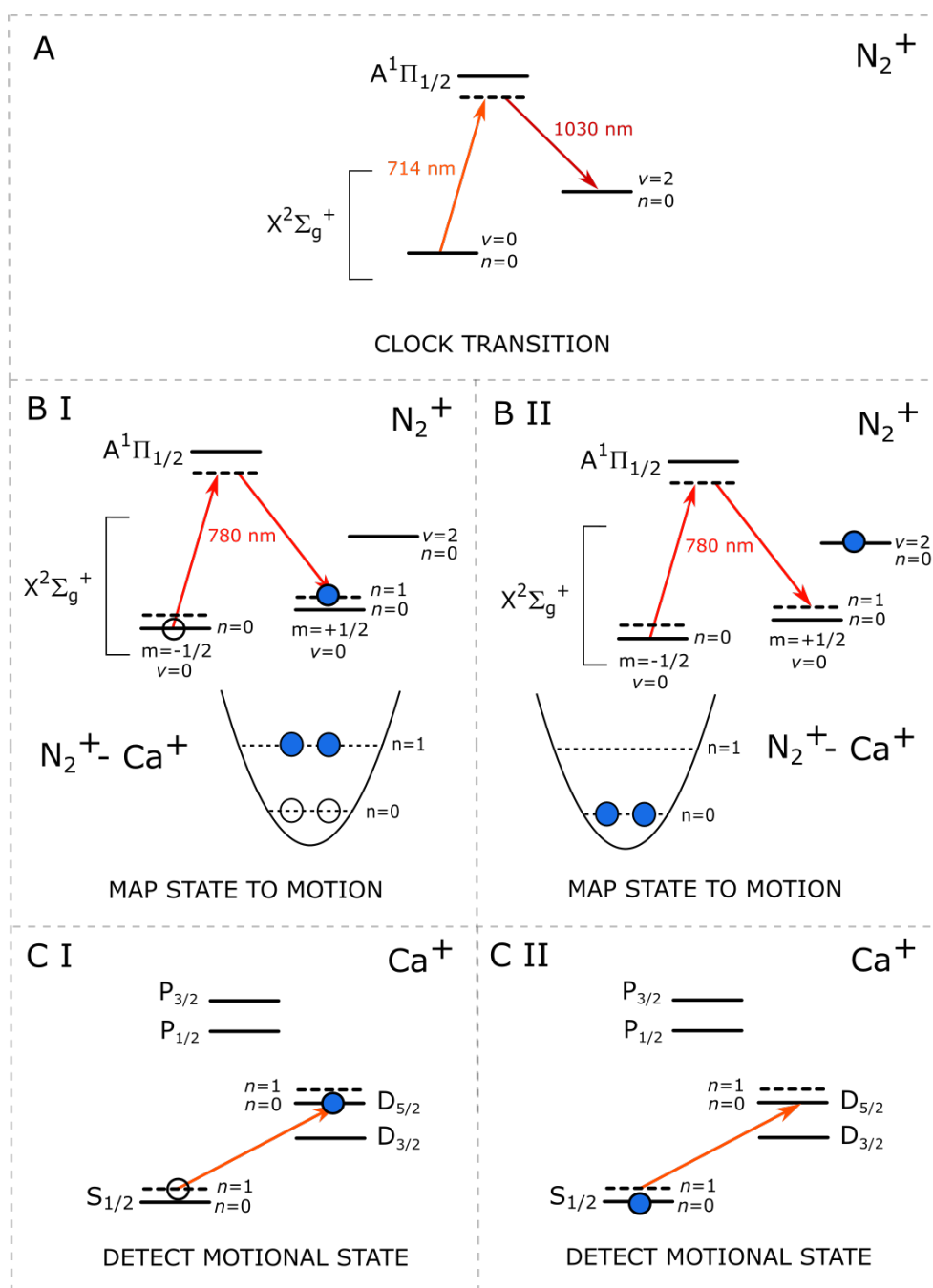


Figure 9.1: The proposed quantum logic spectroscopy scheme. The crystal of one nitrogen ion and one calcium ion is cooled to the motional ground state. A) The clock transition in nitrogen is probed using a Raman transition. B) A walking wave at 780 nm excited the motional state of the nitrogen ion if step A was unsuccessful and not if the transition was successfully completed. The motion of the nitrogen ion is also transferred to the co-trapped calcium ion. C) The first red sideband of the calcium ion is driven and if the crystal is still in the motional ground state (if the nitrogen ion is in the  $v = 2$  state) the calcium ion will remain in the light  $S_{1/2}$  state. If the crystal has gained motional energy during the logic scheme (if the nitrogen is in the  $v = 0$  state) then this transition can occur and the calcium ion will be excited to the dark  $D_{5/2}$  state. The state of the calcium ion can be read out by detecting fluorescence.

statistics, the state of the nitrogen ion can then be determined.

## Bibliography

- [1] A. Corney, *Atomic and laser spectroscopy*, Clarendon Press, Oxford, 2006.
- [2] D. James, Quantum dynamics of cold trapped ions with application to quantum computation, *Applied Physics B: Lasers and Optics*, 1998, **66**, 181–190, DOI: 10.1007/s003400050373.
- [3] A. A. Gardner, *Ph.D. thesis*, University of Sussex, 2016.
- [4] S. Willitsch, M. T. Bell, A. D. Gingell and T. P. Softley, Chemical applications of laser- and sympathetically-cooled ions in ion traps, *Physical Chemistry Chemical Physics*, 2008, **10**, 7200, DOI: 10.1039/b813408c.
- [5] S. Ospelkaus, K.-K. Ni, D. Wang, M. H. G. de Miranda, B. Neyenhuis, G. Quéméner, P. S. Julienne, J. L. Bohn, D. S. Jin and J. Ye, Quantum-State Controlled Chemical Reactions of Ultracold Potassium-Rubidium Molecules, *Science*, 2010, **327**, 853–857, DOI: 10.1126/science.1184121.
- [6] E. R. Hudson and W. C. Campbell, Dipolar quantum logic for freely rotating trapped molecular ions, *Physical Review A*, 2018, **98**, 040302, DOI: 10.1103/PhysRevA.98.040302.
- [7] J.-P. Karr, S. Patra, J. C. J. Koelemeij, J. Heinrich, N. Sillitoe, A. Douillet and L. Hilico, Hydrogen molecular ions: new schemes for metrology and fundamental physics tests, *Journal of Physics: Conference Series*, 2016, **723**, 012048, DOI: 10.1088/1742-6596/723/1/012048.
- [8] M. Safronova, D. Budker, D. DeMille, D. F. J. Kimball, A. Derevianko and C. W. Clark, Search for new physics with atoms and molecules, *Reviews of Modern Physics*, 2018, **90**, 025008, DOI: 10.1103/RevModPhys.90.025008.
- [9] R. Rugango, J. E. Goeders, T. H. Dixon, J. M. Gray, N. B. Khanyile, G. Shu, R. J. Clark and K. R. Brown, Sympathetic cooling of molecular ion motion to the ground state, *New Journal of Physics*, 2015, **17**, 035009, DOI: 10.1088/1367-2630/17/3/035009.
- [10] P. O. Schmidt, Spectroscopy Using Quantum Logic, *Science*, 2005, **309**, 749–752, DOI: 10.1126/science.1114375.

- [11] D. DeMille, S. Sainis, J. Sage, T. Bergeman, S. Kotochigova and E. Tiesinga, Enhanced Sensitivity to Variation of  $m_e/m_p$  in Molecular Spectra, *Physical Review Letters*, 2008, **100**, 043202, DOI: 10.1103/PhysRevLett.100.043202.
- [12] M. Kajita, G. Gopakumar, M. Abe, M. Hada and M. Keller, Test of  $m_p/m_e$  changes using vibrational transitions in  $N_2^+$ , *Physical Review A*, 2014, **89**, 032509, DOI: 10.1103/PhysRevA.89.032509.
- [13] M. Kajita, Accuracy estimation of the  $^{16}O_2^+$  transition frequencies targeting the search for the variation in the proton-electron mass ratio, *Physical Review A*, 2017, **95**, 023418, DOI: 10.1103/PhysRevA.95.023418.
- [14] M. G. Kokish, P. R. Stollenwerk, M. Kajita and B. C. Odom, Prospects for a polar-molecular-ion optical probe of varying proton-electron mass ratio, *Physical Review A*, 2018, **98**, 052513, DOI: 10.1103/PhysRevA.98.052513.
- [15] S. Schiller and V. Korobov, Tests of time independence of the electron and nuclear masses with ultracold molecules, *Physical Review A*, 2005, **71**, 032505, DOI: 10.1103/PhysRevA.71.032505.
- [16] J.-P. Karr, L. Hilico, J. C. J. Koelemeij and V. I. Korobov, Hydrogen molecular ions for improved determination of fundamental constants, *Physical Review A*, 2016, **94**, 050501, DOI: 10.1103/PhysRevA.94.050501.
- [17] J. Biesheuvel, J.-P. Karr, L. Hilico, K. S. E. Eikema, W. Ubachs and J. C. J. Koelemeij, Probing QED and fundamental constants through laser spectroscopy of vibrational transitions in  $HD^+$ , *Nature Communications*, 2016, **7**, 10385, DOI: 10.1038/ncomms10385.
- [18] E. R. Meyer, J. L. Bohn and M. P. Deskevich, Candidate molecular ions for an electron electric dipole moment experiment, *Physical Review A*, 2006, **73**, 062108, DOI: 10.1103/PhysRevA.73.062108.
- [19] W. B. Cairncross, D. N. Gresh, M. Grau, K. C. Cossel, T. S. Roussy, Y. Ni, Y. Zhou, J. Ye and E. A. Cornell, Precision Measurement of the Electron's Electric Dipole Moment Using Trapped Molecular Ions, *Physical Review Letters*, 2017, **119**, 153001, DOI: 10.1103/PhysRevLett.119.153001.
- [20] D. Patterson, Method for preparation and readout of polyatomic molecules in single quantum states, *Physical Review A*, 2018, **97**, 033403, DOI: 10.1103/PhysRevA.97.033403.
- [21] M. Quack, J. Stohner and M. Willeke, High-Resolution Spectroscopic Studies and Theory of Parity Violation in Chiral Molecules, *Annual Review of Physical Chemistry*, 2008, **59**, 741–769, DOI: 10.1146/annurev.physchem.58.032806.104511.
- [22] A. Borschevsky, M. Iliaš, V. A. Dzuba, K. Beloy, V. V. Flambaum and P. Schwerdtfeger, Nuclear-spin-dependent parity violation in diatomic molecular ions, *Physical Review A*, 2012, **86**, 050501, DOI: 10.1103/PhysRevA.86.050501.

- [23] S. Chatrchyan *et al.*, Observation of a new boson at a mass of 125 GeV with the CMS experiment at the LHC, *Physics Letters B*, 2012, **716**, 30–61, DOI: 10.1016/j.physletb.2012.08.021.
- [24] G. Aad *et al.*, Observation of a new particle in the search for the Standard Model Higgs boson with the ATLAS detector at the LHC, *Physics Letters B*, 2012, **716**, 1–29, DOI: 10.1016/j.physletb.2012.08.020.
- [25] F. Gianotti and T. S. Virdee, The discovery and measurements of a Higgs boson, *Philosophical Transactions of the Royal Society A*, 2015, **373**, 20140384, DOI: 10.1098/rsta.2014.0384.
- [26] M. Dine and A. Kusenko, Origin of the matter-antimatter asymmetry, *Reviews of Modern Physics*, 2003, **76**, 1–30, DOI: 10.1103/RevModPhys.76.1.
- [27] The T2K Collaboration *et al.*, Constraint on the matter–antimatter symmetry-violating phase in neutrino oscillations, *Nature*, 2020, **580**, 339–344, DOI: 10.1038/s41586-020-2177-0.
- [28] S. Perlmutter, Nobel Lecture: Measuring the acceleration of the cosmic expansion using supernovae, *Reviews of Modern Physics*, 2012, **84**, 1127–1149, DOI: 10.1103/RevModPhys.84.1127.
- [29] A. G. Riess, Nobel Lecture: My path to the accelerating Universe, *Reviews of Modern Physics*, 2012, **84**, 1165–1175, DOI: 10.1103/RevModPhys.84.1165.
- [30] B. P. Schmidt, Nobel Lecture: Accelerating expansion of the Universe through observations of distant supernovae, *Reviews of Modern Physics*, 2012, **84**, 1151–1163, DOI: 10.1103/RevModPhys.84.1151.
- [31] G. Bertone and D. Hooper, History of dark matter, *Reviews of Modern Physics*, 2018, **90**, 045002, DOI: 10.1103/RevModPhys.90.045002.
- [32] J.-P. Uzan, Varying Constants, Gravitation and Cosmology, *Living Reviews in Relativity*, 2011, **14**, 2, DOI: 10.12942/lrr-2011-2.
- [33] J. Khoury and A. Weltman, Chameleon Fields: Awaiting Surprises for Tests of Gravity in Space, *Physical Review Letters*, 2004, **93**, 171104, DOI: 10.1103/PhysRevLett.93.171104.
- [34] Y. Stadnik and V. Flambaum, Can Dark Matter Induce Cosmological Evolution of the Fundamental Constants of Nature?, *Physical Review Letters*, 2015, **115**, 201301, DOI: 10.1103/PhysRevLett.115.201301.
- [35] J.-P. Uzan, The fundamental constants and their variation: observational and theoretical status, *Reviews of Modern Physics*, 2003, **75**, 403–455, DOI: 10.1103/RevModPhys.75.403.

- [36] J. C. Berengut and V. V. Flambaum, Astronomical and laboratory searches for space-time variation of fundamental constants, *Journal of Physics: Conference Series*, 2011, **264**, 012010, DOI: 10.1088/1742-6596/264/1/012010.
- [37] J. K. Webb, J. A. King, M. T. Murphy, V. V. Flambaum, R. F. Carswell and M. B. Bainbridge, Indications of a Spatial Variation of the Fine Structure Constant, *Physical Review Letters*, 2011, **107**, 191101, DOI: 10.1103/PhysRevLett.107.191101.
- [38] S. João, C. Martins, I. Mota and P. Vianez, On the stability of fundamental couplings in the Galaxy, *Physics Letters B*, 2015, **749**, 389–392, DOI: 10.1016/j.physletb.2015.08.018.
- [39] L. Hart and J. Chluba, Updated fundamental constant constraints from Planck 2018 data and possible relations to the Hubble tension, *Monthly Notices of the Royal Astronomical Society*, 2020, **493**, 3255–3263, DOI: 10.1093/mnras/staa412.
- [40] H. Chand, R. Srikanand, P. Petitjean and B. Aracil, Probing the cosmological variation of the fine-structure constant: Results based on VLT-UVES sample, *Astronomy & Astrophysics*, 2004, **417**, 853–871, DOI: 10.1051/0004-6361:20035701.
- [41] J. Lodewyck, On a definition of the SI second with a set of optical clock transitions, *Metrologia*, 2019, **56**, 055009, DOI: 10.1088/1681-7575/ab3a82.
- [42] B. L. S. Marlow and D. R. Scherer, A Review of Commercial and Emerging Atomic Frequency Standards, *IEEE Transactions on Ultrasonics, Ferroelectrics, and Frequency Control*, 2021, **68**, 2007–2022, DOI: 10.1109/TUFFC.2021.3049713.
- [43] X. Calmet and M. Keller, Cosmological evolution of fundamental constants: From theory to experiment, *Modern Physics Letters A*, 2015, **30**, 1540028, DOI: 10.1142/S0217732315400283.
- [44] T. Zelevinsky, S. Kotochigova and J. Ye, Precision Test of Mass-Ratio Variations with Lattice-Confined Ultracold Molecules, *Physical Review Letters*, 2008, **100**, 043201, DOI: 10.1103/PhysRevLett.100.043201.
- [45] S. Brewer, J.-S. Chen, A. Hankin, E. Clements, C. Chou, D. Wineland, D. Hume and D. Leibbrandt,  $^{27}\text{Al}^+$  Quantum-Logic Clock with a Systematic Uncertainty below  $10^{18}$ , *Physical Review Letters*, 2019, **123**, 033201, DOI: 10.1103/PhysRevLett.123.033201.
- [46] R. Godun, P. Nisbet-Jones, J. Jones, S. King, L. Johnson, H. Margolis, K. Szymaniec, S. Lea, K. Bongs and P. Gill, Frequency Ratio of Two Optical Clock Transitions in  $^{171}\text{Yb}^+$  and Constraints on the Time Variation of Fundamental Constants, *Physical Review Letters*, 2014, **113**, 210801, DOI: 10.1103/PhysRevLett.113.210801.
- [47] B. M. Roberts *et al.*, Search for transient variations of the fine structure constant and dark matter using fiber-linked optical atomic clocks, *New Journal of Physics*, 2020, **22**, 093010, DOI: 10.1088/1367-2630/abaace.

- [48] R. Lange, N. Huntemann, J. Rahm, C. Sanner, H. Shao, B. Lipphardt, C. Tamm, S. Weyers and E. Peik, Improved Limits for Violations of Local Position Invariance from Atomic Clock Comparisons, *Physical Review Letters*, 2021, **126**, 011102, DOI: 10.1103/PhysRevLett.126.011102.
- [49] R. Hobson, W. Bowden, A. Vianello, A. Silva, C. F. A. Baynham, H. S. Margolis, P. E. G. Baird, P. Gill and I. R. Hill, A strontium optical lattice clock with  $1 \times 10^{17}$  uncertainty and measurement of its absolute frequency, *Metrologia*, 2020, **57**, 065026, DOI: 10.1088/1681-7575/abb530.
- [50] M. S. Safronova, S. G. Porsev, C. Sanner and J. Ye, Two Clock Transitions in Neutral Yb for the Highest Sensitivity to Variations of the Fine-Structure Constant, *Physical Review Letters*, 2018, **120**, 173001, DOI: 10.1103/PhysRevLett.120.173001.
- [51] M. Takamoto *et al.*, Frequency ratios of Sr, Yb, and Hg based optical lattice clocks and their applications, *Comptes Rendus Physique*, 2015, **16**, 489–498, DOI: 10.1016/j.crhy.2015.04.003.
- [52] G. Barontini *et al.*, Measuring the stability of fundamental constants with a network of clocks, *EPJ Quantum Technology*, 2022, **9**, 12, DOI: 10.1140/epjqt/s40507-022-00130-5.
- [53] S. S. Kondov, C.-H. Lee, K. H. Leung, C. Liedl, I. Majewska, R. Moszynski and T. Zelevinsky, Molecular lattice clock with long vibrational coherence, *Nature Physics*, 2019, **15**, 1118–1122, DOI: 10.1038/s41567-019-0632-3.
- [54] Y. Huang, B. Zhang, M. Zeng, Y. Hao, Z. Ma, H. Zhang, H. Guan, Z. Chen, M. Wang and K. Gao, Liquid-Nitrogen-Cooled  $\text{Ca}^+$  Optical Clock with Systematic Uncertainty of  $3 \times 10^{-18}$ , *Physical Review Applied*, 2022, **17**, 034041, DOI: 10.1103/PhysRevApplied.17.034041.
- [55] J.-P. Karr,  $\text{H}_2^+$  and  $\text{HD}^+$ : Candidates for a molecular clock, *Journal of Molecular Spectroscopy*, 2014, **300**, 37–43, DOI: 10.1016/j.jms.2014.03.016.
- [56] I. V. Kortunov, S. Alighanbari, M. G. Hansen, G. S. Giri, V. I. Korobov and S. Schiller, Proton–electron mass ratio by high-resolution optical spectroscopy of ion ensembles in the resolved-carrier regime, *Nature Physics*, 2021, **17**, 569–573, DOI: 10.1038/s41567-020-01150-7.
- [57] M. Kajita and Y. Moriwaki, Proposed detection of variation in  $m_p/m_e$  using a vibrational transition frequency of a  $\text{CaH}^+$  ion, *Journal of Physics B: Atomic, Molecular and Optical Physics*, 2009, **42**, 154022, DOI: 10.1088/0953-4075/42/15/154022.
- [58] M. Kajita, M. Abe, M. Hada and Y. Moriwaki, Estimated accuracies of pure  $\text{XH}^+$  (X: even isotopes of group II atoms) vibrational transition frequencies: towards the test of the variance in  $m_p/m_e$ , *Journal of Physics B: Atomic, Molecular and Optical Physics*, 2011, **44**, 025402, DOI: 10.1088/0953-4075/44/2/025402.

- [59] M. Kajita, M. Abe, M. Hada and Y. Moriwaki, Proposed detection of variation in  $m_p/m_e$  using a vibrational transition frequency of a  $\text{CaH}^+$  ion, Estimated accuracies of pure  $\text{XH}^+$  (X: even isotopes of group II atoms) vibrational transition frequencies: towards the test of the variance in  $m_p/m_e$ , *Journal of Physics B: Atomic, Molecular and Optical Physics*, 2011, **44**, 209802, DOI: 10.1088/0953-4075/44/20/209802.
- [60] V. V. Flambaum and M. G. Kozlov, Enhanced sensitivity to the time variation of the fine structure constant and  $m_p/m_e$  in diatomic molecules, *Physical Review Letters*, 2007, **99**, 150801, DOI: 10.1103/PhysRevLett.99.150801.
- [61] M. G. Kozlov, M. S. Safronova, J. R. Crespo López-Urrutia and P. O. Schmidt, Highly charged ions: Optical clocks and applications in fundamental physics, *Reviews of Modern Physics*, 2018, **90**, 045005, DOI: 10.1103/RevModPhys.90.045005.
- [62] P. Micke, T. Leopold, S. A. King, E. Benkler, L. J. Spieß, L. Schmöger, M. Schwarz, J. R. Crespo López-Urrutia and P. O. Schmidt, Coherent laser spectroscopy of highly charged ions using quantum logic, *Nature*, 2020, **578**, 60–65, DOI: 10.1038/s41586-020-1959-8.
- [63] J. C. Berengut, V. A. Dzuba, V. V. Flambaum and A. Ong, Electron-Hole Transitions in Multiply Charged Ions for Precision Laser Spectroscopy and Searching for Variations in  $\alpha$ , *Physical Review Letters*, 2011, **106**, 210802, DOI: 10.1103/PhysRevLett.106.210802.
- [64] J. C. Berengut, V. A. Dzuba, V. V. Flambaum and A. Ong, Highly charged ions with  $E1$ ,  $M1$ , and  $E2$  transitions within laser range, *Physical Review A*, 2012, **86**, 022517, DOI: 10.1103/PhysRevA.86.022517.
- [65] J. C. Berengut, V. A. Dzuba, V. V. Flambaum and A. Ong, Optical Transitions in Highly Charged Californium Ions with High Sensitivity to Variation of the Fine-Structure Constant, *Physical Review Letters*, 2012, **109**, 070802, DOI: 10.1103/PhysRevLett.109.070802.
- [66] P. G. Thirolf, B. Seiferle and L. von der Wense, The 229-thorium isomer: doorway to the road from the atomic clock to the nuclear clock, *Journal of Physics B: Atomic, Molecular and Optical Physics*, 2019, **52**, 203001, DOI: 10.1088/1361-6455/ab29b8.
- [67] E. Peik, T. Schumm, M. S. Safronova, A. Pálffy, J. Weitenberg and P. G. Thirolf, Nuclear clocks for testing fundamental physics, *Quantum Science and Technology*, 2021, **6**, 034002, DOI: 10.1088/2058-9565/abe9c2.
- [68] V. V. Flambaum and A. F. Tedesco, Dependence of nuclear magnetic moments on quark masses and limits on temporal variation of fundamental constants from atomic clock experiments, *Physical Review C*, 2006, **73**, 055501, DOI: 10.1103/PhysRevC.73.055501.
- [69] E. Peik and C. Tamm, Nuclear laser spectroscopy of the 3.5 eV transition in Th-229, *Europhysics Letters (EPL)*, 2003, **61**, 181–186, DOI: 10.1209/epl/i2003-00210-x.

- [70] P. W. Atkins and R. Friedman, *Molecular quantum mechanics*, Oxford University Press, Oxford ; New York, 5th edn., 2011.
- [71] M. Safronova, Dansha Jiang, Bindiya Arora, C. Clark, M. Kozlov, U. Safronova and W. Johnson, Black-body radiation shifts and theoretical contributions to atomic clock research, *IEEE Transactions on Ultrasonics, Ferroelectrics and Frequency Control*, 2010, **57**, 94–105, DOI: 10.1109/TUFFC.2010.1384.
- [72] K. Gao, The  $^{40}\text{Ca}^+$  ion optical clock, *National Science Review*, 2020, **7**, 1799–1801, DOI: 10.1093/nsr/nwaa119.
- [73] A. Gardner, T. Softley and M. Keller, Multi-photon ionisation spectroscopy for rotational state preparation of  $\text{N}_2^+$ , *Scientific Reports*, 2019, **9**, 506, DOI: 10.1038/s41598-018-36783-5.
- [74] X. Tong, A. H. Winney and S. Willitsch, Sympathetic Cooling of Molecular Ions in Selected Rotational and Vibrational States Produced by Threshold Photoionization, *Physical Review Letters*, 2010, **105**, 143001, DOI: 10.1103/PhysRevLett.105.143001.
- [75] X. Tong, D. Wild and S. Willitsch, Collisional and radiative effects in the state-selective preparation of translationally cold molecular ions in ion traps, *Physical Review A*, 2011, **83**, 023415, DOI: 10.1103/PhysRevA.83.023415.
- [76] P. R. Stollenwerk, I. O. Antonov and B. C. Odom, IP determination and 1+1 REMPI spectrum of SiO at 210–220 nm in an ion trap: Implications for  $\text{SiO}^+$  ion trap loading, *Journal of Molecular Spectroscopy*, 2019, **355**, 40–45, DOI: 10.1016/j.jms.2018.11.008.
- [77] P. K. Ghosh, *Ion traps*, Clarendon Press ; Oxford University Press, Oxford : New York, 1995.
- [78] E. I. Butikov, Analytical expressions for stability regions in the Ince–Strutt diagram of Mathieu equation, *American Journal of Physics*, 2018, **86**, 257–267, DOI: 10.1119/1.5021895.
- [79] H. Li, Y. Zhang, S. He and X. Tong, Determination of the geometric parameters and of a linear Paul trap, *Chinese Journal of Physics*, 2019, **60**, 61–67, DOI: 10.1016/j.cjph.2019.03.017.
- [80] D. J. Berkeland, J. D. Miller, J. C. Bergquist, W. M. Itano and D. J. Wineland, Minimization of ion micromotion in a Paul trap, *Journal of Applied Physics*, 1998, **83**, 5025–5033, DOI: 10.1063/1.367318.
- [81] E. L. Pollock and J. P. Hansen, Statistical Mechanics of Dense Ionized Matter. II. Equilibrium Properties and Melting Transition of the Crystallized One-Component Plasma, *Physical Review A*, 1973, **8**, 3110–3122, DOI: 10.1103/PhysRevA.8.3110.

- [82] L. S. Petralia, A. Tsikritea, J. Loreau, T. P. Softley and B. R. Heazlewood, Strong inverse kinetic isotope effect observed in ammonia charge exchange reactions, *Nature Communications*, 2020, **11**, 173, DOI: 10.1038/s41467-019-13976-8.
- [83] B. Friedrich and H. Schmidt-Böcking, *Molecular beams in physics and chemistry: from Otto Stern's pioneering exploits to present-day feats*, Springer International Publishing, 2021.
- [84] *Atomic and molecular beam methods*, ed. G. Scoles, Oxford University Press, New York, 1988.
- [85] M. Patel, J. Thomas and H. C. Joshi, Flow characterization of supersonic gas jets: Experiments and simulations, *Vacuum*, 2021, **192**, 110440, DOI: 10.1016/j.vacuum.2021.110440.
- [86] T. E. Wall, Preparation of cold molecules for high-precision measurements, *Journal of Physics B: Atomic, Molecular and Optical Physics*, 2016, **49**, 243001, DOI: 10.1088/0953-4075/49/24/243001.
- [87] T. Moriyama, H. Yamaguchi, K. Ide, Y. Matsuda, Y. Egami and T. Niimi, 1511 Measurement of rotational energy distribution in nitrogen molecular beam by REMPI, *The Proceedings of the Fluids engineering conference*, 2010, **2010**, 455–456, DOI: 10.1299/jsmefed.2010.455.
- [88] P. M. Mayer and T. Baer, A photoionization study of vibrational cooling in molecular beams, *International Journal of Mass Spectrometry and Ion Processes*, 1996, **156**, 133–139, DOI: [https://doi.org/10.1016/S0168-1176\(96\)04422-9](https://doi.org/10.1016/S0168-1176(96)04422-9).
- [89] J. Bolton and S. Freake, *The Quantum World: Quantum mechanics of matter*, Open University, Milton Keynes, 2007.
- [90] B. H. Bransden, C. J. Joachain and B. H. Bransden, *Quantum mechanics*, Prentice Hall, Harlow, England ; New York, 2nd edn., 2000.
- [91] F. Le Kien, T. Ray, T. Nieddu, T. Busch and S. Nic Chormaic, Enhancement of the quadrupole interaction of an atom with the guided light of an ultrathin optical fiber, *Physical Review A*, 2018, **97**, 013821, DOI: 10.1103/PhysRevA.97.013821.
- [92] T. Ray, R. K. Gupta, V. Gokhroo, J. L. Everett, T. Nieddu, K. S. Rajasree and S. N. Chormaic, Observation of the  $^{87}\text{Rb } ^5\text{S}_{1/2}$  to  $^4\text{D}_{3/2}$  electric quadrupole transition at 516.6 nm mediated via an optical nanofibre, *New Journal of Physics*, 2020, **22**, 062001, DOI: 10.1088/1367-2630/ab8265.
- [93] G. Mainfray and G. Manus, Multiphoton ionization of atoms, *Reports on Progress in Physics*, 1991, **54**, 1333–1372, DOI: 10.1088/0034-4885/54/10/002.
- [94] N. V. Vitanov, A. A. Rangelov, B. W. Shore and K. Bergmann, Stimulated Raman adiabatic passage in physics, chemistry, and beyond, *Reviews of Modern Physics*, 2017, **89**, 015006, DOI: 10.1103/RevModPhys.89.015006.

- [95] M. Šimečková, D. Jacquemart, L. S. Rothman, R. R. Gamache and A. Goldman, Einstein A-coefficients and statistical weights for molecular absorption transitions in the HITRAN database, *Journal of Quantitative Spectroscopy and Radiative Transfer*, 2006, **98**, 130–155, DOI: 10.1086/190149.
- [96] J. B. Tatum, The Interpretation of Intensities in Diatomic Molecular Spectra, *Astrophysical Journal Supplement*, 1967, **14**, 21, DOI: 10.1086/190149.
- [97] H. J. Metcalf and P. van der Straten, Laser cooling and trapping of atoms, *Journal of the Optical Society of America B*, 2003, **20**, 887–908, DOI: 10.1364/JOSAB.20.000887.
- [98] D. J. Wineland, R. E. Drullinger and F. L. Walls, Radiation-Pressure Cooling of Bound Resonant Absorbers, *Physical Review Letters*, 1978, **40**, 1639–1642, DOI: 10.1103/PhysRevLett.40.1639.
- [99] W. Neuhauser, M. Hohenstatt, P. Toschek and H. Dehmelt, Optical-Sideband Cooling of Visible Atom Cloud Confined in Parabolic Well, *Physical Review Letters*, 1978, **41**, 233–236, DOI: 10.1103/PhysRevLett.41.233.
- [100] F. Diedrich, J. C. Bergquist, W. M. Itano and D. J. Wineland, Laser Cooling to the Zero-Point Energy of Motion, *Physical Review Letters*, 1989, **62**, 403–406, DOI: 10.1103/PhysRevLett.62.403.
- [101] D. J. Wineland, J. Dalibard and C. Cohen-Tannoudji, Sisyphus cooling of a bound atom, *Journal of the Optical Society of America B*, 1992, **9**, 32, DOI: 10.1364/JOSAB.9.000032.
- [102] D. Egorov, T. Lahaye, W. Schöllkopf, B. Friedrich and J. M. Doyle, Buffer-gas cooling of atomic and molecular beams, *Physical Review A*, 2002, **66**, 043401, DOI: 10.1103/PhysRevA.66.043401.
- [103] M. Lara, J. L. Bohn, D. Potter, P. Soldán and J. M. Hutson, Ultracold Rb-OH Collisions and Prospects for Sympathetic Cooling, *Physical Review Letters*, 2006, **97**, 183201, DOI: 10.1103/PhysRevLett.97.183201.
- [104] Y. Wan, F. Gebert, F. Wolf and P. O. Schmidt, Efficient sympathetic motional-ground-state cooling of a molecular ion, *Physical Review A*, 2015, **91**, 043425, DOI: 10.1103/PhysRevA.91.043425.
- [105] S. Ribeiro and H. Terças, Sympathetic laser cooling of graphene with Casimir-Polder forces, *Physical Review A*, 2016, **94**, 043420, DOI: 10.1103/PhysRevA.94.043420.
- [106] M. J. Winter, *Chemical Bonding*, Oxford Science Publications, 1994.
- [107] P. W. Atkins and J. De Paula, *Atkins' Physical chemistry*, Oxford University Press, Oxford ; New York, 9th edn., 2010.

- [108] N. Seymour-Smith, P. Blythe, M. Keller and W. Lange, Fast scanning cavity offset lock for laser frequency drift stabilization, *Review of Scientific Instruments*, 2010, **81**, 075109, DOI: 10.1063/1.3455830.
- [109] K. Sheridan and M. Keller, Weighing of trapped ion crystals and its applications, *New Journal of Physics*, 2011, **13**, 123002, DOI: 10.1088/1367-2630/13/12/123002.
- [110] J. B. M. Warntjes, F. Robicheaux, J. M. Bakker and L. D. Noordam, Autoionizing Rydberg states of NO in strong electric fields, *The Journal of Chemical Physics*, 1999, **111**, 2556–2564, DOI: 10.1063/1.479533.
- [111] W. A. Chupka, Factors affecting lifetimes and resolution of Rydberg states observed in zero-electron-kinetic-energy spectroscopy, *The Journal of Chemical Physics*, 1993, **98**, 4520–4530, DOI: 10.1063/1.465011.
- [112] M. S. Child, *Theory of Molecular Rydberg States*, Cambridge University Press, Cambridge, 2011, DOI: 10.1017/CBO9780511994814.
- [113] S. Mackenzie, F. Merkt, E. Halse and T. Softley, Rotational state selectivity in  $N_2^+ X^2\Sigma_g^+$  ( $v^+ = 0$ ) by delayed pulsed field ionization spectroscopy via the  $a''^1\Sigma_g^+$  ( $v' = 0$ ) state, *Molecular Physics*, 1995, **86**, 1283–1297, DOI: 10.1080/00268979500102731.
- [114] G. S. Agarwal, Field-Correlation Effects in Multiphoton Absorption Processes, *Physical Review A*, 1970, **1**, 1445, DOI: 10.1103/PhysRevA.1.1445.
- [115] R. Singh, Potential-energy curves for  $O_2^+$ ,  $N_2^+$ , and  $CO^+$ , *Journal of Molecular Spectroscopy*, 1966, **19**, 424, DOI: 10.1016/0022-2852(66)90265-7.
- [116] N. Deb, L. L. Pollum, A. D. Smith, M. Keller, C. J. Rennick, B. R. Heazlewood and T. P. Softley, Coulomb crystal mass spectrometry in a digital ion trap, *Physical Review A*, 2015, **91**, 033408, DOI: 10.1103/PhysRevA.91.033408.
- [117] J. H. Wesenberg *et al.*, Fluorescence during Doppler cooling of a single trapped atom, *Physical Review A*, 2007, **76**, 053416, DOI: 10.1103/PhysRevA.76.053416.
- [118] T. Sikorsky, Z. Meir, N. Akerman, R. Ben-shlomi and R. Ozeri, Doppler cooling thermometry of a multilevel ion in the presence of micromotion, *Physical Review A*, 2017, **96**, 012519, DOI: 10.1103/PhysRevA.96.012519.
- [119] N. Deb, B. R. Heazlewood, M. T. Bell and T. P. Softley, Blackbody-mediated rotational laser cooling schemes in  $MgH^+$ ,  $DCl^+$ ,  $HCl^+$ ,  $LiH$  and  $CsH$ , *Physical Chemistry Chemical Physics*, 2013, **15**, 14270, DOI: 10.1039/c3cp51839f.
- [120] P. Stollenwerk, M. Kokish, A. de Oliveira-Filho, F. Ornellas and B. Odom, Optical Pumping of  $TeH^+$ : Implications for the Search for Varying  $m_p/m_e$ , *Atoms*, 2018, **6**, 53, DOI: 10.3390/atoms6030053.
- [121] T. Schneider, B. Roth, H. Duncker, I. Ernsting and S. Schiller, All-optical preparation of molecular ions in the rovibrational ground state, *Nature Physics*, 2010, **6**, 275–278, DOI: 10.1038/nphys1605.

- [122] P. F. Sta anum, K. Høj bjerre, P. S. Skyt, A. K. Hansen and M. Drewsen, Rotational laser cooling of vibrationally and translationally cold molecular ions, *Nature Physics*, 2010, **6**, 271–274, DOI: 10.1038/nphys1604.
- [123] C.-w. Chou, C. Kurz, D. B. Hume, P. N. Plessow, D. R. Leibbrandt and D. Leibfried, Preparation and coherent manipulation of pure quantum states of a single molecular ion, *Nature*, 2017, **545**, 203–207, DOI: 10.1038/nature22338.
- [124] S. Mark, T. Glenewinkel-Meyer and D. Gerlich, REMPI in a focusing rf-quadrupole: a new source for mass-, energy-, and state-selected ions, *International Reviews in Physical Chemistry*, 1996, **15**, 283–298, DOI: 10.1080/01442359609353185.
- [125] S. Opitz, D. Proch, T. Trickl and K. Kompa, State-selective ionization of nitrogen by resonance-enhanced three- and four-photon excitation, *Chemical Physics*, 1990, **143**, 305–323, DOI: 10.1016/0301-0104(90)89108-3.
- [126] T. Trickl, E. F. Cromwell, Y. T. Lee and A. H. Kung, State-selective ionization of nitrogen in the  $X^2\Sigma_g^+$   $v_+=0$  and  $v_+=1$  states by two-color (1+1) photon excitation near threshold, *The Journal of Chemical Physics*, 1989, **91**, 6006–6012, DOI: 10.1063/1.457417.
- [127] X. Tong, T. Nagy, J. Y. Reyes, M. Germann, M. Meuwly and S. Willitsch, State-selected ion–molecule reactions with Coulomb-crystallized molecular ions in traps, *Chemical Physics Letters*, 2012, **547**, 1–8, DOI: 10.1016/j.cplett.2012.06.042.
- [128] A. J. Dempster, A new Method of Positive Ray Analysis, *Physical Review*, 1918, **11**, 316–325, DOI: 10.1103/PhysRev.11.316.
- [129] G. Gamez, L. Zhu, T. A. Schmitz and R. Zenobi, Photoelectron Emission as an Alternative Electron Impact Ionization Source for Ion Trap Mass Spectrometry, *Analytical Chemistry*, 2008, **80**, 6791–6795, DOI: 10.1021/ac8007187.
- [130] M. Chwalla *et al.*, Absolute Frequency Measurement of the  $^{40}\text{Ca}^+$   $4s^2S_{1/2} - 3d^2D_{5/2}$  Clock Transition, *Physical Review Letters*, 2009, **102**, 023002, DOI: 10.1103/PhysRevLett.102.023002.
- [131] Y. Huang, J. Cao, P. Liu, K. Liang, B. Ou, H. Guan, X. Huang, T. Li and K. Gao, Hertz-level measurement of the  $^{40}\text{Ca}^+$   $4s^2S_{1/2} - 3d^2D_{5/2}$  clock transition frequency with respect to the SI second through the Global Positioning System, *Physical Review A*, 2012, **85**, 030503, DOI: 10.1103/PhysRevA.85.030503.
- [132] P. Sta anum, I. S. Jensen, R. G. Martinussen, D. Voigt and M. Drewsen, Lifetime measurement of the metastable  $3d^2D_{5/2}$  state in the  $^{40}\text{Ca}^+$  ion using the shelving technique on a few-ion string, *Physical Review A*, 2004, **69**, 032503, DOI: 10.1103/PhysRevA.69.032503.
- [133] P. A. Barton, C. J. S. Donald, D. M. Lucas, D. A. Stevens, A. M. Steane and D. N. Stacey, Measurement of the lifetime of the  $3d^2D_{5/2}$  state in  $^{40}\text{Ca}^+$ , *Physical Review A*, 2000, **62**, 032503, DOI: 10.1103/PhysRevA.62.032503.

- [134] K. T. Sheridan, *Ph.D. thesis*, University of Sussex, 2013.
- [135] F. Papoff, F. Mauri and E. Arimondo, Transient velocity-selective coherent population trapping in one dimension, *Journal of the Optical Society of America B*, 1992, **9**, 321–331, DOI: 10.1364/JOSAB.9.000321.
- [136] C. Cohen-Tanouji, Atom-Photon Interactions, *Lillienfeld Prize Lecture*, MIT, 1992.
- [137] D. J. Berkeland and M. G. Boshier, Destabilization of dark states and optical spectroscopy in Zeeman-degenerate atomic systems, *Physical Review A*, 2002, **65**, 033413, DOI: 10.1103/PhysRevA.65.033413.
- [138] T. Lindvall, M. Merimaa, I. Tuttonen and A. A. Madej, Dark-state suppression and optimization of laser cooling and fluorescence in a trapped alkaline-earth-metal single ion, *Physical Review A*, 2012, **86**, 033403, DOI: 10.1103/PhysRevA.86.033403.
- [139] R. E. Ryan and T. H. Bergeman, Hanle effect in nonmonochromatic laser light, *Physical Review A*, 1991, **43**, 6142.
- [140] A. G. Riley-Watson, *Ph.D. thesis*, University of Sussex, 2013.
- [141] C. Roos, *Ph.D. thesis*, Universität Innsbruck, 2000.
- [142] G. Poulsen, *Ph.D. thesis*, University of Aarhus, 2012.

## Appendix A

# Data Availability

Data plotted in Chapter 5 can be found at <https://doi.org/10.25377/sussex.13060295>. The simulation code used in the same chapter can be found at <https://doi.org/10.25377/sussex.13063628>.

## Appendix B

# Automation of the Loading Process

The automation procedure was developed to enable recording of the necessary data without the need for intensive human intervention and to enable timing and efficient recording of all relevant data. The automated loading sequence was programmed as a state machine in LabVIEW. This enabled the program to make decisions based on synchronous analysis of photon count, crystal weighing and CCD imaging data via Python nodes.

### B.1 Overview

Automated loading was used for the loading probability data taken in Chapter 7. The state machine was based on the flowchart in Figure B.1. Further detail is shown in the following subsections for the highlighted sections. This program facilitated loading of calcium ions, loading of nitrogen ions, tracking of crystal composition and the scanning of parameters.

This automated system was operated with two different measurement schemes. In the first, used for the molecular beam and rf phase scans, the crystal was imaged and weighed at each time step. In the second, used for the scan of the  $S_0$  transition with REMPI, the crystal image was recorded at each time step and the crystal was weighed at the end of the measurement. This was to allow us to extract the cooling times without the crystal weighing disrupting the cooling rate.

#### B.1.1 Calcium Loading Sequence

Calcium is loaded as described in Chapter 4. First, the oven is turned on by a switch controlled by a TTL pulse. Next the shutters for the calcium ionisation lasers are opened. The count rate on the PMT above the trap is measured by a DAQ at intervals of approximately 200 ms. If the count rate exceeds a threshold, the oven and ionisation lasers are switched off. Otherwise, they are switched off once the loading time limit is exceeded.

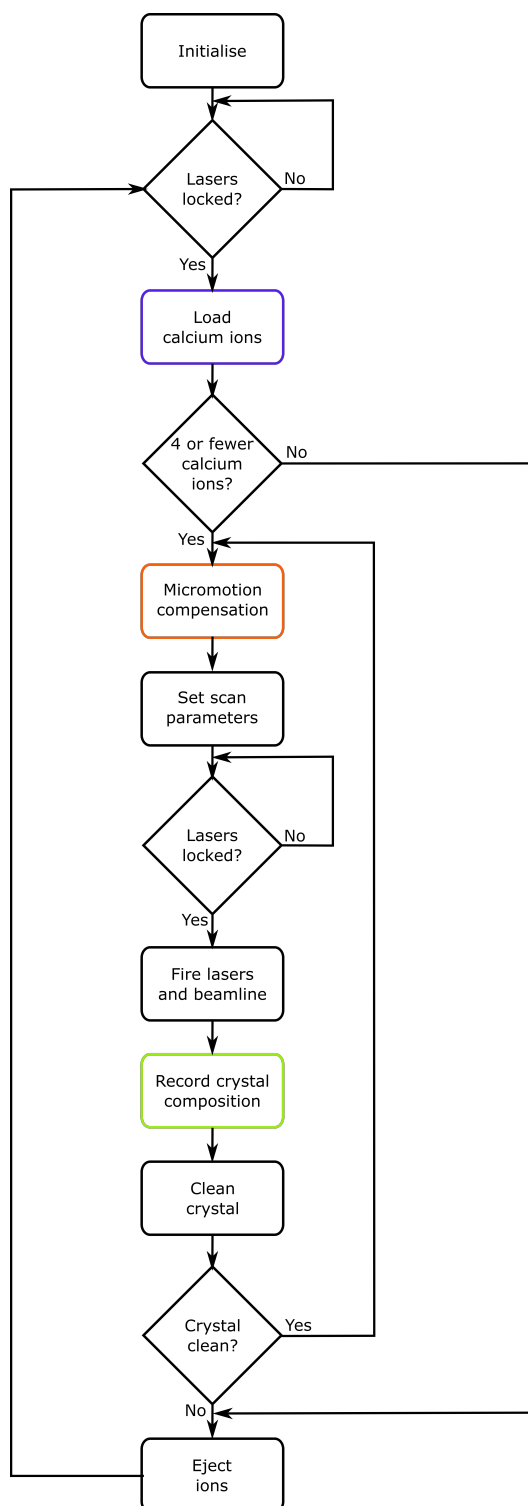


Figure B.1: Flowchart showing the automation sequence.

After the oven is switched off, the program checks whether ions have been loaded. It compares the count rate measured on the PMT to the aforementioned threshold. When the count rate exceeds the threshold, the program moves to the next phase. Otherwise, once the wait time is over the trap is switched off briefly to eject any uncrystallised ions and the loading process begins again from the start.

In the next phase of the program, the count rate is measured at intervals of 10 s over at least 70 s to check that all loaded ions have crystallised into the trap. This is to reduce confusion later on when conducting measurements and to prevent any effect that uncrystallised calcium ions could have on the cooling dynamics of arriving nitrogen ions. When the difference between consecutive measurements was less than 1,500 counts per second, the ions were presumed to have settled. If the ions had settled, the program would move on to the next stage in the general flow chart. If the ions do not settle in the designated time frame, they are ejected and the loading process restarts.

## B.2 Micromotion Compensation Sequence

The nitrogen ionisation lasers can create patch potentials on the electrodes that change the dc electric field in the ion trap. This in turn will shift the ion crystal away from the rf minimum in the trap and increase the excess micromotion. As the cycle was repeated many times to build up loading statistics, the micromotion compensation sequence should be as short as possible. To ensure accuracy, the micromotion compensation was only performed when a single ion was loaded.

### B.2.0.1 The Principle of the Method

Due to the linear geometry of the trap, the micromotion along the axial axis and within the radial plane can be considered separately. For the axial field compensation, the measurement time can be reduced by measuring the micromotion amplitude for a small number of axial compensation voltages ( $X$ ). A straight line can be fitted to this data to extract the zero-crossing of the amplitude (as in Chapter 4).

In the radial plane, the method differs from measurements described in Chapter 4. In the previous method, the compensation voltages were set to the intersection point of two lines where the micromotion amplitude was minimised for the two radial lasers (see Figure 4.25). The gradients of these lines depend on the geometry of the lasers and the trap, but are constant unless the angles of the lasers with respect to the trap change. Changes in the stray fields will manifest as a change in the offset of these lines.

All that is needed to define each line is the gradient, which will be unchanged from the previous measurements, and a single point on the line. By choosing to measure the micromotion at  $(H, V)$  coordinates that lie on the normal to the line, a small number of points may be used. If possible, points either side of the minimum micromotion point

should be used so that the zero-crossing of the micromotion amplitude lies within the probed range. Points on the normal can be found by solving the simultaneous equations:

$$d = \sqrt{(H_1 - H_{\text{line}})^2 + (V_1 - V_{\text{line}})^2}, \quad (\text{B.1})$$

and

$$V_1 = \frac{-1}{m} \cdot H_1 + \zeta_1. \quad (\text{B.2})$$

The intercept,  $\zeta_{1/2}$  of each line can be determined from the zero-crossing of the normal,  $(H_{\text{point}}, V_{\text{point}})$ , and the gradient,  $m_{1/2}$ , according to

$$\zeta_{1/2} = V_{\text{point}} - m_{1/2} \cdot H_{\text{point}}. \quad (\text{B.3})$$

This can be done for both lasers. The intersection of the two lines,  $(H_{\text{best}}, V_{\text{best}})$ , can then be calculated from the two intercepts and gradients

$$H_{\text{best}} = \frac{\zeta_2 - \zeta_1}{m_1 - m_2}; \quad V_{\text{best}} = m_1 \cdot H_{\text{best}} + \zeta_1. \quad (\text{B.4})$$

A generalised version of this method to compensate micromotion in three coupled dimensions is described in A. Riley-Watson's thesis.<sup>140</sup>

### B.2.1 The Practical Implementation of the Method

In practice, this method of micromotion compensation was implemented within the larger state machine using a combination of LabVIEW and Python code. LabVIEW was used to control the TDC, DAQ and lasers while Python nodes provided the functionality to fit sine waves to the photon-correlation histograms, select H,V pairs on the normal to the lines of minimum micromotion and calculate the relevant intersections. To avoid applying voltages that could significantly destabilise the ions, the voltages are coerced to within a sensible range and discarded if outside it.

## B.3 Crystal Weighing

The crystal weighing sequence uses the method described in Chapter 4. The secular frequency is determined using a Python script to perform a FFT followed by a fit to the tallest peak. From the centre of this peak, the secular frequency is determined.

## B.4 Crystal Cleaning

In the case of nitrogen ions being loaded or calcium ions reacting with water, it is necessary to start the next cycle of the loading process with a clean crystal of only  $\text{Ca}^+$  ions. This can be achieved by discarding the trapped ions and reloading the trap with calcium. However,

this is time consuming and so it is preferable to find a way to clean an existing crystal contaminated with non- $\text{Ca}^+$  ions. This is implemented by applying a signal to one of the axial electrodes at the secular frequency for a pure crystal of each contaminant. In this case, the crystal was cleaned using a frequency for  $[\text{Ca-OH}]^+$  followed by a frequency for  $\text{N}_2$ . It was not possible to clean  $[\text{N}_2\text{-OH}]^+$  from the crystal because its mass-to-charge ratio is very similar to that of calcium. Exciting at the secular frequency of  $[\text{N}_2\text{-OH}]^+$  causes considerable excitation of the motion of the calcium ions.

## Appendix C

# Nitrogen Ionisation Laser

The excitation laser at 255 nm is a pulsed dye laser<sup>a</sup> pumped with a Nd:YAG laser<sup>b</sup>. The dye used is Coumarin 307 in ethanol (0.4 g/l for oscillator and 0.1 g/l for amplifier). The output from the dye laser passes through a doubling crystal to obtain light at 255 nm.

Due to the dynamics of the laser, the delay in the arrival of the laser pulse depends on the pulse energy of the pump laser. This is in turn controlled by the Q-switch delay of the Nd:YAG laser. As the Q-switch delay (and pulse energy) is increased, the pulse arrives earlier (Figure C.1).

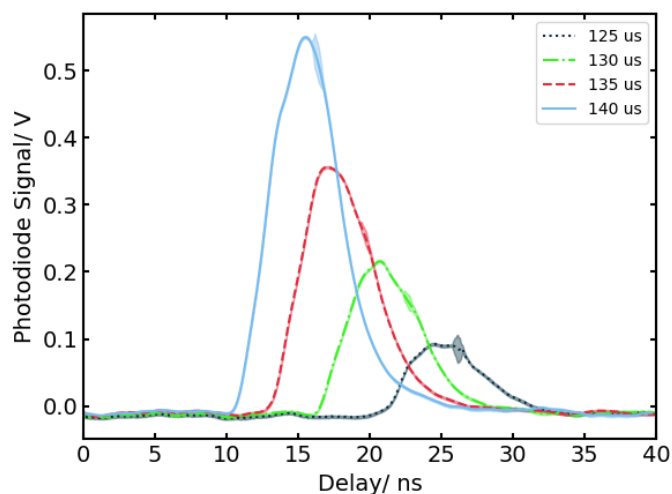


Figure C.1: The temporal profiles of laser pulses for different Q-switch delays of the Nd:YAG laser used to pump the 255 nm dye laser.

The most probable cause of this is the excitation dynamics. Changing the dye, which effectively increased the gain of the dye laser, shifted the peaks to shorter delays. Maintaining the synchronisation of the laser is complicated by the changing dynamics as the dye degrades and the gain drops.

<sup>a</sup>Radiant Dyes, Narrowscan

<sup>b</sup>Continuum, Surelite 2

The pulse energy of the excitation laser was stabilised to ensure the photon energy was constant across the full scanning range (Figure C.2). This was done at higher pulse energies than the operational energies used to ensure reliable measurement with the pulse energy meter<sup>c</sup>.

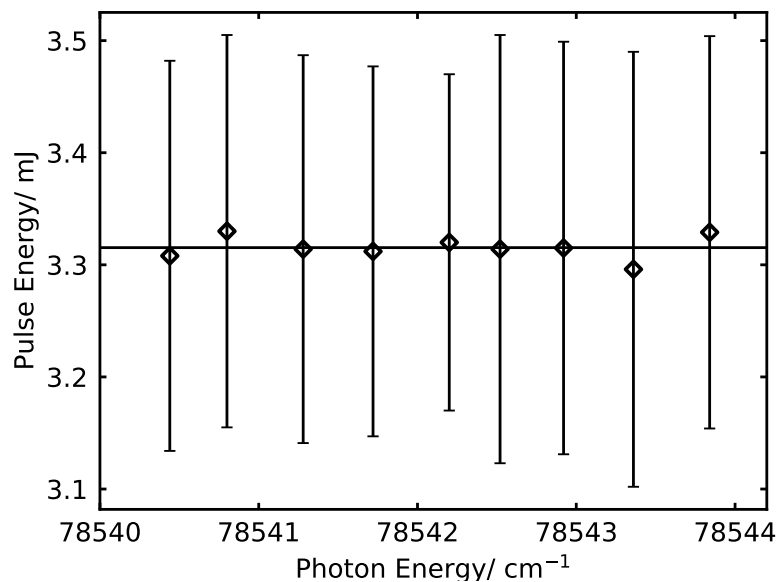


Figure C.2: The pulse energy of the excitation laser at different photon energies. The Q switch delays used in these measurements correspond to higher energies than were used in the experiment.

<sup>c</sup>Thorlabs, PM100USB with ES220C head

## Appendix D

# Simulation Methods: Quadrupole Spectra

There are ten peaks in the quadrupole spectrum which correspond to the ten possible transitions satisfying the selection rule  $\Delta m_j = 0, \pm 1, \pm 2$  for transitions from the  $S_{1/2}$  state to the  $D_{5/2}$  state. In addition to changes in the atomic state, the ion can also undergo transitions between motional states. That is, an atomic transition can be accompanied by a change in the motional quantum number.

### D.1 The Quadrupole Spectrum

For the purposes of the simulations, zero detuning is defined as the zero-field transition frequency of the  $S_{1/2} \rightarrow D_{5/2}$  transition. The ten observed transitions are split by a magnetic field due to the Zeeman effect. The frequency shift,  $\Delta\nu$ , of each peak due to the weak magnetic field is,

$$\Delta\nu = \frac{\mu_B \mathcal{B}}{h} (g_S m_{j_S} - g_D m_{j_D}), \quad (\text{D.1})$$

where  $\mathcal{B}$  is the magnetic field strength,  $\mu_B$  is the Bohr magneton,  $g_S$  and  $g_D$  are the gyromagnetic ratios, and  $m_{j_S}$  and  $m_{j_D}$  are the magnetic quantum numbers of the S and D states respectively. Equation D.1 can be used to find the positions of each peak in the spectrum. The coupling strengths for the different magnetic transitions are respectively given by (see<sup>141,142</sup>):

$$\begin{aligned} g_0 &= \frac{1}{2} |\cos(\gamma) \sin(2\phi)|, \\ g_{\pm 1} &= \frac{1}{\sqrt{6}} |\cos(\gamma) \cos(2\phi) + i \sin(\gamma) \cos(\phi)|, \\ g_{\pm 2} &= \frac{1}{\sqrt{6}} \left| \frac{1}{2} \cos(\gamma) \sin(2\phi) + i \sin(\gamma) \sin(\phi) \right|, \end{aligned} \quad (\text{D.2})$$

Table D.1: Table of Clebsch-Gordan (CG) coefficients and couplings for the relevant transitions in the calcium-40 ion<sup>141</sup>

Initial State	Final State	CG Coefficient	Coupling	Strength
$S_{1/2}, m_J = -1/2$	$D_{5/2}, m_J = -5/2$	1	$g_2$	$g_2$
$S_{1/2}, m_J = -1/2$	$D_{5/2}, m_J = -3/2$	$\sqrt{\frac{4}{5}}$	$g_1$	$\sqrt{\frac{4}{5}}g_1$
$S_{1/2}, m_J = -1/2$	$D_{5/2}, m_J = -1/2$	$\sqrt{\frac{3}{5}}$	$g_0$	$\sqrt{\frac{3}{5}}g_0$
$S_{1/2}, m_J = -1/2$	$D_{5/2}, m_J = +1/2$	$\sqrt{\frac{2}{5}}$	$g_1$	$\sqrt{\frac{2}{5}}g_1$
$S_{1/2}, m_J = -1/2$	$D_{5/2}, m_J = +3/2$	$\sqrt{\frac{1}{5}}$	$g_2$	$\sqrt{\frac{1}{5}}g_2$
$S_{1/2}, m_J = +1/2$	$D_{5/2}, m_J = -3/2$	$\sqrt{\frac{1}{5}}$	$g_2$	$\sqrt{\frac{1}{5}}g_2$
$S_{1/2}, m_J = +1/2$	$D_{5/2}, m_J = -1/2$	$\sqrt{\frac{2}{5}}$	$g_1$	$\sqrt{\frac{2}{5}}g_1$
$S_{1/2}, m_J = +1/2$	$D_{5/2}, m_J = +1/2$	$\sqrt{\frac{3}{5}}$	$g_0$	$\sqrt{\frac{3}{5}}g_0$
$S_{1/2}, m_J = +1/2$	$D_{5/2}, m_J = +3/2$	$\sqrt{\frac{4}{5}}$	$g_1$	$\sqrt{\frac{4}{5}}g_1$
$S_{1/2}, m_J = +1/2$	$D_{5/2}, m_J = +5/2$	1	$g_2$	$g_2$

where  $\phi$  is the angle between the wavevector of the incident photon and the magnetic field vector, in this case parallel; and  $\gamma$  is the angle between the magnetic field vector and the plane spanned by the polarisation and wavevector of the photon. The Clebsch-Gordan coefficients and the coupling strengths of the transitions are shown in Table D.1.

## D.2 The Motional Spectrum

Sidebands appear in the experimental quadrupole spectrum at frequencies of  $\nu_0 \pm \Delta n \nu_{\text{sec}}$ , where  $\Delta n$  is the change in motional quantum number during the transition, with a positive  $\Delta n$  corresponding to a gain of phonons (a blue sideband) and a negative  $\Delta n$  corresponding to loss of phonons (a red sideband). In addition to red and blue sidebands, there is also a central band corresponding to a transition in which the motion state of the ion is unchanged ( $\Delta n = 0$ ).

The strengths of the different sidebands,  $\rho_{\Delta n}$ , depend on the initial distribution of motional states and the Rabi frequencies for each sideband, according to

$$\rho_{\Delta n} = \sum_{n=0}^{\infty} P_n \cdot \sin^2(\Omega_{n,n+\Delta n} t / 2), \quad (\text{D.3})$$

where  $P_n$  is the probability that the ion is in motional state  $n$  initially and  $\Omega_{n,n+\Delta n}$  is the Rabi frequency for the quadrupole transition between motional states  $n$  and  $n + \Delta n$ .

The initial state population was assumed to be a Boltzmann distribution for an estimated ion temperature. The probability of a given motional state,  $n$ , being occupied is given by

$$P_n = \frac{\exp\left(\frac{-E_n}{k_B T}\right)}{Z}, \quad (\text{D.4})$$

where the partition function,  $Z$ , is

$$Z = \sum_{\kappa=0}^{\infty} \exp\left(\frac{-E_{\kappa}}{k_{\text{B}}T}\right), \quad (\text{D.5})$$

and  $E_{n/\kappa}$  are the motional energy levels.

The Rabi frequency  $\Omega_{n,n+\Delta n}$  is, in general, given by (see<sup>141</sup>)

$$\Omega_{n,n+\Delta n} = \Omega_0 \exp\left(-\frac{\eta^2}{2}\right) \eta^{|m|} L_n^{|m|}(\eta^2) \left(\frac{n!}{(n+\Delta n)!}\right)^{\text{sign}(m)/2}, \quad (\text{D.6})$$

where  $\eta$  is the Lamb-Dicke parameter

$$\eta = \frac{2\pi}{\lambda} \sqrt{\frac{\hbar}{2m_{\text{Ca}}\omega}}, \quad (\text{D.7})$$

$\Omega_0$  is the Rabi frequency of the central band and  $L_n^{|m|}(\eta^2)$  is a Laguerre polynomial of the form

$$L_n^{\alpha}(x) = \sum_{\kappa=0}^n (-1)^{\kappa} \binom{n+\alpha}{n-\kappa} \frac{x^{\kappa}}{\kappa!}. \quad (\text{D.8})$$

The Rabi frequency for each possible motional transition was calculated and the probabilities for transitions were summed according to Equation D.3.

For small magnetic fields where the Zeeman splitting is smaller than the secular frequency, the spectrum consists of bands of peaks. Each series corresponds to a different motional transition and the peaks within the band correspond to the different quadrupole transitions. The positions of the peaks were determined by adding the positions of the sidebands to the positions of the quadrupole transitions. The strength of each peak was taken to be the product of the atomic transition probability and sideband strength. The peak shape was assumed to be Lorentzian.